

https://dspace.org/

Effects of Ni-Mo binder and laser surface engineering of NbC based cutting inserts during face-milling of automotive grey cast iron

Rabothata, Mahlatse Solomon

2024

University of the Witwatersrand, Johannesburg

https://hdl.handle.net/10539/45541

Rabothata, Mahlatse Solomon . (2024). Effects of Ni-Mo binder and laser surface engineering of NbC based cutting inserts during face-milling of automotive grey cast iron [PhD thesis, University of the Witwatersrand, Johannesburg]. WIReDSpace. https://hdl.handle.net/10539/45541

Downloaded from a DSpace repository. https://dspace.org/

EFFECTS OF NI-MO BINDER AND LASER SURFACE ENGINEERING OF NbC BASED CUTTING INSERTS DURING FACE-MILLING OF AUTOMOTIVE GREY CAST IRON

Mahlatse Solomon Rabothata

Supervisors:

Prof. Rodney Genga

Prof. Claudia Polese

A thesis submitted to the Faculty of Engineering and the Built Environment, University of the Witwatersrand, Johannesburg, in fulfilment of the requirements for the degree of Doctor of Philosophy.

Johannesburg, October 2024

Declaration

I Mahlatse Solomon Rabothata, declare that this thesis is my own, unaided work, except where otherwise acknowledged. It is being submitted for the degree of Doctor of Philosophy at the University of Witwatersrand, Johannesburg. It has not been submitted before for any degree or examination at any other university.



Signature

07th day of October 2024

Abstract

The main aim of this study was to design, develop and produce NbC-Ni cermet based cutting inserts as potential substitutes for conventional WC-Co based inserts for the face-milling machining of automotive grey cast iron (a-GCI), an alloy that plays a critical role in the automotive manufacturing industry. For this purpose, rapid pulsed electric current sintering (PECS), additions of Mo as a partial binder replacement and TiC and TiC_7N_3 as secondary hard phases, and femtosecond laser surface modification (LSM) technique were used in an effort to enhance the NbC-Ni based cutting inserts' machining capabilities during face-milling of a-GCI. All the sintered samples achieved relative densities of 97% and above, irrespective of the sintering process. Adding Mo, TiC and TiC_7N_3 to the NbC-12Ni (wt%) composition refined the NbC grain size in PECS samples, enhancing hardness and wear resistance. Mechanical impact shock and wear resistance of inserts were further improved via femtosecond LSM, creating pyramid (P) LSM and shark skin (S) LSM based micro-patterns on the surface of the cutting inserts. Face milling machining tests of a-GCI were performed at 200-400 m/min cutting speed (V_c) and 0.25-1.0 mm depth of cut (a_p). The inserts' cutting-edge wear and failure were evaluated after every pass using optical microscopy and analysed via high angular annular dark field (HAADF)-scanning electron transmission microscopy (STEM). Machining performance was assessed by technique for order of preference by similarity to ideal solution (TOPSIS) based model using insert tool life (I_l), specific cutting energy (U_c) and maximum resultant cutting forces (F_{max}) as criteria and including surface roughness (Ra) during finishing operations. The pyramid LSM PECS NbC-10TiC-12N[Ni/Mo] (wt%) (R2MS-P1) insert was the top performer during semi-finishing, with 20 min I_l, 22 J/mm^3 U_c and 1087 N F_{max}, obtaining an overall preference score (O_i) of 0.953. The best inserts during finishing 2 were the blank (B) (i.e. unmodified cutting edge) PECS NbC-10TiC_7N_3-12Ni (wt.%) (TCN1S-B3) and LPS WC-10TiC-10[Co/Mo] (wt.%) (T1ML-B3) inserts with both inserts obtaining O_is of 0.826, respectively. In general, additions of Mo, TiC, TiC_7N_3, PECS and LSM improved hardness and abrasion wear resistance, resulting in enhanced performance of NbC-Ni based cutting inserts during machining.

Dedication

I dedicate this work to God Almighty, my source of wisdom, knowledge and understanding. His divine guidance has been the bedrock of my strength, sustaining me with resilience and inspiration throughout the entirety of this program. This would not have been possible without You. To God be the Glory!

I also dedicate this work to the following:

To my beloved parents, Mrs Sewela Idah Rabothata and Mr Masilo Oscar Rabothata, who are the basis of my existence. Thank you for your unwavering support and for always believing in me.

To my beloved wife, Nompumelelo Perseverence Rabothata, whose unwavering support and inspiration propelled me to finish this thesis.

To my children, Thatego Masilo Rabothata and Aya Išago Tshimega Rabothata, thank you, and I love you.

To my late uncle, Mr Tebogo Ramango, who believed that I was destined to reach far in life. Thank you so much for your love and for believing in me. Your words of motivation will never depart my heart. Continue to Rest in Peace Molaudzi.

Acknowledgements

To God be the Glory! Firstly, I thank the Almighty God for his grace and for granting me the strength as well as the wisdom to successfully complete this research. I will forever be grateful.

I would also like to acknowledge the following:

Professors Rodney Genga and Claudia Polese, for their outstanding supervision. Thank you so much for all your patience, guidance, support and advice during this study. I truly appreciate it.

Mr Nthape Mphasha: My dear brother, thank you so much for your assistance. Thank you for all the laboratory work that you helped me with, and for partnering with me in all the experiments that I had to do. I truly appreciate all your help. May God bless you.

Dr Shuigen Huang and Dr Josef Vleugels, for assisting with the sintering of the samples at their facilities in KU Leuven, Belgium.

Dr Pavel Zeman, for assisting with the design and fabrication of the laser surface patterns on the cutting edges of the inserts at their laser facilities in RCMT, Czech Technical University, Prague, Czech Republic.

Auto Industrial Group (AIG) (Pty) Ltd, Staff (Mr James Shepperd, Mr Christian Botha and all the workshop personnel), for donating the workpiece material used in this study as well as providing all the information that we required. I am grateful for all your help.

School of Mechanical, Industrial and Aeronautical Engineering, North-West Engineering Workshop, Wits University, Staff (All the workshop personnel): Special thanks to Mr Klass Phaka for assistance with the machining tests, thank you Sir.

School of Chemical and Metallurgical Engineering, Wits University, for assistance with their laboratory and SEM facilities.

Mr Ndivhuwo Nelwalani and Zaynab Cader for assistance with the SEM and EDS analysis of the samples. Thank you so much.

Centre for High Resolution Transmission Electron Microscopy (CHRTEM), Nelson Mandela University, for providing STEM facilities and assisting with HAADF-STEM analyses. Special thanks to Dr Samkelo Ngongo for all the help, thank you Sir.

SITA UK Foundation, for their generous donation and financial support throughout this research. Special thanks to Ms Lynda Murry who has been my point of contact to SITA. I am truly grateful.

Academic Development Unit, Wits University, Colleagues, and friends, thank you for all your prayers and support.

Lastly, I would like to thank my wonderful wife, son, and daughter, Nompumelelo, Masilo, and Aya Rabothata, as well as the rest of my family for being an inspiration and a source of motivation. I sincerely appreciate your patience, love, and prayers. I am grateful to every one of you.

Contents

Declaration i
Abstract ii
Dedication iii
Acknowledgements iv
Contents vi
List of Figures xiii
List of Tables xxi
1. Introduction 1
1.1. Problem statement 4
1.2. Objectives 6
1.3. Hypothesis 7
1.4. Overview 7
2. Literature Review 9
2.1. History of cemented carbide cutting inserts 9
2.2. Production of cemented carbide inserts 12
2.2.1. Production of raw powder, mixing and milling 12
2.2.2. Consolidation of cemented carbides 13
2.2.3. Sintering 15
2.3. Sintering techniques and effects of sintering variables 16
2.3.1. Sintering techniques 17
2.3.2. Effects of sintering variables in cemented carbides 22
2.4. Characterisation of the cemented carbides microstructure 26
2.4.1. Optical microscopy 26
2.4.2. Scanning electron microscopy 26
2.4.3. X-ray diffraction 26

2.4.4. Transmission electron microscopy and high-resolution transmission electron microscopy 27
2.4.5. Energy-dispersive X-ray spectroscopy 27
2.5. Mechanical properties of cemented carbides 27
2.5.1. Hardness and fracture toughness 27
2.5.2. Elastic and shear modulus 32
2.6. Face milling machining 32
2.6.1. Face milling machining parameters 33
2.6.2. Energy consumption in face milling 35
2.7. Modern cutting insert design 38
2.7.1. Cutting insert geometry optimisation 38
2.7.2. Chip formation during machining 40
2.7.3. Workpiece material – Grey Cast Iron 41
2.7.4. Laser surface modification of cemented carbides and cermets 44
2.8. Cutting insert failure, gradual wear and insert life 47
2.8.1. Gradual wear and wear resistance of cutting inserts 50
2.8.2. Cutting insert wear mechanisms 51
2.8.3. Cutting insert “tool” life 54
2.9. Surface roughness measurements 57
2.10. Summary of factors affecting machining operations 58
2.11. Face milling machining cutting parameters optimisation 59
2.11.1. MCDM problem formulation 60
2.11.2. Optimal solution based on the TOPSIS technique 61
2.12. Study approach 64
3. Experimental Procedure 66
3.1. Materials, powder milling and drying 66
3.2. Sintering 66

3.2.1. Liquid phase sintering 66
3.2.2. Pulsed electric current sintering 68
3.3. Cutting inserts production 69
3.4. Characterisation of sintered samples 72
3.4.1. Density measurements 72
3.4.2. Samples preparation 73
3.4.3. Mechanical properties 74
3.4.4. Modulus of Elasticity 75
3.4.5. Microstructural analysis and characterisation 76
3.5. Grey cast iron (GCI) face milling 77
3.5.1. The workpiece (GCI) 77
3.5.2. Face milling tests 78
3.5.3. Surface roughness measurements 81
3.5.4. Processing, interpretation, and presentation of face milling test results 81
4. Physical, Microstructural, and Mechanical Properties 88
4.1. Densification of the sintered samples 88
4.2. Microstructural characteristics of the sintered samples 89
4.3. Mechanical properties of the sintered samples 95
4.3.1. Hardness and fracture toughness properties 95
4.3.2. Elastic (Young's modulus) and shear modulus (modulus of rigidity) properties 97
5. Semi-finishing (Test 1) Results 100
5.1. Analyses of the blank (B1) cutting inserts 100
5.1.1. Analyses of the resultant forces, specific cutting energy, and temperature of the B1 cutting inserts 100
5.1.2. Analyses of insert tool life and wear performance of blank (B1) cutting inserts 104

5.1.3. Analyses of micrographs of the flank and rake faces of the blank (B1) cutting inserts 107

5.1.4. Machining performance evaluation and analyses of B1 cutting inserts 111

5.2. Analyses of the shark skin LSM (S1) cutting inserts 112

5.2.1. Analyses of the resultant forces, specific cutting energy, and temperature of S1 cutting inserts. 112

5.2.2. Analyses of insert tool life and wear performance of S1 cutting inserts. 116

5.2.3. Analyses of micrographs of the flank and rake faces of the S1 cutting inserts120

5.2.4. Machining performance evaluation and analyses of S1 cutting inserts.....125

5.3. Analyses of the pyramid LSM (P1) cutting inserts 126

5.3.1. Analyses of the resultant forces, specific cutting energy, and temperature of P1 cutting inserts 126

5.3.2. Analyses of insert tool life and wear performance of P1 cutting inserts 130

5.3.3. Analyses of optical micrographs of the flank and rake faces of P1 cutting inserts 135

5.3.1. Machining performance evaluation and analysis of P1 cutting inserts.....137

5.4. Consolidated results for semi-finishing (Test 1) 138

6. Finishing (Test 2 and Test 3) Results 140

6.1. Analyses of the blank (B2) cutting inserts 140

6.1.1. Analysis of the resultant forces, specific cutting energy, and temperature of the B2 cutting inserts 140

6.1.2. Analyses of insert life and wear performance of blank (B2) cutting inserts ...144

6.1.3. Analyses of micrographs of the flank and rake faces of the blank (B2) cutting inserts 147

6.1.4. Machining performance evaluation and analyses of B2 cutting inserts 149

6.2. Analysis of the shark skin LSM (S2) cutting inserts.....150

6.2.1. Analysis of the resultant forces, specific cutting energy, and temperature of the S2 cutting inserts.....150

6.2.2. Analyses of insert tool life and wear performance of S2 cutting inserts. 153
6.2.3. Analyses of micrographs of the flank and rake faces of S2 cutting inserts 157
6.2.4. Machining performance evaluation and analyses of S2 cutting inserts 159
6.3. Analyses of the pyramid LSM (P2) cutting inserts 160
6.3.1. Analysis of the resultant forces, specific cutting energy, and temperature of the P2 cutting inserts 160
6.3.2. Analyses of insert tool life and wear performance of P2 cutting inserts 163
6.3.3. Analyses of micrographs of the flank and rake faces of P2 cutting inserts 167
6.3.4. Machining performance evaluation and analyses of P2 cutting inserts 169
6.4. Consolidated results for finishing 1 (Test 2) 171
6.5. Analyses of the blank (B3) cutting inserts 173
6.5.1. Analyses of the resultant forces, specific cutting energy, and temperature of the B3 cutting inserts 173
6.5.2. Analyses of insert tool life and wear performance of B3 cutting inserts 176
6.5.3. Analyses of micrographs of the flank and rake faces of B3 cutting inserts 178
6.5.4. Machining performance evaluation and analyses of B3 cutting inserts 180
6.6. Analyses of the shark skin LSM (S3) cutting inserts 182
6.6.1. Analysis of the resultant forces, specific cutting energy, and temperature of the S3 cutting inserts 182
6.6.2. Analyses of insert tool life and wear performance of S3 cutting inserts. 185
6.6.3. Analyses of micrographs of the flank and rake faces of S3 cutting inserts 189
6.6.4. Machining performance evaluation and analyses of S3 cutting inserts 191
6.7. Analyses of the pyramid LSM (P3) cutting inserts 193
6.7.1. Analysis of the resultant forces, specific cutting energy, and temperature of the P3 cutting inserts 193
6.7.2. Analyses of insert tool life and wear performance of P3 cutting inserts 196
6.7.3. Analyses of micrographs of the flank and rake faces of P3 cutting inserts 200
6.7.4. Machining performance evaluation and analyses of P3 cutting inserts 202

6.8. Consolidated results for finishing 2 (Test 3) 204
7. Discussion 206
7.1. Densification 206
7.2. Microstructure 207
7.2.1. Microstructure of WC-10TiC-10[Co/Mo] (wt%.) (T1ML) sample 207
7.2.2. Microstructure of NbC-12Ni based sintered samples 208
7.3. Mechanical properties 211
7.3.1. Hardness properties 211
7.3.2. Fracture toughness properties 212
7.3.3. Elastic modulus and shear modulus 213
7.4. Semi-finishing face milling 214
7.4.1. Blank (B1) cutting inserts 214
7.4.2. Shark skin LSM (S1) cutting inserts 218
7.4.3. Pyramid LSM (P1) cutting inserts 221
7.4.4. Consolidated overall semi-finishing machining performance 223
7.5. Finishing-1 face milling 224
7.5.1. Blank (B2) cutting inserts 224
7.5.2. Shark skin LSM (S2) cutting inserts 227
7.5.3. Pyramid (P2) cutting inserts 229
7.5.4. Consolidated overall finishing-1 machining performance 230
7.6. Finishing-2 face milling 231
7.6.1. Blank (B3) cutting inserts 232
7.6.2. Shark skin LSM (S3) cutting inserts 234
7.6.3. Pyramid LSM (P3) cutting inserts 235
7.6.4. Consolidated overall finishing-2 machining performance 237
8. Conclusions and recommendations 239
8.1. Conclusions 239

8.2. Recommendations 241
9. Research outputs 242
References 244
A. Appendix: 265
Research outputs 265

List of Figures

Figure 2-1. General flowsheet of sintered components production [50] 13
Figure 2-2. Schematics of (a) a rolling ball mill [54], and (b) an attritor mill [51] 13
Figure 2-3. Shrinkage of the green compact due to sintering [16]. 14
Figure 2-4. Basic phenomena occurring during sintering under the driving force for sintering [56] 16
Figure 2-5. Microstructure changes during LPS, starting with mixed powders till the final densification [54] 18
Figure 2-6. Schematic of a PECS machine [69] 21
Figure 2-7. Pulsed electric current sintering stages [68] 22
Figure 2-8. HV-K_{IC} relationships for various grain sizes in WC-Co cemented carbides produced via conventional sintering methods [87] 30
Figure 2-9. HV-K_{IC} relationships for various binder volume fractions in WC-Co cemented carbides produced via conventional sintering methods [87] 30
Figure 2-10. HV-K_{IC} relationship for cemented carbides containing cubic carbides and cermets of various compositions [87] 31
Figure 2-11. Face milling machining, showing (a) the action of a cutting insert; (b) climb milling; (c) conventional milling; (d) machined surface with face milling dimensions [110] 33
Figure 2-12. Cutter reference (a) [27] vs. table force reference systems (b) [114] 34
Figure 2-13. Classification of energy consumption in face milling [121] 36
Figure 2-14. Schematic of a four-tooth face milling cutter illustrating the insert geometry and the associated cutting edge angles: (a) side view and (b) bottom view [125]. 38
Figure 2-15. Common types of chips [129] 41
Figure 2-16. Chip formation in orthogonal machining [128] 41
Figure 2-17. Different types of graphite flakes [6] 43
Figure 2-18. Schematic machining sequences of GCI showing the formation of chips and subsequent shearing from the workpiece [133] 43
Figure 2-19. Illustration of a laser modified flank and rake face of the cutting insert; and (b) magnified SEM micrograph of the cutting edge showing the pyramid shaped micro patterns [134] 44
Figure 2-20. (a) SEM micrograph of a dimple cross-section and path of EDX analysis, and (b) the EDX results [139]. 46

Figure 2-21. Laser process definitions [141]. 47
Figure 2-22: (a) Some features of wear in single point cutting inserts, with VB indicating the average flank wear. (b) - (e) illustrates different cutting insert wear: (b) flank wear, (c) crater wear, (d) thermal cracking (temperature failure), (e) and flank wear and built-up edge [110] 50
Figure 2-23. Causes of wear, different types of wear and their consequences during machining [147] 51
Figure 2-24. An illustration of abrasive wear mechanisms [150]. 52
Figure 2-25. Cutting insert flank wear vs. cutting time [125] 55
Figure 2-26. General flowchart for a TOPSIS technique 64
Figure 3-1. Temperature and pressure profile of WC-10TiC-10Co (wt%) sintered via LPS .. 67
Figure 3-2. Temperature and pressure profiles of PECS samples 69
Figure 3-3. Dimensions of the cutting inserts 69
Figure 3-4. Insert design geometry and dimensional specifications 70
Figure 3-5: Optical micrographs of (a) shark skin pattern and (b) pyramid pattern on the rake and flank faces of the cutting inserts 71
Figure 3-6. Sample grinding and polishing procedure 74
Figure 3-7. Vickers hardness (HV_{30}) testing 75
Figure 3-8. Pilot F75SN12080 cutting insert holder schematic and CAD rendition. Adapted from [177] 79
Figure 3-9. Thermal imaging during face-milling 79
Figure 3-10: SRT-6210 digital portable surface roughness tester [178] 81
Figure 3-11. Example of cutting insert designation 82
Figure 4-1. SEM-BSE image of WC-10TiC-10[Co/Mo] (wt%) (T1ML) sample prepared by LPS showing WC (light), Co (light grey), (W, Ti, Co) C solid solution (dark grey phase), and TiC- rich (dark) phases 90
Figure 4-2. HAADF-STEM images of WC-10TiC-10[Co/Mo] (wt%) (T1ML) sample produced by LPS showing: WC (green), Co (cyan), Ti (blue), Mo (purple) and C (yellow). . 90
Figure 4-3. (a) SEM-BSE image of NbC-12Ni (wt%) (N2S) prepared by PECS, NbC-12[Ni/Mo] (wt%) of (b) N2ML prepared by LPS and (c) N2MS prepared by PECS showing NbC (light) and Ni (medium dark) phases 91
Figure 4-4. SEM-BSE image of NbC-10 TiC-12Ni (wt%) (a) R2L prepared by LPS and R2S prepared by PECS, and (c) NbC-10TiC-12[Ni/Mo] (wt%) of R2MS prepared by PECS showing NbC (light), Ni (medium) and TiC-rich (dark) phases 92

Figure 4-5. HAADF-STEM images of NbC-10TiC-12[Ni/Mo] (wt%) of R2MS prepared by PECS showing: Nb (green), Ni (red), Ti (blue), Mo (purple) and C (yellow).....93
Figure 4-6. SEM-BSE images of NbC-10TiC$_7$N$_3$-12Ni (wt%) of (a) TCN1L prepared by LPS and (b) TCN1S prepared by PECS showing NbC (light), Ni (medium dark), and TiCN-rich (darkest) phases.....94
Figure 4-7. Variation of Vickers hardness (HV_{30}) with fracture toughness (K_{IC}).....97
Figure 4-8. Variation of elastic modulus (E) with the Vickers hardness, HV_{30}.....99
Figure 5-1. Average resultant force (F) and maximum resultant force (F_{max}) for B1 cutting inserts during semi-finishing at n = 800 rpm and a_p = 1.0 mm.....102
Figure 5-2. Variation of the specific cutting energy (Uc) with the average resultant force (F) for B1 cutting inserts during semi-finishing at n = 800 rpm and a_p = 1.0 mm.....103
Figure 5-3. Variation of the average machining temperature (T) with the average resultant force (F) for B1 cutting inserts during semi-finishing at n = 800 rpm and a_p = 1.0 mm.....104
Figure 5-4. Variation of the maximum flank wear (VB_{max}) with cutting time (Il) for blank (B1) cutting inserts during semi-finishing at n = 800 rpm and a_p = 1.0 mm.....106
Figure 5-5. Variation of the flank wear rate (FWR) with the average resultant force (F) for blank (B1) cutting inserts during semi-finishing at n = 800 rpm and a_p = 1.0 mm.....106
Figure 5-6. Optical micrographs of the flank and rake faces of (a) T1ML-B1, (b) N2S-B1 and (c) TCN1L-B1 cutting edges during semi-finishing machining.....108
Figure 5-7. HAADF-STEM map of a cross-section of T1ML-B1 insert cutting edge/workpiece interface showing: WC (green), Co (cyan), Ti (blue), Mo (purple) and C (yellow).....110
Figure 5-8. Variation of specific cutting energy (Uc) with cutting time (Il) for blank (B1) cutting inserts during semi-finishing at n = 800 rpm and a_p = 1.0 mm.....111
Figure 5-9. Overall preference score (Oi) and rank of B1 cutting inserts (alternatives).....112
Figure 5-10. Average resultant force (F) and maximum resultant force (F_{max}) for S1 cutting inserts during semi-finishing at n = 800 rpm and a_p = 1.0 mm.....114
Figure 5-11. Variation of the specific cutting energy (Uc) with the average resultant force (F) for S1 cutting inserts during semi-finishing at n = 800 rpm and a_p = 1.0 mm.....115
Figure 5-12. Variation of the average machining temperature, (T) with the average resultant force, (F) for S1 cutting inserts during semi-finishing.....116
Figure 5-13. Variation of the maximum flank wear, (VB_{max}) with cutting time, (Il) for shark skin LSM (S1) cutting inserts during semi-finishing at n = 800 rpm and ap = 1.0 mm.....118

Figure 5-14. Effect of shark skin LSM technique on the S1 cutting insert tool life performance benchmarked against B1 cutting inserts during semi-finishing at n = 800 rpm and a_p = 1.0 mm 119
Figure 5-15. Variation of the flank wear rate (FWR) with the average resultant force (F) for shark skin LSM (S1) cutting inserts during semi-finishing 119
Figure 5-16. Comparison of the flank wear rate of blank (B1) vs. shark skin LSM (S1) cutting inserts during semi-finishing 120
Figure 5-17. Optical micrographs of the flank and rake faces of (a) R2MS-S1, (b) R2S-S1 and (c) TCN1S-S1 cutting edges during semi-finishing machining 122
Figure 5-18. Illustration of entrapped workpiece debris (bright contrast spots) on the shark skin surface layer of the rake face of T1ML-S1 cutting insert 123
Figure 5-19. HAADF-STEM map of a cross-section of R2MS-S1 insert cutting edge/workpiece interface showing: Nb (green), Ni (red), Ti (blue), Mo (purple), C (yellow), and Fe (orange). 124
Figure 5-20. Variation of specific cutting energy (Uc) with cutting time (Il) for shark skin LSM (S1) cutting inserts during semi-finishing at n = 800 rpm and a_p = 1.0 mm 125
Figure 5-21. Overall preference score (Oi) and rank of S1 cutting inserts (alternatives) 126
Figure 5-22. Average resultant force (F) and maximum resultant force (F_{max}) for the pyramid (P1) cutting inserts during semi-finishing at n = 800 rpm and a_p = 1.0 mm 128
Figure 5-23. Variation of the specific cutting energy (Uc) with the average resultant force (F) for P1 cutting inserts during semi-finishing at n = 800 rpm and a_p = 1.0 mm 129
Figure 5-24. Variation of the average machining temperature (T) with the average resultant force (F) for pyramid LSM (P1) cutting inserts during semi-finishing 130
Figure 5-25. Variation of the maximum flank wear (VB_{max}) with cutting time (Il) for pyramid LSM (P1) cutting inserts during semi-finishing at n = 800 rpm and ap = 1.0 mm 132
Figure 5-26. Effect of pyramid LSM technique on the cutting insert life performance benchmarked with the blank (B1) cutting inserts during semi-finishing at n = 800 rpm and a_p = 1.0 mm 133
Figure 5-27. Variation of the flank wear rate (FWR) with the average resultant force (F) for pyramid LSM (P1) cutting inserts during semi-finishing 134
Figure 5-28. Comparison of the flank wear rate of blank vs. pyramid LSM cutting inserts during semi-finishing 134

Figure 5-29. Optical micrographs of the flank and rake faces of (a) R2MS-P1, (b) T1ML-P1 and (c) R2S-P1 cutting edges during semi-finishing machining 136
Figure 5-30. Variation of specific cutting energy (U_c) with cutting time (Il) for pyramid LSM (P1) cutting inserts during semi-finishing at n = 800 rpm and a_p = 1.0 mm..... 137
Figure 5-31. Overall preference score (Oi) and rank of P1 cutting inserts (alternatives)..... 138
Figure 6-1. Average resultant force (F) and maximum resultant force (F_{max}) for B2 cutting inserts during finishing at n = 1600 rpm and ap = 0.5 mm 142
Figure 6-2. Variation of the specific cutting energy (Uc) with the average resultant force (F) for B2 cutting inserts during finishing 1 at n = 1600 rpm and ap = 0.5 mm..... 143
Figure 6-3. Variation of the average machining temperature (T) with the average resultant force (F) for blank (B2) cutting inserts during finishing 1..... 144
Figure 6-4. Variation of the maximum flank wear (VB_{max}) cutting time (Il) for blank (B2) cutting inserts during finishing at n = 1600 rpm and ap = 0.5 mm 146
Figure 6-5. Variation of the flank wear rate, FWR with the average resultant force, F for blank (B2) cutting inserts during finishing at n = 1600 rpm and ap = 0.5 mm..... 147
Figure 6-6. Optical micrographs of the flank and rake faces of (a) T1ML-B2, (b) R2MS-B2 and (c) R2S-B2 cutting edges during finishing 1 machining..... 148
Figure 6-7. Variation of specific cutting energy (Uc) with cutting time (Il) for blank (B2) cutting inserts during finishing 1 at n = 1600 rpm and a_p = 0.5 mm 149
Figure 6-8. Overall preference score (Oi) and rank of B2 cutting inserts (alternatives) 150
Figure 6-9. Average resultant force (F) and maximum resultant force (F_{max}) for S2 cutting inserts during finishing at n = 1600 rpm and ap = 0.5 mm 152
Figure 6-10. Variation of the specific cutting energy (Uc) with the average resultant force (F) for S2 cutting inserts during finishing 1 at n = 1600 rpm and ap = 0.5 mm 152
Figure 6-11. Variation of the average machining temperature (T) with the average resultant force (F) for shark skin (S2) cutting inserts during finishing 1 153
Figure 6-12. Variation of the maximum flank wear (VB_{max}) cutting time (Il) for shark skin LSM (S2) cutting inserts during finishing at n = 1600 rpm and ap = 0.5 mm..... 155
Figure 6-13. Effects of shark skin LSM technique on the S2 cutting inserts tool life performance benchmarked against B2 cutting inserts during finishing at n = 1600 rpm and ap = 0.5 mm 155
Figure 6-14. Variation of the flank wear rate (FWR) with the average resultant force (F) for shark skin LSM (S2) cutting inserts during finishing 1..... 156

Figure 6-15. Comparison of the flank wear rate of blank (B2) vs. shark skin LSM (S2) cutting inserts during finishing 1 157
Figure 6-16. Optical micrographs of the flank and rake faces of (a) T1ML-S2, (b) TCN1S-S2 and (c) R2S-S2 cutting edges during finishing 1 machining 158
Figure 6-17. Variation of specific cutting energy (Uc) with cutting time (Il) for shark skin LSM (S2) cutting inserts during finishing 1 at n = 1600 rpm and a_p = 0.5 mm 159
Figure 6-18. Overall preference score (Oi) and rank of S2 cutting inserts (alternatives)..... 160
Figure 6-19. Average resultant force (F) and maximum resultant force (F_{max}) for P2 cutting inserts during finishing at n = 1600 rpm and ap = 0.5 mm 162
Figure 6-20. Variation of the specific cutting energy (Uc) with the average resultant force (F) for P2 cutting inserts during finishing 1 at n = 1600 rpm and ap = 0.5 mm 162
Figure 6-21. Variation of the average machining temperature (T) with the average resultant force (F) for pyramid (P2) cutting inserts during finishing 1 163
Figure 6-22. Variation of the maximum flank wear (VB_{max}) cutting time (Il) for pyramid LSM (P2) cutting inserts during finishing at n = 1600 rpm and ap = 0.5 mm 165
Figure 6-23. Effects of pyramid LSM technique on the P2 cutting inserts tool life performance benchmarked against B2 cutting inserts during finishing at n = 1600 rpm and ap = 0.5 mm 165
Figure 6-24. Variation of the flank wear rate (FWR) with the average resultant force (F) for pyramid LSM (P2) cutting inserts during finishing 1 166
Figure 6-25. Comparison of the flank wear rate of blank (B2) vs. pyramid LSM (P2) cutting inserts during finishing 1 167
Figure 6-26. Optical micrographs of the flank and rake faces of (a) T1ML-P2, (b) R2S-P2 and (c) TCN1S-P2 cutting edges during finishing 1 machining..... 168
Figure 6-27. Variation of specific cutting energy (U_c) with cutting time (Il) for pyramid LSM (P2) cutting inserts during finishing 1 at n = 1600 rpm and a_p = 0.5 mm 170
Figure 6-28. Overall preference score (Oi) and rank of P2 cutting inserts (alternatives)..... 170
Figure 6-29. Average resultant force (F′) and maximum resultant force (F_{max}') for B3 cutting inserts during finishing at n = 1600 rpm and ap = 0.25 mm 174
Figure 6-30. Variation of the specific cutting energy (Uc') with the average resultant force (F′) for B3 cutting inserts during finishing 2 at n = 1600 rpm and ap = 0.25 mm..... 175
Figure 6-31. Variation of the average machining temperature (T′) with the average resultant force (F′) for blank (B3) cutting inserts during finishing 2 176

Figure 6-32. Variation of the maximum flank wear (VB_{max}') cutting time (Il') for blank (B3) cutting inserts during finishing 2 at n = 1600 rpm and ap = 0.25 mm 177
Figure 6-33. Variation of the flank wear rate (FWR′) with the average resultant force (F′) for blank (B3) cutting inserts during finishing 2 178
Figure 6-34. Optical micrographs of the flank and rake faces of (a) T1ML-B3, (b) TCN1S-B3 and (c) R2S-B3 cutting edges during finishing 2 machining 179
Figure 6-35. Variation of specific cutting energy (Uc') with effective cutting time (Il') for blank (B3) cutting inserts during finishing 2 at n = 1600 rpm and a_p = 0.25 mm 181
Figure 6-36. Overall preference score (Oi) and rank of B3 cutting inserts (alternatives) 182
Figure 6-37. Average resultant force (F′) and maximum resultant force (F_{max}') for S3 cutting inserts during finishing at n = 1600 rpm and ap = 0.25 mm 183
Figure 6-38. Variation of the specific cutting energy (Uc') with the average resultant force (F') for S3 cutting inserts during finishing 2 at n = 1600 rpm and ap = 0.25 mm 184
Figure 6-39. Variation of the average machining temperature (T′) with the average resultant force (F′) for shark skin LSM (S3) cutting inserts during finishing 2 185
Figure 6-40. Variation of the maximum flank wear (VB_{max}') cutting time (Il') for shark skin LSM (S3) cutting inserts during finishing 2 at n = 1600 rpm and ap = 0.25 mm 187
Figure 6-41. Effects of shark skin LSM technique on the S3 cutting inserts tool life performance benchmarked against B3 cutting inserts during finishing at n = 1600 rpm and ap = 0.25 mm 187
Figure 6-42. Variation of the flank wear rate (FWR') with the average resultant force (F') for shark skin LSM (S3) cutting inserts during finishing 2 188
Figure 6-43. Comparison of the flank wear rate of blank (B3) vs. shark skin LSM (S3) cutting inserts during finishing 2 189
Figure 6-44. Optical micrographs of the flank and rake faces of (a) T1ML-S3, (b) R2S-S3 and (c) R2MS-S3 cutting edges during finishing 2 machining 190
Figure 6-45. Variation of specific cutting energy (Uc') with effective cutting time (Il') for shark skin (S3) cutting inserts during finishing 2 at n = 1600 rpm and a_p = 0.25 mm 192
Figure 6-46. Overall preference score (Oi) and rank of S3 cutting inserts (alternatives) 193
Figure 6-47. Average resultant force (F′) and maximum resultant force (F_{max}') for P3 cutting inserts during finishing at n = 1600 rpm and ap = 0.25 mm 195
Figure 6-48. Variation of the specific cutting energy (Uc') with the average resultant force (F′) for P3 cutting inserts during finishing 2 at n = 1600 rpm and ap = 0.25 mm 195

Figure 6-49. Variation of the average machining temperature (T′) with the average resultant force (F′) for pyramid LSM (P3) cutting inserts during finishing 2 196
Figure 6-50. Variation of the maximum flank wear (VB_{max}') cutting time (Il') for pyramid LSM (P3) cutting inserts during finishing 2 at n = 1600 rpm and ap = 0.25 mm 198
Figure 6-51. Effects of pyramid LSM technique on the P3 cutting inserts tool life performance benchmarked against B3 cutting inserts during finishing at n = 1600 rpm and ap = 0.25 mm 198
Figure 6-52. Variation of the flank wear rate (FWR′) with the average resultant force (F′) for pyramid LSM (P3) cutting inserts during finishing 2.....199
Figure 6-53. Comparison of the flank wear rate of blank (B3) vs. pyramid LSM (P3) cutting inserts during finishing 2 200
Figure 6-54. Optical micrographs of the flank and rake faces of (a) TCN1S-P3, (b) T1ML-P3 and (c) R2MS-P3 cutting edges during finishing 2 machining.....201
Figure 6-55. Variation of specific cutting energy (Uc') with effective cutting time (Il') for pyramid LSM (P3) cutting inserts during finishing 2 at n = 1600 rpm and a_p = 0.25 mm....203
Figure 6-56. Overall preference score (Oi) and rank of P3 cutting inserts (alternatives).....204

List of Tables

Table 1.1. Comparison of material properties between NbC and WC [15].....3
Table 2.1: Combinations of the cutting edges angles and their effects on machining [126]...39
Table 2.2. Typical mechanical properties of grey cast iron [130]. 42
Table 2.3. Different types of cutting edge failure and their causes 48
Table 2.4: Factors influencing machining operations [110] 58
Table 3.1. Starting powders specifications 66
Table 3.2. Sintering profiles of liquid phase sintering.....67
Table 3.3. Sintering profiles of pulsed electric current sintering.....68
Table 3.4. LPS samples.....70
Table 3.5. PECS samples 71
Table 3.6. Laser patterning parameters.....72
Table 3.7: Chemical composition 77
Table 3.8: Characteristics of graphite and matrix of the GCI.....77
Table 3.9: Hardness and tensile strength of GCI 77
Table 3.10: Face milling tests parameters.....78
Table 3.11: Cutting inserts nomenclature and cutting edges. 80
Table 3.12. Weights of the performance criteria (performance weighted index) for semi-finishing and finishing 1 machining tests 84
Table 3.13. Surface roughness dependent variables 86
Table 4.1. Sintered samples densification.....88
Table 4.2. Sintered samples mean carbide grain sizes.....95
Table 4.3. Vickers hardness (HV_{30}) and fracture toughness (K_{IC}) of the sintered samples.....96
Table 4.4. Elastic modulus (E) and shear modulus (G) of the sintered samples 98
Table 5.1 Machining forces, specific energy consumption, and average machining temperature results of B1 cutting inserts during semi-finishing at n = 800 rpm and ap = 1.0 mm.....101
Table 5.2 Cutting insert tool life, maximum flank wear, and flank wear rate results of B1 cutting inserts during semi-finishing at n = 800 rpm and ap = 1.0 mm 105
Table 5.3. Machining forces, specific cutting energy, and temperature results of shark skin LSM cutting inserts during semi-finishing at n = 800 rpm and ap = 1.0 mm.....113
Table 5.4. Cutting insert tool life, maximum flank wear, and flank wear rate results of S1 cutting inserts during semi-finishing at n = 800 rpm and ap = 1.0 mm 117

Table 5.5. Machining forces, specific cutting energy, and temperature results of pyramid LSM cutting inserts during semi-finishing at n = 800 rpm and ap = 1.0 mm 127
Table 5.6. Cutting insert tool life, maximum flank wear, and flank wear rate results of P1 cutting inserts during semi-finishing at n = 800 rpm and ap = 1.0 mm 131
Table 5.7. Machining performance criteria, overall preference scores, and rank of all the cutting inserts used during semi-finishing. 139
Table 6.1. Machining forces, specific energy consumption, and temperature results of B2 cutting inserts during finishing at n = 1600 rpm and ap = 0.5 mm 141
Table 6.2. Cutting insert tool life, maximum flank wear, and flank wear rate results of B2 cutting inserts during finishing at n = 1600 rpm and ap = 0.5 mm 144
Table 6.3. Machining forces, specific energy consumption, and temperature results of S2 cutting inserts during finishing at n = 1600 rpm and ap = 0.5 mm 151
Table 6.4. Cutting insert tool life, maximum flank wear, and flank wear rate results of S2 cutting inserts during finishing at n = 1600 rpm and ap = 0.5 mm 154
Table 6.5. Machining forces, specific energy consumption, and temperature results of P2 cutting inserts during finishing at n = 1600 rpm and ap = 0.5 mm 161
Table 6.6. Cutting insert tool life, maximum flank wear, and flank wear rate results of P2 cutting inserts during finishing at n = 1600 rpm and ap = 0.5 mm 164
Table 6.7. Machining performance criteria, overall preference scores, and rank of combined cutting inserts used during finishing 1 172
Table 6.8. Machining forces, specific energy consumption, and temperature results of B3 cutting inserts during finishing 2 at n = 1600 rpm and ap = 0.25 mm 173
Table 6.9. Effective insert tool life, maximum flank wear, flank wear rate, and surface roughness results of B3 cutting inserts during finishing at n = 1600 rpm and ap = 0.25 mm 177
Table 6.10. Machining performance evaluation criteria for B3 cutting inserts 180
Table 6.11. Machining forces, specific energy consumption, and temperature results of S3 cutting inserts during finishing 2 at n = 1600 rpm and ap = 0.25 mm 183
Table 6.12. Effective insert tool life, maximum flank wear, flank wear rate, and surface roughness results of S3 cutting inserts during finishing at n = 1600 rpm and ap = 0.25 mm 186
Table 6.13. Machining performance evaluation criteria for S3 cutting inserts 191

Table 6.14. Machining forces, specific energy consumption, and temperature results of P3 cutting inserts during finishing 2 at n = 1600 rpm and ap = 0.25 mm 194
Table 6.15. Effective insert tool life, maximum flank wear, flank wear rate, and surface roughness results of P3 cutting inserts during finishing at n = 1600 rpm and ap = 0.25 mm 197
Table 6.16. Machining performance evaluation criteria for P3 cutting inserts 202
Table 6.17. Machining performance criteria, overall preference scores, and rank of combined cutting inserts used during finishing 2 205

1. Introduction

Africa's human population is currently at ~1.4 billion and it is expected to double by the year 2050 [1] The population growth necessitates investments in innovation, technology, and infrastructure development. Urbanisation, which is typically brought by population increase, often brings about economic and social challenges including housing, power, water and sanitation, transportation, etc. The interest of this study is in transportation where the need for mobility will increase. It is widely known that automotive (or road transport) is one of the major modes of transport in many African countries including South Africa [2]. Also, automotive manufacturing is one of the fastest growing industries in Africa [3]. Furthermore, in South Africa, the industry has been reported to contribute ~6.8% to the manufacturing GDP of the country [4]. Therefore, it could play a crucial role in answering to the transportation needs as well as boosting the country's economy through skills development, technology and innovation, and global investments.

The current study is concerned with the design, development and manufacturing of cemented carbide or hardmetals based cutting inserts for face milling machining of automotive components made from grey cast iron (a-GCI). Grey cast iron is widely utilised to make numerous automotive components (i.e. flywheels, clutch plates, brake discs and brake drums) due to its good combinations of properties including wear resistance, high stiffness, anti-squeal, vibration damping and machinability [5, 6]. Furthermore, given the current energy crisis gripping South Africa, it is critical to emphasize the importance of sustainable manufacturing in this context. As a result, the study will examine the energy consumption during the face milling process of a-GCI. The goal is to design cutting insert tools that not only support efficient machining but also adhere to the tenets of sustainable production, thereby contributing to the overall improvement of both manufacturing processes and environmental well-being.

Cemented carbides and cermets are composite materials made of a predominant hard and relatively brittle ceramic phase (WC or TiC), contained in a metallic ductile matrix binder phase (Co, Fe, or Ni) [7]. These materials have good combinations of high-performance durability, abrasive wear resistance, strength, fracture toughness, high hot hardness and thermal shock resistance [8]. The main difference between cemented carbides and cermets is their composition. For instance, typically cemented carbides are WC-Co based; however, cermets are formed when large amounts of cubic carbides, including Mo_2C, VC, TiC, or Ti (C, N) are

added to the microstructure [8]. In cermets, the WC phase is replaced by cubic carbides, forming a core-rimmed structure [8, 9]. Cutting inserts made of cemented carbide are tougher and more durable, but they also have a lower fracture resistance. On the other hand, cermets-based cutting may be less durable but is more resistant to wear than cemented carbides [10].

Cemented carbides and cermets have been extensively used for numerous tribological applications including engineered components, wear parts and machining tools (i.e. cutting inserts for boring, drilling, milling and/or turning) [8, 11]. Both WC and Co appear on the list of "critical raw materials" compiled by the European Union (EU). This is mainly due to their high relative supply risk, high economic importance and unstable market prices [7]. Additionally, ~69% of the global production of WC is from China and its cost has been on a steady rise due to significant increases in global and domestic consumption, mining costs, labour costs and taxes [7, 12]. Also, Co has been reported to pose some health hazards for its manufacturing plant personnel [12]. Furthermore, the WC-Co cutting inserts exhibit poor high-temperature hardness and chemical stability in certain applications, such as machining of steels and cast irons (owing to iron's higher affinity for carbon than WC) [12-14]. For these reasons, materials such as niobium carbide (NbC) and nickel (Ni) have been investigated as possible replacements for WC and Co, respectively [8].

Niobium carbide exhibits good mechanical and physical properties which are comparable to those of WC. Table 1.1 gives a comparison of the material properties between NbC and WC [15]. Nickel, on the other hand, has a higher plasticity than Co and can retain its ductile FCC structure at temperatures below solidus [13], thus, it could improve the fracture toughness of NbC cemented carbides. In addition, Ni has better resistance to corrosion and oxidation compared to Co and can improve the hot hardness and resistance to thermal cracking in NbC-Ni based cemented carbides [16]. Despite the promising properties exhibited by both NbC and Ni, the NbC-Ni based cutting inserts manufactured by conventional liquid phase sintering (LPS) techniques yield poor mechanical properties (low hardness and fracture toughness) compared to the WC-Co based cutting inserts [17]. This is attributed to NbC's higher drive for grain growth due to coalescence and Oswald ripening as a result of high sintering temperatures and longer dwelling times associated with the LPS [18]. Therefore, new rapid sintering techniques such as pulsed electric current sintering (PECS) are now being used to control and prevent grain growth by using externally applied pressure, high heating sintering rates and shorter sintering times to consolidate powder compacts to a high density [19].

The use of PECS, the substitution of WC by NbC and Co by nickel (Ni), and the additions of secondary hardening phases (titanium carbide (TiC), titanium carbonitride (TiCN) and molybdenum carbide (Mo_2C)) and grain growth inhibitors (GGI's) can significantly refine the grain size and improve the properties of NbC-Ni based cermets [7, 9, 10]. The addition of molybdenum (Mo) is known to improve the wetting behaviour of the metallic binder in the LPS of WC-Ni bonded carbides [13]. The enhancement in the wettability creates a diffusion gradient through the liquid-solid interphase, allowing Mo to diffuse freely into the carbide phase and lowering the interfacial energy [13]. Molybdenum addition results in grain size refinement [13]. Consequently, the improvement in the microstructure brings about a substantial increase in strength and hardness [20]. In addition, the partial substitution of Ni by Mo or its addition in the form Mo_2C was reported to improve densification [13].

Table 1.1. Comparison of material properties between NbC and WC [15]

Property	NbC	WC	Effect
Density, ρ [g/cm^3]	7.78	15.63	- More volumes could be purchased per unit kilogram. - Centrifugal forces in rotating and dynamic inserts could be reduced.
Melting Point, T_m [°C]	3520	2870	- Improved resistance to softening of the cutting edge at high cutting temperatures
Thermal conductivity, λ [W/m.K]	14	84	- Reduction of thermally induced wear
Microhardness [GPa]	15 – 20	20 – 28	- Higher hot hardness of NbC at elevated temperatures
Solubility in solid: Nickel, Cobalt, Iron at T = 1250 °C [wt%]	 3 5 1	 12 22 7	- Reduction of crater wear during machining of materials containing Ni, Co, and Fe as alloying elements

Another way to improve the properties of cemented carbide cutting inserts is by using laser surface modification (LSM) techniques via the introduction of micro-features [21]. Laser

surface modification, through either laser peening or laser ablation, is an advanced processing technique that can be used for surface texturing or complex shaping of hard engineering materials which are difficult to machine using conventional methods such as milling and grinding [22]. The technique has advanced from nanosecond to now femtosecond-based technology whereby high-quality innovative patterns can be processed over large surface areas [21]. The LSM was reported to reduce friction of contact areas during dry sliding as well as improve fatigue life, thermal stability, fracture toughness and hardness properties of some [22-24]. Hence the current work attempts to improve the machining performance of NbC-Ni based cemented carbide cutting inserts by using LSM technique.

1.1. Problem statement

The global manufacturing industry is currently grappling with a series of interrelated problems that threaten both economic viability and sustainable production. One such issue is the growing instability in the supply chain and fluctuating prices of essential raw materials used in cutting tools, particularly the WC-Co based cutting inserts that dominate the market. Tungsten carbide-cobalt cemented carbides, widely used due to their excellent mechanical properties such as hardness, toughness, and wear resistance, are increasingly subject to supply shortages and increasing costs due to geopolitical tensions and scarcity of raw materials, particularly tungsten and cobalt. Furthermore, WC-Co cutting inserts exhibit significant limitations in high-temperature machining environments, especially when machining ferrous materials like a-GCI, a common material in the automotive industry. These limitations include poor thermal stability and chemical reactivity during machining, which contribute to reduced tool life, increased wear, and compromised machining efficiency. Considering this, it is imperative to find alternative materials for cutting inserts that offer comparable or superior performance, while addressing the material supply chain vulnerabilities and sustainability concerns. Niobium carbide-nickel bonded cemented carbides are one possible substitute. Niobium is more abundant and less susceptible to supply chain fluctuations than tungsten and exhibits good mechanical and physical properties comparable to those of WC. Nickel can potentially replace Co as a metallic binder due to its higher plasticity as well as better resistance to corrosion, oxidation and thermal cracking. However, the viability of NbC-Ni composites as an effective alternative to WC-Co cutting inserts for machining of a-GCI remains underexplored.

Current research has demonstrated the potential of NbC as a hard phase with promising wear resistance and thermal stability, but there are significant gaps in understanding the mechanical

and physical properties of NbC-Ni systems, particularly when subjected to real-world machining conditions. Moreover, the influence of secondary hardening phases, such as titanium carbide (TiC) and titanium carbonitride (TiCN), on the overall performance of these cutting inserts requires further investigation. Additionally, there is limited knowledge regarding the microstructural changes and mechanical enhancements that can be achieved through advanced processing techniques such as liquid-phase sintering (LPS) and pulsed electric current sintering (PECS), as well as post-processing treatments like femtosecond laser surface modification (LSM). This research, therefore, aims to systematically investigate the development, characterisation, and performance evaluation of NbC-Ni bonded cemented carbides as a sustainable alternative to WC-Co inserts for machining a-GCI components. The study will focus on the following key areas:

1. **Material synthesis and optimisation:**
   The research will involve synthesising NbC-Ni cemented carbides using LPS and PECS techniques, substituting WC with NbC and Co with Ni, and incorporating secondary hardening phases (TiC, TiCN), and metallic binder strengtheners (Mo) to enhance the mechanical properties of the cutting inserts. The impact of these compositional changes on key properties such as hardness, toughness, wear resistance, and thermal stability will be thoroughly examined.
2. **Surface modification techniques:**
   The application of femtosecond LSM will be explored to enhance the surface morphology and microstructure of NbC-Ni based cutting inserts. LSM has the potential to improve wear resistance, reduce friction, and optimise cutting performance, especially in high-temperature environments. The study will evaluate the microstructural changes, surface morphology, and mechanical properties induced by LSM and their correlation with cutting performance during the face milling of a-GCI components.
3. **Energy efficiency and sustainable manufacturing:**
   Given the ongoing energy crisis in South Africa, the research will also investigate the energy consumption during the face milling process using NbC-Ni cutting inserts. By comparing the energy efficiency of NbC-Ni and WC-Co cutting inserts, the study aims to address a critical aspect of sustainable manufacturing (i.e. reducing energy usage while maintaining or improving machining performance). The insights gained will contribute to the development of cutting tools that support energy-efficient machining

processes, thereby aligning with the principles of green manufacturing and helping to mitigate the impact of the energy crisis on the manufacturing sector.

4. **Environmental and industrial implications:**
   The research is expected to provide significant insights into the long-term industrial feasibility of NbC-Ni based cutting inserts, particularly for the automotive and broader manufacturing sectors, where cost, performance, and sustainability are critical. By addressing the limitations of WC-Co cutting tools, particularly in terms of supply chain disruptions, fluctuating costs, and poor high-temperature performance, this study could pave the way for more resilient, efficient, and environmentally friendly cutting tool technologies.

Through a combination of experimental and theoretical analyses, this research seeks to bridge existing knowledge gaps and contribute to the development of a new class of cutting tools that are not only more sustainable but also capable of withstanding the demanding requirements of modern machining processes. The outcomes of this research have the potential to influence both the economic and environmental landscape of the manufacturing industry, providing a pathway toward the adoption of more sustainable materials and processes.

1.2. Objectives

The main aim of this study is to design and manufacture alternative cemented carbide cutting inserts for machining of automotive components made from GCI.

The objectives of the research are as follows:

- To determine the effect of sintering techniques (LPS and PECS) on the densification and microstructure of Ni/Mo bonded NbC-based cermets, aiming to achieve full density and optimised mechanical properties.
- To investigate the relationship between NbC-[Ni/Mo] cermet composition and its physical, mechanical, chemical, and wear properties, comparing these properties to conventional WC-Co cermets to assess improvements or equivalence in performance.
- To evaluate the performance of NbC-[Ni/Mo] based cutting inserts in face milling of automotive a-GCI components and compare their machining efficiency, insert tool life, and wear behaviour to that of WC-Co inserts under identical conditions.

- To analyse the wear behaviour and mechanisms of NbC-[Ni/Mo] cutting inserts during the face milling of automotive a-GCI, correlating wear mechanisms with the cutting conditions, material composition, and microstructural characteristics.
- To assess the impact of femtosecond laser surface modification (LSM) on the surface morphology, mechanical properties, and cutting performance of NbC-[Ni/Mo] and WC-based cutting inserts, establishing how LSM enhances the wear resistance and overall performance during the machining of a-GCI.
- To quantify the effect of NbC-[Ni/Mo] cutting inserts on energy consumption during face milling processes, determining the relationship between insert material composition and machining energy efficiency, with a focus on sustainable manufacturing.
- To develop a predictive model for evaluating the machining performance of cutting inserts (NbC-[Ni/Mo] and WC-Co) in face milling, incorporating parameters such as tool wear, surface finish, energy consumption, and cutting efficiency to optimise tool design and operational conditions.

1.3. Hypothesis

Niobium carbide (NbC) cermets, when bonded with nickel-molybdenum (Ni-Mo) metallic binders, and sintered using conventional LPS or rapid PECS techniques, have the potential to exhibit comparable or superior mechanical, chemical, and wear resistance properties to traditional WC-Co based cutting inserts for machining a-GCI components. Furthermore, the application of femtosecond LSM to NbC and WC-based cutting inserts can enhance cutting performance by improving surface morphology, increasing insert tool life, and reducing energy consumption during face milling of a-GCI, leading to more efficient and cost-effective machining.

1.4. Overview

In this study, an investigation of the effects of Ni-Mo binder, additions of TiC and TiCN, and LSM of NbC based cutting inserts during face-milling of a-GCI was done. Various attempts were made to improve the mechanical properties of cutting inserts made of different combinations of powder compositions. The cutting inserts were produced via LPS and PECS techniques. In addition, LSM was further used to produce micro-patterns on the cutting edge

to improve the machining performance of the cutting inserts. The overall structure of the thesis is as follows:

- Chapter 2: Literature review
- Chapter 3: Experimental approach and equipment used.
- Chapter 4: Microstructure and mechanical properties analyses of the sintered samples.
- Chapter 5: Analyses of semi-finishing (test 1) face milling of a-GCI.
- Chapter 6: Analyses of finishing 1 (test 2) and finishing 2 (test 3) face milling of a-GCI.
- Chapter 7: Detailed overall discussion of the results and findings.
- Chapter 8: Conclusions and recommendations for future work.
- Chapter 9: Research outputs.

2. Literature Review

This chapter introduces cemented carbides and their significance in face milling operations. The chapter offers a brief historical account as well as an overview of the key characteristics of cemented carbides and their various industrial applications. The various processing techniques (powder metallurgy and sintering) of cemented carbide based cutting inserts, microstructural characteristics and mechanical properties are presented. In addition, an introduction to face milling, the design of cutting inserts, wear mechanisms of cutting inserts during machining, cutting inserts machining performance and optimisation methods for enhancing the performance of cemented carbide cutting inserts in face milling are also presented.

2.1. History of cemented carbide cutting inserts

Cutting inserts are indexable tools that shear deform the workpiece to remove material during machining (turning, drilling, or milling) operations. The cutting inserts are typically made to function in conditions with high cutting forces, excessive heat generation and high wear [25]. According to research, these circumstances shorten the operating insert life [26], cause inconsistent product quality and raise production costs by reducing the hardness, fracture toughness, wear resistance and strength of the inserts. Cutting inserts must be properly designed to have an extended life, withstand challenging machining conditions and produce dependable high-quality parts to address these problems [27].

Since their invention in the early 1920s, sintered WC-Co based cemented carbides have been among the most successful materials in the field of tribology [28]. These materials' success in a variety of applications (such as manufacturing, building, and specialised structural engineering components) is attributable to a good combination of their physical, mechanical, and behavioural characteristics [13, 29, 30]. Schroter of Osram Studiengesellschaft, who was able to successfully produce the WC-Co alloy to replace the more expensive diamond wire drawing dies for tungsten filaments, is responsible for the creation of tungsten-based cemented carbides and subsequent developments [31]. Due to the alloy's remarkable properties, Krupp of Germany continued to develop it in 1927 [13] for use as cutting inserts, wear parts and engineering components. The initial composition of the cutting inserts consisted of 6wt% of Co bound to WC. These cutting inserts had good performance when machining non-ferrous and non-metallic materials but were unable to handle the machining of steel and cast iron [32].

Later, more ground-breaking advancements were made, such as the 1930s introduction of TiC and TaC (VC, NbC) to WC-Co based cutting inserts to enhance performance during metal cutting [13]. The partial substitution of WC with other carbides and the use of multi-carbide cutting inserts were also introduced, resulting in the formation of cemented carbides with superior properties than the plain WC-Co cemented carbides [31, 33]. These discoveries led to further improvements in the cemented carbides such as increased hardness and wear resistance through the introduction of submicron WC (in 1946) and the development of multi-carbide cutting inserts for high-speed machining of steel [13].

It should be noted that in the 1960s, because of worries about the supply and availability of WC raw material, researchers and scientists started to also develop WC free alloys (TiC based cemented carbides) [13]. Then titanium cemented carbides were created, which were nickel-molybdenum bonded. More initiatives to replace WC-based cemented carbides have been made. Such materials, however, could only be put to certain uses. Additionally, WC-Co cemented carbides still performed better in several applications [13], emphasising the importance of WC in the growth of cermets.

The development of cemented carbides has undergone significant changes throughout the years. In the late 1960s and early 1970s, coating carbide cutting inserts with a thin film of TiC and/or TiN through Chemical Vapor Deposition (CVD) significantly improved cutting speeds and life of the cutting inserts, extending their use in new applications [34]. The introduction of Physical Vapor Deposition (PVD) coatings in the 1980s demonstrated superior toughness and similar wear resistance to CVD coated cemented carbides [35].

In the early 1990s, Plasma CVD, a combination of CVD and PVD, was introduced, utilising diamond or "diamond-like" amorphous coatings but failed to meet industry demands due to poor adhesion [31, 33]. New coatings are still being developed, utilising multilayer coatings like Al_2O_3, Ti (C, N), Zr (C, N), and (Ti, Al) N [36]. The interest in submicron, ultrafine and nanoscale WC-Co based cemented carbides persisted from the 1990s to the present, leading to notable advancements in their mechanical properties, such as resistance to attrition wear, hardness and strength [13]. Investigations revealed that, due to grain growth, the ultrafine grains could not retain their structure after sintering, and this limited their applications [37]. The increase in grain size was attributed to high temperatures and prolonged sintering times, which are inherent to traditional liquid phase sintering techniques [38-39]. Additionally, grain coalescence and Oswald ripening, both of which are thermally activated, were found to

exacerbate grain growth in cemented carbides [39]. Coalescence occurs when two or more grains merge to form larger grains through a process driven by the minimisation of grain boundary energy. Grain boundary refers to the regions in a material where the atoms are not arranged in a regular crystalline pattern and the regions have a higher energy than the interior grains. As a result, the grains tend to merge in order to reduce the total grain boundary area and therefore reduce the overall energy of the material [13]. Oswald ripening is the process by which smaller particles dissolve and their atoms are transported to larger particles causing them to grow. The driving mechanism for Ostwald ripening is the difference in surface energy between the small and the large particles. The small particles have a higher surface energy than the large particles, as a result, they are more likely to dissolve and diffuse to the large particles [13]. To reduce continuous Oswald ripening and coalescence [40], and thereby prevent grain growth while enhancing hardness and wear resistance, rapid sintering techniques such as PECS are often used. Cemented carbides frequently have VC, Cr_3C_2, TaC, NbC, and specific combinations of these additives added as grain growth inhibitors [41]. Furthermore, these materials have been applied to improve the chemical stability, corrosion resistance and high temperature performances of WC based cemented carbides [42].

The 21st century has seen the continued development of highly optimised cemented carbide based cutting inserts for specific machining applications such as high-speed machining and hard turning. This is also made possible through the development of new alloys using various powder compositions, the use of computer-aided design, innovative manufacturing technologies, and the improved understanding of the cutting processes [43]. For instance, Mo or Mo_2C has been added to various cemented carbides to enhance the wettability between the hard (WC, NbC, TiC, and Ti (C, N) and the binder (Co and Ni) phases in cemented carbides [44]. As a result, the microstructures are improved, which enhances the mechanical properties such as hardness, fracture toughness, and elastic modulus [45]. Surface modification by means of short and ultra-short, pulsed laser were also introduced in the fabrication of cutting inserts in the late 20th century and early 21st century [46].

Recent research has compared cutting inserts made of WC- and NbC-based cemented carbides, such as WC-Co, WC-Ni, NbC-Co, and NbC-Ni [17, 47, 48]. The cutting insert characteristics and machining capabilities were compared. This was accomplished in accordance with several variables, such as the sintering methods (LPS vs. SPS), the use of Co or Ni as the reinforcement binder, LSM, and the addition of Mo_2C and TiC to the starting powders of the cutting inserts. The studies' findings suggested that the mechanical properties of NbC-based cutting inserts and

those of WC-based cutting inserts were comparable. These studies show that, despite being created more than a century ago, WC carbide-based cemented carbides are still being researched and developed, with the main motivations being increased cutting insert life and technological advancements.

2.2. Production of cemented carbide inserts

Production of raw powder, mixing and milling of the powders, consolidation of the powders, sintering, and post-sintering treatment are just a few of the complex powder metallurgical steps involved in the conventional fabrication of cemented carbides [8]. A general flowchart for the manufacture of sintered components is shown in Figure 2.1. The ensuing subsections contain a description of the steps in detail.

2.2.1. Production of raw powder, mixing and milling

In powder metallurgy (PM), refinement comes after the production of raw powder. The process of reducing particle size (the diameter of the powder measured in micrometres (μm)) is referred to as powder refinement. It has been demonstrated that fine grain size enhances the mechanical properties of cemented carbides [49], so it is crucial to obtain the proper size of powder grains prior to the consolidation phase. Milling is widely used to facilitate, (i) the mixing of the carbide and binder powders to a desired composition, (ii) uniform distribution of the binder powders among the carbide particles (i.e. ensuring that every WC particle is coated with Co), and (iii) break up the agglomeration of particles [16].

Some of the most popular mills used for powder refinement include attritor mills and rolling ball mills. Depending on the needed microstructure of the final sintered product, both processes are currently employed in the industry. When it comes to reducing particle sizes of 2 μm and under, rolling ball mills are less successful. As a result, they are frequently employed to reduce the size of big particles (>2 μm). Attritor mills are primarily used for milling fine particles (< 2 m), and they are roughly 11 times more effective than ball mills in terms of particle size reduction [16]. Figure 2.2 gives schematics of both the rolling ball mill and the attritor mill.

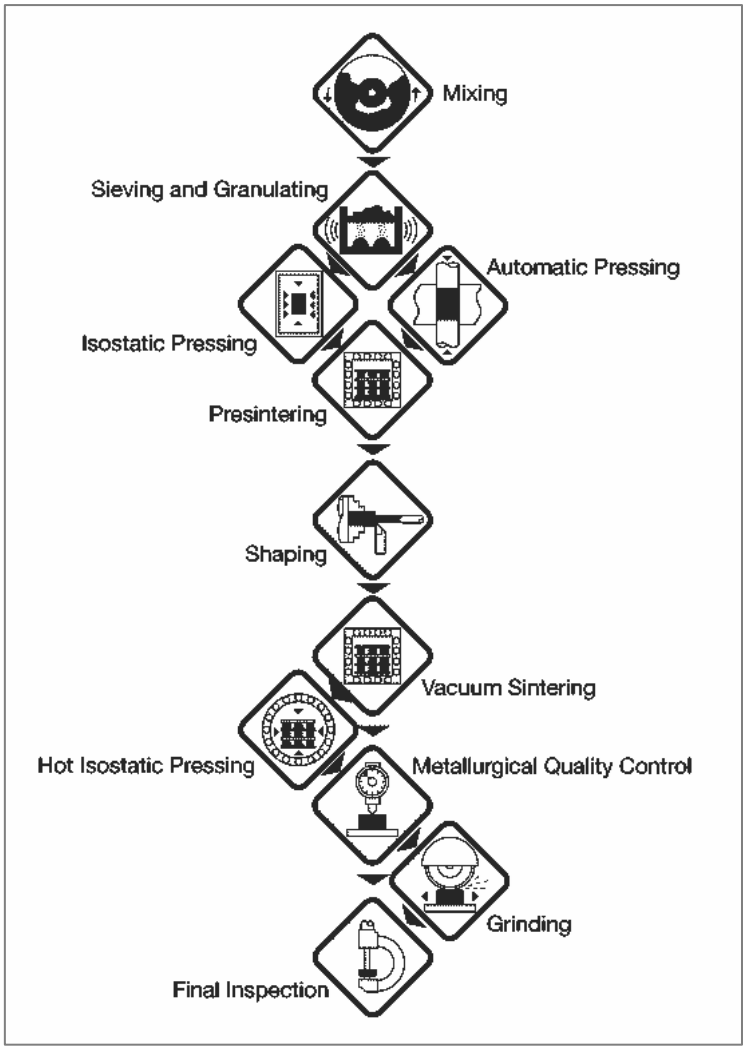


Figure 2-1. General flowsheet of sintered components production [50]

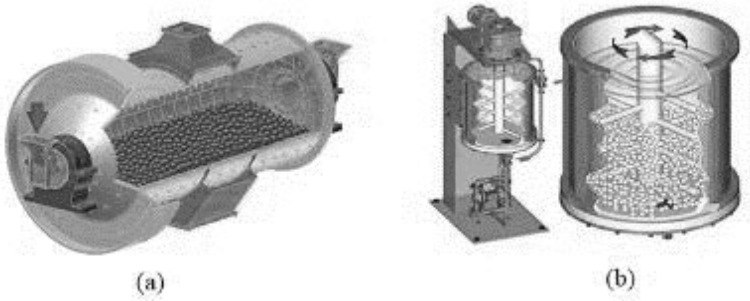


Figure 2-2. Schematics of (a) a rolling ball mill [54], and (b) an attritor mill [51]

2.2.2. Consolidation of cemented carbides

Following milling, the powders are granulated to dry them and make them ready for consolidation. It should be mentioned that each step in the production of sintered parts is essential. However, because they influence the final microstructure and characteristics, consolidation of powders and sintering processes are thought to be the most crucial stages [52].

Powder pressing and compacting, extrusion into the desired shape, dewaxing and pre-sintering are all steps in the consolidation process.

2.2.2.1. Compaction

Compaction is a process whereby external pressure is applied to the loose powder composition for shaping so that it can be sintered to full density. The compacted or shaped part is often referred to as the "green compact or body". During this process, specific dimensional requirements and metallurgical specifications must be considered. This is to ensure that the desired dimensions, density, microstructure and mechanical properties are attained in the final product [16]. The highest theoretical density that green compacts can reach has been reported to be between 60 to 65% [13]. This density level is difficult for green compacts to surpass; however, hardmetals usually attain almost full densification upon sintering depending on the effectiveness of the applied compacting pressure [53].

Green bodies with densities of less than 60% have a high shrinkage percentage coupled with difficulties in dimensional control. Hence, a high green density of compacts is preferred prior to sintering [54]. Figure 2.3 illustrates the shrinkage of a green compact due to sintering. Common methods for green body shaping include magnetic pulse compaction, rapid omni compaction, equal channel angular pressing and conventional uniaxial pressing [49].

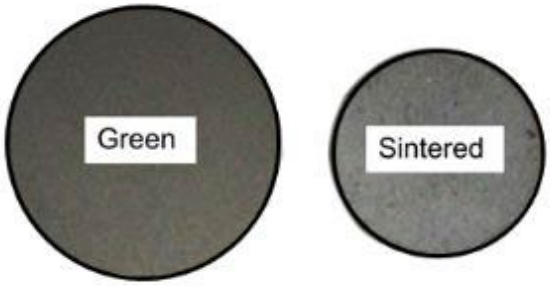


Figure 2-3. Shrinkage of the green compact due to sintering [16].

2.2.2.2. Dewaxing

Following compaction, a procedure known as dewaxing is used to remove the milling wax, which is a lubricant typically added to the starting powders to help reduce friction between the powders and compacting inserts. By heating the compacts to temperatures of about 400ºC in hydrogen or in a vacuum during this procedure, the wax is volatilised [13]. Dewaxing is

essential because any wax left in the green body could cause porosity, which would negatively impact the mechanical properties of the finished product.

2.2.2.3. Pre-sintering

Pre-sintering is a heat treatment process performed after dewaxing and before final sintering, aimed at increasing the mechanical stability of the compact and limiting oxidation effects. This process strengthens the fragile dewaxed compact by heating it in a controlled atmosphere (often hydrogen) at temperatures typically ranging from 750 to 1000 °C [13]. The improved stability allows for subsequent machining operations, such as brown machining, to be performed without damaging the compact. Pre-sintering prepares the component for more complex shaping or dimensional adjustments, ensuring that it remains intact during machining before undergoing full densification in the final sintering stage.

2.2.3. Sintering

Sintering follows the consolidation phase. This process involves heating of green compact at temperatures below the melting point of the major constituent, for a set amount of pressure and time to induce bonding between particles and increase the compact's strength and stability [16]. The green compact powder particles become very active at high temperatures. This results in the formation of interparticle bonds that are enhanced by coalescence, Ostwald ripening and coarsening of the microstructure leading to compaction [54, 55]. The driving force behind sintering is the reduction in interfacial energy (a combination of the specific interface energy and the grain boundary energy) of the particles [56]. The reduction of interfacial energy is related to a few factors including the elimination of pores, the reduction of the surface area of the material and the reduction of grain boundary energy. For example, as the particles bond together and the material becomes denser, the total interface energy of the material decreases. The reduction in surface area is because of densification (pore shrinkage), while the change in boundary area is due to grain coarsening. Figure 2.4 shows that densification results from the elimination of pores and the shrinkage in pore size is due to particle coarsening as the contact between the particles widens [56]. The volume of the green compact reduces during sintering until full density is reached, thus volume shrinkage is also used as an indication of densification.

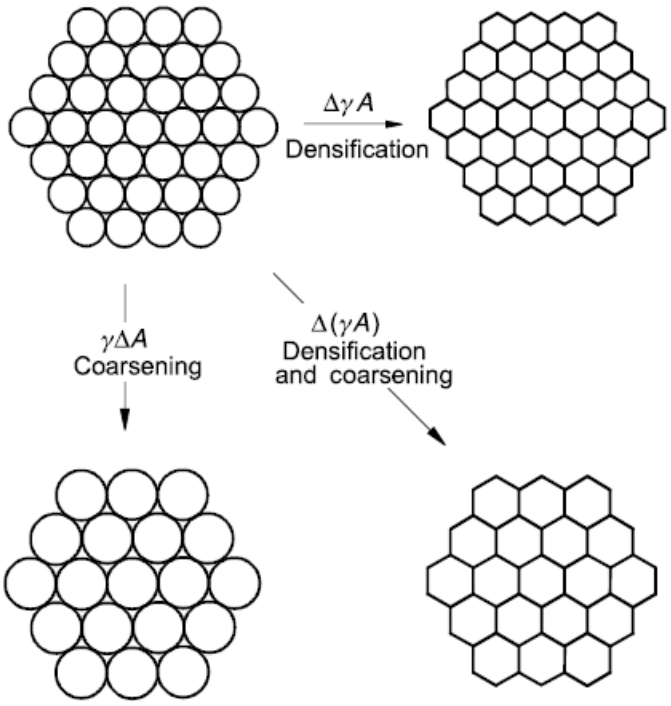


Figure 2-4. Basic phenomena occurring during sintering under the driving force for sintering [56]

Particle bonding, neck formation and growth, pore elimination, and pore shrinkage with grain growth are the four main stages of densification [57]. Particle bonding occurs in the initial stage because of diffusion brought on by the driving forces. As the particles bond together, necks (bridges made of solid material) are then formed. Volume diffusion, grain boundary diffusion, surface diffusion, dislocation climb, and evaporation-condensation all contribute to the movement of atoms that results in the formation and growth of necks [56]. During neck growth, about 2-3% of volume shrinkage is experienced by the compact and this corresponds to between 58 and 68% densification [56]. Interconnected pores develop between the interconnected particles as necking continues. The connected pores become unstable and separate into isolated closed pores because of increased grain growth and densification. At this stage, densification of the compact is at about 91-95%. Full densification (95-99%) of the compact is achieved when the isolated pores round out and completely contract [57].

2.3. Sintering techniques and effects of sintering variables

Depending on the methods used during compaction, the sintering conditions and characteristics of powder compacts can vary greatly. The sinterability, microstructure and other properties of powder compacts can also vary depending on several sintering techniques and processing factors. The variables that affect sintering can be split into two groups: those that affect the

materials and those that affect the process. Most material-related factors, such as the chemical composition of the powder compact, the shape and size distribution of the powder particles, the degree of agglomeration, etc., have an impact on densification and grain growth [52]. On the other hand, factors that affect the sintering process include temperature, time, pressure, rates of heating and cooling, and atmosphere [56]. The following sub-sub sections discuss some of the most common sintering techniques as well as the effects of the sintering variables.

2.3.1. Sintering techniques

Sintering techniques have evolved over time, and new ones are constantly being created to increase the process' effectiveness and efficiency. Some of the techniques include, but are not limited to, microwave sintering, solid state sintering, liquid phase sintering (LPS), gradient sintering, hot isostatic pressing (HIP) and pulsed electric current sintering (PECS) [16]. Among these techniques, LPS has been the most used method for cemented carbide component production [52]. However, in the last decade, techniques such as PECS have also gained popularity in the industry [58]. The current study focuses on both LPS and PECS methods.

2.3.1.1. Liquid phase sintering (LPS) technique

Liquid phase sintering (LPS), also called conventional sintering, is the most used sintering process for fabricating high-performance multi-phase components from powder compacts (alloys and composites) [54]. Liquid phase sintering involves sintering under conditions where solid grains coexist with the wetting liquid. In general, the solid grains are soluble in the liquid since the solubility causes the liquid to spread and wet the solid grains, providing a capillary force that pulls the grains together. In other words, the presence of the liquid phase promotes diffusion and therefore facilitates material transport and densification without external pressure [16]. Concurrently, the high sintering temperatures soften the solid grains, further assisting densification [52]. The LPS process takes place in four main steps, solid state heating, rearrangement (liquid spreading), solution-reprecipitation and final densification (coarsening) [54]. A schematic of the microstructure changes during LPS is shown in Figure 2.5.

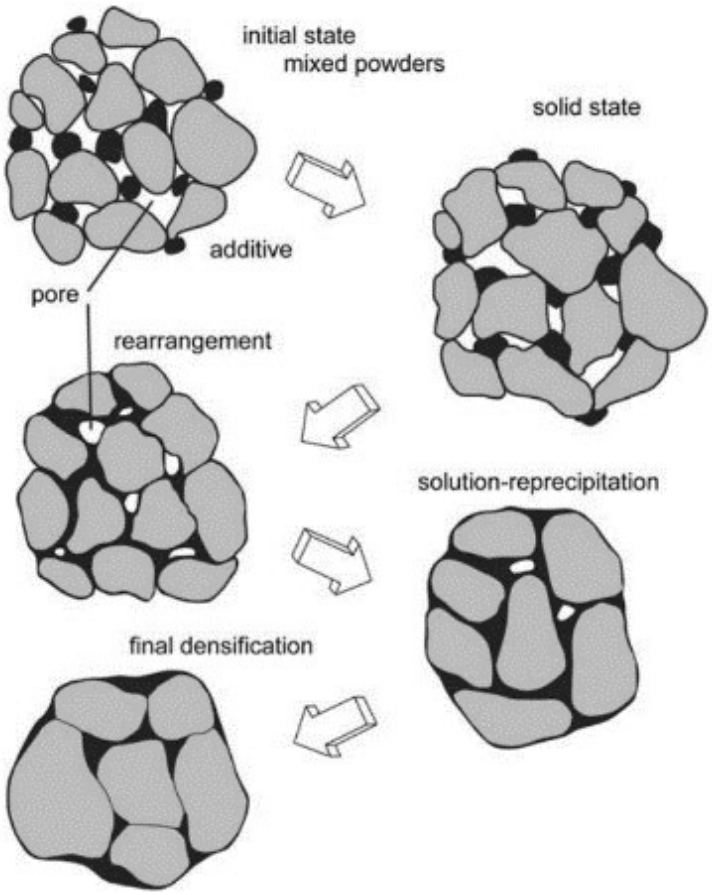


Figure 2-5. Microstructure changes during LPS, starting with mixed powders till the final densification [54]

The four main stages of liquid phase sintering are discussed as follows:

2.3.1.1.1. Solid state heating

In the initial stage, the powder compact begins to undergo solid state sintering upon heating [54]. No liquid is present at this stage and the joining of particles, densification or reduction of porosity is through atomic diffusion [59]. Solid state heating is characterised mainly by the bonding between the adjacent particles along with the formation and significant growth of necks, and limited densification [60]. Densification during this stage is highly dependent on the solubility relationship between the binder and the hard phase [13]. In the sintering of WC-Co cemented carbides, more than 50% of the densification is achieved before reaching the eutectic temperature (typically 0.5-0.9 of the melting point) [13].

2.3.1.1.2. Primary re-arrangement (liquid spreading)

Primary re-arrangement occurs on the first formation of liquid [61]. The grain surfaces are dissolved while the capillary force from the wetting liquid pulls the solid grains together to produce more stable packing [62]. As a result, rapid densification is observed due to the

increased rate of heat transfer and the specific heat needed to form the liquid [16]. Additionally, the newly formed liquid further improves the transport rates responsible for coarsening and densification because the solid is soluble in the liquid [54]. Pore elimination is also observed during this stage, and most of the densification is achieved as the liquid phase fills up the pores within the compact [63]. Rearrangement stops either when all the pores have been filled by the liquid or when the maximum volumetric density of the compact has been reached without any deformation of the solid particles [61].

2.3.1.1.3. Solution-reprecipitation

The next stage is solution-reprecipitation (secondary re-arrangement). During this stage, the solid phase material dissolves into the liquid at the points where touching solid grains make contact, diffuses, or moves through the liquid, and then precipitates in other locations along the liquid-solid interface [61]. The dissolved grains may rearrange to create new compounds or solid phases that differ from the original solid phase during the reprecipitation stage [56]. Therefore, this process can result in changes in grain size and structure and changes in the overall material properties. Here, densification is associated with the formation of the stable necks between the solid grains and the surrounding liquid, large grains shape accommodation, and grain growth due to Oswald ripening and grain coalescence [13]. The large grains undergo shape accommodation, due to the precipitate material from the dissolved smaller grains resulting in the availability of a liquid phase for filling the pores as illustrated in Figure 2.5 [52]

Ostwald ripening is the process by which small grains dissolve while larger grains reprecipitate, resulting in the growth of the larger grains and the disappearance of the smaller grains. As a result, the grain structure becomes coarser and there are fewer grains overall in the material's microstructure [64]. Ostwald ripening is controlled by two main mechanisms: interface reaction-controlled Ostwald ripening and diffusion-controlled Ostwald ripening [65]. Interface-controlled Ostwald ripening occurs when the rate at which the small grains dissolve is limited by the rate of reaction between the liquid and the surface of the grain. In this instance, the rate of dissolution is determined by the kinetics of the reaction at the grain-liquid interface, as opposed to the diffusion of the grains through the liquid. Diffusion-controlled Ostwald ripening, on the other hand, occurs when the rate at which the small grains dissolve is constrained by the rate of diffusion through the liquid. In this instance, the rate of dissolution is determined by the rate at which the grains diffuse through the liquid and reach the surface of the larger grains, where they can then dissolve. Interface-controlled Ostwald ripening usually occurs in materials where the liquid phase forms a product with the surface of the solid phase

whereas, diffusion-controlled Ostwald ripening is more prevalent in materials where the liquid does not react with the surface of the solid phase [40, 65]. Ostwald ripening due to grain growth can be described by Equation (2.1) [40]:

$$G^n - G_0^n = k(t - t_0) \quad 2.1$$

where, G is the size of the grain at the end of sintering or holding time (t), G_0 is the size of the grain at the initial sintering time (t_0), grain growth rate parameter k (given by Equation (2.2) [40]) is a materials constant that is related to the transport mechanism and is dependent on the temperature, and n takes up the values of n = 2 for interface-controlled Ostwald ripening, and n = 3 for diffusion-controlled Ostwald ripening [16].

$$k = k_0 e^{\left(-\frac{Q}{RT}\right)} \quad 2.2$$

where, Q is the apparent activation energy for grain growth, R is the gas constant and T is the absolute sintering temperature. Equations 2.1 and 2.2 show that the grain growth due to Ostwald ripening is influenced by the sintering time, the activation energy for grain growth and temperature.

2.3.1.1.4. Final densification (coarsening)

The final stage of LPS is the extension of the solution-reprecipitation process and it is mainly characterised by microstructural coarsening. Densification still occurs simultaneously with grain coarsening, however, during this stage, grain growth is more dominant [13]. The microstructural changes (i.e. grain size and distribution, grain shape and the distribution of the binder) due to grain coarsening in the final stage influence the mechanical properties (wear resistance, strength, fracture toughness, electrical arcing characteristics, magnetic behaviour, and ductility) of the sintered product [52]. Hence, the control of these microstructural changes during this stage of LPS is desirable.

2.3.1.2. Pulsed electric current sintering (PECS) technique.

Pulsed electric current sintering (PECS) also known as SPS, or field assistant sintering technique (FAST) is a type of pressure-assisted sintering process. PECS is a rapid sintering method which uses high pressures and high heating rates to consolidate powder compacts [66]. Thus, full densification could be accomplished with limited grain growth (even for nano-sized powders) and shorter sintering times. This contrasts with conventional sintering techniques that can take several hours to complete [67]. In this technique, the powder compact that is to be

sintered is placed into a graphite die and subjected to concurrent heating and compaction by means of a pulsed direct electric current (i.e. the die acts as a heating element when the electric current is passed through it). The electrical field generates a spark that rapidly heats the powder compact, leading to the formation of solid-state bonds between the particles. Densification is aided by the removal of pores or voids caused by the uniaxial pressure that is applied during the sintering process. For compacts which are conductive, the current passes through it as well, resulting in additional internal heating. Hence, very high heating rates (up to 1100°C/min) at sintering temperatures that are a few hundred degrees lower than conventional LPS could be attained through PECS [66], [68]. Figure 2.6 shows a schematic of a PECS machine [69].

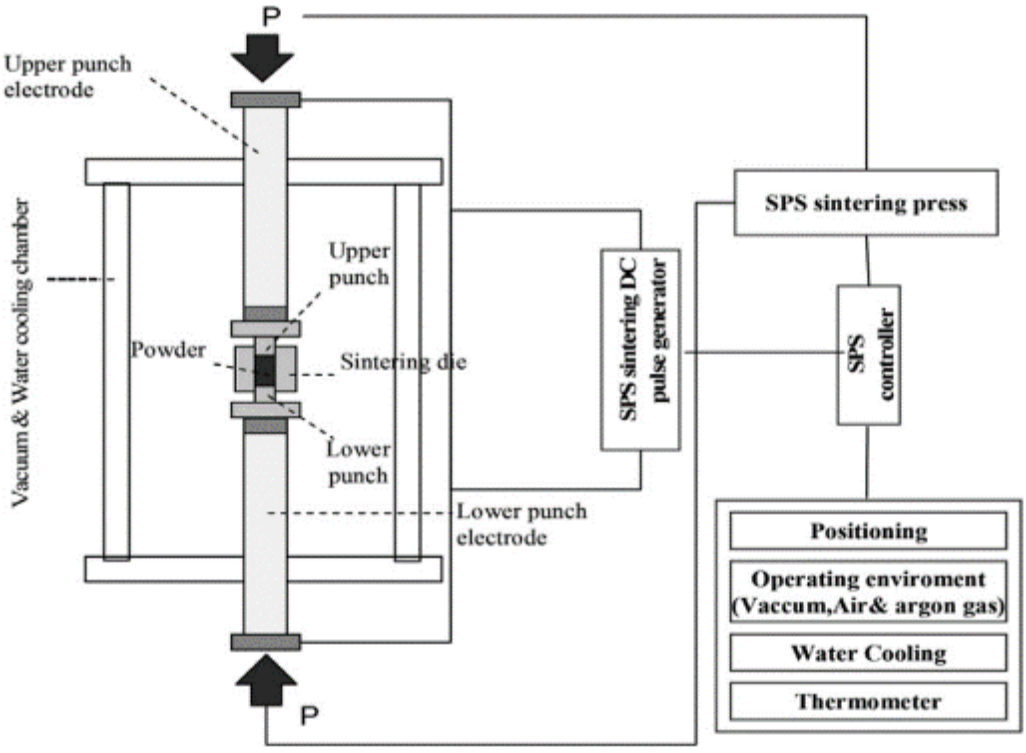


Figure 2-6. Schematic of a PECS machine [69]

Usually, PECS is carried out in four main stages as illustrated in Figure 2.7. The creation of a vacuum and removal of gases (residual moisture) occurs during the first stage. The second stage involves applying pressure to activate the surface energy of the powder particles. This is then followed by resistance heating in the third stage. During this stage, a high-power direct current is applied to generate a spark. Within a few milliseconds, the spark raises the material's temperature to the sintering temperature, which is typically between 1000 °C and 2000 °C [68]. This results in evaporation and melting on the powder particle surfaces and necks form in the

vicinity of the particle contact points. The external applied pressure, together with the high localised temperatures generated via the resistance pulse heating, causes the powder particles to diffuse into one another, thus leading to the homogeneous densification of the material. The spark also results in the evaporation of any residual impurities in the powder, promoting the formation of a clean and high-quality material [70]. It is also worth noting that the PECS is not only a metal-binderless sintering method, but also does not require a pre-compaction step. This is because, the powder is directly filled into the graphite die through which the pressure is applied and the electric current is passed, resulting in a fully dense material with promising mechanical properties [68]. Cooling the material to room temperature is then done in the fourth and last stage [68].

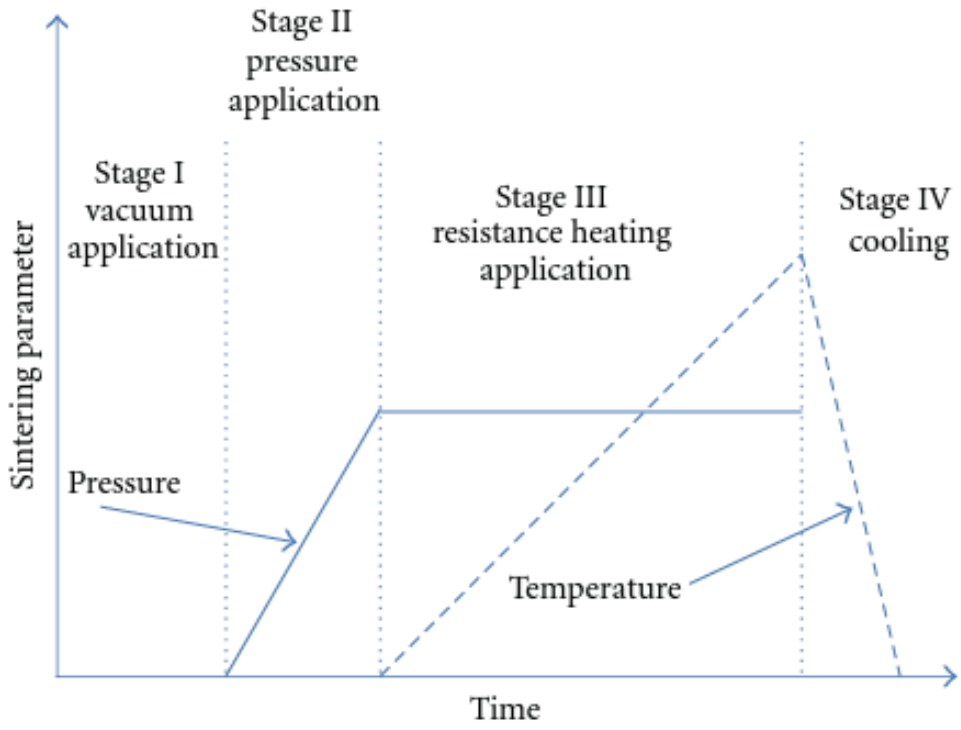


Figure 2-7. Pulsed electric current sintering stages [68]

2.3.2. Effects of sintering variables in cemented carbides

Sintering is influenced by several variables which affect the microstructure, properties, and the final performance of the sintered component. Some of these variables include (i) composition, (ii) sintering temperature, (iii) time, (iv) pressure, (v), atmosphere and (vi) cooling rate. The effects of the variables are codependent and can differ depending on the type of the material and the specific conditions of the sintering technique [70].

2.3.2.1. Composition

When sintering two or more materials, powder composition homogeneity is critical. If this is not done correctly, the desired mechanical properties and control of the compact's dimensional changes may be difficult to achieve. Bonding between two or more different powder compositions occurs simultaneously when they are sintered. As a result, milling is performed to ensure that the binder is evenly dispersed in the carbide matrix. Homogeneous phase distribution within the green compact results in uniform material transport during sintering and improved sintered component properties [38].

Sintered components with ultrafine powder particle grain sizes have been found to exhibit improved mechanical properties. These finer powders sinter faster and at lower temperatures than those with coarse grained particles as demonstrated in studies by Schubert et al. [71] and Maheshwari et al. [72]. In particular, Schubert et al. found that WC-Co powders with grain sizes of less than 0.3 μm could be densified by 85% at a sintering temperature of 1280 °C, compared to 70% for powders with grain size of 0.7 μm. This observation can be explained by the fact that smaller grain sizes result in a higher surface area-to-volume ratio, which accelerates diffusion and the development of interparticle bonds. Due to the faster and more effective sintering process, the final material will have better mechanical properties because of the finer microstructure. In addition, research studies also indicated that it is very important to add grain growth inhibitors (VC, Cr_3C_2, TaC, NbC, etc.) when dealing with ultrafine powder particles, as they can help in retaining the ultrafine carbide structure in the consolidated (dense) material [38]. The addition of the grain growth inhibitors in ultrafine WC-Co manufacture promotes the occurrence of individual fine WC particles instead of agglomerates resulting in sintered components with improved mechanical properties.

2.3.2.2. Temperature

The sintering temperature of carbide matrix materials is influenced by various factors, including the composition of the carbide matrix. In the case of WC-Co cemented carbides, the solubility of WC in Co, the wetting WC by Co and diffusion increase as the temperature increases [13]. The amount of the cobalt binder present also plays a role in the sintering temperature. For example, when the cobalt content is high the sintering temperature can be as low as 1350 °C and increase up to 1600 °C or higher for compositions having high proportions of TiC, TaC, and/or NbC and low cobalt contents [13, 73]. Increasing the sintering temperature

can lead to shorter sintering times due to faster diffusion and higher volumes of the liquid phase [13, 29]. However, high sintering temperatures can also result in microstructural coarsening and distortion of compacts [13]. A study by Zhou et al. [74] found that densification of WC-6Co (wt%) increased with increasing the sintering temperature. The same study also demonstrated that increasing the carbide particle size can result in an increase of the sintering temperature.

2.3.2.3. Time

Time is one of the most important factors that influences the sintering of cemented carbides. Prolonged sintering duration provides more time for particles to diffuse and bond together, resulting in better densification [13]. However, longer periods of sintering can also lead to grain growth. In contrast, shorter sintering periods lead to finer grained microstructures with smaller binder pools and uneven distribution, resulting in higher hardness and poor fracture toughness [12]. The sintering time is also sensitive to the powder particle sizes. For example, in comparison to the micrometre sized cemented carbides, the sintering nanosized powder particles pose a challenge in retaining the nanoscale size upon full densification. This challenge arises from rapid grain growth, which intensifies with higher sintering temperature and time during LPS [40]. In addition, an investigation by Lou et al. [75] concluded that the sintering time also varies with sintered compact thickness, with thicker compacts typically taking longer to sinter. Hence, it is important to find a good time-temperature and composition trade-off to optimise densification whilst minimising grain growth, avoiding compact distortion, and obtaining the desired properties of the final product.

2.3.2.4. Pressure

Applying external pressure to a powder compact during sintering increases densification driving force and densification kinetics, reduces porosity and improves mechanical properties [56]. Grain growth, on the other hand, is unrelated to the applied external pressure and is typically influenced by other factors such as temperature and time. As a result, the external pressure has a negligible effect on grain growth [56]. The effect of external pressure is more pronounced in systems where the rate of grain growth exceeds the rate of densification. In such systems, the grains tend to grow rapidly compared to the densification process. Therefore, applying external pressure will increase the densification rate. The sintering temperature and time can be reduced as the densification rate is increased by external pressure and grain growth

is inhibited as a consequence [56]. Azcona et al. [76] successfully consolidated WC-10Co (wt%) nanometre powders to full density using HIP sintering at 1000 ºC, a temperature significantly lower than that typically required for achieving full densification in the conventional sintering of WC-Co based cemented carbides. Akimov et al. [77] investigated the use of cold isostatic pressing (CIP) and HIP on the structure and mechanical properties of WC-8Co (wt%). Their study revealed that preliminary CIP of green compacts leads to sintered cemented carbide products with higher hardness and finer WC grains than those fabricated using other sintering methods.

2.3.2.5. Atmosphere

The sintering atmosphere is another important sintering process variable. As already mentioned, the heating of compacts is done at temperature ranges of 1350 °C to 1600 °C and above depending on the powder composition. At these temperatures, possible chemical interactions between the compacts and the surrounding atmosphere could occur. For example, during the sintering of cemented carbides, most reactions involve carbon. This can cause slight deviations from stoichiometric carbon content resulting in the formation of either eta phase or free graphite, both of which reduce the mechanical properties [78]. Additionally, hardmetals are highly reactive in nature and this makes the compacts very susceptible to reaction with the sintering atmosphere [13]. Hence, the sintering of these materials is usually done in a hydrogen or vacuum atmosphere.

2.3.2.6. Cooling rate

The rate of cooling during sintering has a significant impact on the microstructure and properties of sintered components [79]. The cooling rate has an effect on grain growth and the final grain size of the material. Low cooling rates give the material more time to grow larger grains, resulting in a coarser microstructure, whereas high cooling rates inhibit grain growth, resulting in a finer microstructure [80]. The rate of cooling also influences the formation and distribution of secondary phases within sintered material. Slower cooling rates may provide enough time for secondary phases to form and expand. However, if the cooling rate is too fast, the secondary phases may not have enough time to form or may not form uniformly [81]. This means that it is important to control and optimise the cooling rate during the sintering process to achieve the desired microstructure and properties of the final product.

2.4. Characterisation of the cemented carbides microstructure

This subsection discusses some of the common techniques used for the characterisation of cemented carbides. These techniques can be used individually or in combination to characterise the microstructure of cemented carbides and to gain a better understanding of their mechanical and physical properties.

2.4.1. Optical microscopy

Optical microscopy (OM) is a popular technique for examining the microstructure of cemented carbides. It allows the observation of the microstructure of the material at various magnifications, which is useful for real-time inspection of topographic or microstructural features of cemented carbides such as the different phases present, porosity and cracks [82]. It is worth noting that the application of OM can be limited by their resolution. The borders of a fine grained (<0.8 μm) material may become blurred due to insufficient sharpness or contrast, resulting in imprecise characterisation of the material's geometric features [82].

2.4.2. Scanning electron microscopy

Scanning electron microscopy (SEM) is a high-resolution imaging technique that provides detailed information about the microstructure of cemented carbides. It can provide information on the size, morphology and distribution phases such as tungsten carbide particles and the binder phase in WC-Co systems [83]. The SEM, rather than using light, generates images of sample surfaces by capturing particles that interact with the sample surface or subsurface, such as secondary electrons (SEs) and backscattered electrons (BSEs) [82]. Backscattered electrons carry compositional information of the material because the sample's backscattering power is proportional to its local atomic number. High resolution SEM can reach resolutions of ~1nm and it is suitable for the microstructural characterization of cemented carbides in the classes below fine grain size [82].

2.4.3. X-ray diffraction

X-ray diffraction (XRD) is a non-destructive technique that can be used in the characterisation of cemented carbides [84]. The technique can be used for phase identification and quantification, thorough understanding of the crystalline structure, size and orientation, phase

transformation, dislocation density, residual stresses and strain in the material and thermal expansion coefficient of the material [84].

2.4.4. Transmission electron microscopy and high-resolution transmission electron microscopy

Transmission electron microscopy (TEM) and high-resolution TEM (HRTEM) are imaging techniques that provide detailed information about the microstructure of cemented carbides at the nano and atomic levels. They are among the commonly used characterisation techniques as they allow for the precise characterisation of materials at extremely high resolutions [85]. In WC-Co cemented carbides, both the TEM and HRTEM can be used to determine the morphology and crystal structure of the carbide and binder, the size and distribution of the particles with the microstructure, and the degree of order and interactions between the atoms within the microstructure [85-86].

2.4.5. Energy-dispersive X-ray spectroscopy

Energy-dispersive X-ray spectroscopy (EDS) is an analytical technique that is often used in conjunction with SEM or TEM to determine the chemical composition of different phases in cemented carbides. It can be used to determine the elemental composition of tungsten carbide particles, the binder phase, and any secondary phases present in the material [82].

2.5. Mechanical properties of cemented carbides

This subsection discusses some of the key mechanical properties of cemented carbides. The mechanical properties depend mainly on the initial chemistry (main carbide, binder and additives), initial geometry (size, size distribution and morphology of the initial powders and homogeneity of their mixture), and the production methods (LPS or PECS) [16]. All these factors are aimed at creating the final chemistry and geometry that have the fewest possible defects and the optimal combination of mechanical properties.

2.5.1. Hardness and fracture toughness

Hardness and fracture toughness are deemed the two most critical mechanical properties of cemented carbides [16]. The hardness of a material is the ability to resist plastic deformation or abrasion wear, while fracture toughness is its ability to absorb impact energy by deformation and resist fracture or crack propagation [87]. The two properties are generally inversely

proportional to each other (i.e. they are trade-off balance properties), whereby when one property increases the other one decreases [87].

2.5.1.1. Hardness measurements

Hardness is determined by measuring the area of an indentation left on a material by an indentation following load penetration. There are several standard hardness tests for cemented carbides including, Vickers hardness (HV), Rockwell hardness (HR), and Brinell hardness (HB) [16, 88, 89]. Vickers hardness test is the most commonly used test for cemented carbides [87]. The standardised method for measuring HV in the cemented carbide industry is outlined in ISO 6507:2018 [90]. The HV is determined by the ratio of the test force (kilogram force [kgf]) and the surface area of indentation (mm^2). The designation of the hardness value is typically given along with the corresponding test force; for instance, 1500 HV_{30} indicates that a test force of 30kgf was used to obtain a Vickers hardness of 1500.

2.5.1.2. Fracture toughness measurements

Fracture toughness (K_{IC}) can be measured in different ways depending on the type of material being tested. Indentation fracture toughness (IFT) is a commonly used method to assess fracture toughness in cemented carbides [87]. The standard for IFT K_{IC} measurements for hardmetals is provided in the ISO 28079 [91]. The IFT method was originally proposed by Palmqvist [92] and is based on the crack length generated by Vickers indentation. The fundamental presumption of this technique is that the ideal crack should begin at the corner of the indent, be straight, and span roughly equal distances while splitting. An unequal crack length indicates a lower quality measurement. It should be acknowledged that the published IFT K_{IC} results may vary significantly due to the use of different loads, measurement errors in terms of hardness, crack shape assumptions, and operator subjectivity in determining where the cracks end [87]. Hence, a larger sample size is required to obtain results with statistical confidence when dealing with IFT measurements of cemented carbides.

2.5.1.3. Hardness and fracture toughness in WC-Co cemented carbides.

The hardness and fracture toughness properties of cemented carbides are heavily influenced by several factors including the microstructural parameters such as grain size, binder volume fraction, average free path for binder, distribution of the binder, contiguity, densification, and composition [16]. Contiguity is a fraction of the total internal surface area of a carbide grain

shared by the neighbouring grains. Hence, it is used to determine the amounts of carbide network or carbide connections (proportion of WC/WC contacts) and the extent to which a continuous skeleton of the carbide phase exists within the microstructure [93]. The average free path for the binder is the mean distance across the binder phase from one carbide-binder interface to another [94].

2.5.1.3.1. Influence of grain size, contiguity and binder phase on hardness and fracture toughness

In contrast to fracture toughness, which behaves in the opposite way, the hardness of WC-Co cemented carbides increases as the carbide grain size decreases [87]. Figure 2.8 illustrates how harder WC-Co grades have finer microstructures compared to grades with coarser grains [87]. Contiguity and the average free path are complementary variables that can be used to describe the hardness and thus fracture toughness [95]. Furthermore, while finer grains improve the hardness of cemented carbides, it should be noted that, in general, microstructural grain refinement and a decrease in binder content often result in a higher contiguity. Emani et al. [96] discovered the highest hardness in samples with the smallest WC grain sizes and the average free path of the Co phase. According to the findings of a study conducted by Sheikh et al. [95] there is a consistent decrease in fracture toughness with increasing carbide contiguity and an opposite trend in fracture toughness with increasing binder average free path.

As per Figure 2.9 [87], while the fracture toughness generally rises with an increase in binder volume fraction, the hardness typically declines. The average free path for the binder increases with the size of the WC grain in WC-Co cemented carbides at constant binder contents, resulting in a reduction in hardness [97]. In addition, the majority of fracture mechanisms involve the cracking of WC grains, which can then cause existing microstructural flaws or processing imperfections to experience crack growth and propagation [98]. This means that since the pores (defects) act as crack initiation spots, poor densification causes a reduction in fracture toughness.

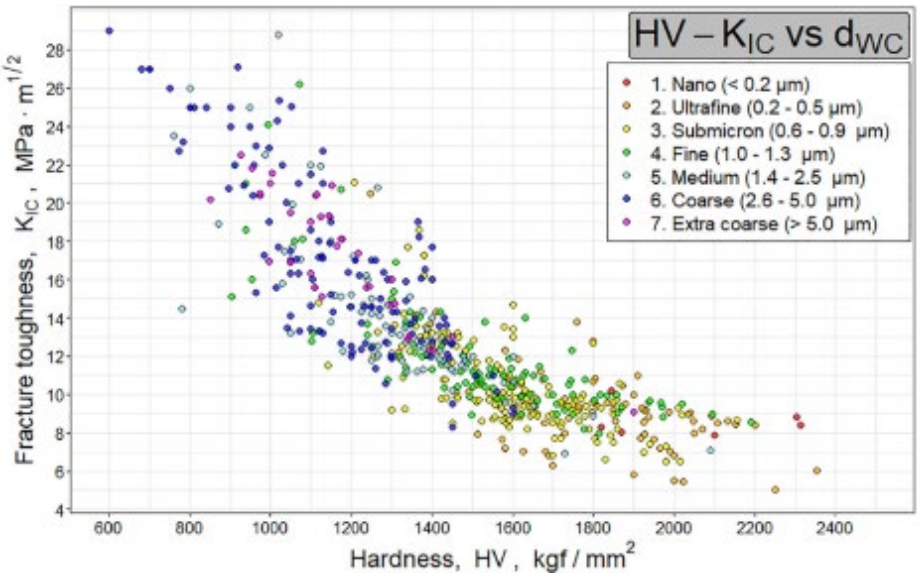


Figure 2-8. HV-K_{IC} relationships for various grain sizes in WC-Co cemented carbides produced via conventional sintering methods [87]

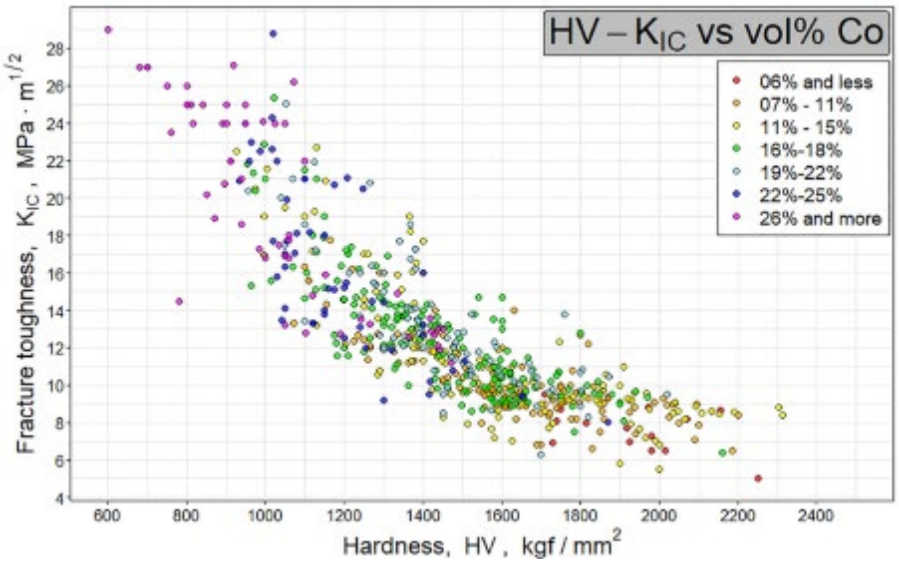


Figure 2-9. HV-K_{IC} relationships for various binder volume fractions in WC-Co cemented carbides produced via conventional sintering methods [87]

2.5.1.3.2. Composition effects on fracture toughness and hardness

As previously stated, the composition of cemented carbides is critical to their hardness and fracture toughness. The carbide and binder phases are primarily responsible for hardness and fracture toughness properties, respectively. The hardness and fracture toughness of a material are affected by its composition, as shown in Figure 2.10. The trend in the figure's fracture toughness vs. hardness plot illustrates the innate trade-off relationship between the two properties. Another notable observation in Figure 2.10 is that in general, the WC-Co based

cemented carbides exhibit higher values of both hardness and fracture toughness compared to the Ti (C, N), NbC, VC and TaC based cermets.

During machining, cemented carbide cutting inserts operate at high temperatures. Temperatures between the cutting edge and the workpiece, for example, can reach 600-1000 °C [99]. As a result, the elevated temperature mechanical properties such as hot hardness (i.e. hardness of cemented carbides at high temperatures) and fracture toughness are also important. The hot hardness of WC-Co cemented carbides could be improved by reducing the WC grain size and the binder content [100]. Furthermore, carbide additions such as TiC, Tac or NbC could also be used to increase the hot hardness [100]. These additions alter the microstructure and result in the formation of complex mixed crystal systems like (W, Ti) C, (W, Ta, Nb) C, or (W, Ta, Nb, Ti) C [101]. The mixed crystals are known as complex solid solutions and are thought to form chain-like structures, which are responsible for slowing WC grain boundary slipping and thus increasing hot harness [101-102].

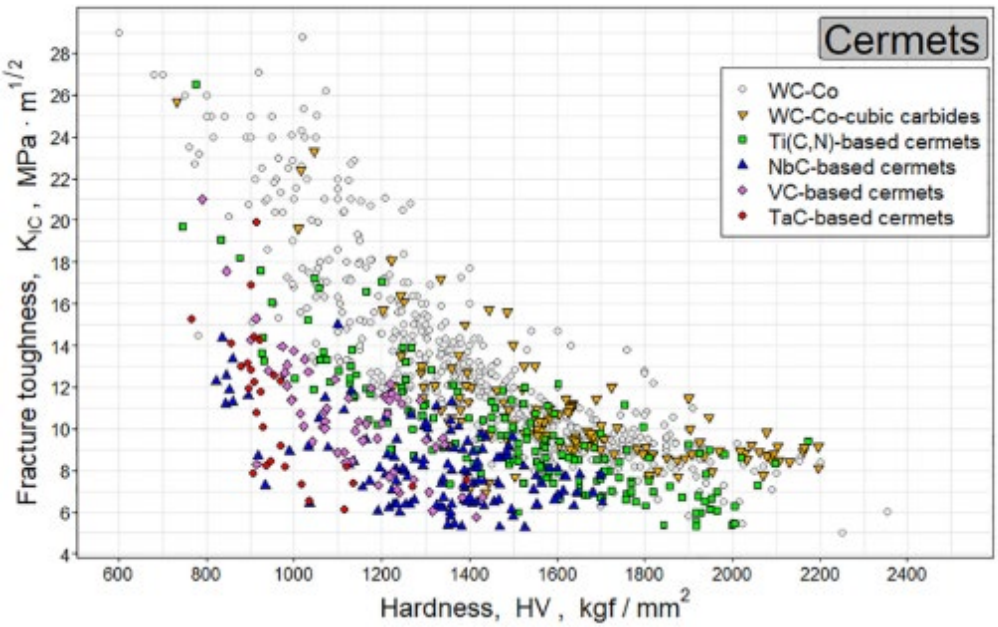


Figure 2-10. HV-K_{IC} relationship for cemented carbides containing cubic carbides and cermets of various compositions [87]

High temperatures, i.e. temperatures above 600 °C, significantly reduce the fracture toughness and strength of WC-Co cemented carbides [103]. According to several studies [45, 99, 103], [104], grades of cemented carbides containing Mo_2C, TiC, TaC, VC, and NbC additions have improved high temperature fracture toughness. Nickel or Fe bonded cemented carbides exhibit inferior toughness compared to those bonded with Co [13]. However, it has been found that

hardmetals or cemented carbides with binders such as Ni-Fe, Ni-Cr, Ni-Co-Cr, or Ni-Co-Cr-Mo retain their toughness at high temperatures [13].

2.5.2. Elastic and shear modulus

Elastic modulus (E) also known as "Young's modulus or modulus of elasticity" measures a material's stiffness or capacity to withstand deformation when subjected to an applied stress. It refers to the ratio of stress to strain on a material's stress-strain curve within the elastic range. The elastic modulus is also a measure of a material's ability to return to its original shape after being deformed by an external force [105]. Shear modulus (G) also known as "modulus of rigidity" is a mechanical property that measures the material's resistance to deformation under applied shear stress. Shear stress is the ratio of the shear stress to the shear strain within the elastic range of a material's stress-strain curve [106].

There are primarily two ways of determining the elastic and shear modulus of materials. One is through measuring the slope of the stress-strain curve after loading (often used for metallic materials) [107]. The other is through the measurement of the speed of the longitudinal and horizontal ultrasonic waves (mainly used for brittle materials and ceramics), following the ISO 3312-1990 and the ASTM E494-2010 standards [108]. The latter is a non-destructive test and is the primary method of focus for measuring the elastic modulus properties of cemented carbides and cermets in this work.

2.6. Face milling machining

The current investigation is focused on milling machining of a-GCI. Milling is a machining operation in which material is removed (or cut) by rotating cutting inserts in the opposite direction of the workpiece's feed [109]. Milling is classified into two main types (face milling and end milling) [109], but only face milling will be considered in this study. A face milling machining operation is shown in Figure 2.11. Cutting parameters, cutting insert life, insert geometry and cutting fluids are just a few examples of the variables that affect machining operations[109]. These elements are crucial in determining the kind of milling or machining operation to be performed, the type of workpiece to be processed, the degree of processing (roughing, semi-finishing, or finishing), the machining conditions (dry machining or lubricant use), etc. [109]. Therefore, it is crucial to consider each of these factors when researching, creating, or enhancing cutting inserts for machining applications.

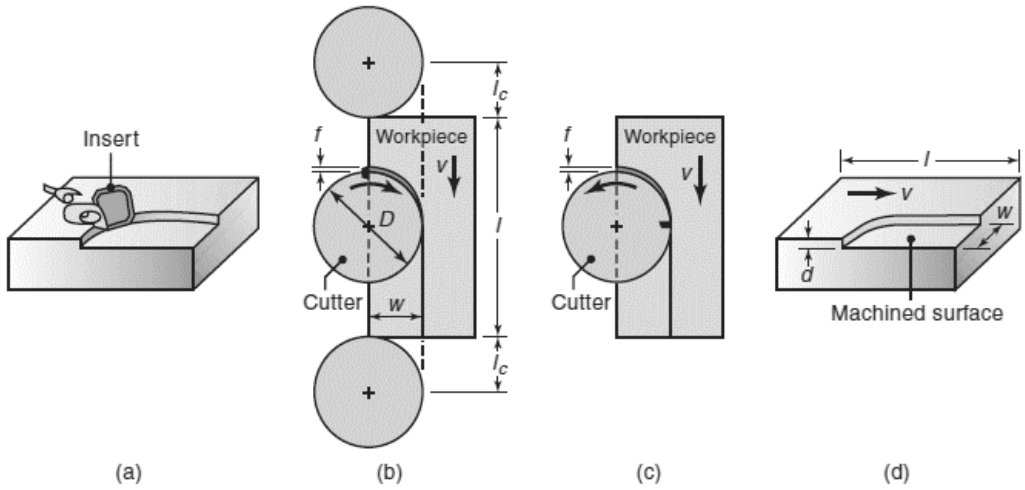


Figure 2-11. Face milling machining, showing (a) the action of a cutting insert; (b) climb milling; (c) conventional milling; (d) machined surface with face milling dimensions [110]

2.6.1. Face milling machining parameters

Some of the most crucial parameters for machining operations include the cutting speed (V_c), feed speed (V_f), depth of cut (a_p), radial depth of cut (a_r), material removal rate ($\dot{m}_{rr}$) and cutting force (F) [111]. Primarily because they have an impact on the surface quality of the machined components as well as the machining forces, temperatures, productivity, and life of the cutting insert [111]. These parameters must be carefully adjusted to account for a variety of cutting conditions, including the range of machining (roughing, semi-finishing, or finishing), and the nature of the workpiece material [112].

The **cutting speed** (m/min) which refers to the speeds at which the cutting edge machines the workpiece material [110], can be determined using Equation 2.3 [110].

$$V_c = \frac{\pi n D}{1000} \qquad 2.3$$

where n is the spindle speed in rpm and D is the cutting diameter (equal to the radial depth of cut) in mm.

The **feed speed** (mm/min), also known as the feed rate or table feed is the feed of the cutting insert relative to the workpiece. The feed rate for milling operations is dependent on the type and number of cutting inserts/teeth on the cutter, and the desired amount of material that each tooth must remove [111]. The feed rate is directly proportional to the number of cutting edges or teeth on the cutter. Like the cutting speed, an increase in the feed rate results in increased

machining forces and temperatures. This is due to the increased level of contact between the cutting inserts and the workpiece material [27]. The feed rate can be calculated using Equation 2.4 [113] as follows:

$$V_f = f_z Z n \qquad 2.4$$

where, f_z is the feed per tooth in (mm/tooth), n is the spindle speed (rpm or mm/min) and Z represents the number of teeth.

The **material removal rate** (mm^3/min) is the amount of material machined from a workpiece for a specific unit of time [113]. The material removal rate can be determined using Equation 2.5 [113]. This parameter increases with the increasing depth of cut; hence, it is usually high when roughing and low when finishing.

$$\dot{m}_{rr} = a_p\, a_r V_f \qquad 2.5$$

The **cutting forces** (N) influence the insert wear and the quality of the surface finish during machining. The forces increase with increasing depth of cut and feed [29, 113]. Thus, it is important to understand the magnitude of the forces that the cutting inserts are likely to experience during machining. This would provide a basis for understanding the mechanics of the cutting insert and the cutting operation which could be used to optimise surface quality (or roughness) and cutting insert life respectively [114]. The cutting forces can be determined using either the cutter reference system or the table reference system [27]. The two systems are illustrated in Figure 2.12.

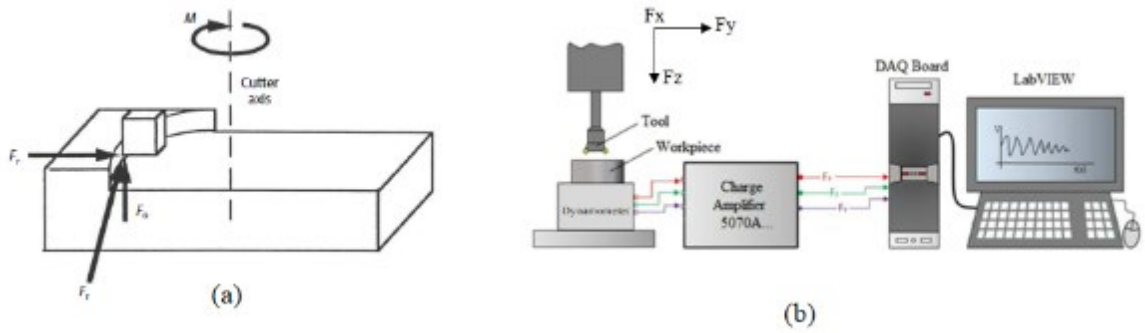


Figure 2-12. Cutter reference (a) [27] vs. table force reference systems (b) [114]

The cutter reference system comprises of the tangential (F_t), the radial (F_r), and the axial (F_a) forces that act on the cutting edge. The table reference system uses a dynamometer to measure the force components (F_x, F_y, and F_z) in the x, y, and z axes respectively. The cutting force

during operation is the resultant force (F_i) which is the vector sum of the force components. For example, the cutting force for a table reference system can be calculated using Equation 2.6 as follows [115]:

$$F_i = \sqrt{F_x^2 + F_y^2 + F_z^2} \quad 2.6$$

where, F_x is the feed force (component parallel to the machined surface and feed direction), F_y is the normal or thrust force (component parallel to the machined surface and perpendicular to the feed direction), and F_z is the vertical or cutting force (component of the force parallel to the cutter axis and perpendicular to the feed direction).

The average resultant force (F) is then calculated using Equation 2.7 [17].

$$F = {(\sum F_i)}/{N} \quad 2.7$$

2.6.2. Energy consumption in face milling

The consumption of energy is a serious challenge in the manufacturing industry. This is due to the considerable costs and environmental impacts that manufacturing companies are confronted with in their operations [116]. According to Abele et al. [117], electrical energy consumption contributes to more than 20% of the total operating costs over the life of a machine tool. This demonstrates the importance of considering energy consumption when manufacturing. South Africa has been facing serious challenges when it comes to generating and supplying electrical energy since 2008. The country's power utility (Eskom) has been implementing various stages of power load shedding, with 2023 being the worst year on record for load shedding thus far [118]. The manufacturing industry and the whole economy of the country have been severely harmed by the energy crisis. The majority of South African manufacturers have been having a difficult time trying to satisfy demand as well as maintaining their operations [118]. In addition, coal continues to dominate South Africa's energy mix, accounting for roughly 80% of the total energy grid [119]. This means that nearly 80% of the energy used to run machine tools is generated by burning coal which emits a significant of CO_2. The environmental performance of manufacturing systems can be improved significantly by reducing the energy consumption of machine tools [120]. Therefore, the maximisation of manufacturing efficiency as well as the minimisation of environmental impact can help in achieving sustainable manufacturing. Face milling's electrical energy consumption can be reduced by carefully selecting process parameters. However, there is always a trade-off

between reducing energy consumption and maintaining a high surface finish on manufactured components [121]. As a result, selecting process parameters is fraught with some difficulties.

2.6.2.1. Classification of energy consumption in face milling

Figure 2.13 shows the classification of energy consumption of a face milling operation. From the figure, it can be seen that the energy consumption of a machining process can be evaluated at different levels, i.e. (a) machine tool, (b) spindle, and (c) process levels [121]. The energy consumed at the machine level refers to the energy consumption by the whole machine tool including control systems, cooling and lubrication units, drive systems, spindle motor, manufacturing process, etc. The relationship between energy consumption and cutting conditions at this level is critical for the improvement of the overall efficiency of the machine tools [116]. However, it is worth noting that it is impractical to compare various manufacturing processes, or even the same process using various machine tools.

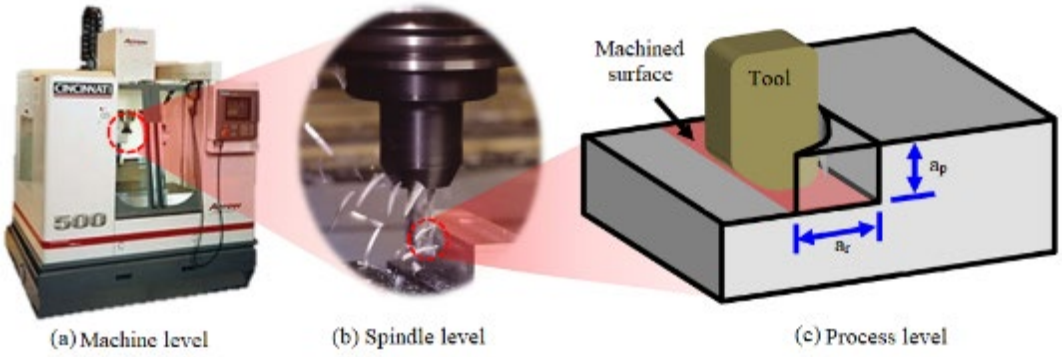


Figure 2-13. Classification of energy consumption in face milling [121]

Only the energy used by the spindle motor is considered at the spindle level. Here electricity is consumed by the spindle motor when rotating the cutting tool (insert holder) during the milling process. Dietmair et al. [122] reported that the spindle can consume more than 15% of the total energy. The energy consumption at the spindle level may be useful when determining the efficiency of the spindle motor. The energy consumed by the spindle is dependent on the type of motor which varies significantly across the different machine tools. Furthermore, the energy consumption of the spindle is incomparable to other manufacturing processes [121]. The process level considers only the energy that is consumed by the actual removal of the material, and it is not influenced by the machine tool. The energy consumption at this level governs the formation of chips and the generation of the surface on the workpiece material. As a result, this energy should be considered when selecting process parameters for optimising both the energy

consumption and machined surface quality (surface roughness) [116, 121]. The current work focuses on the energy consumption at the process level.

2.6.2.2. Specific energy consumption and efficiency

In machining, specific energy is the energy required to remove a unit volume of workpiece material. Specific energy is widely used to assess the efficiency or energy consumption for machining processes [116]. Similar to the energy consumption levels, the specific energy can be evaluated at three levels. However, as already mentioned, only the specific energy at the process level will be considered in this work. The specific cutting energy (U_c) of abrasive machining processes (milling in this instance), is defined as the ratio of machining power to the material removal rate as shown in Equation 2.8 [123].

$$U_c = \frac{E_c}{V} = \frac{P_c}{\dot{m}_{rr}} \tag{2.8}$$

where E_c is the cutting energy (J), V is the volume of material removed (mm^3), and P_c is the cutting power (W).

The cutting power (P_c) which is the power needed to dissipate material during machining can be expressed in terms of the resultant cutting force and cutting speed as follows:

$$P_c = FV_c \tag{2.9}$$

Thus, the specific cutting energy can be determined using Equation 2.10.

$$U_c = \frac{FV_c}{\dot{m}_{rr}} \tag{2.10}$$

According to Marinescu et al. [123] machining processes such as milling involve the removal of larger volumes of material per unit time. In comparison to other manufacturing processes like grinding, lapping, honing, and polishing, these processes typically operate at lower specific energies [123]. This is because abrasive machining processes typically have high rates of material removal. They will therefore typically be anticipated to be at the lower end of a particular energy range. For example, in the context of grinding ferrous materials, a specific cutting energy of 10 J/mm^3 is considered very low, and the process is considered to be highly efficient. However, the same cannot be said for milling or turning, where the specific cutting

energy may be an order of magnitude lower than that of grinding [123]. Kalpakjian et al. [110] reported U_c values of 1.1 – 5 J/mm^3 for machining cast irons.

2.7. Modern cutting insert design

Several key features are included in modern cutting insert designs. For instance, composition design and insert geometry optimisation are incorporated to reduce the cutting forces and surface roughness. Additionally, chip breakers and deflectors are designed to facilitate efficient chip flow during machining. Lastly, microgeometry design through surface texturing to improve mechanical properties and extend the insert lifespan [124]. This section discusses some of the key features of modern insert design.

2.7.1. Cutting insert geometry optimisation

The geometry of the cutting insert plays a critical role in its performance. The efficiency of milling operations has been increased through improvements in the geometries of the cutting inserts. For instance, using a modern insert geometry design instead of conventional flat inserts when milling steels, cast irons and titanium alloys could increase milling productivity by about 30% and insert life by about 50% [124]. Figure 2.14 illustrates face milling cutting insert geometry including the insert geometry and the cutting-edge angles which include axial (GAMP), radial (GAMF) and lead (KAPR) angles [125]. Table 2.1 lists the effects of the cutting-edge angles on machining [126].

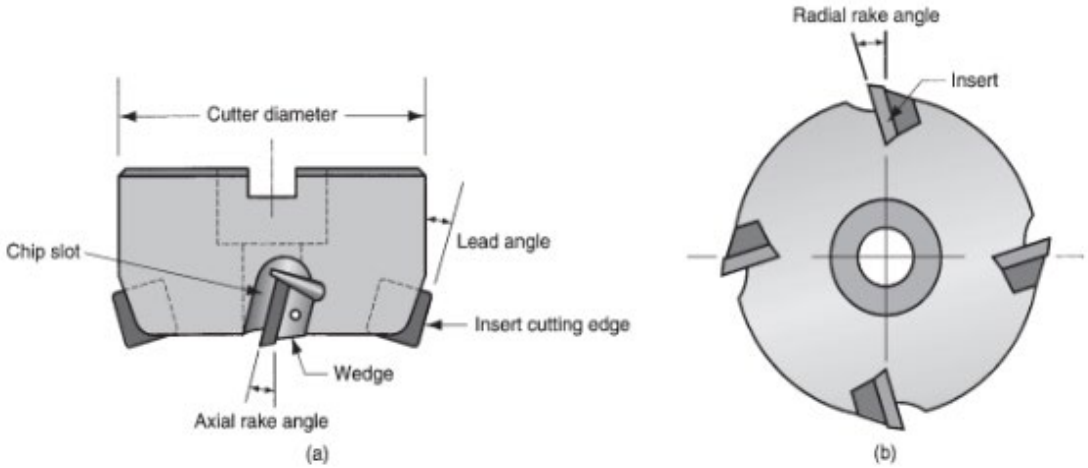


Figure 2-14. Schematic of a four-tooth face milling cutter illustrating the insert geometry and the associated cutting edge angles: (a) side view and (b) bottom view [125].

Table 2.1: Combinations of the cutting edges angles and their effects on machining [126]

Angles combination	**Effect on machining**
(+ GAMP and + GAMF)	Pros - Smooth cutting action with low cutting forces - Provides good chip disposal. - Smooth surface finish - Reduced machining vibrations, and risk of chip jamming. Cons - May tend to pull up the workpiece from the machine table. - Undesirable entry contact
(- GAMP and - GAMF)	Pros - Provides a strong cutting-edge geometry. - Increased productivity - Allows for higher feed rates. - Can endure interrupted machining. - Tends to press down the workpiece towards the machine table (**can be an advantage in some cases and a disadvantage in others) Cons - Higher cutting forces may be generated. - High risk of chip jamming
(+ GAMP and – GAMF)	Pros - Good chip disposal - Favourable for machining sticky materials with a tendency for having built-up edges
Lead angle (KAPR)	Influences the direction of the forces applied during the machining process (both axial and radial forces). - Higher lead angles are used for high depths of cut. - Increased lead angles result in very high radial cutting forces.

2.7.2. Chip formation during machining

In machining, chips are shavings or strips from the workpiece which are usually formed due to plastic deformation of the workpiece. The type of machined chips depends on the geometry of the cutter, cutting conditions (feed, velocity, and depth of cut), workpiece material and machining environment or cutting fluid. There are three basic chip types as shown in Figure 2.15, i.e. continuous chips, discontinuous chips, and continuous with a built-up edge (BUE) on the cutting insert rake face [127].

The turning (orthogonal cutting) process, cutting tool geometry, and the formation of chips during machining are shown in Figure 2-16 [128]. During the cutting process, the material in front of the cutting tool is compressed as it is advanced into the workpiece until the compression limit is reached. Following separation from the workpiece, the compressed material flows plastically as chips. As shown in the figure, the compressed material deforms along line AB, which is known as the primary shear zone. In this region, the material shears and flows due to the intense stresses induced by the cutting action. The chips are thus formed from the deformed material and slide over the cutting insert rake face in the direction of the insert's rake angle. The rake angle is the angle between the cutting face of the insert and a line perpendicular to the workpiece. Chips may undergo additional plastic deformation upon contact with the rake surface, along the contact length known as the secondary shear zone [128]. This occurs when the frictional stress between the chips and the rake face reach levels comparable to that of the shear yield stress of the workpiece material. Furthermore, this zone also governs the material flow behaviour during the cutting process. The shape of the chips produced during machining is critical because it relates to the nature and behaviour of the workpiece under machining conditions, as well as the degree of interaction between the cutting insert and the workpiece and chips.

In addition to the primary and secondary shear zones, the cutting process involves a tertiary shear zone, which forms at the interface between the newly created workpiece surface and the tool's flank face. In this zone, localised deformation occurs due to the frictional interaction between the tool and the workpiece surface, influencing surface finish, cutting forces, and insert tool wear. Moreover, after the material is removed as chips, the new workpiece surface zone (or clearance zone) forms as the fresh, machined surface is exposed and gradually separates from the contact area with the tool. The characteristics of this zone are critical in determining the surface integrity and overall precision of the machining operation.

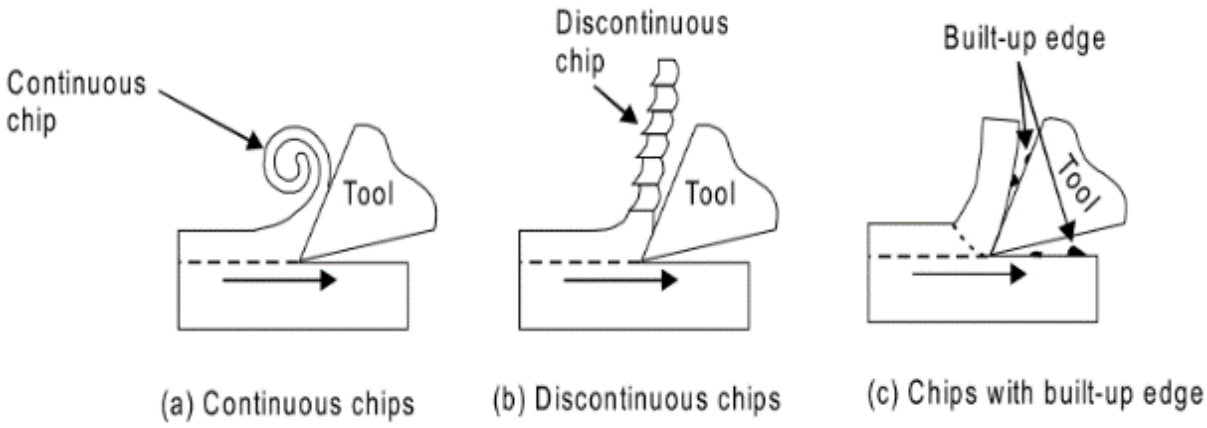


Figure 2-15. Common types of chips [129]

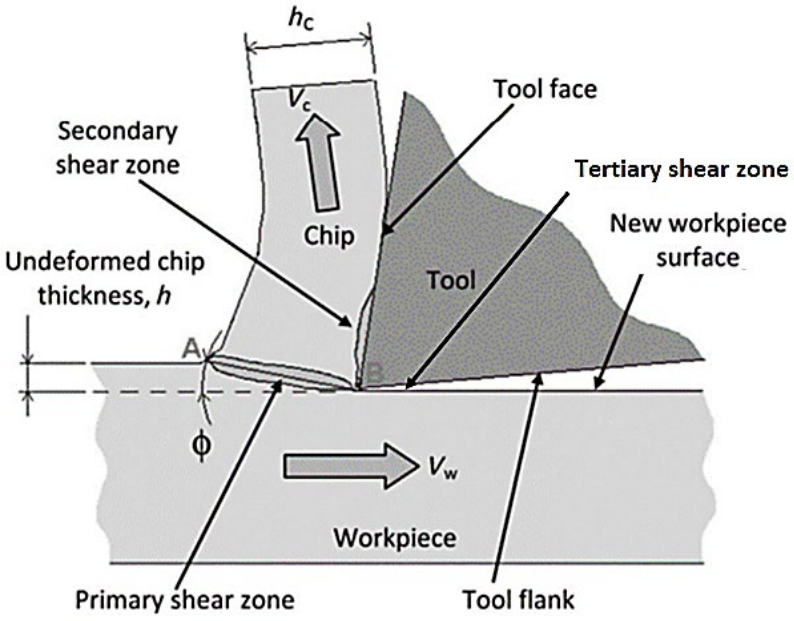


Figure 2-16. Chip formation in orthogonal machining [128]

2.7.3. Workpiece material – Grey Cast Iron

Grey cast iron (GCI) is the workpiece material for this project. GCI is formed when austenite and graphite phases solidify during the stable equilibrium process [130]. The graphite in GCI has a flake-like structure, which, when combined with the carbon content, forms the total carbon equivalent (CE) of the material. The chemical composition and cooling rate during the solidification process have a significant impact on the microstructure and mechanical properties of cast irons. For example, reducing silicon (Si) and/or increasing the cooling rate could prevent the complete dissociation of cementite to form graphite. The resulting microstructure would be graphite flakes embedded in a pearlite matrix [130].

Grey cast irons have good mechanical properties such as wear resistance, friction, anti-squeal, and vibration dumping [6]. The mechanical properties of GCI are shown in Table 2.2. The mechanical properties of GCI are shown in Table 2 1. These properties, combined with the ease with which components can be manufactured, make the material suitable for a variety of applications in the automotive industry, including but not limited to pistons, cylinder heads of gasoline and diesel engines, camshafts, brake parts and clutch plates [131]. Grey cast iron is mostly made up of iron (Fe), carbon (C), and silicon (Si). In general, the composition contains 2.5 to 4% C, 1 to 3% Si, and the remainder Fe, which may contain trace amounts of manganese (Mn), sulphur (S) and phosphorus (P) [132].

Table 2.2. Typical mechanical properties of grey cast iron [130].

Property	**Value [Units]**
Ultimate tensile strength (UTS)	235 MPa
Hardness	200 HB
Young Modulus	110 GPa
Fatigue resistance	100 MPa
Thermal conductivity	48 W/mK
Relative vibration damping capacity	1.0 *measured on a scale of 0 to 1

2.7.3.1. Machinability of the grey cast iron

The ability of a material to be machined easily and accurately into components or parts is referred to as machinability [130]. A material's machinability is primarily determined by its ability to plastically deform and withstand the stresses and temperatures associated with machining. This property has frequently been quantified using a variety of measurements, including but not limited to insert wear, surface finish, chip type, power consumption and material removal rate [130]. Many manufacturers have discovered that the machinability of GCI varies greatly [133]. Several factors influence the machinability of this material, including carbide content, pearlite content, pearlite hardness, non-metallic inclusions and alloy segregation [133]. The presence of near-continuous graphite flakes in the microstructure of GCI is the source of the machinability variability. This is because the graphite morphology and matrix structure influence the micro mechanisms of chip formation and hence machinability of the GCI [133]. Figure 2.17 shows different types of graphite flakes found in GCI alloys.



Figure 2-17. Different types of graphite flakes [6]

Voigt et al. [133] studied the influence of three type A and two type D graphite flakes morphologies and matrix structures on the micro mechanism of chip formation of GCI. The graphite irons of type A ranged from short and thick flakes in a fine pearlitic matrix to long and thin flakes in a coarse pearlitic matrix. One specimen of type D graphite had a pearlitic matrix, while the other had a ferritic matrix. Figure 2.18 illustrates the fundamental elements of the cast iron chip formation process.

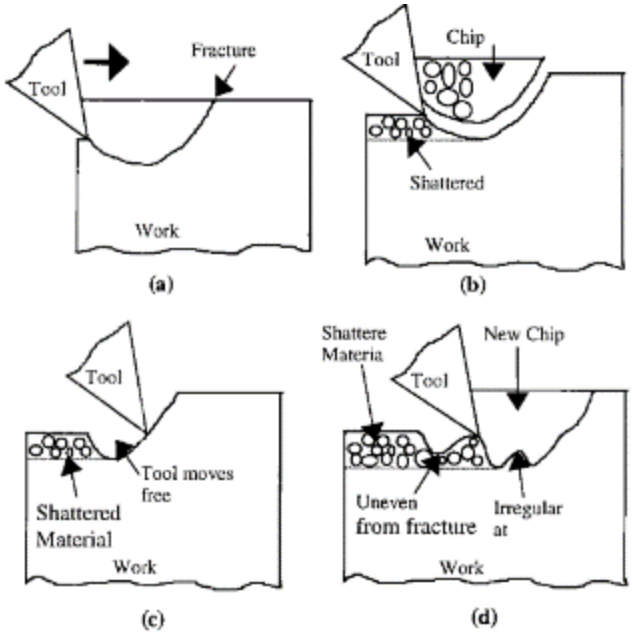


Figure 2-18. Schematic machining sequences of GCI showing the formation of chips and subsequent shearing from the workpiece [133]

According to Voigt et al.'s findings, a chip segment (known as chip fragment) fractures and separates completely as the cutting insert moves forward into the GCI workpiece (see Figure 2.18 (b)) [133]. Concurrently, a damaged region with compacted material fragments is formed beneath the insert. This subsurface damaged region is called the fracture depth. Irregular fracture can occur when machining flake graphite, resulting in craters ahead of the cutting insert, as illustrated in Figure 2.18 (c). When this happens, the cutting insert moves freely for a short distance before re-engaging with the workpiece. Figure 2.18 (d) shows an uneven

surface caused by an irregular fracture of the workpiece at the boundaries. This behaviour is an important factor limiting the machined surface finish of cast irons in general. The study concluded that, for GCI the forming chips were highly discontinuous and only stayed in contact with the insert for a very short time [133]. Another study by Sousa et al. [130] concluded that type A graphite flakes are generally preferred compared to other types. This is mainly because they are responsible for the formation of discontinuous chips during machining. During machining, the graphite flakes act as fracture zones or crack initiation points. In addition, the graphite flakes provide a self-lubricating source at the edge of the cutting insert during machining thus improving the machinability of the material [130].

2.7.4. Laser surface modification of cemented carbides and cermets

Laser surface modification (LSM) through laser ablation is a technique that can be used to improve the performance of cemented carbide cutting inserts. During machining, the surface of cutting insert is subjected to high stress, temperature, and wear, resulting in insert failure and reduced insert life [17]. Laser ablation can be used to modify the surface properties of cutting inserts in order to improve their wear resistance, toughness and other characteristics [24]. In addition to properties enhancement, LSM can also be used to create innovative patterns such as micro groves, micro pits, or dimples on the edge of the cutting insert to reduce the machining forces and improve the frictional behaviour, and thus improving the insert life of the cutting insert during operation [134]. Figure 2.19 shows a micro patterned cutting insert used for the turning of Alloy 718 and other heat resistant superalloys.

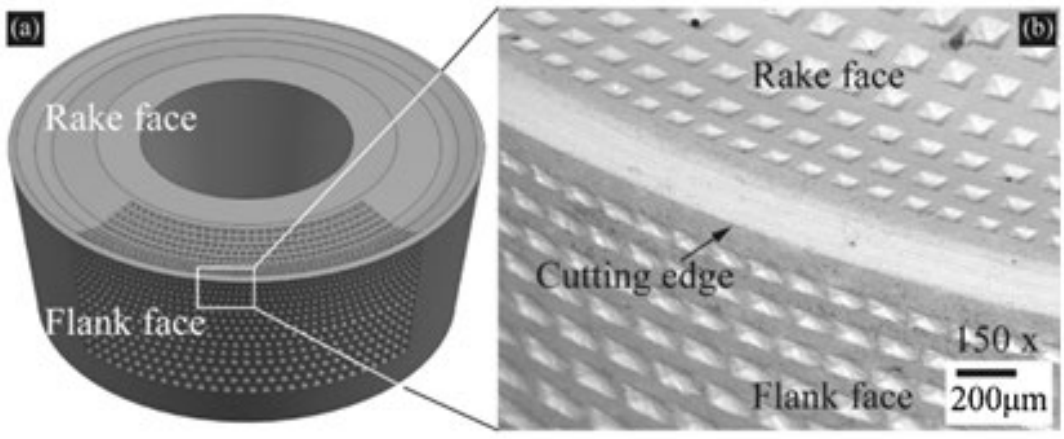


Figure 2-19. Illustration of a laser modified flank and rake face of the cutting insert; and (b) magnified SEM micrograph of the cutting edge showing the pyramid shaped micro patterns [134]

The laser ablation technique involves using a high energy laser beam to remove material from the surface of the cutting insert. The material is vaporised by the high energy photons in the laser beam when it is focused on its surface [135]. A patterned surface is left behind after the vaporised substance is ejected from the surface. The laser beam's shape and its movement in relation to the material's surface determine the pattern in laser ablation. Computer-aided systems (3D visualisations) can be used to control the movement of the laser beam, enabling the creation of accurate and complex patterns[134], [136]. Laser ablation has been demonstrated to be a promising technique for selective phase removal of cemented carbides, based on the difference in melting and boiling temperatures between the various phases [22].

In general, the ablation of WC-Co systems results in two distinct laser-matter behaviour or response from the carbide and the binder phases [22]. For instance, the melting temperature of WC is twice that of Co (i.e., T_{WC} = 2870 °C and T_{Co} = 1495 °C). So, during laser ablation of the material, Co undergoes melting and vaporisation first whilst WC experiences melting only [22]. Due to the large heat-affected zone (HAZ) involved, laser ablation with conventional nanosecond (*ns*) laser pulses typically induces surface remelting, incomplete Co removal, and metallurgical changes in the WC phase. Because of their low HAZ and thermal stresses, ultrashort pulsed lasers such as picosecond (*ps*) and femtosecond (*fs*) laser pulses have emerged as an alternative for cold ablation. The use of *ns*, *ps*, and *fs* laser pulses to pattern the WC-Co surface was recently compared by Fang et al. [137]. The Co phase vaporised as a result of the *ns* laser ablation's dominant thermal diffusion, and the thermal residual stress caused the WC surface to develop an oxide layer, cracks, and pores. Using the *ps* laser, the Co binder and the WC grains were both ablated at the processing zone's centre, with Co experiencing a significantly higher ablation than the WC grains. During the *fs* laser ablation, only a 1 m thick oxide layer was produced, and no other obvious damages beneath the layer were seen.

Nagarajan et al. [138] studied the effects of femtosecond laser (*fs*) process variables including laser pulse energy, number of pulses and scanning speed during the selective removal of Co binder in WC-Co based cemented carbides. Their study concluded that optimised processing parameters could successfully remove the Co phase selectively from the WC-Co surface with minimal morphological changes or thermal effects on the WC grains. Dumitru et al. [139] used *fs* laser ablation to create dimples (small holes) on the surface of WC-Co cemented carbide to improve the microstructure and properties of the material. The scanning electron microscopy (SEM) analyses of the cross-sectional cuts revealed zones of modified material at dimple walls, situated near the dimple entrances. The authors discovered redeposition layers within the

dimple walls that are distinct from the WC-Co microstructure. Figure 2.20 depicts the SEM and Energy-dispersive X-ray spectroscopy (EDX) results of the dimple cross-section [139]. As shown in Figure 2.20 (a), the white line passes through grain interstices in (1) and (2); the W content decreases, and a Co peak is visible. Between (1) and (2), as well as (2) and (3), the line passes through WC grains, and relatively constant W and Co amounts are measured. Following (3), the line enters the new layer, where there are noticeable changes: the W content decreases, the Co content increases, and both have nearly identical element counts [139]. These results led the authors to the logical conclusion that the material that was removed from the dimple's bottom was redeposited at the dimple walls.

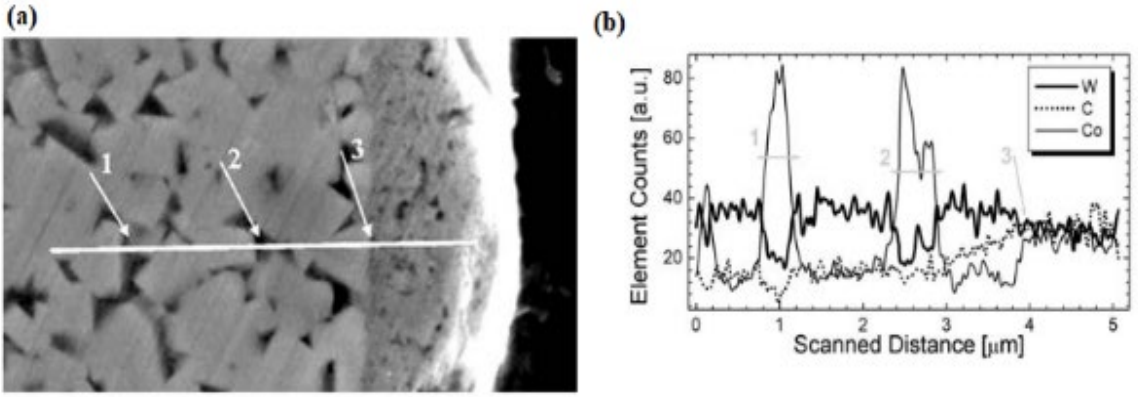


Figure 2-20. (a) SEM micrograph of a dimple cross-section and path of EDX analysis, and (b) the EDX results [139].

The amount of material removed during laser ablation process is dependent on laser parameters including, laser pulse fluence or energy, pulse duration, spot size, and wavelength [23]. The laser pulse fluence is given by Equations 2.11 - 2.13.

$$F_p = \frac{E_p}{\pi \left(\frac{d_f}{2}\right)^2} \tag{2.11}$$

with,

$$E_p = \frac{P_m}{f_p} \tag{2.12}$$

and areal fluence

$$F_A = \frac{E_p}{PD(TD)} \tag{2.13}$$

where E_p is the pulse energy, d_f is the focus diameter (spot size), P_m represent the average laser power and f_p is the pulse frequency. PD and TD represent the pulse distance and the track

distance as shown in Figure 2.21, respectively [140]. The laser power P_m is mean power over time and the peak power P_p can be determined by:

$$P_p = \frac{E_p}{\tau_p} \qquad 2.14$$

with τ_p representing the pulse length [141].

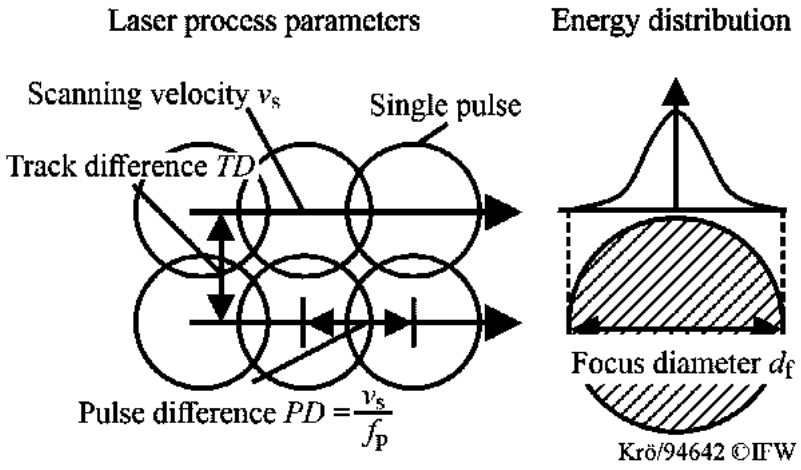
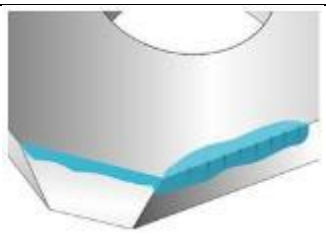
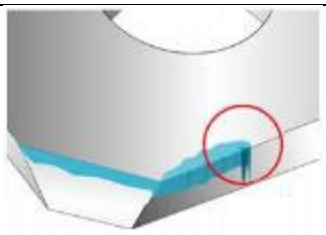
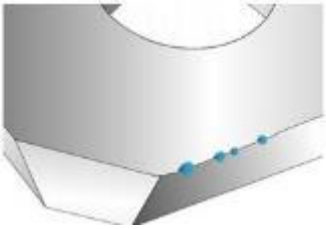
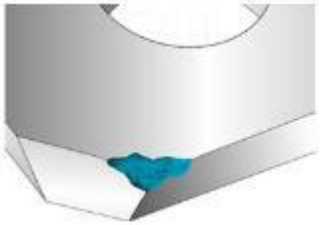
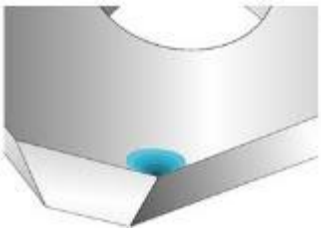
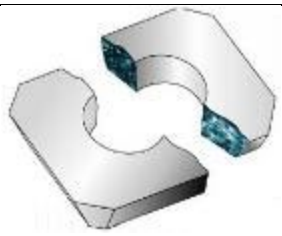


Figure 2-21. Laser process definitions [141].

2.8. Cutting insert failure, gradual wear and insert life

Due to the repetitive contact between the workpiece and the cutters during machining operations, cutting inserts undergo high forces as well as quick heating and cooling cycles [109]. High forces and fluctuating temperatures cause wear, thermal shock at the inserts' cutting edges, and chemical reactions between the material of the cutting insert and the workpiece. Any kind of wear on the cutting insert could result in insert failure, which would shorten the insert's lifespan. Hence, cutting inserts with a good combination of high hardness and toughness, high thermal stability, and low tendency to diffusion and oxidation are needed for machining applications. Cutting insert failure or damage can generally be divided into three categories: temperature failure, mechanical breakage (rapture), and gradual wear of the insert cutting edge [142]. Table 2.3 gives the different types of cutting edge failure, with an illustration of the failure and the respective causes [143].

Table 2.3. Different types of cutting edge failure and their causes

Type of failure	Illustration	Causes
(a) Thermal cracks		- Large cutting diameter used. - Coolant was used.
(b) Notch wear		- Hard workpiece surface. - Oxidation occurs at the boundary. - Rubbing of burrs.
(c) Chipping		- High insert hardness. - Thermal cracks or notching have occurred. - High feed rate. - Chips contacting with the cutting edge. - Vibrations occurred.
(d) Mechanical fracture		- Same reasons as chipping.
(e) Flaking		- Cutting edge experienced compressive stresses. - Welded sections peel away from the cutting edge.
(f) Breakage		- Cutting inset not correctly placed. - Very high cutting conditions leading to vibrations.

Temperature failure is the term used to describe the cutting edge's plastic deformation and the cutting edge's cracking as a result of high temperatures and thermal stresses, respectively. Mechanical fracture or breakage typically occurs when an insert's cutting edge chips or falls off due to mechanical impact and chip built-up edge (BUE). Mechanical and temperature failure both result in the premature loss of the cutting insert material and can be extremely hazardous to the machine and the workpiece material. As a result, they should be completely avoided by incorporating a high design factor of safety and ensuring favourable machining conditions. On the other hand, gradual wear which includes flank wear, crater wear, notch wear, and nose radius wear [142], cannot be avoided or eliminated entirely, but can only be reduced. This is primarily due to (i) the high localised stresses at the insert tip, (ii) high temperature along the rake face, (iii) sliding of the insert along the rake face, and (iv) contact between the insert's cutting edge and the newly machined surface of the workpiece [110]. However, of the three types of insert failure, gradual wear is preferred because it allows for longer periods of insert use. These potentially longer periods of use have an additional economic benefit. As a result, when machining, it is always preferable to choose machining conditions that favour gradual insert wear rather than mechanical breakage or temperature failure [17, 125]. Furthermore, when investigating insert wear and insert-life criteria, features of gradual wear are typically considered. Figure 2.22 shows the different types of cutting insert wear on the flank and rake faces of the cutting insert.

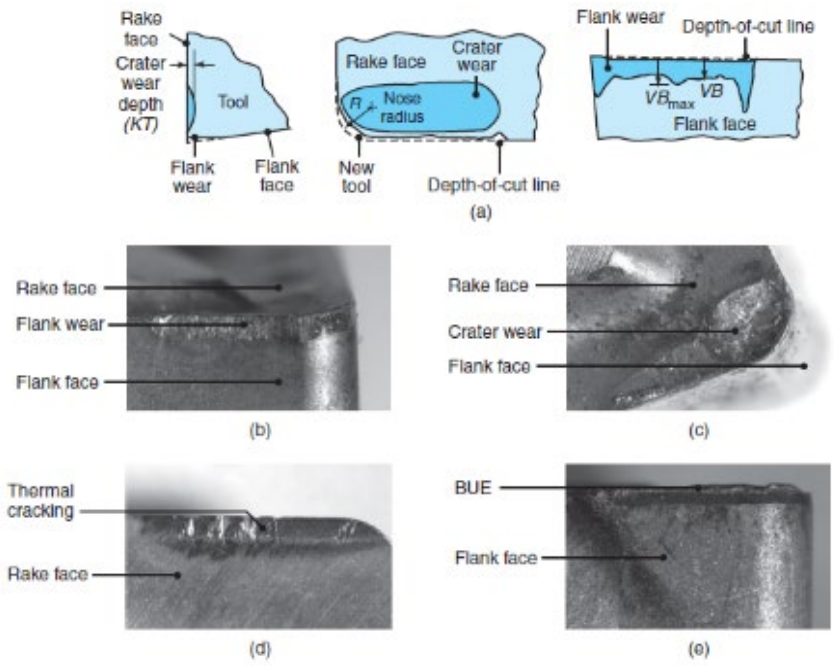


Figure 2-22: (a) Some features of wear in single point cutting inserts, with VB indicating the average flank wear. (b) - (e) illustrates different cutting insert wear: (b) flank wear, (c) crater wear, (d) thermal cracking (temperature failure), (e) and flank wear and built-up edge [110]

2.8.1. Gradual wear and wear resistance of cutting inserts

The gradual loss of material from a cutting insert during a machining operation is referred to as cutting insert wear. Wear resistance refers to a cutting insert's ability to withstand mechanical actions (material removal from a workpiece) without material loss [144]. This property is regarded as one of the most important parameters for evaluating cutting insert machining performance (insert life). The wear resistance of cemented carbides is said to be proportional to the material's hardness. Wear resistance of cemented carbides, like hardness, generally increases with decreasing binder phase content and carbide phase grain sizes [144, 145]. However, reducing the binder content and the size of the carbide grains compromises the material's toughness, which is required during impact loads [17]. During machining, the cutting insert edge is subjected to extremely high temperatures, significant compressive and shear stresses, and temperature gradients of the order of 1 ^{o}C/µm [13]. his causes a variety of wear processes such as abrasion, attrition, diffusion, adhesion on the cutting insert's edge (BUE), chemical reaction and oxidation [146].

2.8.2. Cutting insert wear mechanisms

The mechanisms that cause wear between cutting insert-chip and insert-workpiece interfaces include abrasion, adhesion, diffusion, chemical reactions (oxidation), and plastic deformation [125]. Figure 2.23 gives a representation of the causes of wear, various wear mechanisms, types of wear and their consequences during machining [147]. The following subsections provide a detailed discussion of different types of cutting insert wear mechanisms.

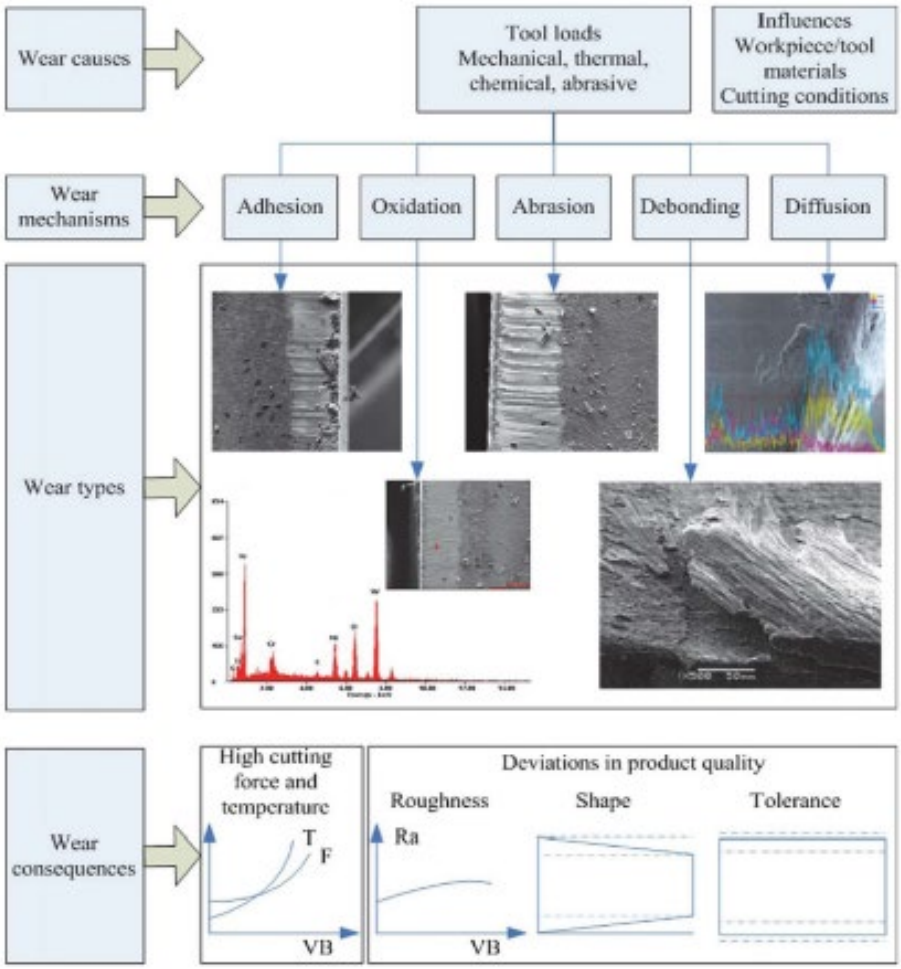


Figure 2-23. Causes of wear, different types of wear and their consequences during machining [147]

2.8.2.1. Abrasive wear

The most common type of wear in tribology is abrasive wear, which occurs when asperities of a rough, hard surface or hard particles slide on a softer surface, causing interface failure through plastic deformation or fracture [148]. Abrasive wear occurs in metal cutting when the workpiece material contains a large number of hard particles. For example, in the case of steel

and cast-iron cutting, it is caused by hard particles present in the workpiece, such as carbides, nitrides, oxides, and non-metallic inclusions [13]. Cemented carbide abrasive wear is closely related to hardness and is affected by composition and microstructure. Abrasive wear is classified into two types: two-body and three-body abrasive wear [149]. Two-body wear occurs when rigid hard particles (protuberances) on the counterface cause wear. When the hard particles are free to roll between the two surfaces, three-body wear occurs. In general, abrasive wear rates in three-body abrasion are approximately ten times lower than in two-body abrasion [149]. This is due to the fact that the average loose abrasive particle spends 90% of its time rolling and 10% of its time abrading sliding surfaces [149].

Abrasive wear can occur in four ways: (i) microploughing, (ii) microfatigue, (iii) microcutting and (iv) microcracking. The various abrasive wear mechanisms are depicted in Figure 2.24 [150]. The abrasive particles in microploughing displace the material in its path to both sides of the wear groove. The action of many abrasive particles or the repeated action of one particle causes material volume loss in this case. Microfatigue may result from the repeated action of microploughing (low cycle fatigue). The formation of chips or shavings equal to the volume of the wear grooves results in material loss due to unadulterated microcutting. When abrasive particles impose highly concentrated stresses on materials, microcracking occurs. Large debris detaches from the surface due to the formation and spread of cracks in this type of wear. Microcracking predominates in brittle materials while microploughing and microcutting are more common in ductile materials [150].

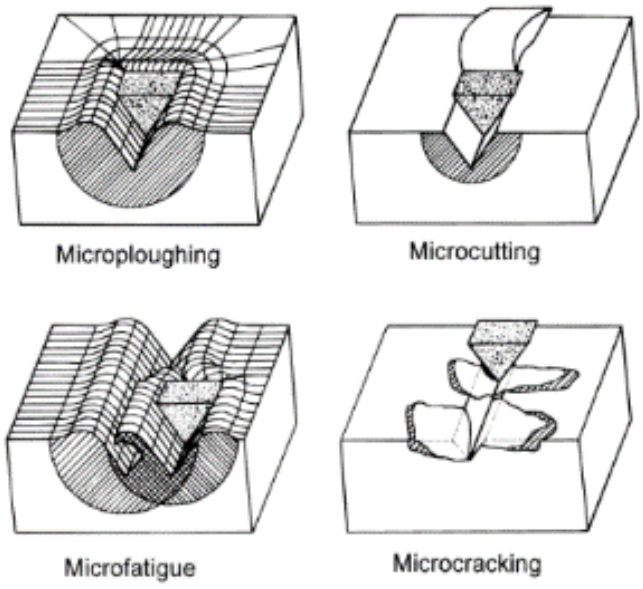


Figure 2-24. An illustration of abrasive wear mechanisms [150].

2.8.2.2. Attrition wear

Attrition wear is also known as adhesion wear, and it refers to a process in which microscopic particles are removed from the surface of the cutting insert and carried away by chips from the workpiece material during machining operation [13]. This type of wear is common when the contacting bodies have a similar chemical structure and good solubility, allowing the atoms of the two bodies to easily interact with one another [151]. In machining, attrition wear usually occurs when there is intermittent localised bonding (cold welding) between the particles of the insert cutting edge and the workpiece surface (chips), especially at low cutting speeds and no lubrication [151]. The welding of the particles and surface interactions lead to the formation of microscopic protrusions or irregularities on the surface of the contacting bodies called asperity junctions [151]. The formation of the asperity junctions is followed by adhesive transfer depending on their bond strength. In some instances, the asperity junctions may remain adhered to the workpiece or become detached as loose wear particles [151]. However, if the bonds at the interface are stronger than those in the workpiece bulk material, chips will detach from the bulk and become attached to the sliding cutting edge [151]. This results in the formation of irregularities and pits on the surface of the workpiece as some material is lost, while the cutting edge gains the transferred material volume. During this process, the sliding interface becomes rough, and both the cutting insert and the workpiece lose their dimensional accuracy and tolerance. In addition, the asperity junctions experience both plastic deformation and strain hardening. This leads to an increased hardness of the asperities by a factor of two [151]. Depending on the length and the duration of sliding, the asperities can be eventually removed as wear particles, and they often result in abrasive action [151]. The attrition wear of WC based cemented carbide cutting inserts occurs when the welded chips break from the workpiece, carrying the particles (i.e. WC grains) from the cutting insert edge with them [152]. For cemented carbides, attrition wear is associated with the grain size rather than the hardness of the material. The rate of attrition in WC based cemented carbides decreases with the reduction of the carbide grain size, i.e. a fine grain WC-6Co with a hardness of 1265 HV can exhibit better resistance to attrition wear than a coarser grain WC-4.5Co with a hardness of 1600 HV [13].

2.8.2.3. Diffusion wear

Diffusion wear, also known as chemical wear, refers to a wear mechanism in which the insert shape at the cutting edge is modified or changed due to the diffusion of atoms between the

cutting insert and the surface of the workpiece [153]. The atomic transfer between the contacting materials (i.e. the cutting insert and the chips) is caused by the high temperatures and pressures experienced during machining operations [154] as well as the good solubility between the two components [13]. The cutting speed and the interface temperature are directly proportional to each other; thus, diffusion wear is a limiting factor when it comes to cutting speeds of cemented carbide-based inserts [13]. The diffusion wear rate is very high when cutting steel using WC-Co based cutting inserts. However, it has been reported that the addition of TiC to the WC-Co cemented carbides improves high temperature hardness and chemical stability, resulting in excellent resistance to crater wear [155].

2.8.3. Cutting insert "tool" life

The useful cutting duration of an insert is defined as its insert life (i.e. this is the time that the insert takes from the start of machining until final catastrophic failure) [156]. The main purpose of insert life testing is to experimentally investigate the influence of one or more factors on the useful life or performance of cutting inserts. This is due to the fact that cutting inserts have varying insert life behaviour depending on the machining conditions. As a result, the current study's insert life testing is critical for understanding how to obtain optimal machining conditions for the a-GCI.

2.8.3.1. Flank wear

Flank wear is the most known type of insert wear, and it occurs on the clearance, relief (or flank) face of the cutting insert, in contact with the machined surface. It is caused by abrasion and attrition at the contact area between the flank face adjacent to the cutting insert and the newly machined surface of the workpiece [125]. Flank wear causes loss of the relief angle on the clearance face of the insert. This increases the contact length between the workpiece and the cutting insert, resulting in increased cutting forces and temperatures [157]. Flank wear is measured by the width of the wear band or the flank wear land, VB (see Figure 2.22). It is also worth noting that as the wear band increases, the quality of the insert is reduced, and the surface roughness is compromised. Figure 2.25 shows a typical graph of the development of flank wear with time for a cemented carbide cutting insert, (a similar relationship occurs for crater) [125]. The curve can be divided into three regions as follows [125], [158]:

(i) Break-in period (AB): where the sharp cutting-edge wear quickly at the beginning of its use and a finite wear land established.

(ii) Steady-state wear region (BC): where wear progresses at a uniform rate. This region is shown as a linear function in the figure, however, deviations from the straight line occur in actual machining.

(iii) Failure region (CD): where wear occurs at an accelerated rate. The region CD indicates the phase where the cutting insert has become more sensitive to increased temperature and forces caused by the presence of large proportions of wear land. This marks the beginning of the failure criterion, whereby the cutting temperatures are higher, and the machining process efficiency is reduced.

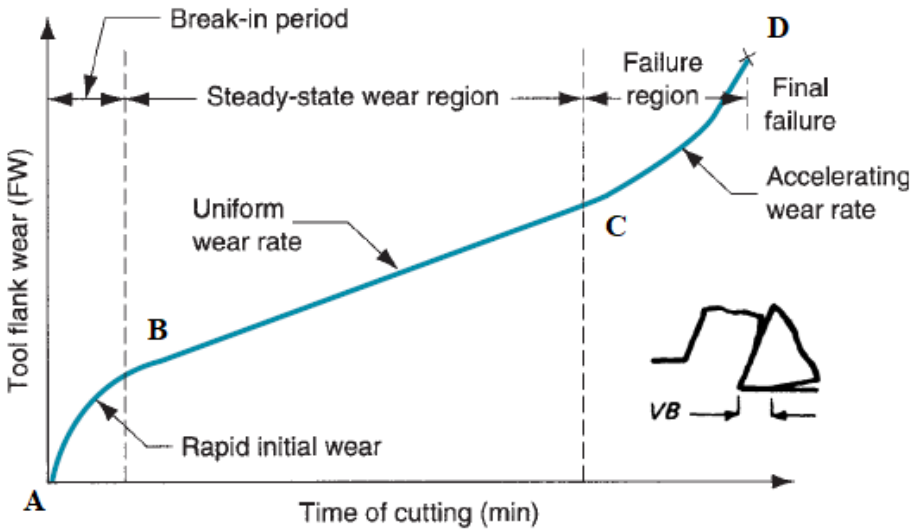


Figure 2-25. Cutting insert flank wear vs. cutting time [125]

2.8.3.2. Crater wear

Crater wear occurs on the cutting insert's rake face due to friction between the tool and the flowing chips. It is characterised by the formation of a crater or depression in the rake face because of chip sliding/flowing action against the insert surface. Crater wear is primarily caused by diffusion as chips flow along the rake face (particularly at high temperatures and stresses), resulting in insert wear [110]. Crater wear increases with increasing cutting speed in milling machining [109]. The depth of the crater, KT, is used to measure crater wear (see Figure 2.22)

2.8.3.3. Notch wear

Notch wear occurs on both the flank and the rake face of the insert near, but not at the point where the major cutting-edge contacts the workpiece surface [159]. Notch wear is frequently

caused by work hardening effects in the workpiece caused by the insert's previous cutting pass [110]. Furthermore, if the notch or groove created is sufficiently deep, this type of wear frequently results in gross chipping and catastrophic insert failure [110]. The notch wear is indicated by the depth of the notch, VN (also known as the depth of the cut line), as shown in Figure 2.22.

2.8.3.4. Cutting insert "tool" life criteria

The insert tool life criteria for cemented carbide cutting inserts as recommended in the International Organisation for Standardisation (ISO) 3685:1993 [159]. Different criteria are applied for normal machining (roughing and semi-finishing) and finishing. In normal machining, where the primary focus in on material removal rate and productivity, the insert tool life criteria are generally more lenient compared to finishing operations. The following insert tool life criteria are used to assess cutting inserts during machining operations.

Insert tool life criteria for roughing and semi-finishing operations:

- The maximum width of the flank wear land VB_{max} = 0.6 mm and if the flank wear land is not regularly worn, scratched, chipped, or badly grooved in the major flank zone. Exceeding this limit can lead to poor surface finish, increased cutting forces and eventually tool failure.
- The average width of the flank wear land VB = 0.3 mm if the flank wear land is regularly worn in the major flank wear zone.
- The depth of the crater KT is given by Equation 2.15.

$$\mathrm{KT} = 0.06 + 0.3f \qquad 2.15$$

  where f is the feed in mm per /rev.
- The crater breaks through at the minor cutting edge, resulting in a poor surface finish on the machined surface. Crater wear can be tolerated up to KT before it starts to affect the cutting performance, particularly chip flow and cutting insert strength.
- Under high temperatures and cutting forces, the insert may deform plastically. Once plastic deformation is visible, the tool life is considered over, as the tool can no longer maintain its geometry or cutting performance.
- Cutting inserts can sometimes fail abruptly due to chipping (fracture) or breakage of the cutting edge, which can occur due to sudden impact or excessive cutting forces. This results in immediate tool replacement.

Insert tool life criteria for finishing operations:

- The maximum width of the flank wear is typically much lower for finishing operations (i.e. VB_{max} = 0.3 mm). Excessive flank wear can degrade the surface finish and dimensional accuracy.
- The surface roughness must meet tight specifications in finishing operations. Any deterioration in surface finish due to cutting insert wear is a strong indicator that the tool should be replaced, even if flank wear is within acceptable limits. The desired surface roughness (Ra) is often used as a benchmark for tool life.
- The sharpness and integrity of the cutting edge are critical in finishing. Any signs of dulling, chipping, or micro-fractures on the cutting edge require immediate replacement of the insert to prevent defects on the machined surface.
- Cutting insert wear that leads to increased vibration (high cutting forces), or unstable cutting conditions is another indicator for tool replacement. Even minor wear can amplify vibrations, which negatively impacts surface quality and part accuracy.
- Precise geometry of the cutting insert tool (i.e. nose radius) is crucial for achieving the desired part geometry. Any distortion in insert geometry due to wear calls for cutting insert replacement.

2.9. Surface roughness measurements

Surface roughness is a material characteristic that is used to describe or assess the level of finish on the surface of a machined component [160]. Depending on the application, surface roughness is typically a technical requirement for mechanical components. Because it significantly affects the functional behaviour of that component, a particular surface roughness is typically desired when milling certain components. Additionally, the surface roughness profile during machining has an indirect impact on the state of the cutting insert, including cutting temperature, insert wear, insert failure, forced vibrations, etc. [160]. According to research, the feed rate, mechanical and material characteristics of the cutting insert and the workpiece, insert geometry, depth of cut, and cutting speed are all factors that directly affect the surface finish of machined components [161].

2.10. Summary of factors affecting machining operations

The summary of the factors that influence the machining operations are given in Table 2.4. The table shows the interrelationship between various machining parameters and how they impact each other.

Table 2.4: Factors influencing machining operations [110]

Parameter	**Influence and interrelationship**
Cutting speed, depth of cut, feed rate, cutting fluids	- Forces, power, temperature rise, insert life, type of chip and surface finish.
Insert geometry	- Forces, power, temperature rise, insert life, type of chip, and surface finish. - Influences chip flow direction. - Resistance to insert wear and chipping.
Continuous chip	- Good surface finish. - Steady cutting forces. - Undesirable (especially in automated machinery).
Built-up edge chip	- Poor surface finish, if thin and unstable. - Can replace the cutting edge of the insert.
Discontinuous chip	- Desirable for ease of chip disposal. - Fluctuating cutting forces which can affect the surface finish and cause vibrations.
Temperature rise	- Influences insert life, in particular crater wear and dimensional accuracy of the workpiece. - May cause thermal damage to the workpiece surface.
Insert wear	- Influences surface finish or surface roughness, dimensional accuracy, temperature, forces and power.
Machinability	- Related to insert life. - Influences surface finish, forces and power. - Type of chip.

2.11. Face milling machining cutting parameters optimisation

The increasing demand for product performance and life, as well as environmental sustainability, has challenged modern machining processes, particularly for machining critical engineering parts or components. In general, machining strives for concurrent high production efficiency, high product quality and reduced environmental impact [162]. These objectives are directly affected by the various machining parameters (i.e. cutting speed, depth of cut, feed rate and insert wear). As a result, the selection process of the cutting parameters and the type of cutting inserts used for machining operations is turned into a multiple criteria decision-making (MCDM) problem [163].

Methods for making multi-criteria decisions have become essential in modern engineering practices. These methods allow decision-makers to solve and evaluate complex problems that have multiple criteria, trade-offs, and uncertainties [164]. The MCDM techniques are particularly useful in sustainable engineering, where the decision-making process requires consideration of economic, environmental, and social factors [164]. Sustainable engineering is mainly concerned with developing and implementing engineering solutions that are economically feasible, environmentally friendly, and acceptable to society [165].

The MCDM or optimisation problems in machining processes can be solved using various techniques [163]. For example, Qu et al. [166] used the Non-dominated Sorting Genetic Algorithm (NSGA-II) to optimise the cutting force and surface roughness to determine the optimal cutting parameters in the milling of walled plates. Yan et al. [167] used a multi-objective optimisation (MOO) method based on weighted grey relational analysis (GRA) and response surface methodology (RSM) to optimise the cutting parameters for evaluating trade-offs between sustainability, production rate and machining quality. Wu et al. [168] proposed a deep learning-based data-driven genetic algorithm and technique for order preference by similarity to an ideal solution (TOPSIS) for MOO of machining process parameters as well as searching for final solutions. Sun et al. [163] also applied TOPSIS and adversarial interpretive structural modelling (AISM) to find optimal cutting parameters for optimising cutting efficiency, surface roughness and cutting force. Li et al. used a combination of RSM, and an improved teaching-learning based optimisation (TLBO) model to find an optimal solution for the cutting force, surface roughness and processing rate. Zainal et al. [169] optimised the machining parameters to minimise surface roughness using a bio-inspired particle swarm optimisation model and online monitoring signals.

Among the different optimisation techniques, the TOPSIS based model is one of the most used in sustainable engineering [164] due to its efficiency and ease of application [163]. The technique has been seen as a practical and useful method for ranking and selecting several possible alternatives (solutions) based on their distance from the ideal solution to the worst solution [164]. As such, TOPSIS has been widely used in numerous situations of manufacturing [163, 170]. To this effect, the current study focuses on the TOPSIS technique to find the cutting inserts that optimise cutting insert tool life, surface roughness (quality) and energy consumption.

2.11.1. MCDM problem formulation

The generic form of the MCDM problem is presented first before explaining how the problem can be solved by TOPSIS. The generic problem is outlined as follows [171]:

The main objective of a generic MCDM problem is to evaluate and rank alternatives A_i (where, $i = 1, 2, \ldots, n$) based on specific criteria C_j (where, $j = 1, 2, \ldots, m$). A_i represents available options that must be ranked by a decision maker. C_j on the other hand, represents a set of criteria with factors influencing the decision maker's choice when ranking the alternatives A_i. Each criterion in C_j is typically weighted according to its relative significance in the data set. W_j (where, $j = 1, 2, \ldots, m$) represents the wights of criteria C_j. It is worth noting that choosing the criteria weights involves a subjective process that is based on the decision maker's preferences or expert knowledge [168]. The criteria weights can be presented in a vector form as shown in Equation 2.16 [172].

$$\mathrm{W} = W_j \tag{2.16}$$

The performance ratings x_{ij} (where, $i = 1, 2, \ldots, n$; $j = 1, 2, \ldots, m$) are the preference scores for every alternative in A_i against every criterion in C_j. The performance ratings can be given in the form of a decision matrix, X as shown in Equation 2.17 [171].

$$\mathrm{X} = \begin{bmatrix} x_{11} & x_{12} & \cdots & x_{1m} \\ x_{21} & x_{22} & \cdots & x_{2m} \\ \vdots & \vdots & \ddots & \vdots \\ x_{n1} & x_{n2} & \cdots & x_{nm} \end{bmatrix} \tag{2.17}$$

Using Equations 2.16 and 2.17, the MCDM problem, Q which can be solved by applying various suitable MCDM methods is represented in Equation 2.18 [171].

$$\mathrm{Q} = \{X, W\} \tag{2.18}$$

2.11.2. Optimal solution based on the TOPSIS technique

The TOPSIS technique's main goal is to choose the best alternative with the shortest distance from the ideal solution and the greatest distance from the negative solution [163]. The solutions are evaluated and then ranked using an overall index based on the distances from the ideal solutions (i.e. positive ideal solution (PIS) and negative ideal solution (NIS)) [168]. The following steps explain technique's fundamentals:

Step 1: Calculate the normalised performance ratings y_{ij} (where, $i = 1, 2, \ldots, n$; $j = 1, 2, \ldots, m$). The goal of normalisation is to obtain dimensionless criterion values. Normalisation is important because it ensures that all criteria are on the same scale (i.e. maintains proportionality), preventing any criterion from dominating as well as eliminating the bias.

The normalised ratings y_{ij} can be calculated using Equation 2.19 as follows [171]:

$$y_{ij} = \frac{x_{ij}}{\sqrt{\sum_{i=1}^{n} x_{ij}^2}} \tag{2.19}$$

The normalised ratings can be expressed as a normalised decision matrix Y as follows:

$$\mathrm{Y} = \begin{bmatrix} y_{11} & y_{12} & \cdots & y_{1m} \\ y_{21} & y_{22} & \cdots & y_{2m} \\ \vdots & \vdots & \ddots & \vdots \\ y_{n1} & y_{n2} & \cdots & y_{nm} \end{bmatrix} \tag{2.20}$$

Step 2: Multiply the normalised ratings y_{ij} by the associated weights W_j obtained in Equation 2.16, to determine the weighted-normalised ratings u_{ij} (where, $i = 1, 2, \ldots, n$; $j = 1, 2, \ldots, m$) as shown in Equation 2.21 [171]:

$$u_{ij} = W_j * y_{ij} \tag{2.21}$$

Equation gives the weighted-normalised decision matrix U.

$$\mathrm{U} = \begin{bmatrix} u_{11} & u_{12} & \cdots & u_{1m} \\ u_{21} & u_{22} & \dots & u_{2m} \\ \vdots & \vdots & \ddots & \vdots \\ u_{n1} & u_{n2} & \dots & u_{nm} \end{bmatrix} \quad 2.22$$

Step 3: Determine the PIS and NIS.

The positive and negative ideal solutions (A^+ and A^-) can be obtained using Equations 2.23 and 2.24, respectively. The PIS is an alternative that maximises the benefit for each criterion and the NIS minimises the benefit. Positive ideal solution is obtained by choosing the maximum value for each criterion, while the NIS is obtained by choosing the minimum value [166, 173].

$$A^+ = [u_1^+, u_2^+, \dots, u_m^+] \quad 2.23$$

$$A^- = [u_1^-, u_2^-, \dots, u_m^-] \quad 2.24$$

where,

$$u_j^+ = \begin{cases} \max u_{ij}, \text{if j is a benefit criterion} \\ \min u_{ij}, \text{if j is a cost criterion} \end{cases}$$

$$u_j^- = \begin{cases} \min u_{ij}, \text{if j is a benefit criterion} \\ \max u_{ij}, \text{if j is a cost criterion} \end{cases}$$

Step 4: Determine the separation distances, (i.e., positive separation distance S_i^+ and negative separation distance S_i^-) from the ideal solutions using the Euclidean distance theory [163]. The separation distance to the PIS represents the similarity of an alternative to the PIS (best solution), while the separation distance to the NIS represents the deviation from the NIS (worst solution). The positive and the negative separation distances can be computed using Equations 2.25 and 2.26, respectively [163]:

$$S_i^+ = \sqrt{\sum_{j=1}^{m} \left(u_{ij} - u_j^+\right)^2} \quad 2.25$$

$$S_i^- = \sqrt{\sum_{j=1}^{m} \left(u_{ij} - u_j^-\right)^2} \quad 2.26$$

Step 5: Calculate the relative closeness to the ideal solution. The relative closeness is an overall preference score O_i for each alternative A_i, and it is determined as shown in Equation 2.27 [166, 172].

$$O_i = \frac{S_i^-}{S_i^- + S_i^+} \qquad 2.27$$

where, $i = 1, 2, \ldots, n$ and $0 \leq O_i \leq 1$.

Step 6: Ranking of the alternatives. The alternatives are ranked according to the overall preference score O_i. Higher values of O_i mean that the rank is better [171].

2.11.2.1. Flowchart for TOPSIS technique

Figure 2.26 shows a general flowchart of an MCDM problem solving based TOPSIS technique for determining the best alternative from a set of options.

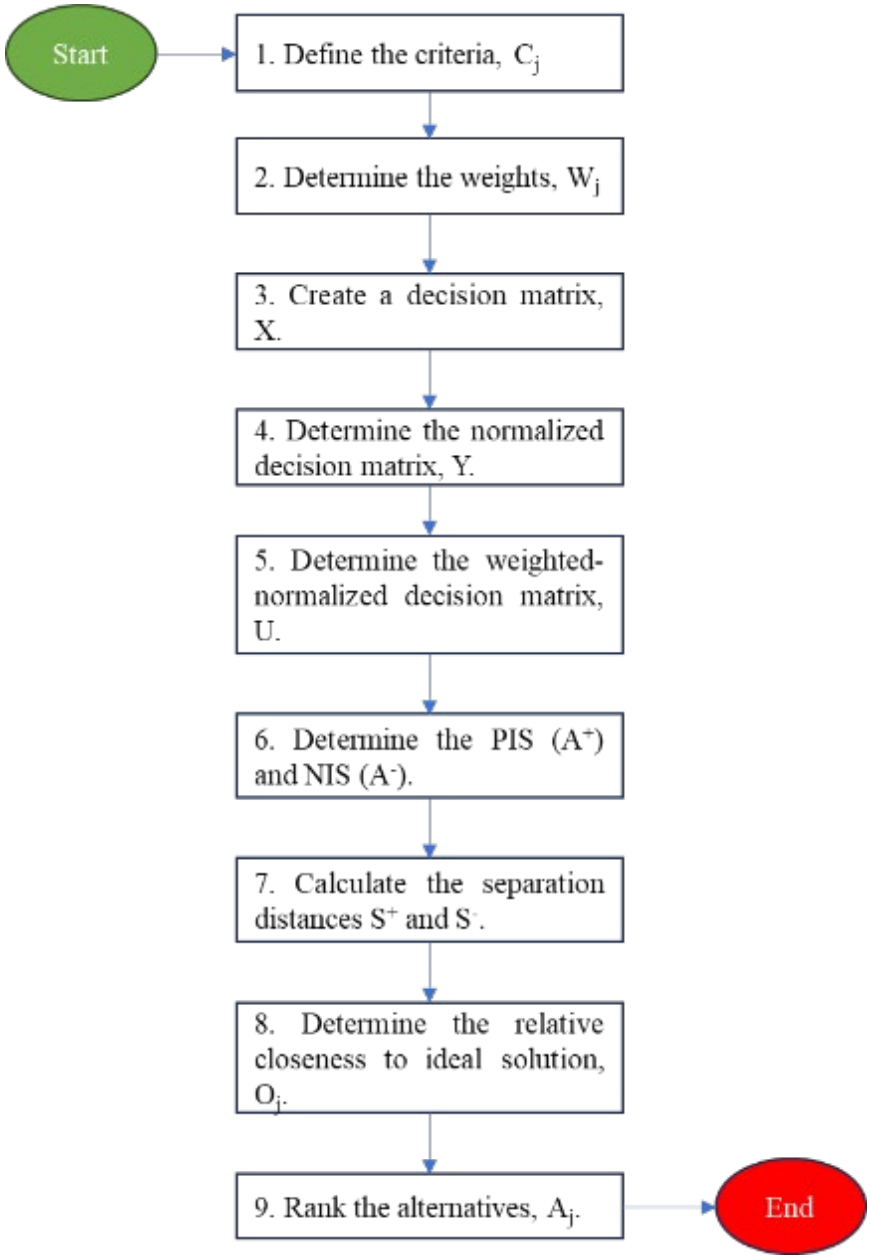


Figure 2-26. General flowchart for a TOPSIS technique

2.12. Study approach

This study was approached in four main parts as follows:

1. The first part of the study was to investigate the physical, microstructural, and mechanical property effects of additions of TiC and TiCN as secondary hardening phases, and the addition of Mo to NbC-Ni and WC-Co based cermets. The effects of using LPS and PECS techniques were also investigated, with the latter being applied as a grain growth inhibitor for grain size refinement and to improve the mechanical

properties of the cermets. Various powder compositions were then used to produce different sintered WC and NbC based cermets.

2. The second part of the study involved density measurements, the determination of hardness, fracture toughness and elastic moduli properties, and microstructure analyses of the sintered samples. The samples were then used to produce cutting inserts through wire-cut electric discharge machining (EDM) and use these manufactured cutting inserts to machine a-GCI.
3. The third part of the study was to investigate the effect of LSM on the mechanical properties and machining performance of the cutting inserts. For this purpose, femtosecond laser surface modification was used to produce various patterns on the cutting edge of the inserts. Semi-finishing and finishing face milling machining trials were conducted to determine the performances of the cutting inserts. The effects of the cutting-edge modification on the machining performance were also investigated. Unmodified (blank) cutting inserts were used as the benchmark for comparison. The machining performance parameters of interest were chosen to be the flank wear rate, resultant cutting force, temperature, and surface roughness.
4. The last part of the study was to optimise the face milling machining cutting parameters for minimising energy consumption and cutting forces as well as maximising the cutting insert life and surface roughness of the machined workpiece.

3. Experimental Procedure

This chapter outlines the procedures, and the equipment used to investigate the effects of Ni-Mo binder and laser surface engineering on NbC and WC based cermets during the face-milling of a-GCI.

3.1. Materials, powder milling and drying

The starting powders and their characteristics are given in Table 3.1.

Table 3.1. Starting powders specifications

Materials	**Particle Size (μm)**	**Crystal Structure**	**Source**
Tungsten (WC)	1 - 2	HCP	Umicore, Belgium
Cobalt (Co)	0.55	HCP	Umicore, Belgium
Nickel (Ni)	3 - 7	FCC	Vale, UK
Molybdenum (Mo)	5	BCC	Plansee, Chile
Titanium Carbonitride (TiC_7N_3)	3	FCC	H.C. Starck, Germany
Titanium Carbide (TiC)	1-1.5	FCC	H.C. Starck, Germany
Niobium Carbide (NbC)	1 - 1.75	FCC	CBMM, Brazil

Powders of different compositions (see Table 3.2 (LPS) and Table 3.3 (PECS)) were milled (homogeneously mixed) in 99% pure ethanol for 48 hours in a multi-directional mixer (Turbula, WAB, Switzerland) using WC-6Co(wt%) milling balls (Ceratizit grade H20C, Ø10 mm). After milling, the wet powders were then dried for one hour with a rotavaporiser at a temperature and speed of 75 °C and 80 rpm, respectively.

3.2. Sintering

3.2.1. Liquid phase sintering

The dried powders were cold isostatically pressed (EPSI, Belgium) into green cylinders at a pressure of 200 MPa. Table 3.2 shows the LPS profiles. Sintering was performed in a graphite furnace (HP, W100/150-2200-50 LAX, FCT Systeme, Frankenblick, Germany) and different sintering profiles were used according to the powder compositions. For example, the sintered

WC-10TiC-10Co (wt%) compacts were first heated to 1050 °C in a dynamic vacuum environment (~10 Pa) at an initial heating rate of 10 °C/min.

Table 3.2. Sintering profiles of liquid phase sintering

Composition (wt%)	**Dwelling Time (min)**	**Temperature (°C)**	**Pressure (Pa)**
WC-10TiC-10Co	90	1390	10
NbC-12[Ni/Mo]	90	1390	10
NbC-10TiC-12Ni	90	1450	10
NbC-10TiC_7N_3-12Ni	90	1450	10

Subsequent heating of compacts to 1250 °C was carried out at a heating rate of 5 °C/min. The compacts were then further heated until a temperature of 1390 °C was reached at a heating rate of 3 °C/min. Sintering was then performed at this temperature for 90 minutes without any external applied pressure. The furnace was then cooled to room temperature at a rate of 3 °C/min. Figure 3.1 shows the temperature and pressure profile of the WC-10TiC-10Co (wt%) sample.

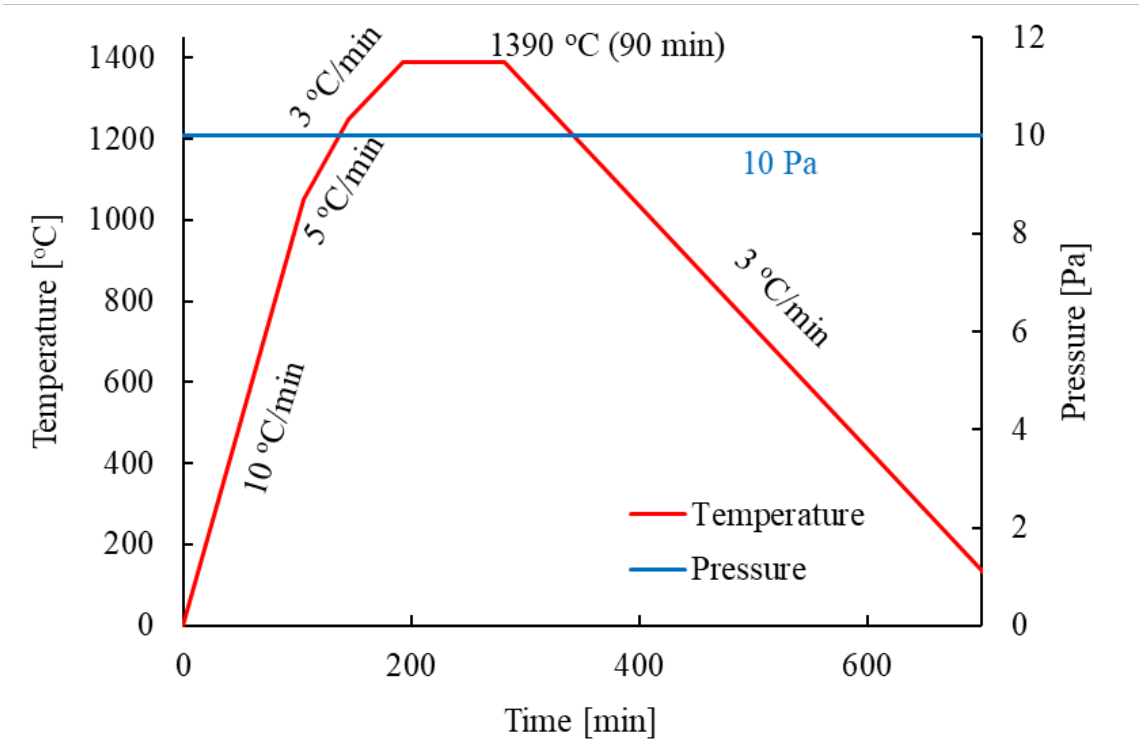


Figure 3-1. Temperature and pressure profile of WC-10TiC-10Co (wt%) sintered via LPS

3.2.2. Pulsed electric current sintering

Like the LPS samples, the dried powders were compacted and then sintered in a PECS furnace (HP D5, FCT Systeme, Germany). The powder compacts were first heated to 1050 °C in a vacuum atmosphere at a pressure of ~2 Pa and 200 °C/min heating rate. The compacts were further heated to 1285 °C at a slower heating rate of 50 °C/min, and then rapidly sintered at this temperature for 10 minutes at 30 MPa. Finally, the samples were cooled to room temperature at a rate of 200 °C/min. Figure 3.2 shows the temperature and pressure relationship of PECS samples.

Table 3.3. Sintering profiles of pulsed electric current sintering

Composition (wt%)	**Dwelling Time (min)**	**Temperature (°C)**	**Pressure (MPa)**
NbC-12Ni	10	1285	30
NbC-12[Ni/Mo]	10	1285	30
NbC-10TiC-12Ni	10	1285	30
NbC-10TiC-12[Ni/Mo]	10	1285	30
NbC-10TiC_7N_3-12Ni	10	1285	30

The powders were separated from the die and punch assembly using horizontal and vertical graphite papers. Diffusion of carbon from the graphite paper into the powder during sintering was prevented by applying hexagonal boron to the graphite paper. A carbon cloth was wrapped around the graphite dies to minimise heat loss from the surface of the die. The temperature was monitored and controlled by an optical pyrometer aimed at a central hole on the anode (upper punch), ~ 1mm above the surface of the sample to optimise the accuracy of the sample temperature [18]. The displacement of the plunger was used to monitor the consolidation of the powder compacts in the axial direction.

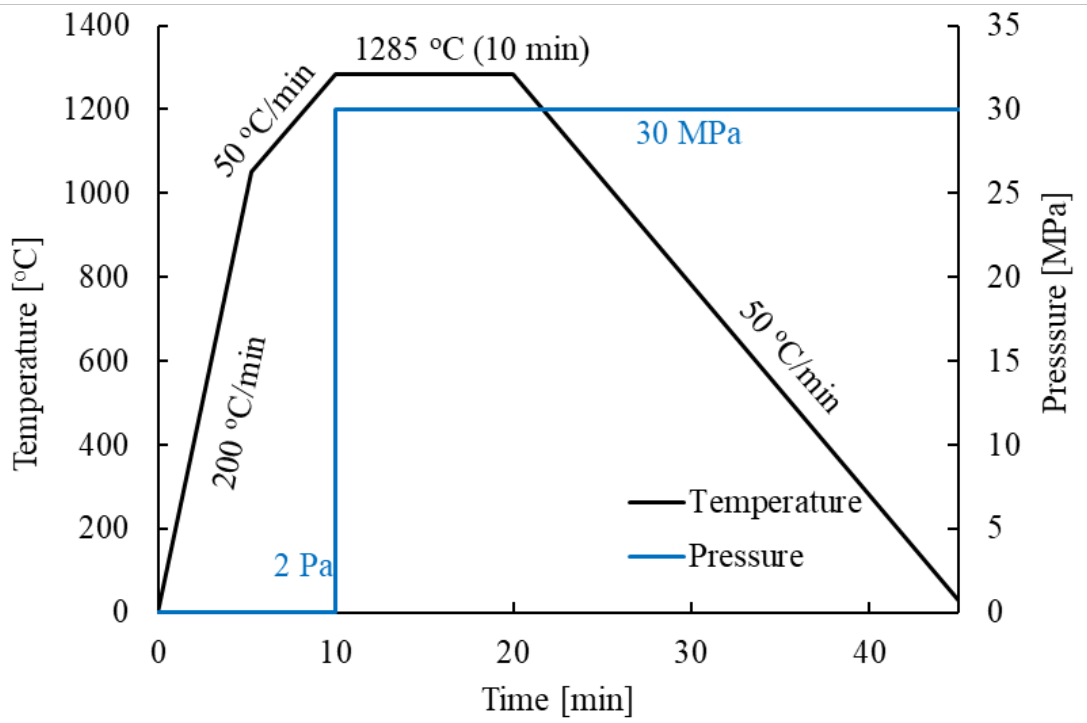


Figure 3-2. Temperature and pressure profiles of PECS samples

3.3. Cutting inserts production

The cutting inserts were cut out from both the LPS, and PECS sintered discs (Ø50mm x 5mm) (see Figure 3.3) using a Fanuc Robocut α-O1A electro-discharge machine (EDM) wire cutter (Fanuc, Japan).

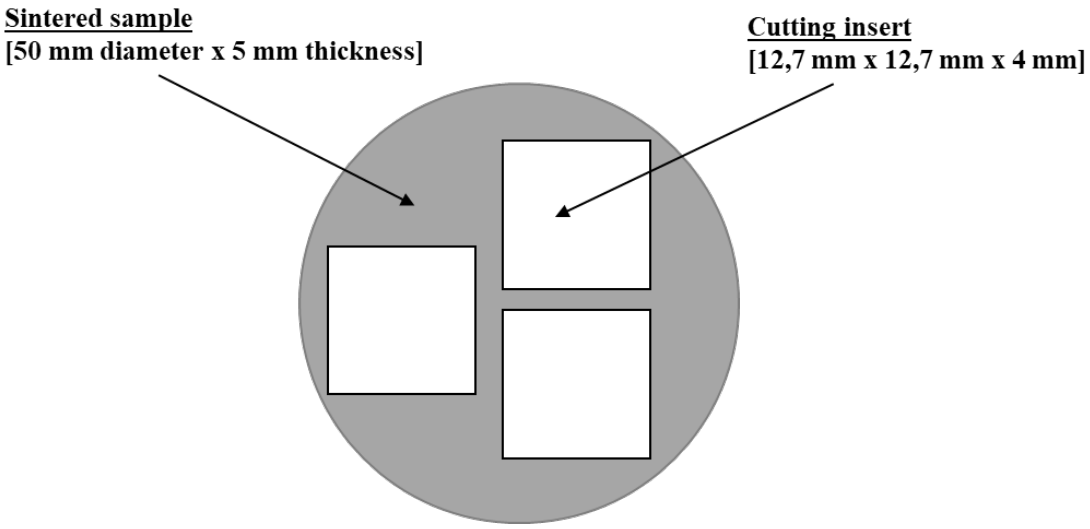


Figure 3-3. Dimensions of the cutting inserts

Initially, the inserts were cut into square shapes with dimensions 12.7 mm x 12.7 mm x 5 mm. This was followed by lapping and grinding of the inserts to a thickness of ~4.2 mm and a nose radius of 1.6 mm according to SNMA shape using a Peter-Wolters 3R-1200 (Peter Wolters, Germany) lapping machine and an EWAG RS12 Edge profile grinder (EWAG, Switzerland) to chamfer-hone the inserts to a radius of 0.2 mm and a chamfer angle of 20º. This was done to eliminate the sharp edges between the faces after grinding and to improve the cutting-edge strength [173]. Thus, preventing premature failure that may occur because of high stress concentration at the cutting edge. Figure 3.4 shows the geometry and dimensions of the inserts. A combined total of 27 cutting inserts were produced for this study (see Table 3.4 and Table 3.5). For every production and composition, the cutting inserts were allocated respective cutting edges, i.e. blank, or unmodified edges and laser surface modified edges.

Table 3.4. LPS samples

Production No.	**Composition**	**Label**	**Quantity**
[1]	WC-10TiC-10(Co/Mo)	T1ML	3
[2]	NbC-12(Ni/Mo)	N2ML	3
[3]	NbC-10TiC-12Ni	R2L	3
[4]	NbC-10TiC_7N_3-12Ni	TCN1L	3

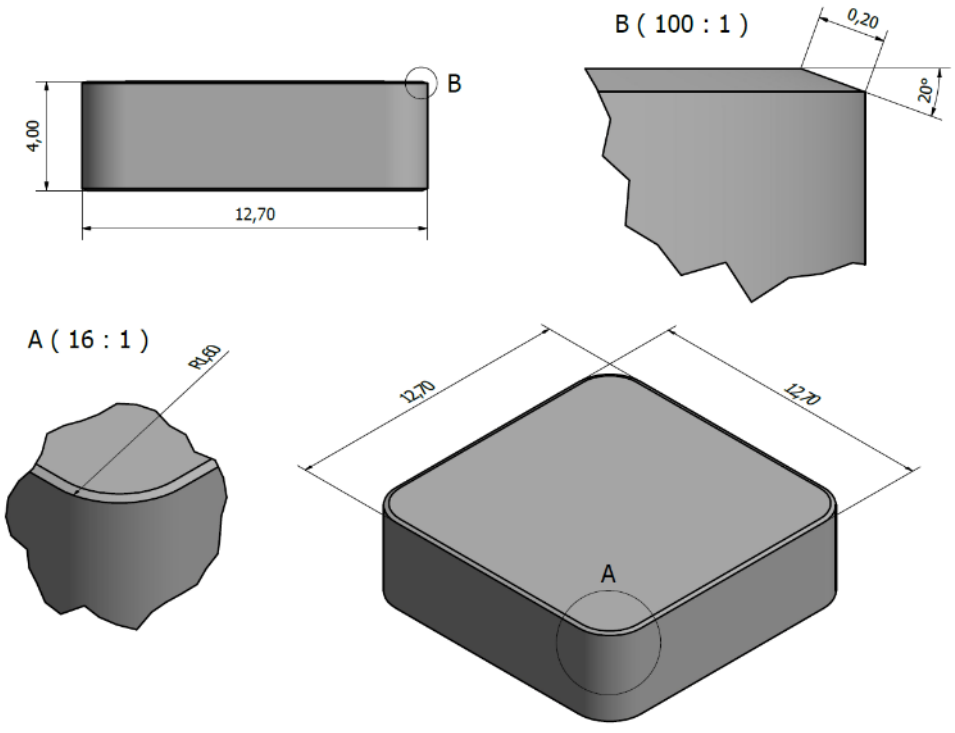


Figure 3-4. Insert design geometry and dimensional specifications

Table 3.5. PECS samples

Production No.	Composition	Label	Quantity
[5]	NbC-12Ni	N2S	3
[6]	NbC-12(Ni/Mo)	N2MS	3
[7]	NbC-10TiC-12Ni	R2S	3
[8]	NbC-10TiC-12(Ni/Mo)	R2MS	3
[9]	NbC-10TiC_7N_3-12Ni	TCN1S	3

The blank, or unmodified cutting edges, refers to the inserts with no additional processing on their rake and flank faces. Thus, the inserts were ready for machining tests in that state. A Medicom LD50C femtosecond laser (Medicom, Czech Republic) was used to create shark skin (S) and pyramid (P) patterns on the cutting edges of the inserts. Figure 3-5 illustrates both the shark skin and the pyramid patterns on the cutting edges of the inserts. The measurements of the patterns on the rake and flank faces of the inserts were performed using the Alicona InfiniteFocus G5 (Bruker Alicona, Austria) 3D optical microscope.

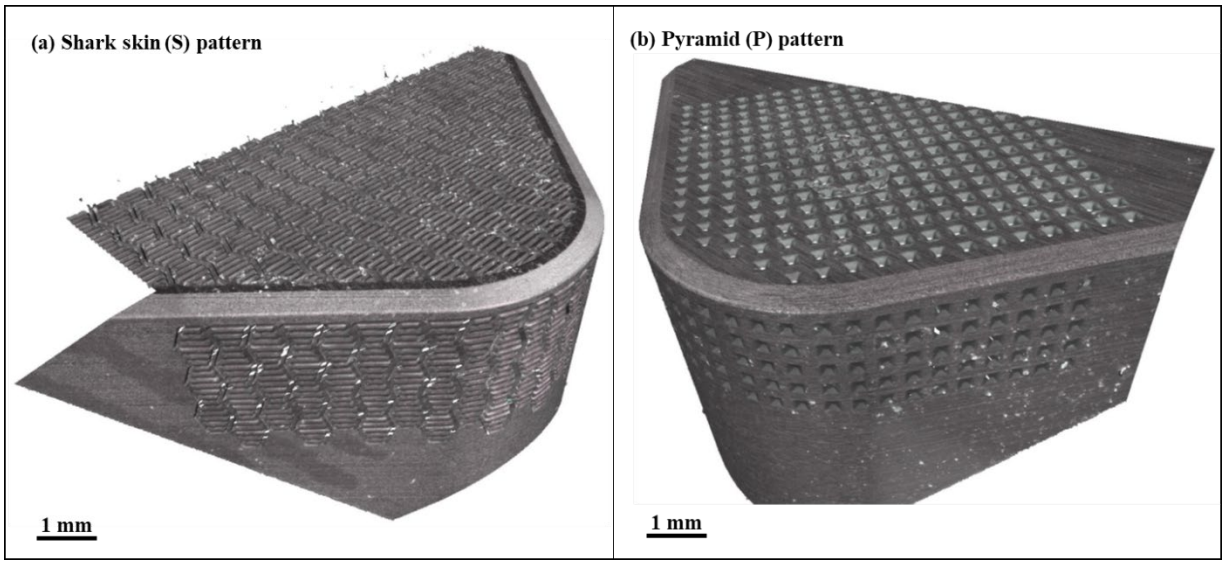


Figure 3-5: Optical micrographs of (a) shark skin pattern and (b) pyramid pattern on the rake and flank faces of the cutting inserts.

Table 3.6 below gives the laser and scanning parameters used for patterning the cutting edges.

Table 3.6. Laser patterning parameters

Parameter	**Quantity**
Laser source	40W
Wavelength (λ)	1030 nm
Repetition rate	200 Hz
Pulse energy	8 μJ
Pulse duration (τ_p)	260 fs
Spot diameter	30 μm
Fluence (intensity)	1.13 J/cm^2
Scanning speed	600 mm/s
Pulse overlap	90%
Pulse pitch	0.003 mm
Number of scanning slices	140
Processing time	293 s

3.4. Characterisation of sintered samples

3.4.1. Density measurements

The density of the sintered samples was determined according to the Archimedes principle using an ED224S density measuring machine (Sartorius, Germany). After sintering, the samples were boiled in distilled water for 5 hours to fill any pores and to remove bubbles on the surface so that the densities could be accurately measured. The samples were then weighed in the air to obtain the wet mass (W_2) and then weighed in distilled water to obtain the suspended mass (W_3). The samples were then dried in an EcoTherm 276 digital oven (Labotec, South Africa) at 80 °C for 24 hours and then weighed in air to obtain the dry mass (W_1).

The true density (ρ) and the % densification (ψ) of the samples were calculated by equations 3.1 and 3.2 respectively.

$$\rho = \frac{W_1 \rho_w}{W_1 - W_3} \qquad 3.1$$

$$\psi = \frac{\rho}{\rho_T} \times 100\% \qquad 3.2$$

where, ρ_w is the density of distilled water at room temperature and ρ_T is the theoretical density of the samples. The theoretical density of the samples was obtained by the rule of mixtures method (see Equation 3.3) using the density and mass (wt%) of the individual constituents of the powder compositions.

$$\rho_T = \left(\frac{m_1(wt\%)}{\rho_1} + \frac{m_2(wt\%)}{\rho_2} + \cdots \frac{m_n(wt\%)}{\rho_n}\right) 100\% \qquad 3.3$$

The example below shows the determination of the theoretical density for WC-10TiC-10Co (wt%) sample.

$$\rho_T = \left(\frac{m_{WC}(wt\%)}{\rho_{WC}} + \frac{m_{TiC}(wt\%)}{\rho_{TiC}} + \frac{m_{Co}(wt\%)}{\rho_{Co}}\right) 100\% \qquad 3.4$$

3.4.2. Samples preparation

Samples were prepared using the standard metallographic preparation procedure. The cutting of samples was done in a Struers Secotom -10 (Cleveland, USA) precision cutting machine, using a 12 cm diameter Struers diamond-coated wheel cutter. The wheel speed and feed rate of 3500 rpm and 0.015 mm/s were used for cutting, and water was used as a coolant during this process. The mounting of the samples was done to provide support for the sample during polishing of the exposed cross section after cutting. The samples were hot mounted in a Struers PolyFast bakelite resin with carbon filler using a Struers Cito-Press 10 (Cleveland, USA) at 500 bar and 180 °C for 15 min. The samples were cooled using water. Samples grinding and polishing were done according to the QATM procedure for ceramics shown in Figure 3.6 [174], using a LaboPol grinding and polishing (Struers, Germany) machine. This was done to eliminate surface damage during cutting and to ensure that the cross section has a smooth surface finish for microstructure analysis and mechanical testing.

STEP	MEDIUM		rpm		N	min
Planar grinding	SiC-paper/foil P240 (180)	H_2O	250-300	►► Syncronous rotation	30	Until plane
Grinding	SiC-paper/foil P800 (280)	H_2O	250-300	►► Syncronous rotation	30	1:30
Pre-polishing	ALPHA/BETA	Dia Complete Poly, 9 µm	120-150	◄ ► Counter rotation	25	5:00-8:00*
Polishing	DELTA	Dia Complete Poly, 3 µm	120-150	►► Syncronous rotation	30	5:00-8:00*
Final polishing	OMEGA	Eposal, 0.06 µm	120-150	◄ ► Counter rotation	25	2:00 (H_2O during final 0:30)

Figure 3-6. Sample grinding and polishing procedure

3.4.3. Mechanical properties

3.4.3.1. Vickers Hardness (HV_{30})

Vickers hardness (HV_{30}) of the polished samples was measured by applying a force of 30N for 10 seconds with a diamond indenter on the AVK-CO testing machine (Mitutoyo Akashi, Japan) and taking the average of five indentations at different locations on each sample. Figure 3.7 illustrates the Vickers hardness indentation test. The diamond indenter has the shape of a right pyramid with a square base. After the removal of the load, two diagonals of lengths d_1 and d_2 are measured using a microscope and then averaged for the determination of the square mm surface area of indentation. The Vickers hardness is the quotient calculated by dividing the kgf load by the area of indentation (Equation 3.5).

$$HV_{30} = 1.854\ \frac{F}{d^2} \qquad 3.5$$

where d (mm) is the arithmetic mean of the diagonal lengths and 1.854 is a constant. The HV_{30} is then converted to GPa using Equation 3.6.

$$H = HV_{30}(0.00987) \qquad 3.6$$

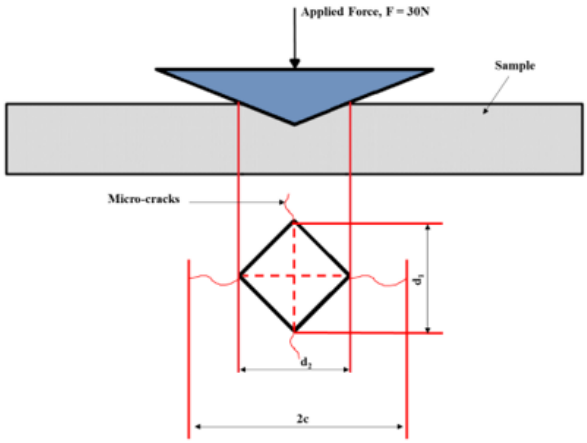


Figure 3-7. Vickers hardness (HV_{30}) testing

3.4.3.2. Fracture Toughness (K_{IC})

The fracture toughness (K_{IC}) of the samples was determined by using the Mitutoyo AVK-Co (Akashi, Japan) hardness indenter and applying Shetty's equation (Equation 3.7). According to Shetty, the radial cracks (see Figure 3.7) produced by the edge of the diamond indenter can be used to accurately determine the fracture toughness of cermets [175]. The value of fracture toughness for each sample was calculated from an average of five indentations. The criteria of $c/a \leq 2.25$ and $0.25 \leq l/a$ 2.5 were satisfied during the K_{IC} calculations, where c is the crack length measured from the centre of the indentation to the crack tip, a is the half diagonal of the indentation, and l is the distance between c and a.

$$K_{IC} = 0.0889H^{0.5}\left(\frac{F}{4l}\right)^{0.5} \qquad 3.7$$

where H is the hardness (GPa) of the sample and F is the applied force (N).

3.4.4. Modulus of Elasticity

The modulus of elasticity was determined using an Olympus 45MG pulse-echo tester (Olympus Corporation, Japan) by measuring the samples' wave sound velocities in the transverse (shear) (v_T) and longitudinal (v_L) directions. The velocities were then used to determine the Poisson's ratio of the samples using Equation 3.8 [176].

$$\mu = \frac{1 - 2(v_T/v_L)^2}{2 - 2(v_T/v_L)^2} \qquad 3.8$$

The transverse velocity (v_T) and the density (ρ) of the material were used to calculate the shear modulus (G) using Equation 3.9 [176].

$$G = {v_T}^2 \rho \tag{3.9}$$

The elastic modulus (E) was then determined by Equation 3.10 [176].

$$E = \frac{{v_L}^2 \rho (1 + \mu)(1 - 2\mu)}{1 - \mu} \tag{3.10}$$

3.4.5. Microstructural analysis and characterisation

The microstructures of the cermets were studied using a Sigma 500 VP (Zeiss, Germany) field emission scanning electron microscope (SEM) in both electron backscattered diffraction (EBSD) mode and secondary electron (SE) mode. The SEMs were run at an acceleration voltage of 10 kV – 30 kV and a working distance of 4 – 8 mm. The SEM micrographs were used to obtain the morphology of the samples (distribution of the phases, precipitate size, grain shape) and surface topology (defects, cracks, and voids) using SE, compositional contrast and phase identification using EBSD, and elemental identification and quantification using energy dispersive X-ray spectroscopy (EDS). Further analyses, including average carbide grain size measurements of the sintered samples, were done through image analysis of the SEM micrographs using ImageJ software. In order to better understand the grain interfaces and variations within the microstructure caused by additions of TiC, TiC_7N_3, and Mo, including the locations of these additives, high-resolution transmission electron microscopy (HRTEM) (JEOL ARM-200F, JEOL, Japan) was used to analyse the samples at an atomic level. Helios Nanolab, which had a dual focused ion beam - scanning electron microscope (FIB-SEM) platform, was used to prepare the samples for HRTEM (FEI Company, USA).

3.5. Grey cast iron (GCI) face milling

3.5.1. The workpiece (GCI)

Auto Industrial Group (Pty) Ltd, a prominent automotive components supplier in South Africa, donated more than thirty a-GCI workpieces for machining experiments. The workpieces had dimensions 160mm x 160mm (square) x 30mm (thick), and one of the 160 mm dimensions was selected as the cutting length. The chemical composition, metallurgical characteristics and mechanical properties of the workpieces as given by the company are provided in Tables 3.7 to 3.9.

Table 3.7: Chemical composition

Element	**C**	**Si**	**P**	**S**	**Mn**	**Cr**	**Mo**	**Ni**	**Cu**	**Sn**	**Ti**	**CE**	**Fe**
%	3.41	2.06	0.04	0.061	0.67	0.25	0.042	0.03	0.032	0.039	0.011	4.05	Balance

Table 3.8: Characteristics of graphite and matrix of the GCI

	Graphite form	**Type**	**Shape**	**Grain size [µm]**	**Matrix**
Specification	I	A	N/A	4 – 5	>95% Pearlitic

Table 3.9: Hardness and tensile strength of GCI

Properties	**Core**	**Surface**
Hardness (BHN) Vickers Hardness	(213) ~218 GPa	(216) ~222 GPa
Ultimate tensile strength (UTS)	263 MPa	

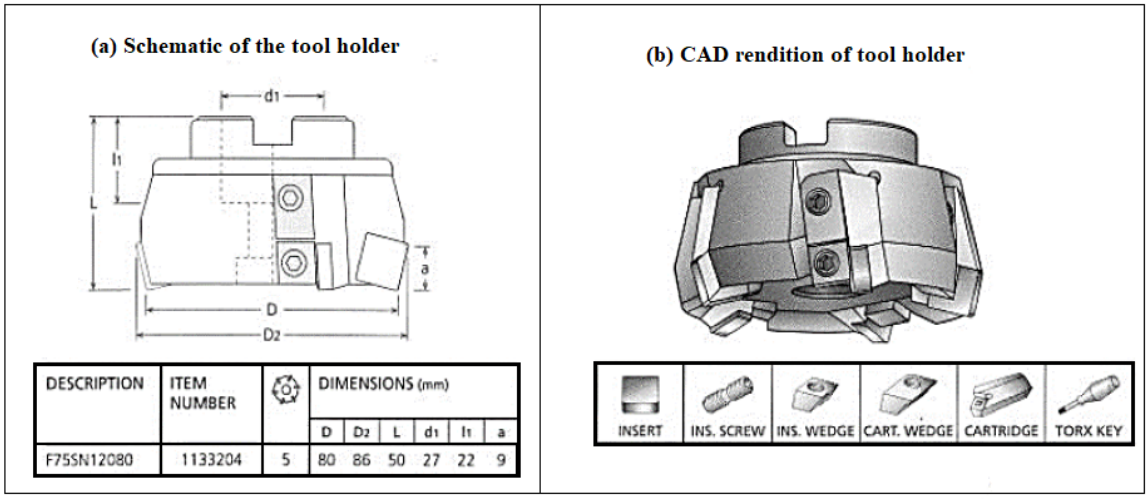
3.5.2. Face milling tests

The machining tests of a-GCI were carried out on a MAHO MH70 (MAHO, Germany) milling machine using the milling conditions given in Table 3.10. The tests were planned according to the parameters for semi-finishing and finishing machining, respectively. Additionally, due to the complexity of the tests as well as the limited number of cutting edges, each face milling test was conducted as a single trial, with no repetition of measurements across any of the machining experiments. It is worth noting that finishing was done in two ways by varying the depth of cut (a_p), i.e. finishing 1 and finishing 2, with a_p values of 0.5 mm and 0.25 mm for the two finishing tests respectively. The total machining duration for semi-finishing and finishing 1, was set to a standard 20 minutes as it allows for optimisation of the machining process. However, for finishing 2, the time was doubled to ensure that the rate of material removal ($\dot{m}_{rr}$) remained constant throughout the milling tests.

Table 3.10: Face milling tests parameters

Type of machining	**Cutting speed (V_c) [m/min]**	**Depth of cut, (a_p) [mm]**	**Radial depth of cut (a_r) [mm]**	**Spindle speed, (n) [rpm]**	**Feed rate (V_f) [mm/min]**	**Feed [mm/tooth]**	**Material removal rate ($\dot{m}_{rr}$) [mm^3/min]**
Semi finishing [Test 1]	200	1.0	80	800	80	0.1	6400
Finishing 1 [Test 2]	400	0.5	80	1600	160	0.1	6400
Finishing 2 [Test 3]	400	0.25	80	1600	160	0.1	6400

Table 3.11 shows the nomenclature and the cutting edges of the cutting inserts used during face milling tests. For each of the machining tests, a Pilot F75SN12080 cutting insert holder connected to the MAHO-MH70 was mounted with just one cutting insert. This made it possible to analyse the insert life (machining performance) of each cutting insert individually. Figure 3.8 shows the cutting insert holder (a) schematic including dimensions and (b) CAD rendition. The figure also shows a lone cutting insert used for each milling test.



DESCRIPTION	ITEM NUMBER		DIMENSIONS (mm)					
			D	D2	L	d1	l1	a
F75SN12080	1133204	5	80	86	50	27	22	9

Figure 3-8. Pilot F75SN12080 cutting insert holder schematic and CAD rendition. Adapted from [177]

A Kistler Multicomponent Force Dynamometer (Kistler, Switzerland) was attached to the workpiece clamping vice to measure the cutting forces. A Nikon D5000 (Nikon, Japan) high speed thermal camera and FLIR Tool software were used to monitor the temperature variations during the machining process. Figure 3.9 shows the thermal imaging of FLIR camera during face-milling trials. A Nikon optical microscope (Nikon, Japan) was used to assess cutting edge failure (fracture or chipping) and wear after every machining pass. In addition, the tool life and or failure criteria of the cutting inserts was evaluated using the ISO-3685:1993 standards. High angle annular dark field scanning transmission electron microscopy (HAADF-STEM) (JEOL 2100, with a LaB_6 filament, JEOL, Japan) was also used to do wear analyses of the cutting edges of the cutting inserts.

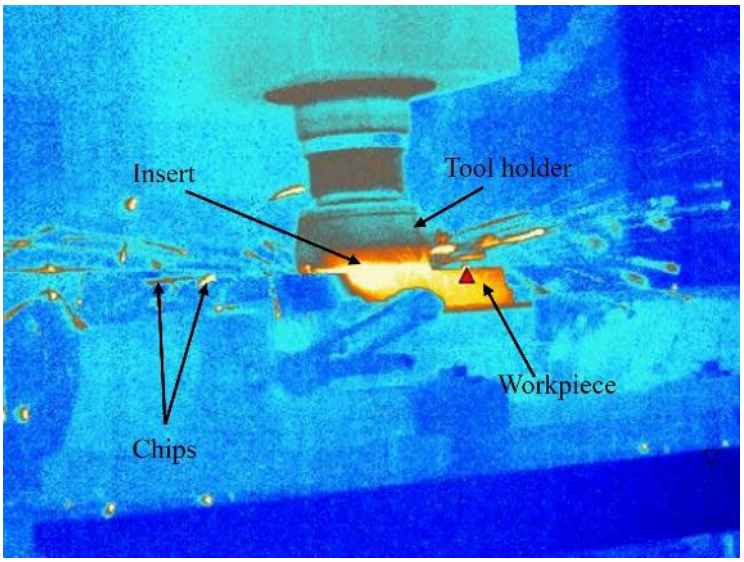


Figure 3-9. Thermal imaging during face-milling

Table 3.11: Cutting inserts nomenclature and cutting edges.

Insert composition	Sintering	Category	Insert name and cutting-edge type	Cutting edge (Test 1)	Cutting edge (Test 2)	Cutting edge (Test 3)
WC-10TiC-10[Co/Mo]	LPS	Blank	T1ML-B	2.0.7	2.2.3	2.2.5
		Shark Skin	T1ML-S	2.1.5	2.1.7	2.1.8
		Pyramid	T1ML-P	2.1.3	2.1.1	2.1.2
NbC-12Ni	PECS	Blank	N2S-B	11.0.5	11.0.6	11.0.7
		Shark Skin	N2S-S	11.1.6	11.1.5	11.1.7
		Pyramid	N2S-P	11.1.1	11.1.3	11.1.4
NbC-12[Ni/Mo]	LPS	Blank	N2ML-B	4.0.5	4.0.6	4.0.7
		Shark Skin	N2ML-S	4.1.7	4.1.5	4.1.6
		Pyramid	N2ML-P	4.1.1	4.1.2	4.1.3
	PECS	Blank	N2MS-B	12.0.6	12.0.7	12.0.8
		Shark Skin	N2MS-S	12.1.7	12.1.5	12.1.6
		Pyramid	N2MS-P	12.1.1	12.1.2	12.1.3
NbC-10TiC-12Ni	LPS	Blank	R2L-B	5.2.5	5.2.6	5.2.7
		Shark Skin	R2L-S	5.1.7	5.1.5	5.1.6
		Pyramid	R2L-P	5.1.1	5.1.2	5.1.3
	PECS	Blank	R2S-B	13.0.5	13.2.6	13.2.7
		Shark Skin	R2S-S	13.1.7	13.1.5	13.1.6
		Pyramid	R2S-P	13.1.1	13.1.2	13.1.3
NbC-10TiC-12[Ni/Mo]	PECS	Blank	R2MS-B	14.0.1	14.0.2	14.0.5
		Shark Skin	R2MS-S	14.1.7	14.1.5	14.1.6
		Pyramid	R2MS-P	14.1.1	14.1.2	14.1.4
NbC-10TiC_7N_3-12Ni	LPS	Blank	TCN1L-B	7.0.7	7.2.1	7.2.2
		Shark Skin	TCN1L-S	7.3.7	7.3.5	7.3.6
		Pyramid	TCN1L-P	7.3.2	7.3.1	7.3.4
	PECS	Blank	TCN1S-B	15.0.8	15.2.6	15.2.7
		Shark Skin	TCN1S-S	15.1.5	15.1.6	15.1.8
		Pyramid	TCN1S-P	15.1.1	15.1.2	15.1.3

3.5.3. Surface roughness measurements

The surface roughness measurements were done only for finishing 2 machining trials. The most used device for measuring the surface roughness of a surface is the surface profilometer. Figure 3.10 shows an SRT-6210 digital surface roughness tester (BESTONE, China) fitted with a tip of 5 µm radius diamond stylus [178]. The device measures the height and width deviations of a machined surface as a function of the position using a diamond stylus which runs perpendicular to the direction of the micro-irregularities pattern on the machined surface. Some of the important basic parameters for calculating the surface roughness are the average roughness (R_a), the root mean square (R_q), the average maximum height (R_z), and the vertical distance between the highest peak and the lowest valley along the assessment length (R_t) [177]. It is worth noting that only the surface roughness of finishing 2 workpieces was considered. The measurements were taken at different time intervals throughout the machining tests. Each machined surface was subjected to a total of 4 measurements (at the cutter entry, midsection and cutter exit areas).



Figure 3-10: SRT-6210 digital portable surface roughness tester [178]

3.5.4. Processing, interpretation, and presentation of face milling test results

This sub section outlines the processing and presentation of the results for each type of machining (semi-finishing, finishing 1, and finishing 2). The designations of the cutting inserts and their respective cutting edges were set according to the sample name, type of cutting edge and machining condition (or test number). As shown in Figure 3.11, a cutting insert with the sample name T1ML, a blank (or unmodified) cutting edge, and used for semi-finishing (test 1) would have a designation of T1ML-B1. In addition, because SNMA type cutting inserts have 8 cutting edges, the designation of

the cutting insert will also refer to its cutting edge to avoid possible confusion between cutting inserts and cutting edges.

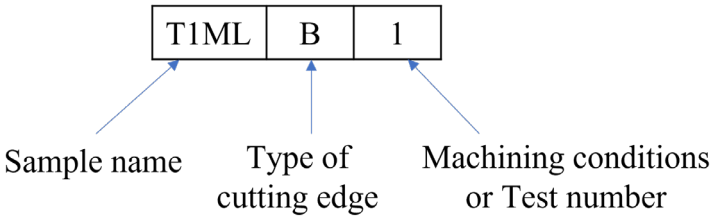


Figure 3-11. Example of cutting insert designation

The results from the face milling tests were processed and interpreted using a combination of Microsoft Excel and MATLAB. The WC-Co based cutting inserts (T1ML) were used as the industry standard. Comparisons of the WC-Co based, and NbC-Ni based cutting inserts were made with respect to the composition, sintering techniques (LPS vs. PECS), type of cutting edge (blank vs. shark skin LSM vs. pyramid LSM) and overall machining performance. The analyses will provide insights into the effects of these factors as well as various machining parameters on the overall performance of the cutting inserts during machining trials. It is worth mentioning that for this study, there were no NbC-Ni LPS manufactured base cutting inserts during the machining tests. For this reason, the PECS produced NbC-12Ni (N2S) cutting inserts were used as the reference or basis of comparison for all the other NbC-Ni based cutting inserts throughout this work. The general presentation of results for the machining tests was done in two ways. The results for semi-finishing and finishing 1 were presented in the same format. The presentation for finishing 2 was slightly altered due to the introduction of surface roughness as a limiting criterion for evaluating machining performance.

3.5.4.1. Processing, interpretation, and presentation of semi-finishing and finishing 1 machining results

The processing, interpretation and presentation of the results for semi-finishing and finishing 1 machining trials were done in five steps which are briefly discussed below.

3.5.4.1.1. Step 1: Resultant forces, specific cutting energy, and temperature.

The analysis of the resulting forces is critical for comprehending the machining conditions under which the cutting inserts were used. The average resultant force (F) and maximum resultant force (F_{max}) experienced by the cutting inserts are compared here. In this study, Fmax refers to the highest recorded resultant force at any arbitrary minute during the machining process. Thus, it reflects the extreme machining case. The specific cutting energy (U_c) analysis allows for the optimisation of the machining

process. The most effective cutting parameters for reducing energy consumption while maximising productivity could be identified by understanding the energy consumption per unit volume of material removed. By using this analysis, the desired tool life and surface finish can be attained. The effects of temperature (T) on the insert are also important during the face milling process. This is because, during machining, the cutting insert generates high amounts of heat due to the friction between the insert and the workpiece. The heat generated may result in thermal damage to the workpiece, as well as deformation, cracking and changes in both the cutting insert and the workpiece's microstructure. In the current study, the average machining temperature is investigated. It is worth noting that the thermal imaging camera provides an average temperature around the cutting zone, which may not necessarily represent the actual temperature of the cutting insert tool and workpiece interface. Thus, the temperature readings are not accurate and will only be used for indication purposes.

3.5.4.1.2. Step 2: Insert tool life and wear performance

The analyses of insert tool life (cutting time), maximum flank wear (VB_{max}), and flank wear rate (FWR) results are critical for measuring performance in machining operations. The insert life gives an indication of the duration that a cutting insert can be used effectively to machine a workpiece before it needs to be replaced. The VB_{max} and FWR show the extent and rate of wear (damage) on the cutting insert which are then applied to the failure criterion to determine if the cutting insert is still usable for machining.

3.5.4.1.3. Step 3: Micrographs of the flank and rake faces of the cutting inserts

The micrographs of the cutting edges were used to provide a visual assessment of the cutting inserts' performance, including the evaluation of wear and identification of insert failure modes (i.e. chipping, mechanical fracture, or deformation). For this purpose, optical and high angular annular dark field (HAADF) – scanning transmission electron microscopy (STEM) micrographs of the flank and rake faces of selected cutting inserts are presented and analysed.

3.5.4.1.4. Step 4: Machining performance evaluation of the cutting inserts

The cutting inserts during semi-finishing and finishing 1 were evaluated and ranked according to a technique for order preference by similarity to an ideal solution (TOPSIS) method for solving multi-criteria decision making (MCDM) problems. The aim of this exercise is to establish a raking from the best to the poorest performing cutting insert for each face milling machining trial. The TOPSIS methodology outlined in Section 2.11 was used for the cutting inserts selection process. The different cutting inserts were evaluated based on the criteria below:

- Criterion 1: Insert tool life (I_l).
- Criterion 2: Specific cutting energy (U_c).
- Criterion 3: Maximum resultant cutting force (F_{max}).

In general, the objectives that are intended to minimise are usually considered as the negative criteria, while those that are intended to maximise tend to be considered as the positive criteria. In this study, I_l is a positive criterion while U_c, and Fmax are the negative criteria respectively. It therefore follows that the best cutting insert should exhibit a good combination of these criteria (i.e. the cutting insert should have the longest insert tool life while having the lowest specific cutting energy and maximum cutting force, respectively).

Weighting of the criteria was done to assign the relative importance of the factors affecting the machining performance of the cutting inserts, and this was termed as the performance weighted index (PWI). As mentioned previously, this is a subjective process based on the decision maker's preferences. Wu et al. [168], for example, assumed PWI of 0.2 to 0.6 for energy consumption, 0.2 to 0.4 for maximum cutting force, and 0.1 to 0.4 for material removal rate in their study. For the current study, in both semi-finishing and finishing 1, I_l, U_c, and Fmax were assigned PWIs of 0.60, 0.30, and 0.10, respectively. The rationale for the assigned weights is given in Table 3.12.

Table 3.12. Weights of the performance criteria (performance weighted index) for semi-finishing and finishing 1 machining tests

Criterion	PWI (%)	Rationale for the weight
1.	60	The cutting insert "tool" life is one of the most important factors in machining. It is also the most used criterion used to assess machining performance and the machinability of the workpiece materials [17, 179]. The insert tool life is effectively the amount of time that a cutting insert can maintain its cutting performance and dimensional accuracy, while minimising cutting forces, heat generation and wear. During machining, cutting inserts that are worn slowly have relatively longer predictable service tool life, resulting in less production costs, consistent dimensional accuracy, and surface finish [179]. For these reasons, a PWI of 60%, which indicates its significant importance, was deemed fitting for this criterion. More details on this will be presented in the discussion.

2.	30	The selection of a cutting insert that offers low energy consumption would be a significant advantage in improving manufacturing efficiency. For a country like South Africa, which has been facing an energy crisis, the development of energy saving manufacturing processes could be key. In addition, carbon footprint in manufacturing continues to be a global concern. As such, there is a need for the development of processes aimed at the reduction of the energy footprint to reduce environmental impacts. Based on these reasons, it can be appreciated that energy consumption plays a critical role (i.e. from the socio-economic aspect to sustainable engineering practices). Hence, the specific energy consumption of the cutting insert was considered as a criterion and assigned a PWI of 30%. While not as critical as the insert tool life, it still significantly impacts the efficiency and cost effectiveness of the cutting process.
3.	10	The cutting forces are widely used for monitoring machining conditions [180]. Too large cutting forces may result in unexpected failure of the cutting inserts and the workpiece. Thus, they could be detrimental to the quality of the surface finish (dimensional accuracy and surface roughness) as well as to the cutting effectiveness. Thus, the maximum average resultant cutting force was selected as one of the criteria and assigned the lowest PWI (i.e. 10%). Though the cutting forces can affect machining (wear and stability), they are typically not as influential as the other criteria. Hence, they are given the least weight in the decision-making process.

3.5.4.1.5. Step 5: Consolidation of the results

The consolidation of results mainly covers the overall comparison and ranking of the machining performances of the blank (B), shark skin LSM (S) and pyramid (P) cutting inserts during the different types of machining trials.

3.5.4.2. Processing, interpretation, and presentation of finishing 2 machining results

As previously discussed, the processing, interpretation and presentation of finishing 2 machining results were slightly altered due to the introduction of surface roughness (Ra) as a key factor. Consequently, new Ra-dependent variables, indicated by a single prime symbol ('), were introduced into the analysis. Table 3.13 shows surface roughness dependent variables used during finishing 2 machining performance analysis and evaluation. The approach in finishing 2 machining mirrored the steps employed in semi-finishing and finishing 1. However, a distinct approach was adopted for the evaluation of machining performance in step 4, as elaborated upon in the following discussion. This change in approach is substantiated by the rationale, which is also presented for reference.

Table 3.13. Surface roughness dependent variables

Variable	**Symbol (Units)**
Average resultant force	F' (N)
Maximum resultant force	F_{max}' (N)
Specific cutting energy	U_c' (J/mm^3)
Average machining temperature	T′ (°C)
Insert tool life	I_l' (min)
Maximum flank wear	VB_{max}' (µm)
Flank wear rate	FWR′ (µm/min)

3.5.4.2.1. Rationale and machining performance evaluation of cutting inserts during finishing 2

Similar to semi-finishing and finishing 1 machining trials, the technique for order of preference by similarity to an ideal solution (TOPSIS) was also used to evaluate and rank finishing 2 cutting inserts. For these trials, the surface roughness was introduced as the fourth criterion to the insert tool life, specific cutting energy and maximum resultant cutting force. This was mainly because Ra is considered one of the most critical variables for finishing and it is an important indicator of machining performance that can be used to assess the effectiveness of the cutting inserts. Auto Industrial Group (Pty) Ltd requires the surface roughness of their brake components to be between 1.6 µm and 2.5 µm. Accordingly, for this study, the Ra of 2.5 µm was used as a limit criterion for the allowable surface

roughness. Furthermore, this value was used to determine the effective insert tool life (I_l') of the cutting inserts which is a function of surface roughness and is defined as the machining time for which the cutting inserts produce surface roughness finish Ra of 2.5 µm and below. Similarly, the other machining variables (in Table 3.13) for finishing 2 were determined based on the surface roughness limit criterion, respectively.

The introduction and inclusion of surface roughness in the machining performance analysis of finishing 2 cutting inserts necessitated a shift in the PWIs of the decision-making criteria. Therefore, the "new" criterions I_l', U_c' Ra, and Fmax′ were assigned weights of 0.4, 0.3, 0.2, and 0.1, for finishing 2, respectively. The PWI of the specific cutting energy and the maximum resultant cutting force experienced by the cutting inserts were not changed from semi-finishing and finishing 1. The specific cutting energy was deemed moderately important and therefore did not need adjustment in its weight. Similarly, the PWI of the maximum resultant cutting force remained relatively low compared to the others. The PWI of the insert tool life was reduced to 40% (i.e. the PWI for effective tool life was set to 40%), and the balance was allocated to surface roughness. The effective insert tool life criterion was still deemed highly important; however, it was necessary to also give the effect of surface roughness consideration. The 20% weight contribution of the surface roughness alludes to the fact that surface quality was deemed an important factor but not as critical as the insert tool life and the specific cutting energy.

4. Physical, Microstructural, and Mechanical Properties

This chapter outlines the effects of composition manipulation, binder replacement and sintering techniques on the physical, microstructural, and mechanical properties of the sintered samples.

4.1. Densification of the sintered samples

Table 4.1 shows the densification of the sintered samples. All sintered samples achieved densification of 97% and above. Regardless of the sintering technique, the N2S sample had a slightly higher densification compared to all the other NbC-Ni based cermets. Apart from the N2ML samples which exhibited similar densification, the LPS produced samples showed slightly higher densification values in comparison to their PECS counterparts. For example, PECS resulted in 0.62% and 0.39 % reductions in the densification of R2L and TCN1L samples.

Table 4.1. Sintered samples densification

Sample name	Densification (%)
T1ML	98.36 ± 0.170
N2S	98.66 ± 0.013
N2ML	98.48 ± 0.372
N2MS	98.54 ± 0.054
R2L	98.43 ± 0.113
R2S	97.82 ± 0.032
R2MS	98.14 ± 0.053
TCN1L	98.01 ± 0.079
TCN1S	97.63 ± 0.055

The addition of Mo to the N2S sample composition did not have a significant effect on densification (i.e. the N2S, N2ML, and N2MS samples had very similar densification values). However, the additions of TiC and TiC_7N_3 to the N2S composition (NbC-Ni) sample slightly inhibited densification in R2S and TCN1S, respectively (see Table 4.1). The TiC addition reduced the densification of the sample N2S by ~ 0.12% in R2S sample. Further addition of Mo to the R2S sample composition slightly improved the densification in the R2MS sample. The sample TCN1S had a densification of 97.63 ± 0.055 which was the lowest compared to all the other samples irrespective of the sintering technique,

indicating that the addition of TiC_7N_3 to the N2S sample resulted in a densification reduction of ~1.04%.

4.2. Microstructural characteristics of the sintered samples

The scanning electron microscope – backscattered electron (SEM-BSE) micrographs of the sintered samples are given in this subsection. The SEM-BSE micrographs were used to provide compositional information including identification of the phases (carbide and binder phases), analyses of homogeneity of the phases' distributions, carbide grain sizes determination. The identification and confirmation of phases (elemental composition) was done using the energy dispersive x-ray spectroscopy (EDS) point and area analyses. The high angular annular dark field (HAADF) – scanning transmission electron microscope (STEM) mapping was also done to provide detailed information on the samples' microstructure at the nano and atomic levels.

Figure 4.1 shows the SEM-BSE micrograph of T1ML sample. The light phase in the microstructure is composed of WC grains, the light grey phase is Co, dark grey phase is the (W, Ti, Co) C solid solution, and the dark phase is a TiC-rich solid solution as confirmed by the EDS mapping. From Figure 4.1, the T1ML sample had homogeneously distributed Co binder pools and TiC rich solid solutions, and fine WC grains (see Figure 4.1 and Table 4.2). The SEM-BSE micrograph of T1ML further shows that the sample is well densified with no apparent presence of pores in the microstructure. In addition, the micrograph also indicates that the WC grain size distribution was homogeneous and that there was no abnormal grain growth during the sintering process. The elemental composition of the T1ML sample was confirmed by EDS mapping with the exception of Mo. Figure 4.2 shows the HAADF-STEM micrograph of T1ML sample. From the figure, the WC phase is composed of a majority of thin platelets of varying sizes and a few truncated triangular prism shaped grains. The HAADF-STEM mapping further confirmed the observations from SEM-BSE, by revealing that the Co binder phase was uniformly distributed and found to coincide with WC grains, especially along its boundaries. The HAADF-STEM mapping detected traces of Mo throughout the microstructure of the T1ML as shown in the figure. Figure 4.2 further indicates that the TiC phase has a tendency to isolate itself from other elements of the composition. In addition, the HAADF-STEM mapping further confirmed the formation of the dark grey contrast (W, Ti, Co, Mo) C solid solutions observed in Figure 4.1 around the dark TiC-rich phases.

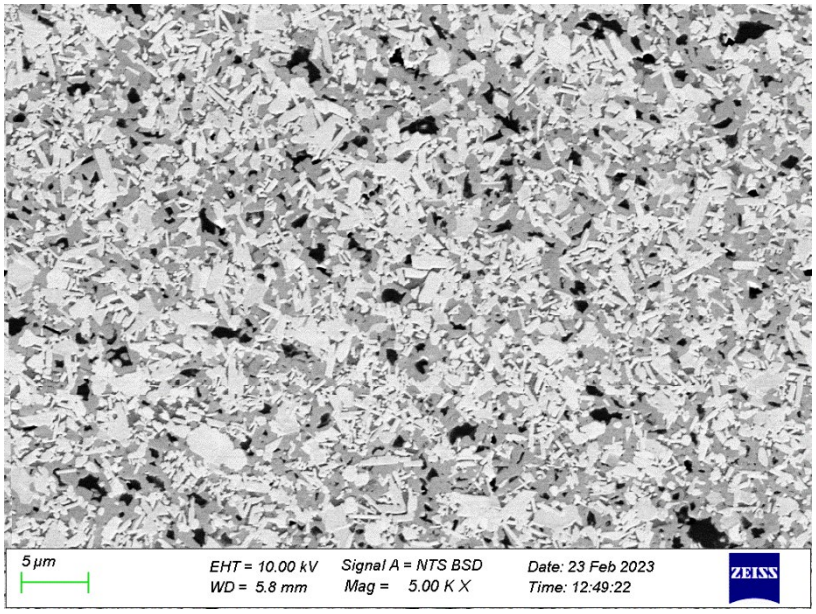


Figure 4-1. SEM-BSE image of WC-10TiC-10[Co/Mo] (wt%) (T1ML) sample prepared by LPS showing WC (light), Co (light grey), (W, Ti, Co) C solid solution (dark grey phase), and TiC- rich (dark) phases

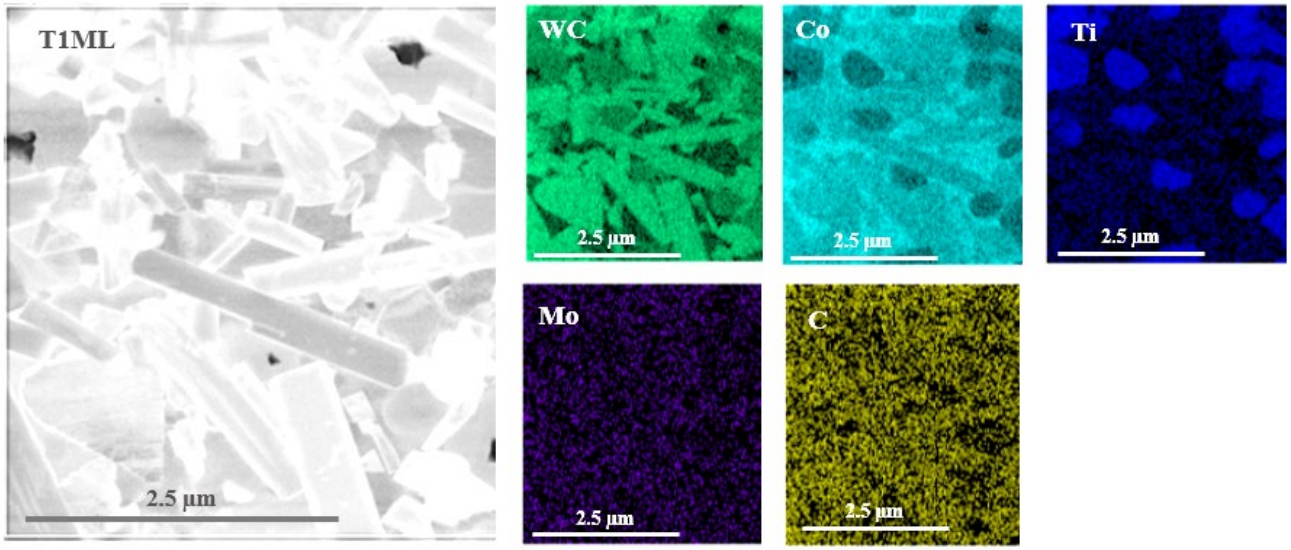


Figure 4-2. HAADF-STEM images of WC-10TiC-10[Co/Mo] (wt%) (T1ML) sample produced by LPS showing: WC (green), Co (cyan), Ti (blue), Mo (purple) and C (yellow).

Figures 4.3 (a), (b) and (c) show the SEM-BSE micrographs of N2S, N2ML and N2MS samples respectively. From Figure 4.3 (a), the light phase represents the NbC grains, and the dark phase is the Ni binder. The micrograph showed a fairly homogeneously distributed Ni binder pool. The microstructure had relatively small spherical NbC grains with a mean size of 1.66 ± 0.12 µm as well as dark spots/phases which could be pores or impurities inside the carbide grains. The EDS area mapping results confirmed the presence of Nb, C and Ni in the microstructure. Figures 4.3 (b) and (c) show the SEM-BSE micrographs of NbC-12 [Ni/Mo] (wt %) prepared by LPS and PECS respectively.

The figures show larger NbC grains in N2ML (2.76 ± 0.95 µm) compared to N2MS (1.49 ± 0.48 µm) (see Table 4.2). The Ni binder pools were homogeneously distributed in the N2ML sample compared to its PECS counterpart. Similar to the N2S sample, the microstructure of both N2ML and N2MS contained pores with the former having slightly pronounced pores than the former. As shown in Figures 4.3 (a) and (c), there was no significant difference in the microstructures of N2S and N2MS samples. However, there was a slightly higher clustering of Ni binder in the microstructure of N2MS than in N2S. The EDS analyses of the N2M based samples were also done to confirm the elemental composition. Unlike with T1ML, elemental Mo was detected in N2MS by EDS map analysis, even if its exact location could not be confirmed through EDS. However, the element was detected to be inside NbC grains by the HAADF-STEM analysis indicating the formation of (Nb, Mo) C solid solutions.

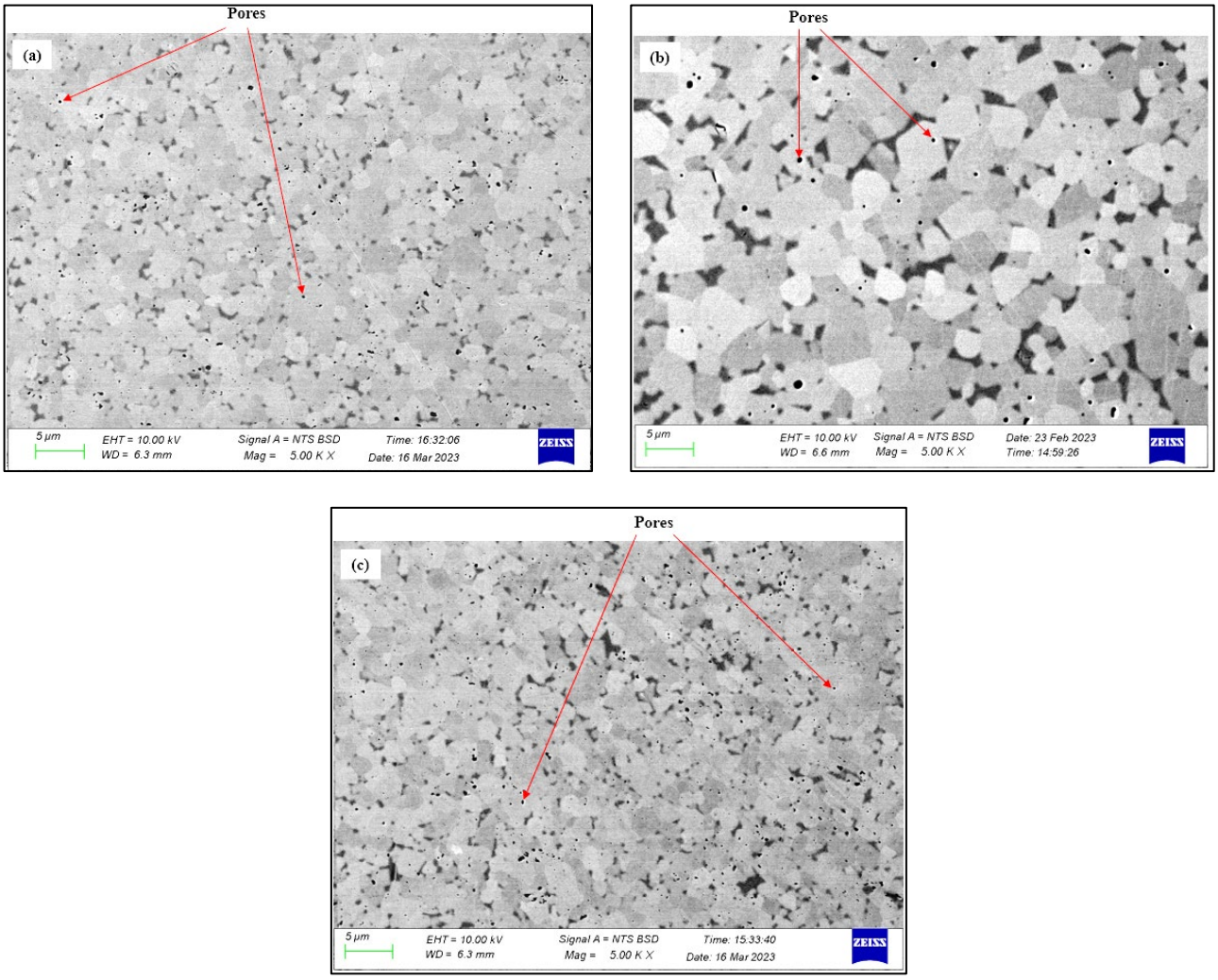


Figure 4-3. (a) SEM-BSE image of NbC-12Ni (wt%) (N2S) prepared by PECS, NbC-12[Ni/Mo] (wt%) of (b) N2ML prepared by LPS and (c) N2MS prepared by PECS showing NbC (light) and Ni (medium dark) phases

Figure 4.4 shows the SEM-BSE micrographs of (a) R2L, (b) R2S and (c) R2MS samples respectively. The light phase present in the microstructures is NbC, the medium grey is Ni, and the dark phase is the undissolved TiC phase, as confirmed by the EDS mapping. The EDS mapping also confirmed the formation of (Nb, Ti, Ni) C solid solutions. The micrograph of the R2L shows that the sample's microstructure is composed of abnormally large facets with edge rounding NbC grains as well as smaller spherical NbC grains. The Ni binder was fairly distributed, and the microstructure also exhibited dark spots/phases inside the carbide grains as well. The well-rounded black spots could be pores or binder inclusions, and the other irregularly shaped spots could be carbide pull-outs or undissolved TiC which was sparse or thinly distributed with the sample's microstructure.

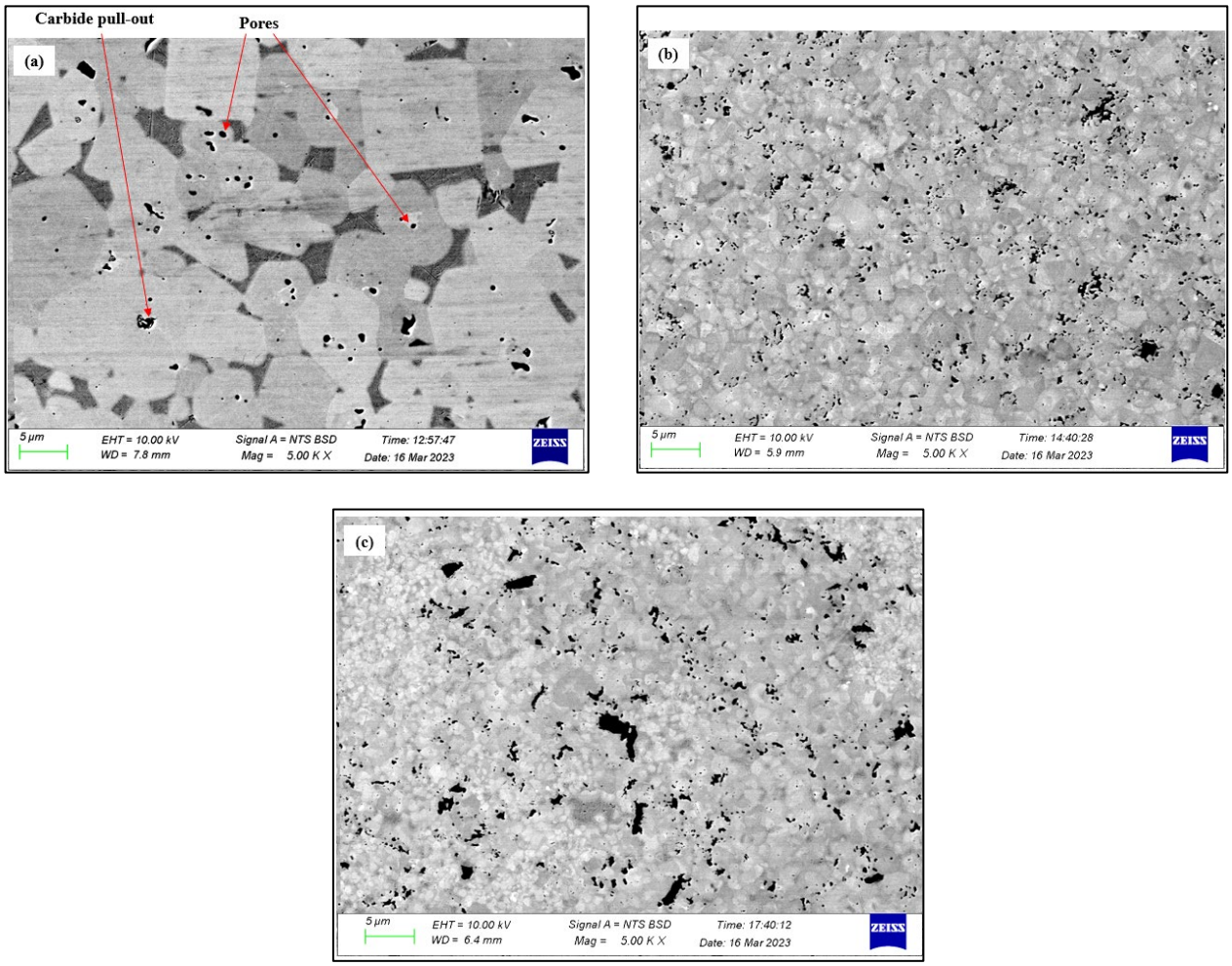


Figure 4-4. SEM-BSE image of NbC-10 TiC-12Ni (wt%) (a) R2L prepared by LPS and R2S prepared by PECS, and (c) NbC-10TiC-12[Ni/Mo] (wt%) of R2MS prepared by PECS showing NbC (light), Ni (medium) and TiC-rich (dark) phases

As shown in Figure 4.4 (b) and (c), the R2S and R2MS samples exhibited very similar microstructures with comparable mean carbide grain sizes of 1.62 ± 0.06 µm and 1.35 ± 0.06 µm, respectively. The micrographs of both samples revealed a continuous NbC skeleton with isolated or clustered Ni binder

phase. The micrographs also exhibited very bright Nb-rich phases inside the carbide grains. The Ni binder pool distribution was not easily visible on both microstructures. Further, both R2S and R2MS had dark phases within microstructures. The prominent (slightly bigger) dark phases were confirmed to be TiC-rich phases by EDS analyses of the samples. From Figures 4.4 (b) and (c), the R2MS exhibited more prominent dark TiC-rich phases than the R2S sample. Similar to the N2MS sample, elemental Mo was also detected by the EDS in the R2MS sample and similarly, the exact location of Mo could not be confirmed through EDS mapping.

Figure 4.5 depicts the HAADF-STEM micrograph of R2MS sample. The figure shows that the NbC grains were mainly interconnected with the Ni binder pools segregated and exhibiting a somewhat poor distribution. As shown in the figure, the HAADF-STEM mapping confirmed that Mo and TiC were located in the NbC grains, thus indicating the formation of (Nb, Mo, Ti) C solid solutions. In addition, Figure 4.5 shows that the Mo coincides with NbC, and this is important to note due to the fact that Mo was added to the composition as a binder and not a carbide phase.

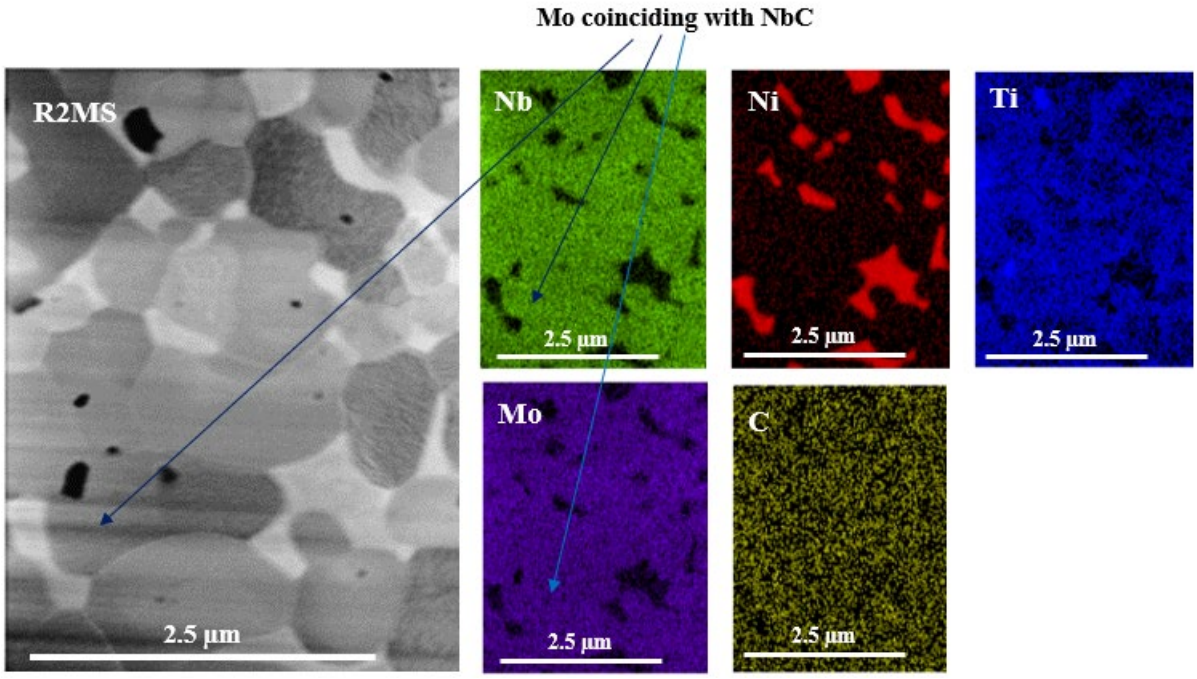


Figure 4-5. HAADF-STEM images of NbC-10TiC-12[Ni/Mo] (wt%) of R2MS prepared by PECS showing: Nb (green), Ni (red), Ti (blue), Mo (purple) and C (yellow)

Figure 4.6 shows the SEM-BSE micrographs of (a) TCN1L and (b) TCN1S samples. The carbide (NbC) is characterised by the light phase, the medium grey is Ni and the darkest is the TiCN-rich phase. The figure shows that the TCN1L microstructure has larger spherical NbC grains compared to the TCN1S. The majority of the grains in the TCN1L microstructure exhibited a bright contrast core, a feature which was not easily detected in the TCN1S sample. The mean carbide sizes of the samples

were determined to be 2.97 ± 0.23 µm and 1.68 ± 0.15 µm for the TCN1L and the TCN1S samples respectively (see Table 4.2). Figure 4.6 (a) shows that the Ni binder pools were fairly distributed in the microstructure. However, there was some evidence of clustering of the Ni binder pools between continuous NbC skeletons. Similar to the R2L, the microstructure of the TCN1L sample exhibited dark spots (as shown in the figure) which could be pores (well-rounded dark spots at the centre of the carbide grains), binder inclusions, impurities, carbide pull-outs or undissolved TiCN phase. The microstructure of TCN1S did not exhibit carbide pull-outs, and the other features were relatively smaller in size and slightly difficult to detect compared to those in TCN1L sample. The distribution of Ni binder pools was not easily detectable on the TCN1S microstructure as shown in Figure 4.6 (b). The microstructure exhibited TiCN-rich dark phases (confirmed via EDS) which were fairly distributed. The EDS analyses were also performed on both the TCN1L and the TCN1S samples to confirm the elemental composition. The EDS was able to detect all the elements in the composition except for nitrogen (N).

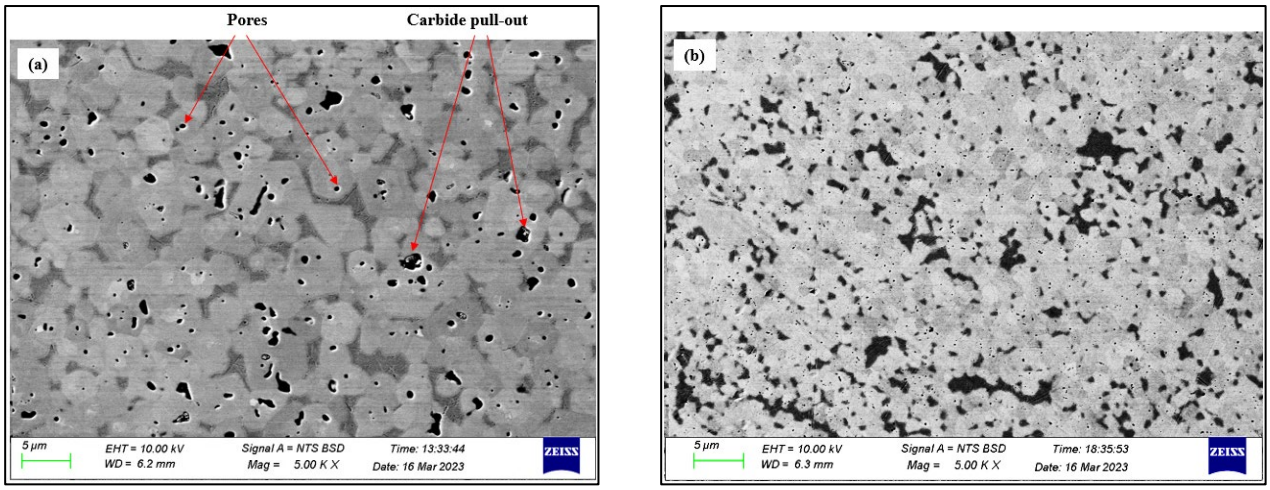


Figure 4-6. SEM-BSE images of NbC-10TiC_7N_3-12Ni (wt%) of (a) TCN1L prepared by LPS and (b) TCN1S prepared by PECS showing NbC (light), Ni (medium dark), and TiCN-rich (darkest) phases

Table 4.2 gives the mean carbide grain sizes of the sintered samples. Overall, the T1ML sample had the smallest mean grain sizes compared to all the other samples irrespective of the composition and the sintering technique. From Table 4.2, samples of NbC-Ni-based cermets produced via LPS had larger carbide grains than samples produced by PECS with similar compositions. For example, the mean carbide grain size values of N2ML, R2L and TCN1L are slightly higher than N2MS, R2S and TCN1S respectively. Among the LPS produced samples, R2L had the largest mean carbide grain size compared to N2ML and TCN1L samples which had comparable carbide grain sizes of 2.52 ± 0.09 and 2.97 ± 0.23 µm, respectively. The PECS produced samples, on the other hand, had comparable mean carbide grain sizes with the values of the grain sizes laying between 1 and 2 µm. It is worth noting that the additions of Mo, TiC and TiC_7N_3 had no significant influence on the mean carbide grain sizes of

samples produced via PECS. As given in the table, the mean carbide grain size of the base composition N2S is similar to those of the other compositions. However, when considering the sintering techniques, it can be observed from Table 4.2 that the LPS technique resulted in significant grain growth in all NbC-Ni based samples. The sample N2ML had ~1.7 times mean grain sizes greater than the N2MS sample, that of the R2L sample was ~3.4 times greater than the R2S sample, and the TCN1L sample was ~1.8 times greater than the TCN1S sample. Thus, it can be deduced that the sintering method plays a crucial role in carbide grain sizes.

Table 4.2. Sintered samples mean carbide grain sizes

Sample name	Mean carbide size (μm)
T1ML	1.02 ± 0.08
N2S	1.66 ± 0.12
N2ML	2.52 ± 0.09
N2MS	1.49 ± 0.48
R2L	5.48 ± 1.86
R2S	1.62 ± 0.12
R2MS	1.35 ± 0.06
TCN1L	2.97 ± 0.23
TCN1S	1.68 ± 0.15

4.3. Mechanical properties of the sintered samples

4.3.1. Hardness and fracture toughness properties

Table 4.3 gives the Vickers hardness and fracture toughness properties of the samples used in this study. Figure 4.7 shows the relationship between the Vickers hardness (HV_{30}) and the fracture toughness (K_{IC}) properties of the samples. As shown in the figure, the T1ML had the highest hardness (14.53 ± 0.13 GPa) compared to all the other samples irrespective of the composition or the sintering technique (see Table 4.3). There were no significant differences between the hardness values of the N2S and R2L samples as both samples exhibited a hardness of ~11 GPa as indicated in the figure and Table 4.3. This was the lowest hardness recorded hardness among the samples used in this study. When considering the PECS produced samples only, the R2MS exhibited the highest hardness (14.11 ± 0.22 GPa), and it was followed by the TCN1S with a hardness of 13.70 ± 0.32 GPa. There was no significant

difference in the hardness exhibited by the R2S and N2MS. The additions of Mo, TiC, TiC_7N_3 and a combination of TiC plus Mo to the base NbC-12Ni (N2S) composition improved the hardness property of the N2MS, R2S, TCN1S and R2MS samples. The R2L sample had the lowest hardness among the LPS produced samples. As shown in the figure, there was no significant difference between the hardness properties of N2ML and TCN1L samples whose hardness value was ~12.8 GPa (see Table 4.3). With the exception of N2M based samples, the NbC-Ni based PECS produced samples had slightly higher hardness than their LPS produced counterparts.

Table 4.3. Vickers hardness (HV_{30}) and fracture toughness (K_{IC}) of the sintered samples

Sample name	Vickers hardness, HV_{30} (GPa)	Fracture toughness, K_{IC} ($MPa.m^{1/2}$)
T1ML	14.53 ± 0.13	8.83 ± 0.11
N2S	11.73 ± 0.33	5.72 ± 0.10
N2ML	12.81 ± 0.12	6.99 ± 0.25
N2MS	12.81 ± 0.58	6.09 ± 0.35
R2L	11.54 ± 0.28	8.57 ± 0.59
R2S	13.06 ± 0.08	5.55 ± 0.08
R2MS	14.11 ± 0.22	6.19 ± 0.24
TCN1L	12.77 ± 0.13	9.31 ± 0.53
TCN1S	13.70 ± 0.32	5.50 ± 0.06

Figure 4.7 shows that the samples prepared with LPS had higher fracture toughness than the samples prepared with PECS irrespective of their composition. From the figure, the TCN1L sample exhibited slightly higher fracture toughness (9.31 ± 0.53 $MPa.m^{1/2}$) than all the samples. However, it is worth noting that the fracture toughness properties of the TCN1L, T1ML and R2L samples largely overlap, as shown by the error bars, indicating that these compositions share a similar range of fracture toughness values (see Table 4.3 and Figure 4.7). The N2ML sample had the lowest fracture toughness (6.99 ± 0.25 $MPa{\cdot}m^{1/2}$) among the LPS produced samples. Figure 4.7 also shows that the fracture toughness values of the PECS produced samples were between the range of 5.5 $MPa{\cdot}m^{1/2}$ and 6.5 $MPa.m^{1/2}$, respectively, with the TCN1S sample having the lowest fracture toughness among these samples respectively. Accordingly, the additions of Mo, TiC, TiC_7N_3 and a combination of TiC plus Mo to the base NbC-12Ni (N2S) composition had no significant change on the fracture toughness properties of the PECS produced samples.

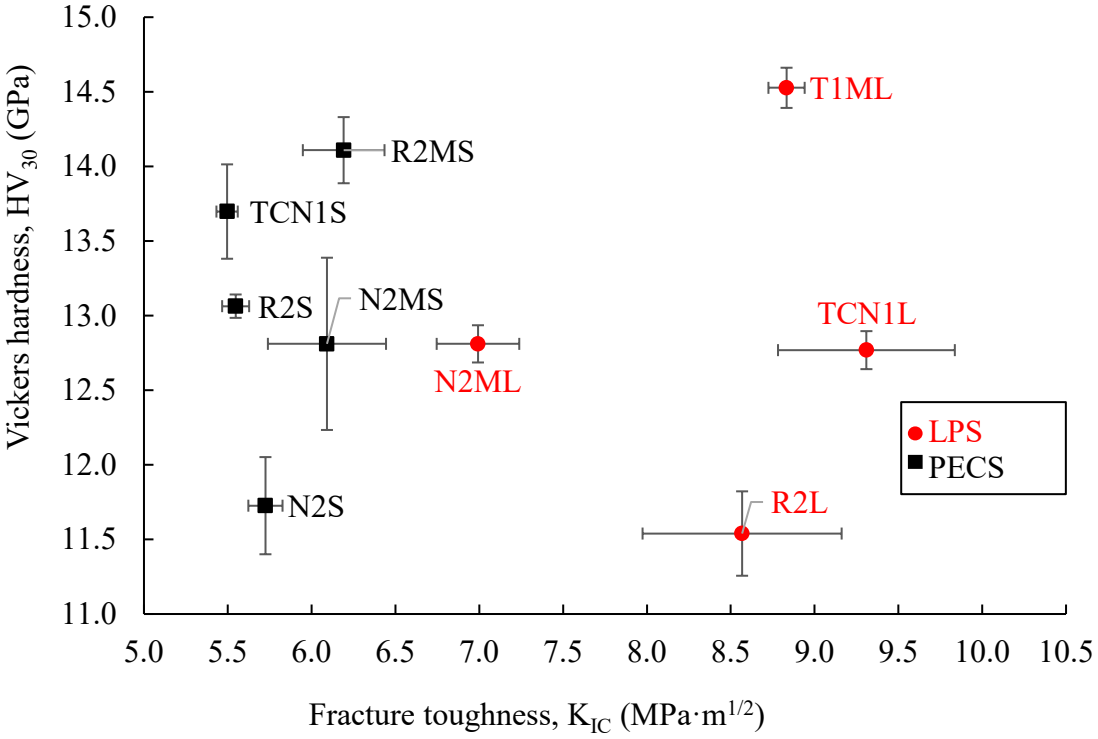


Figure 4-7. Variation of Vickers hardness (HV_{30}) with fracture toughness (K_{IC})

4.3.2. Elastic (Young's modulus) and shear modulus (modulus of rigidity) properties

Table 4.4 gives the elastic and shear modulus properties of the sintered samples used in this study. Figure 4.8 depicts the variation of the elastic modulus and the Vickers hardness of the samples. From the figure, the LPS produced N2ML sample had the lowest elastic modulus (372.47 ± 1.84 GPa) compared to the rest of the samples irrespective of composition and sintering technique (see Table 4.4). The R2L had the highest elastic modulus (475.55 ± 0.08) among the LPS produced samples. However, its value was slightly similar to that of the T1ML sample as indicated in the figure. From Figure 4.8, samples R2S and TCN1S exhibited very similar elastic modulus values (547.54 ± 2.06 GPa and 549.60 ± 1.15 GPa, respectively). This was the highest compared to all the samples irrespective of composition and sintering technique. The R2MS sample exhibited the lowest elastic modulus property among the PECS produced samples (see Table 4.4 and Figure 4.8). In general, the PECS produced samples had higher elastic modulus properties than LPS produced samples irrespective of composition. The additions of Mo as well as a combination of Mo plus TiC to the base NbC-Ni (N2S) composition resulted in a slight reduction in the elastic modulus of N2MS and R2MS respectively. However, contrasting observations were made with the additions of TiC and TiC_7N_3 to a similar composition whereby the elastic modulus properties of R2S and TCN1S were improved as shown in Figure 4.8 respectively.

Table 4.4. Elastic modulus (E) and shear modulus (G) of the sintered samples

Sample name	Elastic modulus (GPa)	Shear modulus, G (GPa)
T1ML	472.11 ± 0.37	183.55 ± 0.16
N2S	495.18 ± 0.38	196.98 ± 0.05
N2ML	372.47 ± 1.84	149.85 ± 0.32
N2MS	482.01 ± 0.42	198.32 ± 0.16
R2L	475.55 ± 0.08	196.99 ± 0.15
R2S	547.54 ± 2.06	216.18 ± 0.12
R2MS	479.19 ± 0.33	204.32 ± 0.04
TCN1L	429.16 ± 0.84	185.65 ± 0.07
TCN1S	549.60 ± 1.15	216.24 ± 0.21

Similar to the elastic modulus, the shear modulus value of the N2ML sample was the lowest (149.85 ± 0.32 GPa) among all the samples. The shear modulus properties of the TCN1L and T1ML samples were similar although the former had a slightly higher G value than the former. The R2L had the highest shear modulus (196.99 ± 0.15 GPa) among the LPS produced samples. When considering the PECS produced samples, the N2S exhibited the lowest shear modulus whereas the sample with the highest shear modulus was the TCN1S (see Table 4.4). The additions of Mo, a combination of Mo and TiC, TiC and TiC_7N_3 to the N2S sample composition improved the shear modulus properties of the N2MS, R2MS, R2S and TCN1S, respectively (see Table 4.4). With the exception of R2L, the LPS produced samples generally had lower shear modulus properties compared to the PECS produced samples. Furthermore, the LPS produced samples exhibited lower combinations of both properties compared to PECS produced samples.

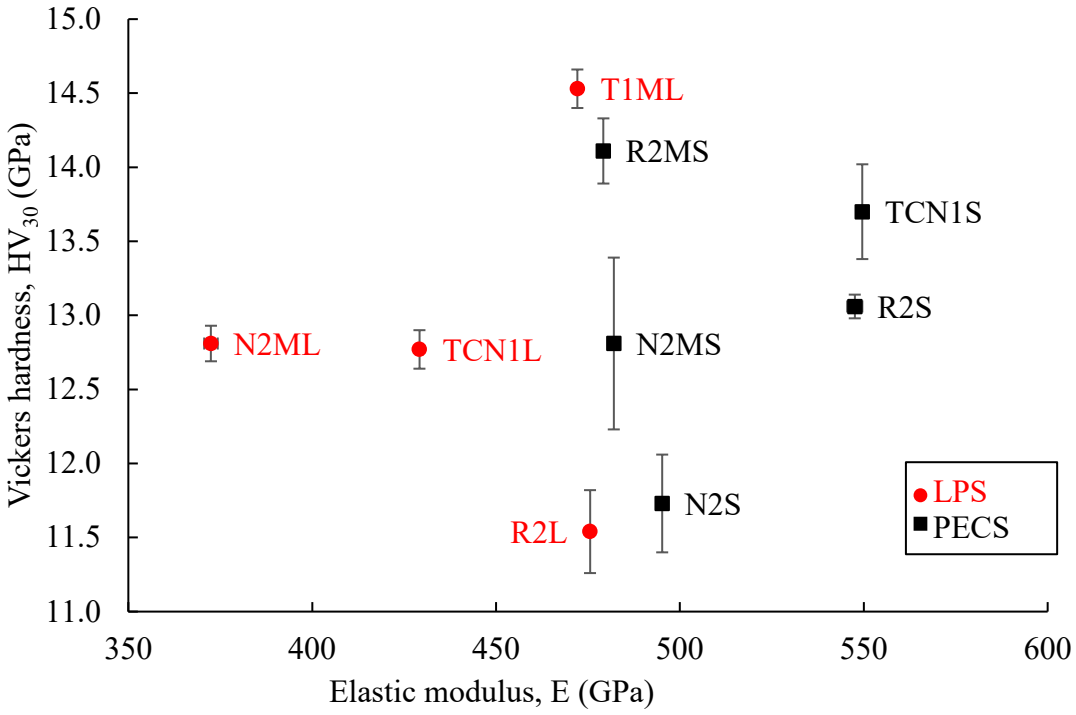


Figure 4-8. Variation of elastic modulus (E) with the Vickers hardness, HV_{30}

5. Semi-finishing (Test 1) Results

This chapter presents the results of once-off semi-finishing trials on a-GCI, where each test was conducted as a singular experiment without any repetition of measurements. The machining conditions for these tests are listed as follows:

- Cutting speed (V_c): 200 m/min,
- Spindle speed (n): 800 rpm,
- Depth of cut (a_p): 1.0 mm,
- Feed (f_z): 0.1 mm/tooth,
- Feed rate (V_f): 80 mm/min,
- Machining duration: 20 minutes.

5.1. Analyses of the blank (B1) cutting inserts

This subsection presents and analyses resultant cutting forces, specific cutting energy, insert life, wear and temperature of the blank cutting inserts during the face milling of a-GCI under semi-finishing conditions. The micrographs of cutting inserts showing the flank and rake faces are also presented in this section. Lastly, the performance evaluation of the blank cutting inserts is done to rank the cutting inserts.

5.1.1. Analyses of the resultant forces, specific cutting energy, and temperature of the B1 cutting inserts

Table 5.1 shows the resultant forces, specific cutting energy, and the average machining temperature of the blank cutting inserts during semi-finishing machining. Figure 5.1 shows the average resultant forces (F) and the maximum resultant forces (F_{max}) experienced by the blank cutting edges during semi-finishing. As shown in Figure 5.1, the maximum resultant forces were significantly higher than the average resultant forces for all the cutting inserts except for the N2MS-B1 which had similar F and Fmax. The figure also shows that the F_{max} values of all the cutting inserts, irrespective of composition and the sintering technique, exceeded 1000 N. When compared to the other B1 cutting inserts, the R2S-B1 had the lowest F_{max}. TCN1L-B1 had the lowest F_{max} and R2L-B1 had the highest F_{max} among the LPS manufactured cutting inserts. The R2S-B1 had the lowest Fmax of the PECS manufactured cutting inserts. When the F_{max} of the base WC-Co grade (T1ML-B1) and the NbC-Ni grade (N2S-B1) were compared, the F_{max} of the N2S-B1 was slightly higher than that of the T1ML-B1. Except for

TCN1 cutting inserts, LPS manufactured NbC-Ni-based cutting inserts had higher F_{max} values than PECS counterparts. When considering the average resultant force (F), it can be seen from Figure 5.1, that it follows the general trend of the F_{max}. The figure indicates that R2S-B1 had the lowest F (609 N) compared to all the other inserts irrespective of composition and sintering technique. This was followed by T1ML-B1 and N2S-B1which experienced average resultant forces of 669 N and 777 N, respectively (see Table 5.1). Among the other cutting inserts, the TCN1S-B1 exhibited a comparable average resultant force (i.e. 793 N) to the N2S-B1. As shown in Figure 5.1 and Table 5.1, N2ML-B1 and TCN1L-B1 experienced similar average resultant forces. The N2MS-B1 had the highest average resultant force compared to all the other inserts irrespective of composition and sintering technique. It should be noted that the R2MS-B1 cutting insert does not have any test 1 results (as shown in Table 5.1 and Figure 5.1). This was due to a damaged (fractured) cutting edge that was unsuitable for machining tests.

Table 5.1 Machining forces, specific energy consumption, and average machining temperature results of B1 cutting inserts during semi-finishing at n = 800 rpm and a_p = 1.0 mm

Insert name	Average resultant force, F (N)	Maximum resultant force, F_{max} (N)	Specific cutting energy, U_c (J/mm^3)	Average temperature, T (^{o}C)
T1ML-B1	669	1569	20.90	92.51 ± 0.88
N2S-B1	777	1615	24.28	104.16 ± 1.06
N2ML-B1	833	1674	26.05	111.28 ± 1.08
N2MS-B1	1358	1394	42.44	124.79 ± 1.22
R2L-B1	1047	1751	32.71	101.61 ± 0.86
R2S-B1	609	1069	19.02	108.07 ± 0.83
R2MS-B1	Damaged	Damaged	Damaged	Damaged
TCN1L-B1	838	1104	26.17	121.38 ± 0.99
TCN1S-B1	793	1302	24.80	112.56 ± 0.89

*NB: The average and maximum resultant force have a fixed error of ±15 N from the Kistler.

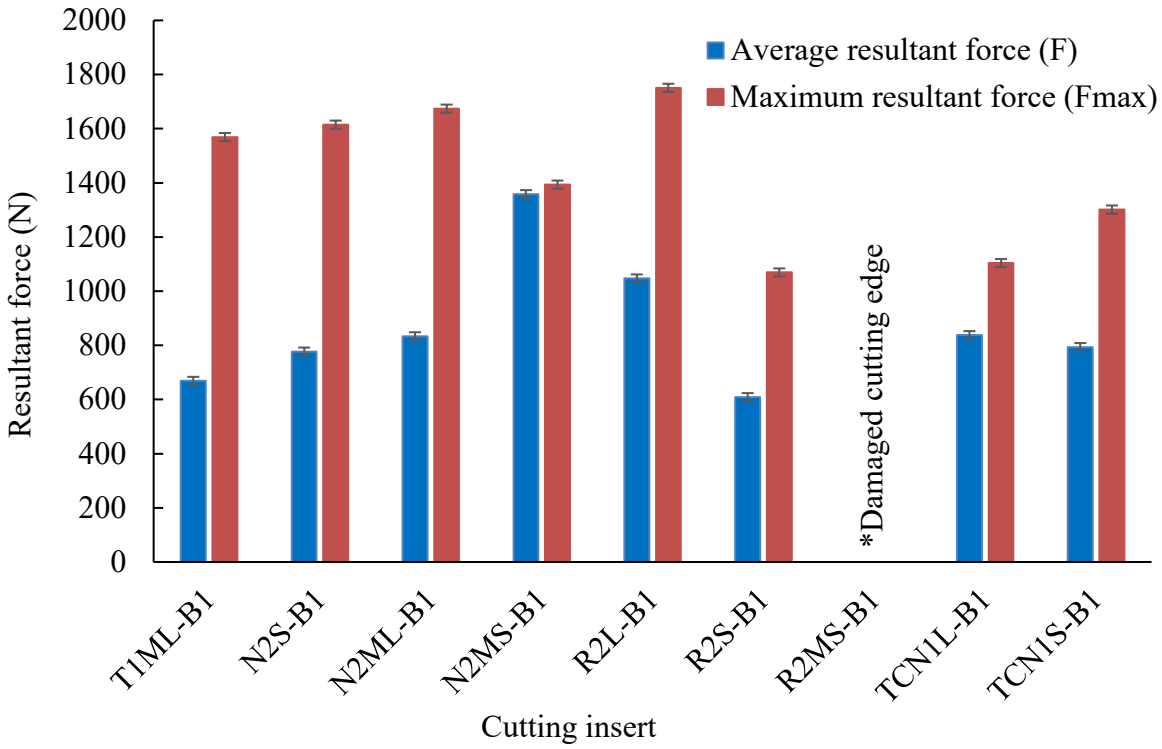


Figure 5-1. Average resultant force (F) and maximum resultant force (F_{max}) for B1 cutting inserts during semi-finishing at n = 800 rpm and a_p = 1.0 mm

The variation of specific cutting energy, U_c with F for B1 cutting inserts is shown in Figure 5.2. The graph shows a linear relationship between the two parameters. From the graph, it can be deduced that the energy required to remove a unit volume of material during machining (i.e. specific cutting energy) is directly proportional to the cutting force. The "cutting energy" is the work done by the cutting forces over a given distance and it represents the energy consumption during machining. As shown in Figure 5.2, the R2S-B1 exhibited the lowest U_c followed by the T1ML-B1 (i.e., ~19 J/mm^3 and ~20 J/mm^3, respectively). This means that the two cutting inserts had lower energy consumption than the rest of B1 cutting inserts. The N2MS-B1 (~44 J/mm^3) had the highest energy consumption compared to the rest of the cutting inserts irrespective of composition and sintering technique. There was no difference in energy consumption between N2ML-B1 and TCN1L-B1 (see Figure 5.2). With the exception of the N2MS-B1, the NbC-Ni based PECS produced cutting inserts had a slightly better energy consumption compared to their LPS counterparts.

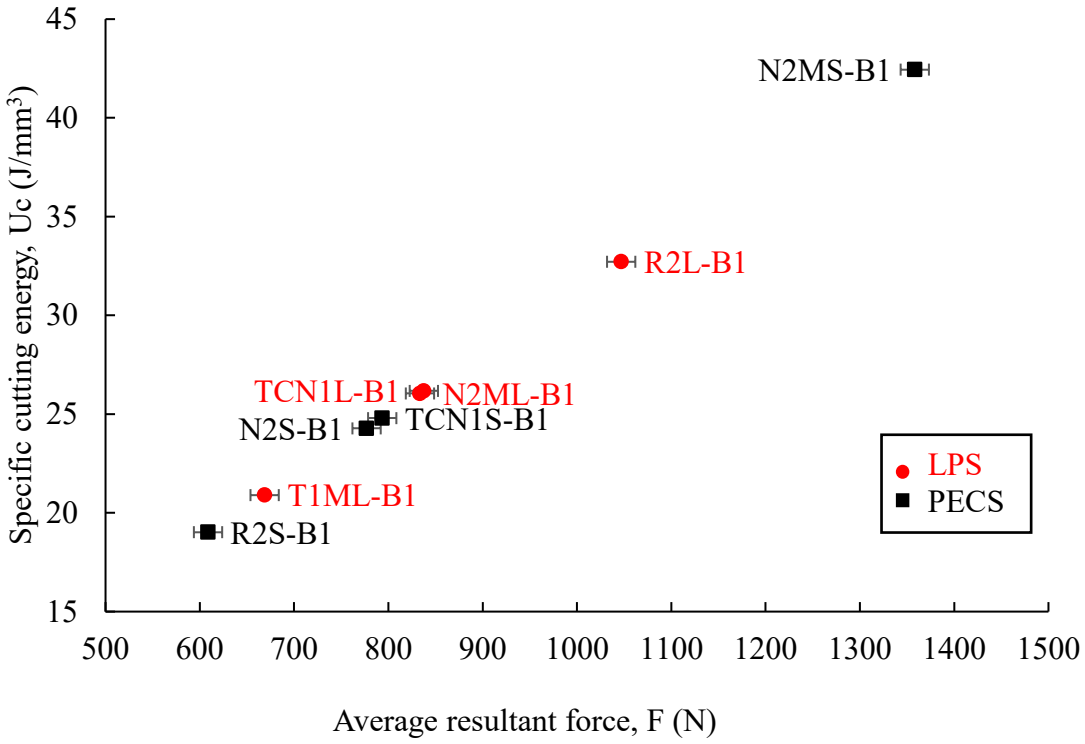


Figure 5-2. Variation of the specific cutting energy (U_c) with the average resultant force (F) for B1 cutting inserts during semi-finishing at n = 800 rpm and a_p = 1.0 mm

Figure 5.3 shows the variations of average machining temperature (T) with the average resultant force for the blank cutting inserts during semi-finishing. From the figure, it can be seen that the T1ML-B1 cutting insert experienced the lowest T (92.51 ± 0.88 °C) compared to the rest of the cutting inserts irrespective of the composition and sintering technique. The average machining temperatures of all the NbC-based B1 cutting inserts were above 100 °C, with the LPS produced R2L-B1 having the lowest T and the PECS produced N2MS-B1 having the highest for this group. Except for the TCN1L-B1 cutting inserts, the LPS produced N2ML-B1 and R2L-B1 had lower average machining temperatures compared to their PECS produced counterparts.

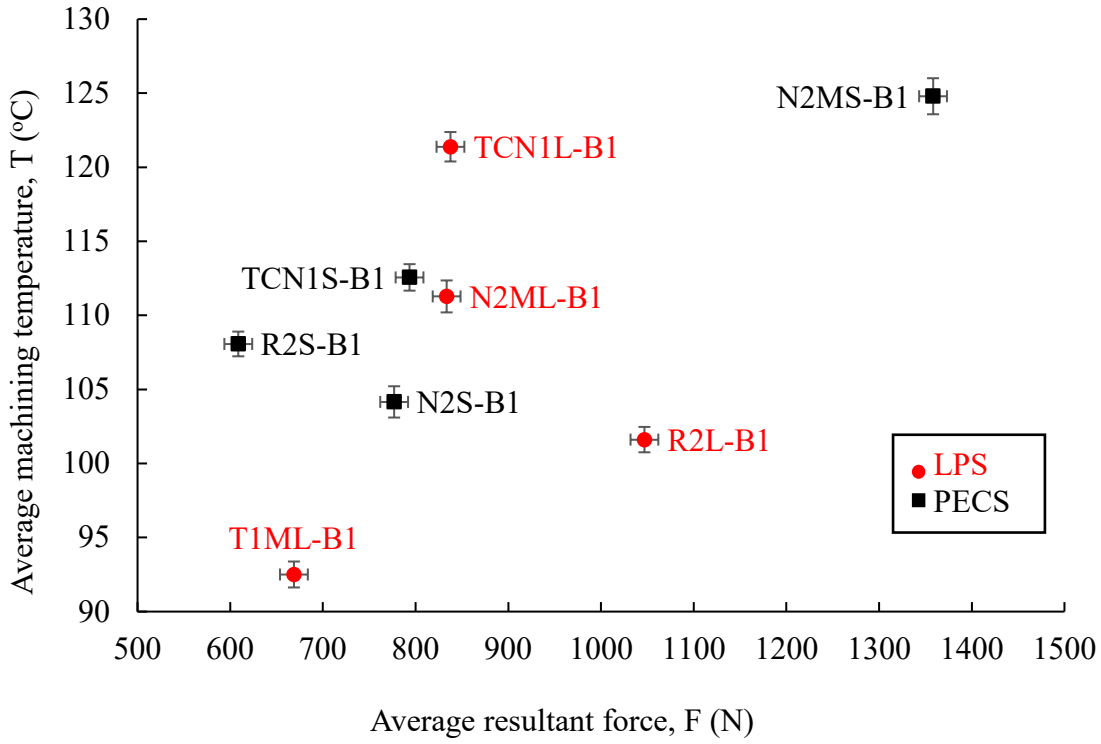


Figure 5-3. Variation of the average machining temperature (T) with the average resultant force (F) for B1 cutting inserts during semi-finishing at n = 800 rpm and a_p = 1.0 mm

5.1.2. Analyses of insert tool life and wear performance of blank (B1) cutting inserts

Table 5.2 shows the cutting insert tool life "cutting time" (I_l) and wear performance results of B1 cutting inserts. Figure 5.4 depicts the variation of the maximum flank wear (VB_{max}) with I_l for blank cutting edges during semi-finishing. From the figure, it can be seen that the VB_{max} for all the cutting inserts irrespective of the sintering technique and composition was below 80 µm which is ~7 times less than the allowable semi-finishing failure criterion of (600 µm). The figure shows that the T1ML-B1, N2S-B1, and TCN1L-B1 were the best performers in terms of I_l, as they all reached the maximum machining time of 20 minutes. In comparison to the other top performers, the T1ML-B1 had the lowest VB_{max}, i.e. 39.45 µm after 20 minutes, followed by the N2S-B1 with a VB_{max} of 53.34 µm. The TCN1L-B1 had a higher VB_{max} (76.11 µm) than both T1ML-B1 and N2S-B1 (see Table 5.2 and Figure 5.4). The N2ML-B1 and the R2L-B1 both failed after 11 minutes with the former achieving a V_{Bmax} of 34.45 µm, and the latter achieving a VB_{max} of 60 µm, respectively. The R2S-B1 had insert life and VB_{max} of 8 minutes and 24.42 µm. After 6 minutes of machining, the TCN1S-B1 had a VB_{max} of 37.39 µm, whereas the N2MS-B1 failed after 2 minutes and had a VB_{max} of 42.07 µm (see Table 5.2). The effect of sintering was clearly indicated on the cutting inserts as, with the exception of N2S-B1, the LPS manufactured cutting inserts generally had higher insert tool life than PECS cutting inserts (see Figure 5.4). In terms of composition, the WC-Co based LPS produced T1ML-B1 outperformed all the

NbC-Ni based cutting inserts. However, when considering only the NbC-Ni based cutting inserts, the PECS produced N2S-B1 had a better insert life performance.

Table 5.2 Cutting insert tool life, maximum flank wear, and flank wear rate results of B1 cutting inserts during semi-finishing at n = 800 rpm and a_p = 1.0 mm

Insert name	Insert tool life, I_l (min)	Maximum flank wear, VB_{max} (µm)	Flank wear rate, FWR (µm/min)
T1ML-B1	20	39.45	1.97
N2S-B1	20	53.34	2.67
N2ML-B1	11	34.45	3.13
N2MS-B1	2	42.07	21.04
R2L-B1	11	60	5.45
R2S-B1	8	24.45	3.06
R2MS-B1	Damaged	Damaged	Damaged
TCN1L-B1	20	76.11	3.81
TCN1S-B1	6	37.39	6.23

Figure 5.5 depicts the relationship between the flank wear rate (FWR) and F for the blank cutting inserts during semi-finishing. In general, the forces experienced by the cutting inserts increase with increased insert flank wear. This relationship, however, was not apparent for the blank cutting inserts used during semi-finishing, as shown in Figure 5.5. For instance, T1ML-B1 and N2S-B1 obtained FWRs of 1.97 and 2.67 m/min, respectively, which were lower than R2S-B1, despite the fact that the two cutting inserts experienced slightly higher forces than R2S-B1 (see Table 5.2 and Figure 5.5). A similar observation could be drawn between the N2ML-B1 and the TCN1S-B1 cutting inserts. It is worth mentioning, however, that the FWR is a factor that is dependent on the cutting insert tool life. Thus, in some cases, the FWR will be higher if the cutting insert has poor insert tool life performance. The flank wear rates (FWRs) of the B1 cutting inserts, with the exception of N2MS-B1, were all less than 7 µm/min, as shown in Figure 5.5.

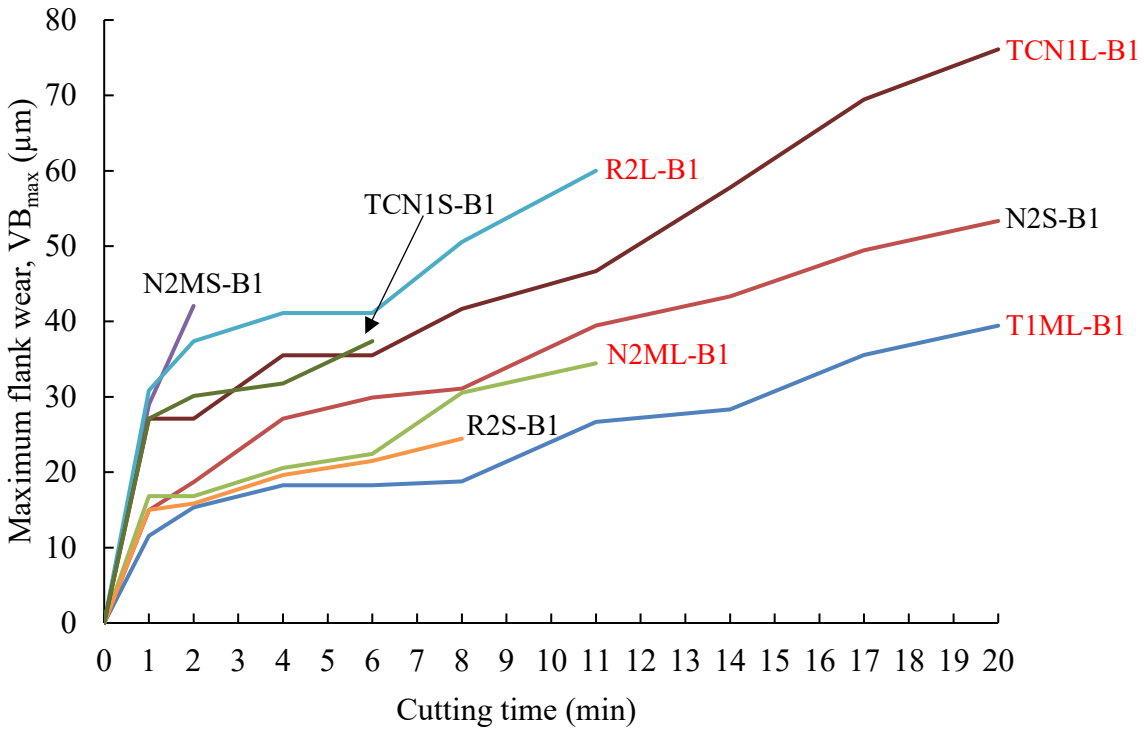


Figure 5-4. Variation of the maximum flank wear (VB_{max}) with cutting time (l_l) for blank (B1) cutting inserts during semi-finishing at n = 800 rpm and a_p = 1.0 mm

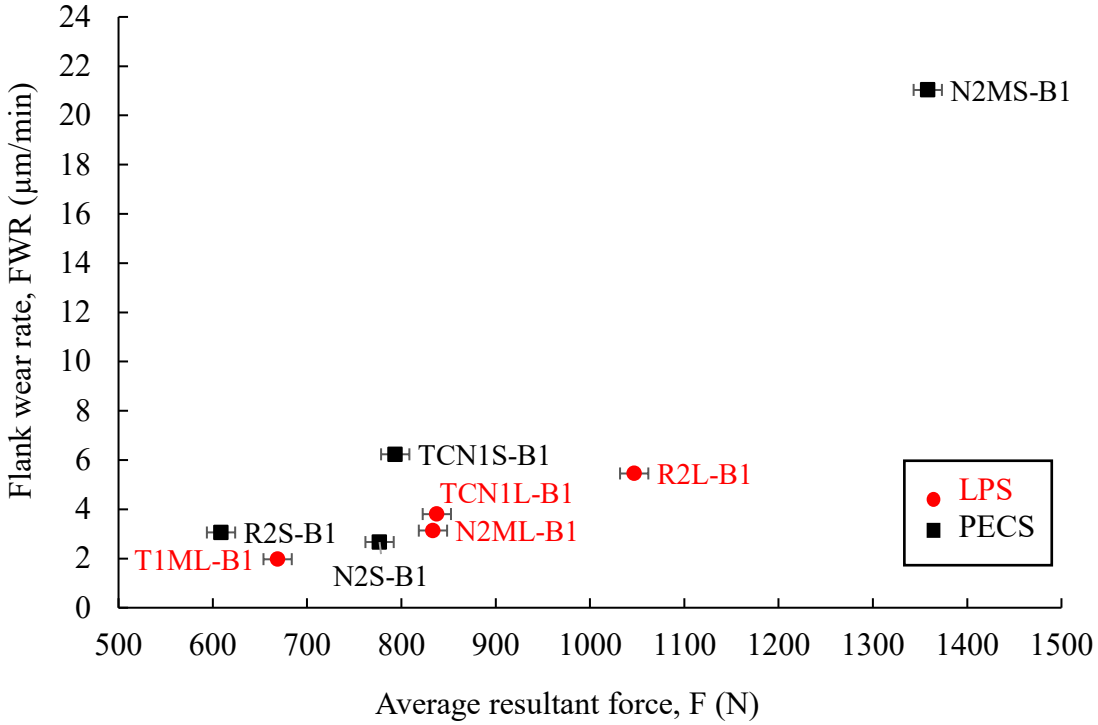


Figure 5-5. Variation of the flank wear rate (FWR) with the average resultant force (F) for blank (B1) cutting inserts during semi-finishing at n = 800 rpm and a_p = 1.0 mm

Apart from the R2-based cutting inserts, the LPS-produced cutting inserts had a better combination of F and FWR than their PECS counterparts. Although the R2L-B1 had higher F and FWR than the R2S-B1, the cutting insert had better insert life performance. When considering the effect of composition on the PECS manufactured NbC-Ni based cutting inserts, the N2S-B1 had the lowest FWR, followed by the R2S-B1. The TCN1S-B1 had a FWR 6.23 μm/min, while the N2MS-B1 had the highest FWR of all the blank edged cutting inserts used during semi-finishing at 21.04 μm/min.

5.1.3. Analyses of micrographs of the flank and rake faces of the blank (B1) cutting inserts

This subsection provides micrograph analyses of blank (B1) cutting inserts. The optical micrographs in Figure 5.6 show the flank and rake faces of (a) T1ML-B1, (b) N2S-B1 and (c) TCN1L-B1 cutting inserts. From the figure, it can be seen that the flank faces of the cutting inserts' edges have abrasion grooves running parallel to the direction the insert slides against the surface of the workpiece. Figure 5.6 also shows that the T1ML-B1 had the smallest wear land and fewer grooves compared to N2S-B1 and TCN1L-B1 cutting inserts. Some cracks were also observed on the rake face of the T1ML-B1 cutting insert. Figure 5.7 depicts the HAADF-STEM map of a cross section of the T1ML-B1 insert cutting edge/workpiece interface. The map revealed fracturing of WC grains close to the cutting edge, pull-out of the carbide grains and cracks on the interface of TiC and WC grains close to the cutting edge.

There was evidence of BUE on the flank face of the N2S-B1 cutting insert as depicted in Figure 5.6 (b). In addition to cracks on the rake face of the N2S-B1, chipping of the cutting edge was also observed. The appearance of cracks was more pronounced on the N2S-B1 cutting insert compared to T1ML-B1. Figure 5.6 (c) shows that the cutting edge of the TCN1L-B1 experienced mechanical fracture whereby the edge was shattered during the cutting operation. Cracks were observed on the rake face of the TCN1L-B1. Although there was the presence of wear on the cutting edges of T1ML-B1 and N2S-B1 cutting inserts, it was minimal, and the inserts could still continue with machining as per the (ISO) 3685:1993 tool life criteria. The optical micrographs of the rest of the B1 cutting inserts were also analysed. The flank wear land of the N2ML-B1 cutting insert exhibited abrasion grooves and some chipping. The flank face of the N2MS-B1 cutting insert on the other hand showed that the cutting edge shattered and had experienced multiple chipping. Cracks were also observed on the rake face of the N2ML-B1 cutting insert, whereas chipping was observed on the rake face of the N2MS-B1 cutting insert respectively. Based on observation of the optical micrographs of N2ML-B1 and N2MS-B1, the wear on the PECS produced N2MS-B1 was greater than that of its LPS produced counterpart.

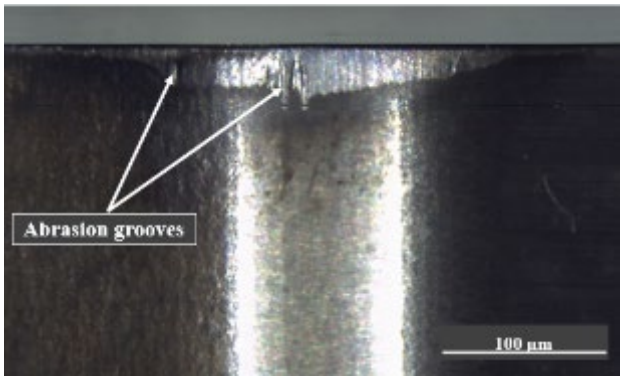
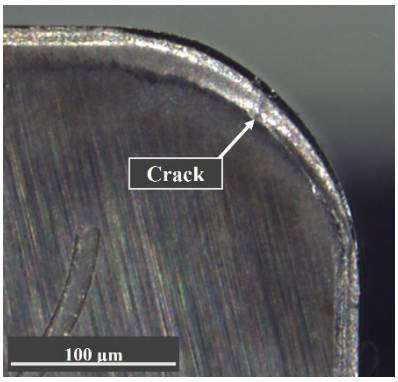
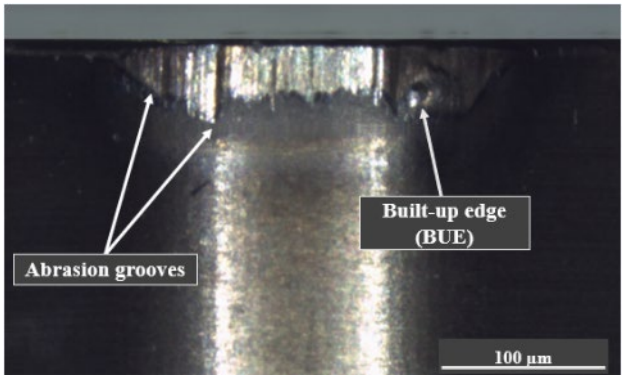
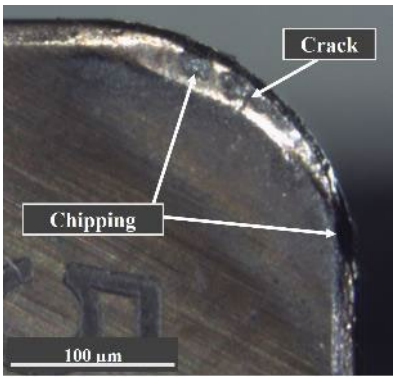
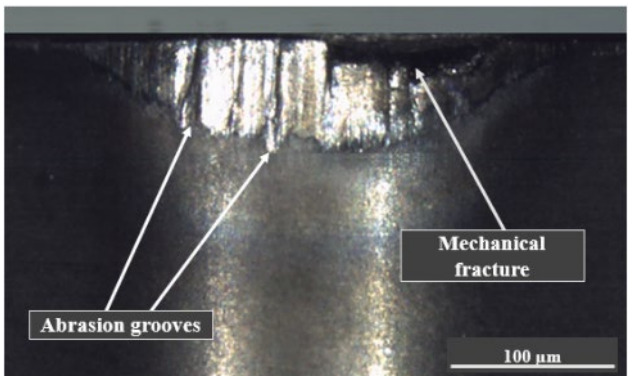
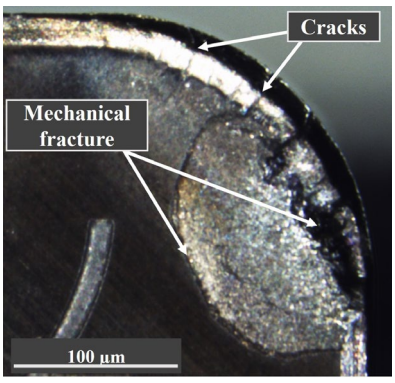
Insert	Flank face	Rake face
(a) T1ML-B1		
	VB_{max} = 39.45 µm Cutting time = 20 minutes	
(b) N2S-B1		
	VB_{max} = 53.34 µm Cutting time = 20 minutes	
(c) TCN1L-B1		
	VB_{max} = 76.11 µm Cutting time = 20 minutes	

Figure 5-6. Optical micrographs of the flank and rake faces of (a) T1ML-B1, (b) N2S-B1 and (c) TCN1L-B1 cutting edges during semi-finishing machining

The optical micrographs of flank and rake faces of R2L-B1, R2S-B1, TCN1L-B1 and TCN1S-B1 cutting inserts revealed that their cutting edges experienced mechanical fracture and shattered. The composition effects on the analyses of the NbC-Ni based PECS produced cutting inserts were observed

by comparing the N2S-B1, N2MS-B1, R2S-B1, and TCN1S-B1. The optical micrographs of these cutting inserts revealed that the additions of Mo, TiC and TiC_7N_3 to the NbC-Ni reduced the cutting inserts' resistance to mechanical shock, respectively. For example, with the exception of the N2S-B1, the edges of these cutting inserts experienced mechanical fracture. When comparing the NbC-Ni based LPS produced cutting inserts, the N2ML-B1 had a lower wear land than the R2L-B1 and TCN1L-B1 respectively. It was also observed that the failure mechanisms of the TCN1L-B1 and R2L-B1 cutting inserts were very similar.

In general, optical micrographs show that the main failure mechanisms of the B1 cutting inserts were abrasive wear, mechanical fracture, and chipping. Irrespective of the composition, the LPS manufactured cutting inserts showed pronounced abrasion grooves as a result of abrasive wear than PECS produced cutting inserts. The LPS cutting inserts also had more wear land (indicating gradual wear) than the PECS manufactured cutting inserts, which had thin wear land and fractured cutting edges.

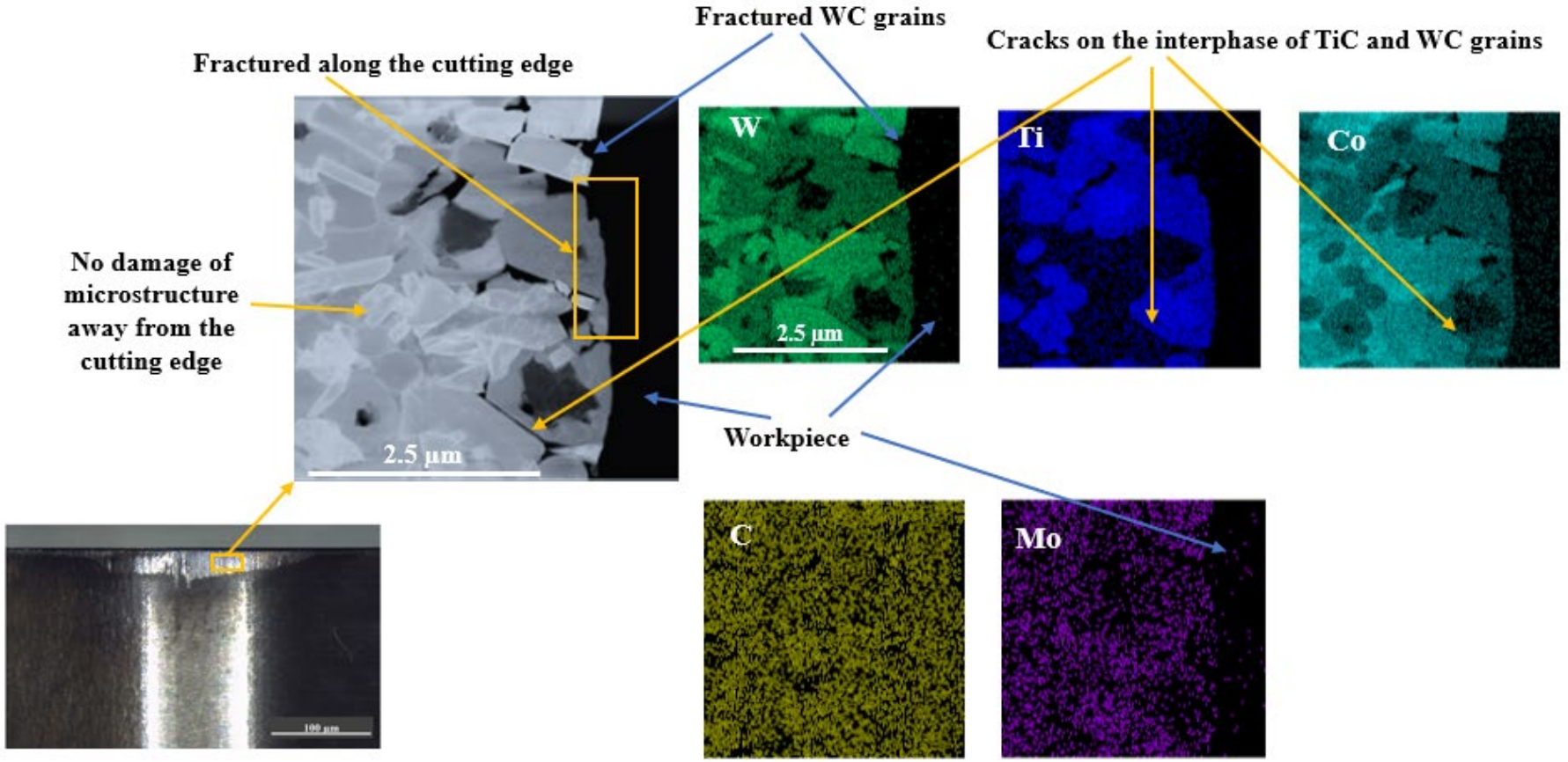


Figure 5-7. HAADF-STEM map of a cross-section of T1ML-B1 insert cutting edge/workpiece interface showing: WC (green), Co (cyan), Ti (blue), Mo (purple) and C (yellow)

5.1.4. Machining performance evaluation and analyses of B1 cutting inserts

Figure 5.8 shows the variation of U_c with I_l , which are criterion 1 and 2 used for TOPSIS MCDM problem, respectively. From the figure, it can be seen that the T1ML-B1 cutting insert had the best combination of the two criteria (i.e. longer insert tool life and lowest specific cutting energy). The N2MS-B1 cutting insert, on the other hand, had the poorest combination of the criteria, respectively. Although the R2S-B1 had the lowest U_c compared to the rest of the B1 cutting inserts, the cutting insert failed after 8 minutes of machining. Hence, it could not be considered among the best cutting inserts. In general, the LPS produced cutting inserts had better combinations of U_c and I_l compared to their PECS produced counterparts. It was also observed from the figure that the additions of Mo, TiC and TiC_7N_3 resulted in poor combinations of the U_c and I_l. For example, the N2S-B1 cutting insert had better combinations of the specific cutting energy and cutting time than the N2MS-B1, R2S-B1 and TCN1S-B1, respectively. Figure 5.9 shows the overall preference score (O_i) and ranking of B1 cutting inserts used during semi-finishing. In the figure, the best performing cutting inserts are coded green, average performing inserts are amber, and the poor performing cutting inserts are coded red. From Figure 5.9, it can be seen that the top three best ranked blank cutting inserts during semi-finishing were T1ML-B1, N2S-B1, and TCN1L-B1. The N2ML-B1, R2L-B1, and R2S-B1 cutting inserts had an average performance, whereas the poorest performing cutting inserts were the N2MS-B1 and TCN1S-B1 respectively.

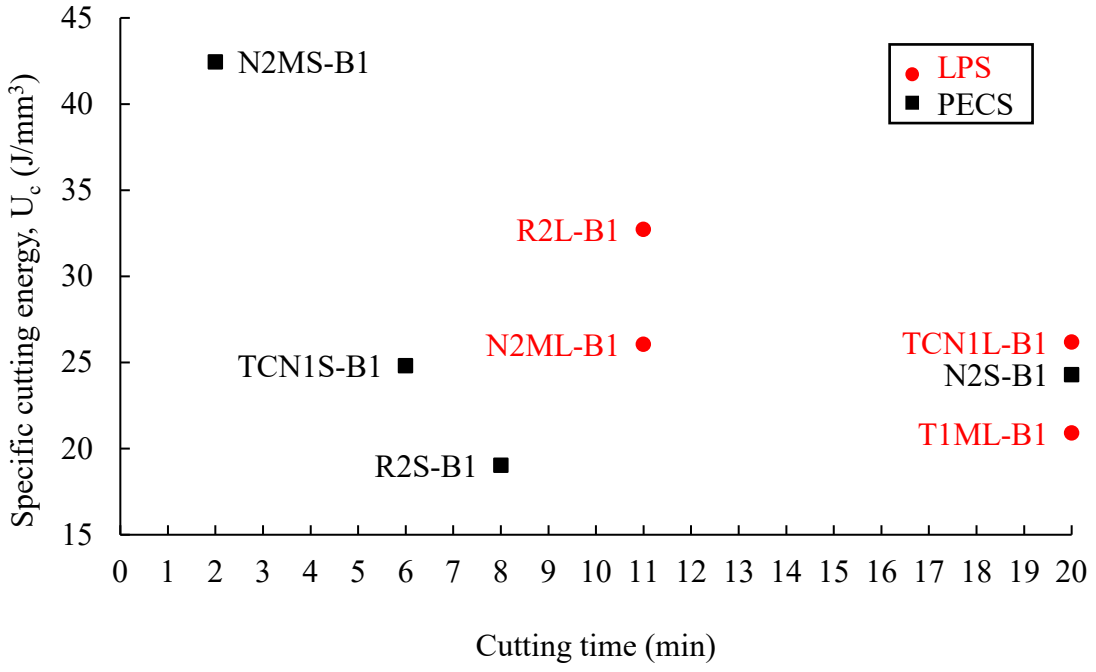


Figure 5-8. Variation of specific cutting energy (U_c) with cutting time (I_l) for blank (B1) cutting inserts during semi-finishing at n = 800 rpm and a_p = 1.0 mm

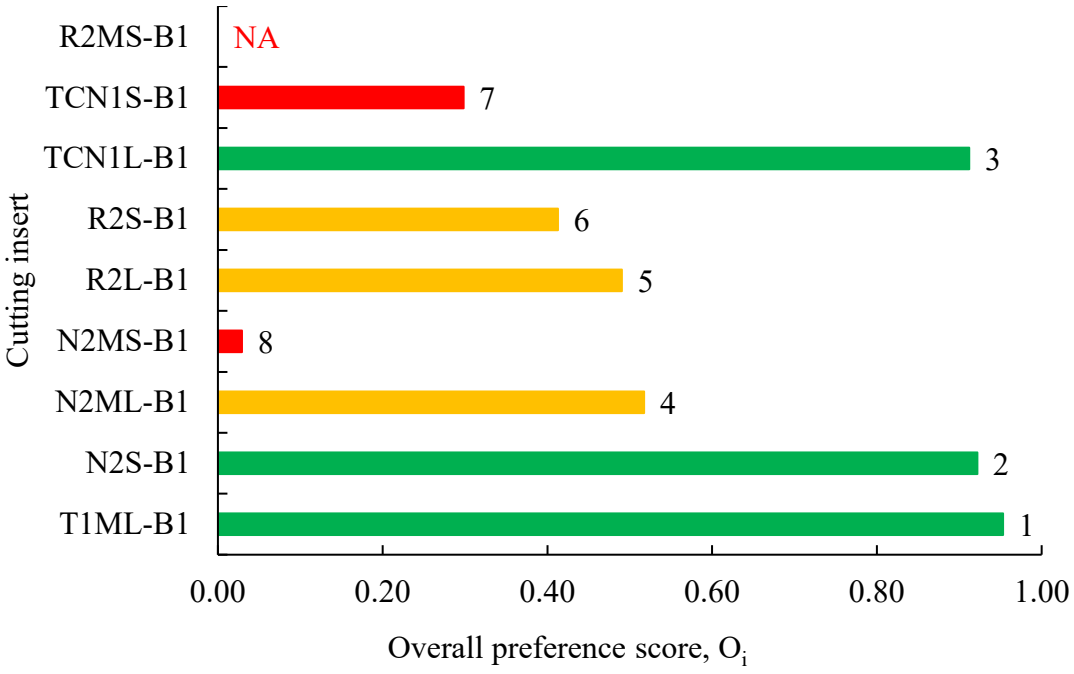


Figure 5-9. Overall preference score (O_i) and rank of B1 cutting inserts (alternatives)

5.2. Analyses of the shark skin LSM (S1) cutting inserts

This subsection presents and analyses resultant cutting forces, specific cutting energy, insert life, wear and temperature of the shark skin LSM cutting inserts during the face milling of a-GCI under semi-finishing conditions. The micrographs of cutting inserts showing the flank and rake faces are also presented in this section. Lastly, the performance evaluation of the shark skin LSM cutting inserts is done to rank the cutting inserts.

5.2.1. Analyses of the resultant forces, specific cutting energy, and temperature of S1 cutting inserts.

Table 5.3 shows the resultant forces, specific energy consumption, and the temperature of the shark skin LSM cutting edges during semi-finishing machining. Figure 5.10 shows the average resultant forces and the maximum resultant forces experienced by the shark skin LSM cutting edges during semi-finishing. According to the figure, F_{max} values were significantly higher than F values. The cutting inserts experienced maximum resultant forces of >1100 N, irrespective of the composition.

Table 5.3. Machining forces, specific cutting energy, and temperature results of shark skin LSM cutting inserts during semi-finishing at n = 800 rpm and a_p = 1.0 mm

Insert name	Average resultant force, F (N)	Maximum resultant force, F_{max} (N)	Specific cutting energy, U_c (J/mm^3)	Average Temperature, T (^{o}C)
T1ML-S1	756	1194	23.62	113.79 ± 0.91
N2S-S1	788	1200	24.62	93.71 ± 0.90
N2ML-S1	793	1233	24.79	139.30 ± 1.35
N2MS-S1	853	1245	26.65	165.20 ± 1.61
R2L-S1	1080	1437	33.75	139.02 ± 1.36
R2S-S1	854	1243	26.68	139.29 ± 1.35
R2MS-S1	881	1259	27.53	144.10 ± 1.41
TCN1L-S1	1141	1462	35.67	141.18 ± 1.38
TCN1S-S1	918	1306	28.69	136.14 ± 1.32

*NB: The average and maximum resultant force have a fixed error of ±15 N from the Kistler.

Figure 5.10 also shows that the T1ML-S1 had the lowest F_{max}, followed by the N2S-S1. The figure indicates that, with the exception of the TCN1S-S1, R2L-S1, and TCN1L-S1, there was no significant difference in the F_{max} values of all the other S1 cutting inserts. The TCN1L-S1 had the highest F_{max} (1462 N), followed by the R2L-S1 (1437 N), and the TCN1S-S1 (1306 N), see Table 5.3 and Figure 5.10, respectively. Similarly, the average resultant force, F appears to follow the trend exhibited by the F_{max} as shown in Figure 5.10. The T1ML-S1 cutting insert had the lowest F (756 N) compared to all the other cutting inserts irrespective of the composition. This was followed by the N2S-S1 and the N2ML-S1 with F values of 788 N and 793 N, respectively. The TCN1L-S1 experienced the highest average resultant cutting forces compared to all the other S1 cutting inserts. The effects of sintering on the cutting forces could be seen on the N2M, R2 and TCN1 cutting inserts. As depicted in Figure 5.10, the LPS manufactured cutting inserts of both the R2 and the TCN1 experienced higher cutting forces than their PECS manufactured counterparts. The N2M on the other hand exhibited a contrasting behaviour as the cutting forces of the N2MS-S1 were slightly higher than those of the N2ML-S1 (see Table 5.3 and Figure 5.10).

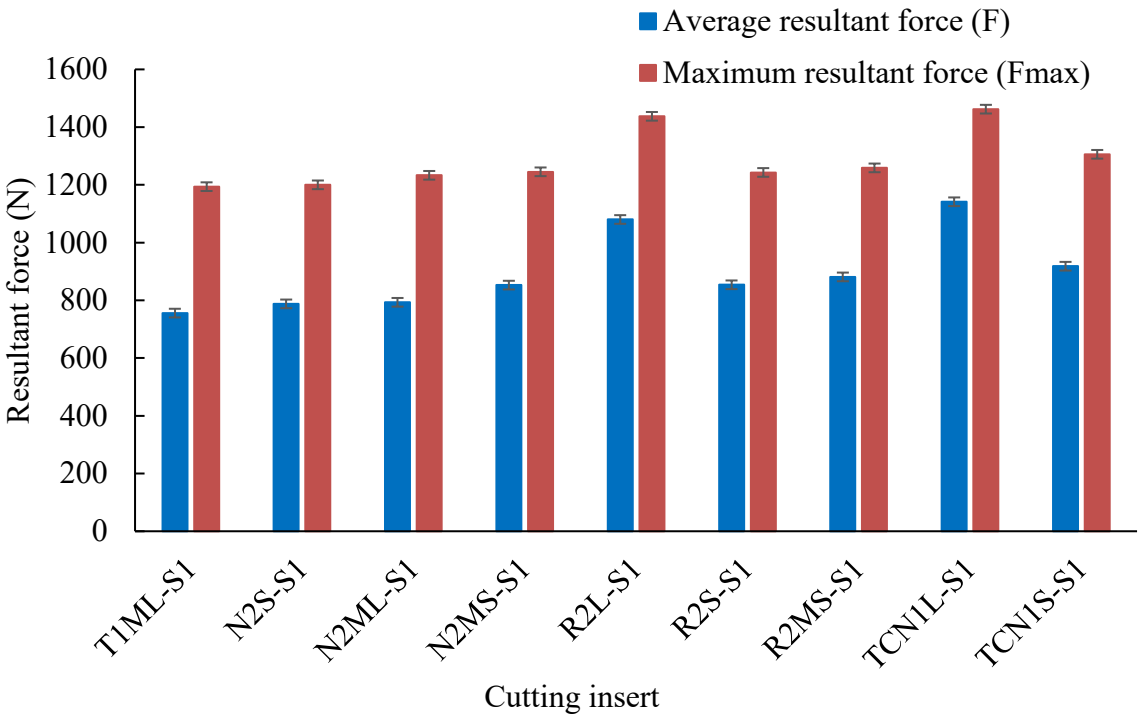


Figure 5-10. Average resultant force (F) and maximum resultant force (F_{max}) for S1 cutting inserts during semi-finishing at n = 800 rpm and a_p = 1.0 mm

Similar to B1 cutting inserts, the relationship between the specific cutting energy and average resultant cutting force of S1 cutting inserts exhibited a linear trend as shown in Figure 5.11. The T1ML-S1 had the lowest specific cutting energy (~23 J/mm^3) per the volume of material removed during machining. As a result, the cutting insert had the lowest energy consumption compared to all the S1 cutting inserts. From the figure, it can be seen that the TCN1L-S1 cutting insert had the highest energy consumption. With the exception of the N2M cutting inserts, the PECS produced NbC-Ni based cutting inserts had better energy consumption compared to their LPS counterparts. The additions of Mo, TiC and TiC_7N_3 to the base NbC-12Ni (wt%) increased the energy consumption of the cutting inserts in all PECS produced cutting inserts. The additions of Mo and TiC had very similar effects (i.e. specific cutting energies of R2S-S1 and N2MS-S1 were both ~26.7 J/mm^3). The simultaneous addition of the two constituents further increased the specific cutting energy resulting in ~27.5 J/mm^3 in R2MS-S1. The addition of TiC_7N_3 had the highest increase in energy consumption, yielding a specific energy consumption of ~28.7 J/mm^3 in TiC_7N_3 as shown in Figure 5.11.

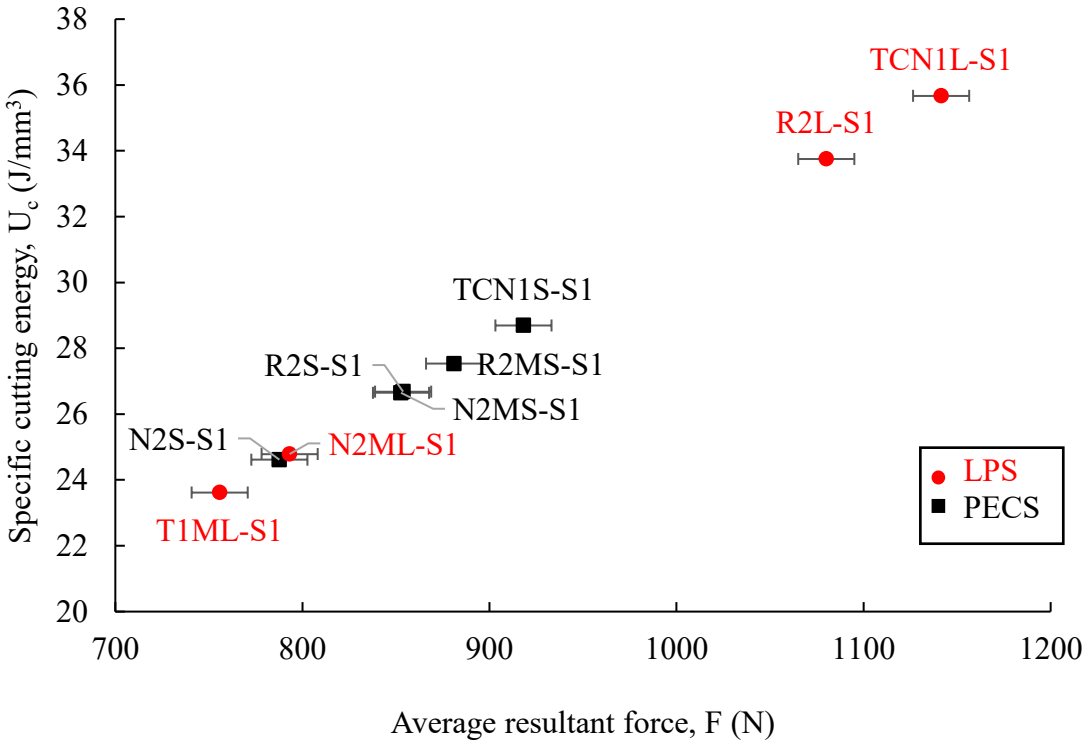


Figure 5-11. Variation of the specific cutting energy (U_c) with the average resultant force (F) for S1 cutting inserts during semi-finishing at n = 800 rpm and a_p = 1.0 mm

Figure 5.12 shows the variations of average machining temperature with the average resultant force for the shark skin LSM cutting inserts during semi-finishing. The N2S-S1 cutting insert had the lowest average machining temperature (93.71 ± 0.90 °C), followed by the T1ML-S1 cutting insert though the former experienced slightly higher average resultant cutting forces than the latter as shown in the figure. From the figure, it was observed that the N2ML-S1, R2S-S1, R2MS-S1 TCN1S-S1, R2L-S1, and TCN1L-S1 cutting inserts had relatively similar T values. As shown in the figure, the average machining temperatures among these cutting inserts were between 134 and 145 °C, despite the inserts having significant variations in the average resultant forces. The N2MS-S1 cutting insert exhibited the highest machining temperature compared to all the inserts irrespective of the sintering technique or composition. When considering the effects of sintering, there was no difference in the average machining temperatures for the R2 and TCN1 cutting inserts as already mentioned. For the N2M cutting inserts, the LPS produced N2ML-S1 cutting insert had lower machining temperature compared to the PECS counterpart. The effects of composition could clearly be seen when considering the NbC-Ni based PECS produced cutting inserts. As shown in Figure 5.12, all composition modifications resulted in higher average machining temperatures.

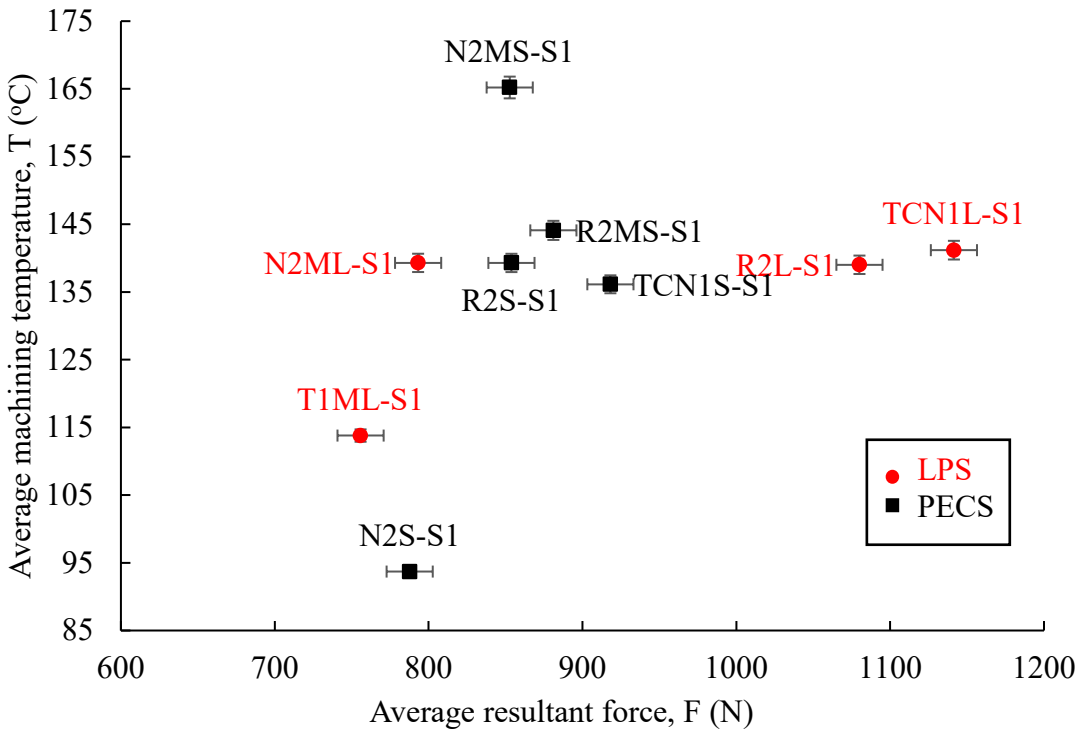


Figure 5-12. Variation of the average machining temperature, (T) with the average resultant force, (F) for S1 cutting inserts during semi-finishing

5.2.2. Analyses of insert tool life and wear performance of S1 cutting inserts.

Table 5.4 shows the cutting insert life and wear performance results of S1 cutting inserts. Figure 5.13 depicts the variation of the maximum flank wear with the cutting time for shark skin LSM cutting edges during semi-finishing. Figure 5.13 shows that the VB_{max} of all the shark skin LSM cutting inserts irrespective of the sintering technique and composition was less than 90 µm. The majority of the S1 cutting inserts, including the T1ML-S1, N2S-S1, N2ML-S1, R2S-S1, TCN1S-S1 and R2MS-S1, achieved the maximum insert life performance of 20 minutes, as it can be seen in Figure 5.13. The R2MS-S1's cutting edge had the lowest VB_{max} (26.67 µm). This performance was followed by that of the R2S-S1 and the TCN1S-S1 cutting inserts whose cutting edges had VB_{max} of 46.67 µm after 20 minutes, respectively. The cutting edges of the T1ML-S1 and the N2S-S1 had VB_{max} of 50.00 µm and 56 µm, respectively. Comparing all the cutting inserts that completed 20 minutes of cutting time, the cutting edge of the N2ML-S1 insert had the highest VB_{max} (63.89 µm). Among the other shark skin LSM cutting inserts for semi-finishing, the TCN1L-S1 achieved 14 minutes cutting time and 87.75 µm VB_{max}, followed by N2MS-S1 with 8 minutes cutting time and 47.78 µm VB_{max}, and lastly the R2L-S1 with 6 minutes cutting time and 67.78 µm VB_{max}, respectively.

Table 5.4. Cutting insert tool life, maximum flank wear, and flank wear rate results of S1 cutting inserts during semi-finishing at n = 800 rpm and a_p = 1.0 mm

Insert name	Insert tool life, I_l (min)	Maximum flank wear, VB_{max} (μm)	Flank wear rate, FWR (μm/min)
T1ML-S1	20	50	2.50
N2S-S1	20	56.11	2.81
N2ML-S1	20	63.89	3.19
N2MS-S1	8	47.78	5.97
R2L-S1	6	67.78	11.30
R2S-S1	20	46.67	2.33
R2MS-S1	20	26.67	1.33
TCN1L-S1	14	87.75	6.27
TCN1S-S1	20	46.67	2.33

The effects of shark skin LSM on the cutting insert life performance are depicted in Figure 5.14. The figure shows the percentage improvement or reduction of insert tool life of the shark skin LSM (S1) cutting inserts compared to the blank unmodified (B1) cutting inserts. From the figure, it can be seen that in general, the shark skin LSM increased the cutting duration of the inserts (insert tool life). The T1ML, N2S and R2MS had 0% improvement. Both the T1ML-B1 and N2S-B1 cutting inserts had an insert life of 20 minutes which was the same as the S1 cutting inserts, and the R2MS-S1 had no blank counterpart. Figure 5.14 shows that N2MS-S1 cutting insert had the highest insert life improvement. The N2MS-S1 cutting insert's life performance was improved by 300%. This was followed by TCN1S-S1, R2S-S1 and N2ML-S1 cutting inserts which had insert life improvements of 233%, 150% and 82%, respectively. Figure 5.14, also shows that the shark skin LSM resulted in the insert life reductions of R2L-S1 and TCN1L-S1 by 45% and 30% respectively.

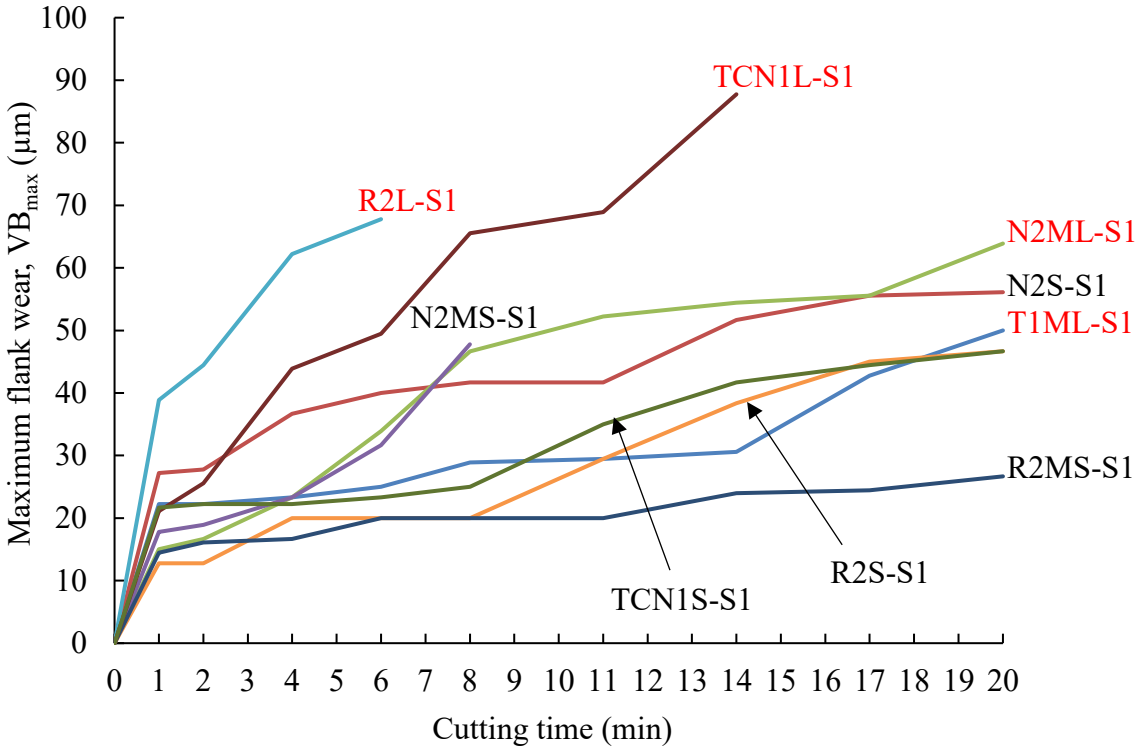


Figure 5-13. Variation of the maximum flank wear, (VB_{max}) with cutting time, (l_l) for shark skin LSM (S1) cutting inserts during semi-finishing at n = 800 rpm and a_p = 1.0 mm

Figure 5.15 shows the variation of the flank wear rate with the average resultant force for shark skin LSM (S1) cutting inserts. The expected trend of the relationship between the FWR and F, i.e. FWR should increase with increasing F, was not easily deductible from the S1 cutting inserts during semi-finishing. For instance, the T1ML-S1 had lower F compared to R2MS-S1 and yet the FWR of the latter was still lower than that of the former. The same observation could be seen for the TCN1S-S1 against N2S-S1 and N2MS-S1 cutting inserts (see Figure 5.15). The FWR of all the S1 cutting inserts were below 11.50 µm/min, with the R2L-S1 having the highest FWR (11.30 µm/min) compared to all the other cutting inserts irrespective of the composition or sintering technique. The R2MS-S1 cutting insert on the other hand had the lowest FWR (1.33 µm/min) compared to all the other cutting inserts (see Figure 5.15 and Table 5.4). The LPS manufactured R2L-S1 and TCNL-S1 cutting inserts exhibited higher FWR in comparison to their PECS manufactured R2S-S1 and TCN1S-S1 counterparts. The opposite observation was made for the N2M cutting inserts whereby the N2MS-S1 had a higher FWR compared to the N2ML-S1 cutting insert. When considering the PECS produced NbC-Ni based cutting inserts, all the inserts with the exception of N2MS-S1 had slightly lower FWRs compared to the base N2S-S1.

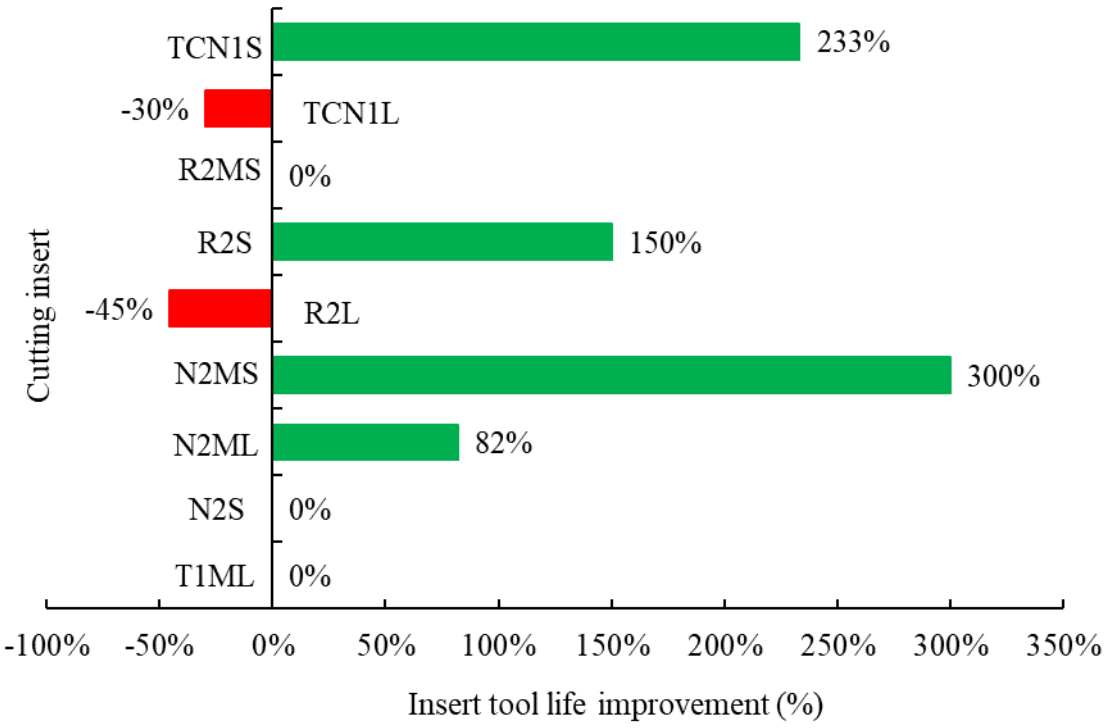


Figure 5-14. Effect of shark skin LSM technique on the S1 cutting insert tool life performance benchmarked against B1 cutting inserts during semi-finishing at n = 800 rpm and a_p = 1.0 mm

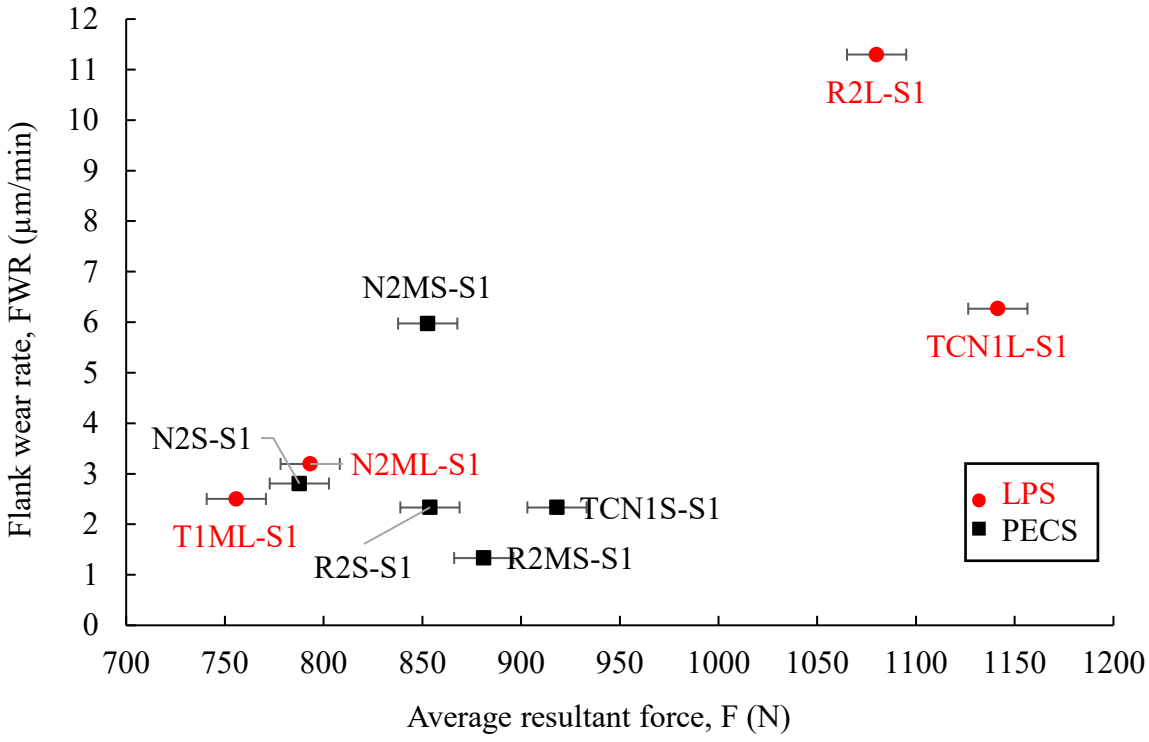


Figure 5-15. Variation of the flank wear rate (FWR) with the average resultant force (F) for shark skin LSM (S1) cutting inserts during semi-finishing

Although the shark skin LSM resulted in insert life improvement, the technique also increased the FWR of the majority of cutting inserts as shown in Figure 5.16. From the figure, it can be observed that the R2L-S1 had the highest increase in FWR compared to all the other cutting inserts. The technique increased the FWR of R2L-S1 cutting insert by 107%. This was followed by the TCN1L-S1 and T1ML-S1 whose FWRs were increased by 63% and 27%, respectively. The figure also shows that the shark skin LSM resulted in a slight increase of FWRs of N2S-S1 and N2ML-S1 cutting inserts whose FWRs were increased by 5% and 2%, respectively. As shown in Figure 5.16, the shark skin LSM generally increased the FWRs of all the LPS produced cutting inserts irrespective of the composition. However, a contrasting observation was made for all the PECS produced cutting inserts except for the N2S-S1. From the figure, it can be observed that the N2MS-S1 had the highest reduction (72%), followed by TCN1S-S1 and R2S-S1 with 63% and 24%, reductions, respectively.

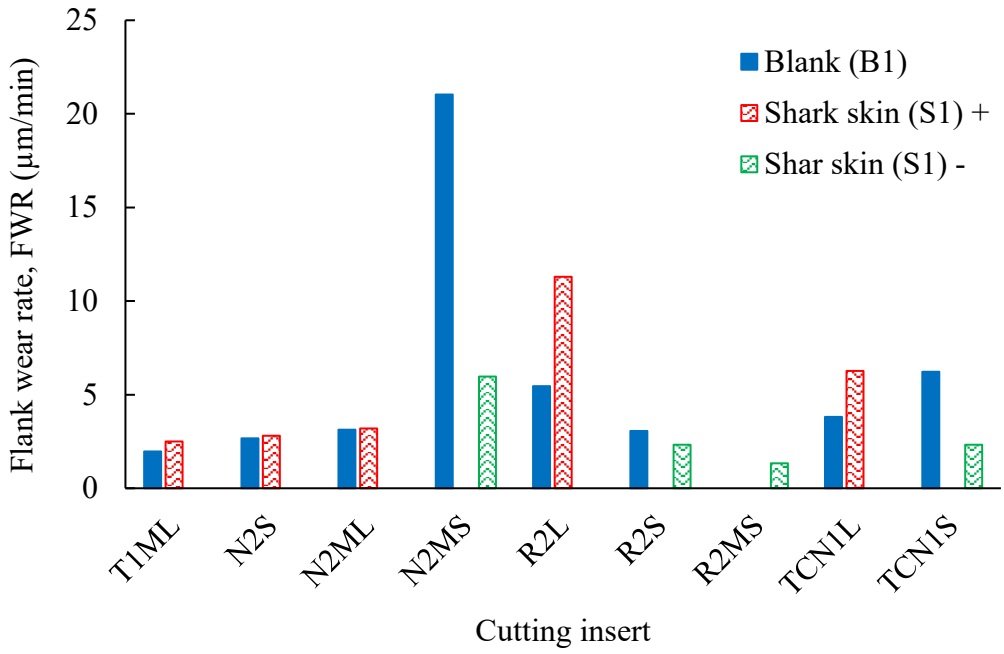


Figure 5-16. Comparison of the flank wear rate of blank (B1) vs. shark skin LSM (S1) cutting inserts during semi-finishing

5.2.3. Analyses of micrographs of the flank and rake faces of the S1 cutting inserts

This subsection provides optical micrograph analyses of shark skin LSM (S1) cutting inserts. Figure 5.17 shows the optical micrographs of the flank and rake faces of (a) R2MS-S1, (b) R2S-S1, and (c) TCN1S-S1 cutting inserts. The flank face of the R2MS-S1 cutting edge had a very thin wear land. The insert also experienced some small degree of chipping as shown on the flank and rake faces. It was also observed that some of the layers of the shark skin surface modifications were removed (peeled

off) from the cutting edge surface during machining as shown on the flank face of the figure. Figure 5.19 shows the HAADF-STEM map of a cross section of the R2MS-S1 insert cutting edge/workpiece interface. The map showed that Nb, TiC and Mo coincided on the top-most (shark skin) layer of approximately 1.3 μm thickness. Thus, suggesting that the surface of the cutting edge is composed mostly of an (Nb, Mo, Ti) C solid solution. In addition, the TiC appears to be completely dissolved in this layer, unlike in the sample microstructure (Figure 4.5). The Ni binder appears to be exposed towards the cutting edge and is distributed in patches within the microstructure. The HAADF-STEM further revealed fragmentation of NbC grains close to the cutting edge, pull-out of the carbide grains, a lighter contrast layer at the insert cutting edge/workpiece interface, and the adherence of Fe (workpiece) on the cutting edge.

Figures 5.17 (b) and (c) show that R2S-S1 and the TCN1S-S1 cutting inserts exhibited very similar wear patterns on both the flank and the rake faces (i.e., the abrasion grooves, peeling off the shark skin surface layer, and chipping). However, as shown on the rake faces, the R2S-S1 cutting insert had some cracks which were not detectable on the TCN1S-S1 cutting insert. Furthermore, the TCN1S-S1 cutting insert had more pronounced chipping compared to R2S-S1 cutting insert. The optical micrographs of the rest of the S1 cutting inserts were also analysed. Similar to the R2MS-S1, the wear and degree of cutting edge wear on the T1ML-S1 cutting insert was minimal and therefore indicating the possibility of the cutting insert to machine beyond 20 minutes as well. It must be noted, however, that the abrasion grooves on the flank of the T1ML-S1 cutting insert were more pronounced compared to the R2MS-S1. The rake face of T1ML-S1 cutting insert indicated the occurrence of minor chipping of the cutting edge. Furthermore, unlike the other S1 cutting inserts, the layer of the shark skin surface modification on T1ML-S1 was not removed beyond the boundary of the VB_{max}. The wear lands of the N2S-S1 and N2MS-S1 cutting inserts had multiple pronounced abrasion grooves.

The optical micrograph of N2S-S1 showed that the inserts experienced cracking and chipping of the cutting edges during the machining process. Despite having a lower VB_{max} than the N2ML-S1, the wear on the N2S-S1 was more compared to that of the N2ML-S1 cutting insert. For example, more layers of the shark skin surface peeled off on the N2S-S1 compared to N2ML-S1. In addition, a mechanical fracture of the cutting edge was observed on the flank face of N2S-S1 as opposed to that of N2ML-S1 cutting insert. The optical micrographs of the flank and rake faces of N2MS-S1, R2L-S1, and TCN1L-S1 cutting inserts indicated that their cutting edges had abrasion wear, mechanical fracture and major chipping.

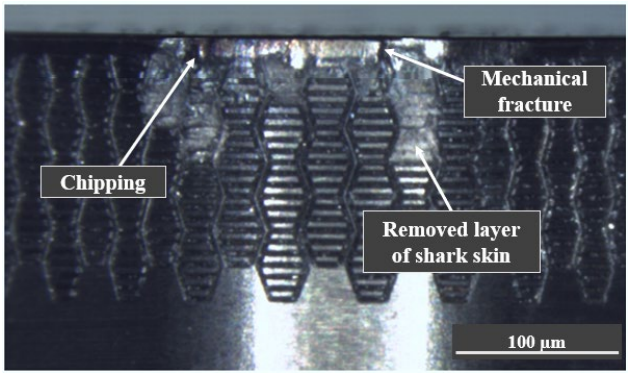
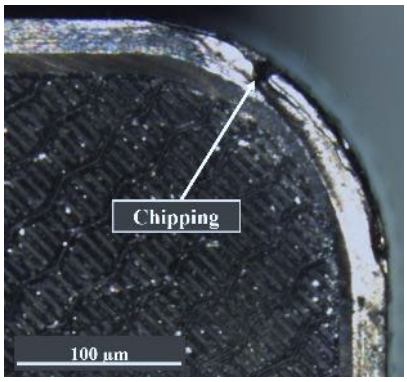
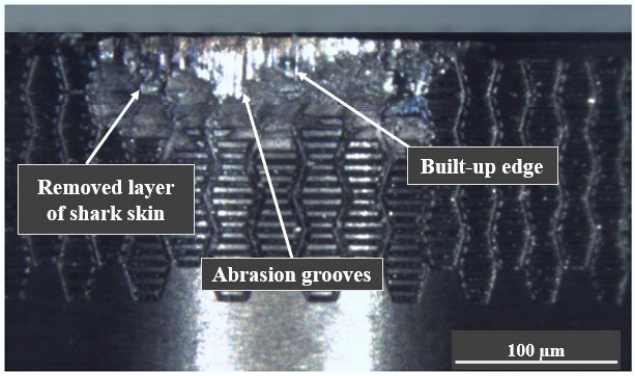
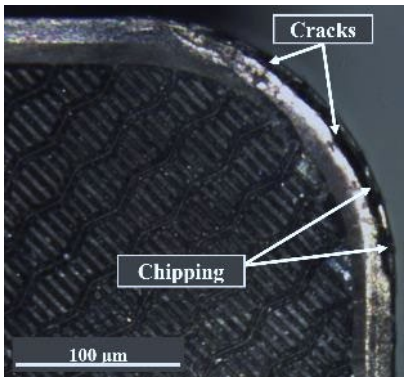
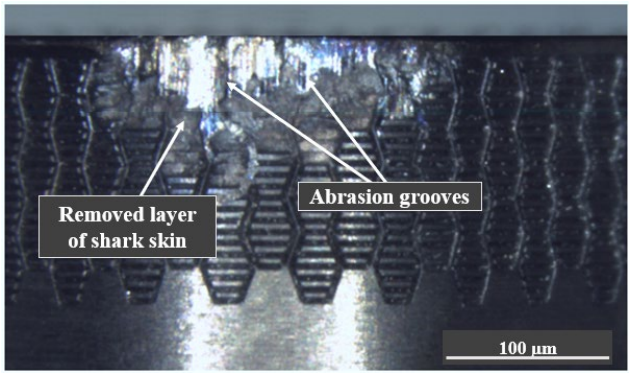
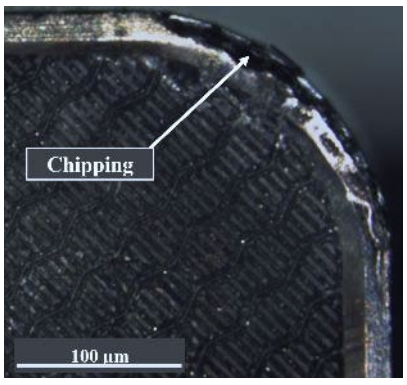
Insert	Flank face	Rake face
(a) R2MS-S1		
	VB_{max} = 26.67 µm Cutting time = 20 minutes	
(b) R2S-S1		
	VB_{max} = 46.67 µm Cutting time = 20 minutes	
(c) TCN1S-S1		
	VB_{max} = 46.67 µm Cutting time = 20 minutes	

Figure 5-17. Optical micrographs of the flank and rake faces of (a) R2MS-S1, (b) R2S-S1 and (c) TCN1S-S1 cutting edges during semi-finishing machining

The micrographs further revealed that the cutting edges of the R2L-S1 and TCN1L-S1 cutting inserts completely shattered during the machining process. Another notable observation was that these cutting inserts had very similar failure mechanisms to their blank counterparts. During machining, fragments

of the chips (debris) from the workpiece would be trapped in between the channels of the shark skin surface. Figure 5.18 gives an illustration of the entrapment of the workpiece debris in the channels of the shark skin surface. This phenomenon was observed on almost all the S1 cutting inserts. However, it was mostly visible on the cutting inserts that achieved longer cutting periods. In general, the optical micrographs of the flank and the rake faces of the cutting inserts show that the shark skin LSM improved wear resistance as well as increased the mechanical shock resistance of the cutting inserts. Additionally, the cutting edges of the shark skin LSM cutting inserts did not exhibit major mechanical fracture where significantly large portions of the cutting edges broke off (which was observed in some of the blank cutting inserts). This indicates that the laser surface modification resulted in edge strengthening.

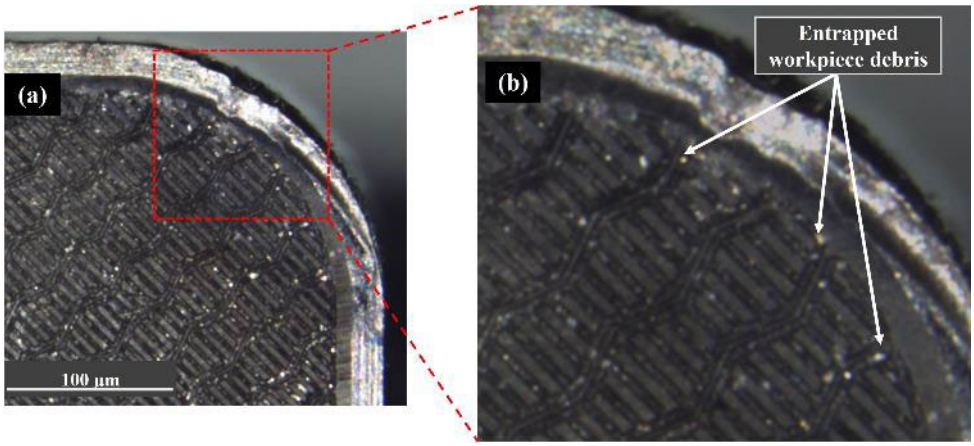


Figure 5-18. Illustration of entrapped workpiece debris (bright contrast spots) on the shark skin surface layer of the rake face of T1ML-S1 cutting insert

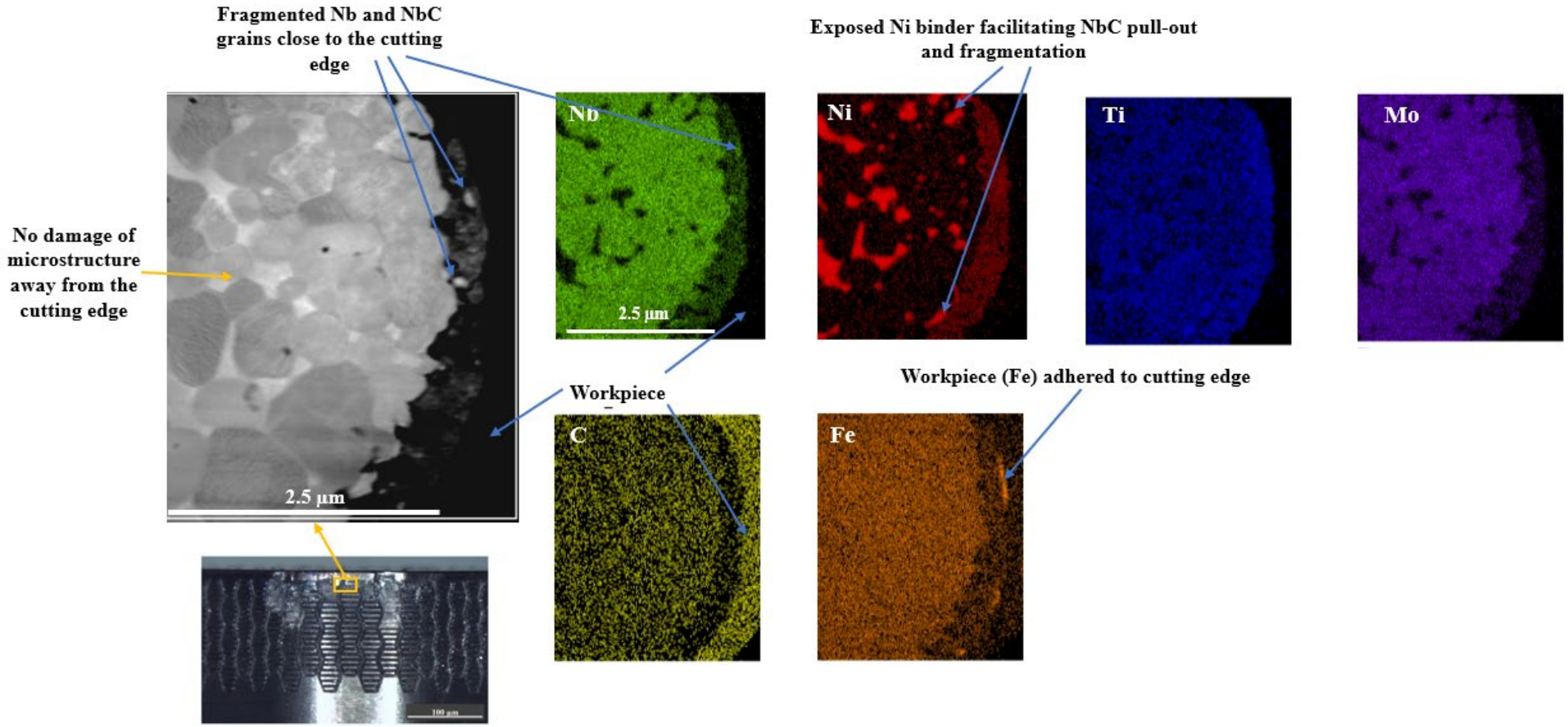


Figure 5-19. HAADF-STEM map of a cross-section of R2MS-S1 insert cutting edge/workpiece interface showing: Nb (green), Ni (red), Ti (blue), Mo (purple), C (yellow), and Fe (orange).

5.2.4. Machining performance evaluation and analyses of S1 cutting inserts

Figure 5.20 shows the variation of specific cutting energy with the cutting time of S1 cutting inserts. The figure indicates that the T1ML-S1 cutting insert had the best combination of these two criteria used for the machining performance evaluation. As shown in the figure, the R2L-S1 cutting insert exhibited the poorest combination of U_c and I_l respectively. Unlike with the B1 cutting inserts, the PECS manufactured S1 cutting inserts had generally better combinations of the machining performance criteria than their LPS counterparts except for the N2MS-S1 cutting insert. Similarly, it was also observed that the additions of TiC, the combination of Mo and TiC, and TiC_7N_3 to the N2S resulted in improved machining performances of the R2S-S1, R2MS-S1 and TCN1S-S1. However, as seen from Figure 5.20, the N2S-S1 still had a better combination of the performance criteria due to its lower specific cutting energy. Figure 5.21 shows the overall preference score (O_i) and rank of S1 cutting inserts used during semi-finishing. As shown in the figure, the top three ranked S1 cutting inserts used for semi-finishing were the T1ML-S1, N2S-S1 and N2ML-S1. The average performers were the R2S-S1, R2MS-S1 and the TCN1S-S1 cutting inserts, whilst the TCN1L-S1, N2MS-S1 and the R2L-S1 cutting inserts were ranked 7th, 8th, and 9th, respectively.

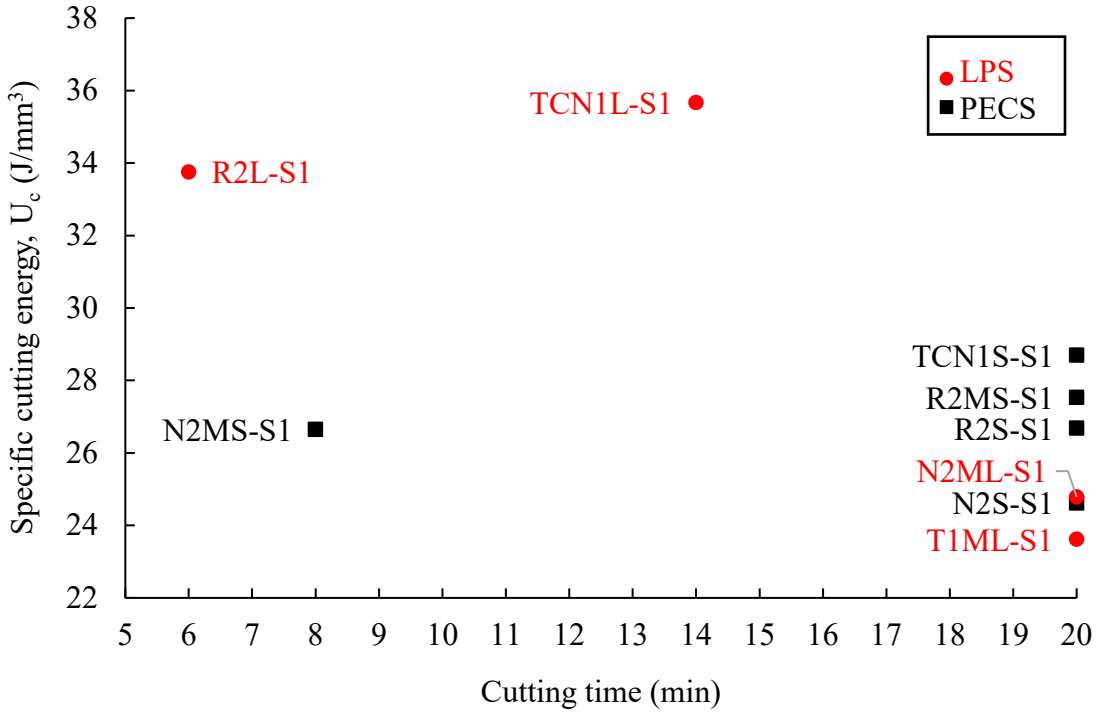


Figure 5-20. Variation of specific cutting energy (U_c) with cutting time (I_l) for shark skin LSM (S1) cutting inserts during semi-finishing at n = 800 rpm and a_p = 1.0 mm

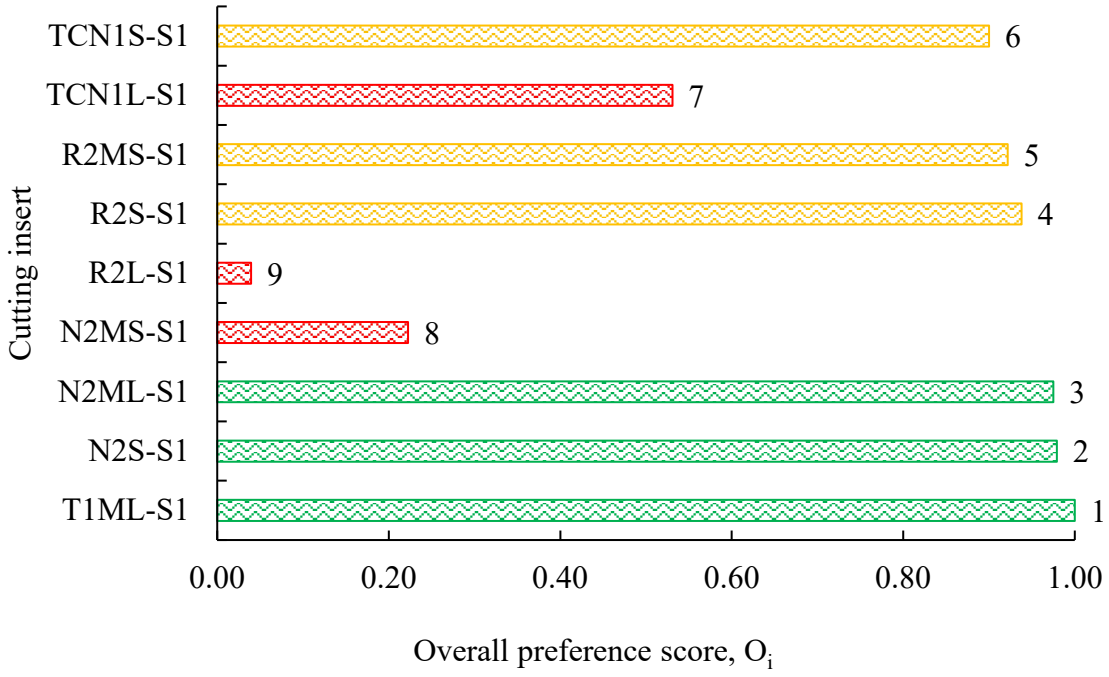


Figure 5-21. Overall preference score (O_i) and rank of S1 cutting inserts (alternatives)

5.3. Analyses of the pyramid LSM (P1) cutting inserts

This subsection presents and analyses resultant cutting forces, specific cutting energy, insert life, wear and temperature of the pyramid LSM cutting inserts during the face milling of a-GCI under semi-finishing conditions. The micrographs of cutting inserts showing the flank and rake faces are also presented in this section. Lastly, the machining performance evaluation of the pyramid LSM cutting inserts is done to rank the cutting inserts.

5.3.1. Analyses of the resultant forces, specific cutting energy, and temperature of P1 cutting inserts

Table 5.5 shows the resultant forces, specific energy consumption and the temperature of the pyramid LSM cutting edges during semi-finishing machining. Figure 5.22 presents the average resultant forces (F) and the maximum resultant forces (F_{max}) experienced by the pyramid LSM cutting edges during semi-finishing. Irrespective of the composition, the F_{max} experienced by all the P1 cutting inserts exceeded 1038 N (see Table 5.5). As shown in the figure, the maximum resultant forces were significantly higher than the average resultant cutting forces experienced by the cutting inserts.

Table 5.5. Machining forces, specific cutting energy, and temperature results of pyramid LSM cutting inserts during semi-finishing at n = 800 rpm and a_p = 1.0 mm

Insert name	Average resultant force, F (N)	Maximum resultant force, F_{max} (N)	Specific cutting energy, U_c (J/mm^3)	Average Temperature, T (°C)
T1ML-P1	763	1131	23.86	108.33 ± 1.01
N2S-P1	820	1132	25.61	114.74 ± 0.88
N2ML-P1	742	1057	23.18	112.60 ± 1.08
N2MS-P1	744	1053	23.26	117.41 ± 1.12
R2L-P1	850	1086	26.57	107.66 ± 1.04
R2S-P1	733	1066	22.91	117.13 ± 1.11
R2MS-P1	706	1087	22.07	109.90 ± 1.07
TCN1L-P1	844	1322	26.38	80.73 ± 0.76
TCN1S-P1	801	1140	25.03	118.57 ± 1.16

*NB: The average and maximum resultant forces have a fixed error of ±15 N from the Kistler.

The N2ML-P1, N2MS-P1 and R2S-P1 cutting inserts exhibited the lowest F_{max} values compared to all the other inserts. This was followed by the R2L-P1 and the R2MS-P1 cutting inserts, whose F_{max} values were 1086 N and 1087 N, respectively (see Table 5.5 and Figure 5.22). From Figure 5.22, it can be seen that there was not any significant difference in the maximum resultant forces of all the other cutting inserts except for the TCN1L-P1 which experienced the highest (1322 N) F_{max} during machining. When considering the average resultant cutting force, the R2MS-P1 experienced the lowest (706 N) compared to all the other cutting inserts. This was followed by the R2S-P1, N2ML-P1 and N2MS-P1, respectively (see Table 5.5 and Figure 5.22). As shown in Figure 5.22, the R2L-P1 had the highest (850 N) average resultant forces. Similar to the shark skin LSM cutting inserts, the LPS produced R2L-P1 and TCN1L-P1 had higher resultant forces (both F_{max} and F) than their PECS produced counterparts. When considering the composition, the NbC-Ni based N2S-P1 had slightly higher average resultant force than the WC-Co based T1ML-P1 cutting insert.

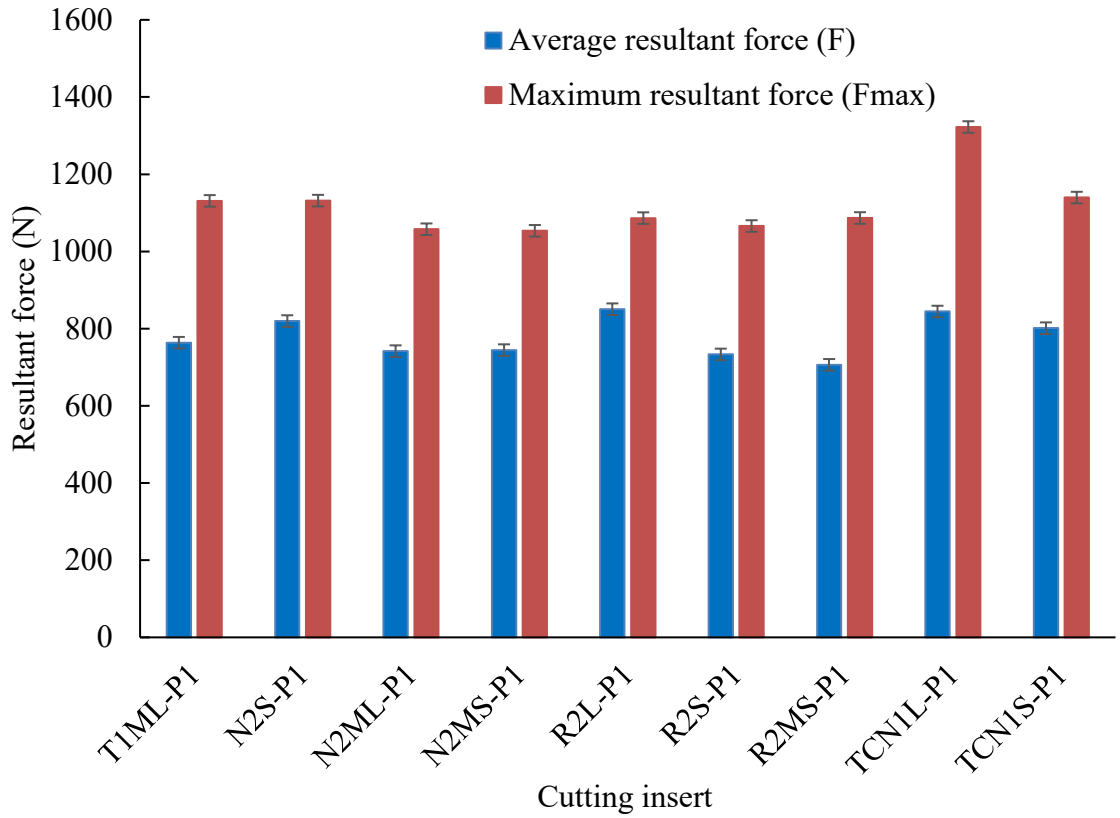


Figure 5-22. Average resultant force (F) and maximum resultant force (F_{max}) for the pyramid (P1) cutting inserts during semi-finishing at n = 800 rpm and a_p = 1.0 mm

Figure 5.23 shows a graph of the variation of specific cutting energy with the average resultant cutting force for P1 cutting inserts. The relationship between the two variables is linear, and the specific cutting energy appears to increase with increasing average resultant cutting force. This observation is similar to that of both the blank and the shark skin LSM cutting inserts. From the figure, it can be seen that compared to all the P1 cutting inserts, the R2MS-P1 had the lowest specific cutting energy (~22 J/mm^3) per volume of material removed during machining. Similar to S1 cutting inserts, the LPS produced R2L-P1 and TCN1L-P1 cutting inserts had the highest energy consumptions having ~26.6 J/mm^3 and ~26.4 J/mm^3 specific cutting energy respectively. Among the LPS produced cutting inserts, the N2ML-P1 had the lowest energy consumption followed by the T1ML-P1. In general, the PECS produced cutting inserts had better energy consumption (lower specific cutting energies) than their LPS counterparts except for the N2M based cutting inserts (N2ML-P1 and N2MS-P1) whose energy consumption was very similar (see Figure 5.23). The additions of Mo, TiC and TiC_7N_3 to the base N2S-P1 resulted in a reduction in energy consumption. As shown in the figure, the simultaneous addition of Mo and TiC (R2MS-P1) had the biggest reduction, followed by TiC (R2S-P1), Mo (N2MS-P1), and TiC_7N_3 (TCN1S-P1), respectively.

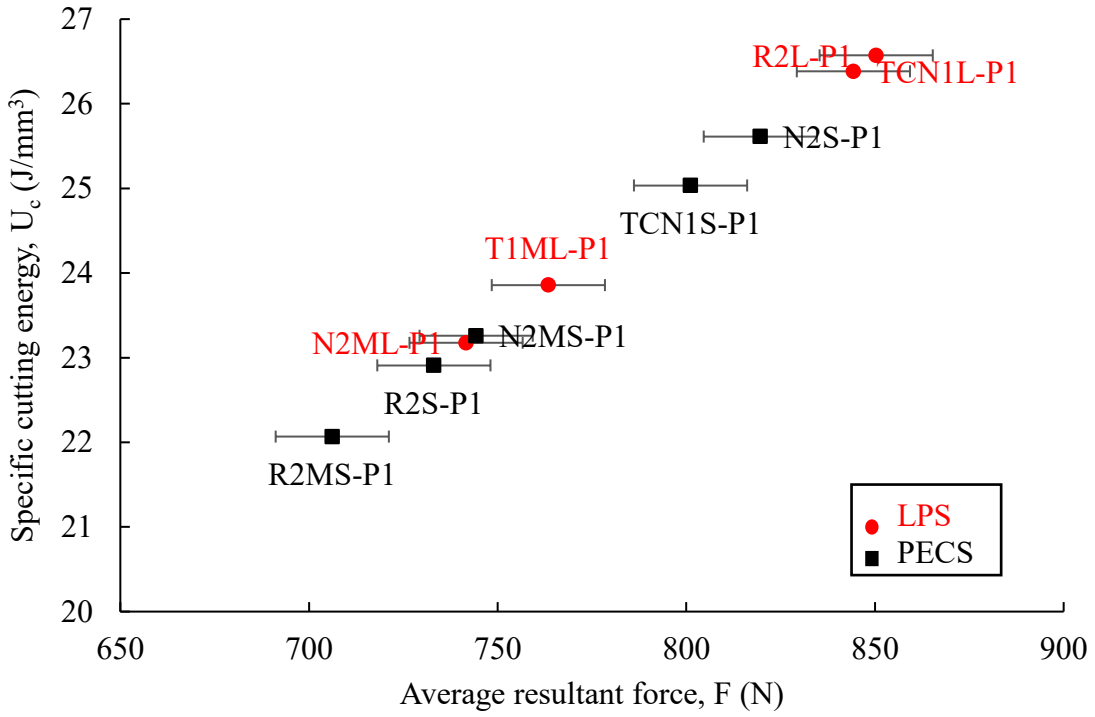


Figure 5-23. Variation of the specific cutting energy (U_c) with the average resultant force (F) for P1 cutting inserts during semi-finishing at n = 800 rpm and a_p = 1.0 mm

Figure 5.24 shows the variations of average machining temperature with the average resultant force for the pyramid LSM cutting inserts during semi-finishing. As seen from the figure, the TCN1L-P1 cutting insert had the lowest average machining temperature (~82 °C) despite experiencing a high average resultant cutting force compared to the other cutting inserts. There was no direct correlation that could be drawn for the relationship between machining temperature and the average resultant force of the pyramid LSM cutting inserts. For instance, the R2MS-P1, T1ML-P1, and R2L-P1 had slightly similar machining temperatures. However, their average resultant forces were significantly different (see Table 5.5 and Figure 5.24). Figure 5.24 also shows that the R2S-P1, N2ML-P1, N2MS-P1 and N2S-P1 cutting inserts also experienced slightly similar average machining temperatures. However, as previously indicated, the N2S-P1 exhibited a higher average resultant cutting force compared to these cutting inserts. In addition, the figure shows that the TCN1S-P1 had a slightly higher average machining temperature compared to the rest of the cutting inserts irrespective of the composition. In general, the LPS produced cutting inserts (i.e. N2ML-P1, R2L-P1 and TCN1L-P1) had lower average machining temperatures compared to their PECS produced counterparts. Furthermore, there were no notable effects of the additions of Mo, TiC and TiC_7N_3 on the PECS produced cutting inserts.

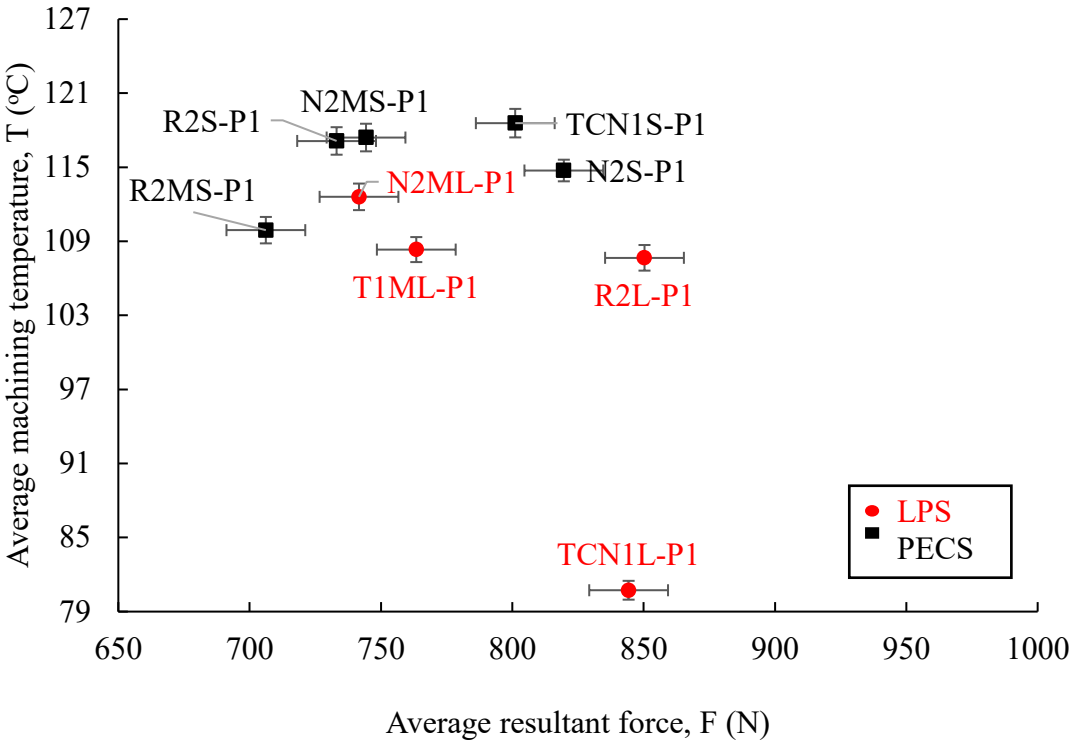


Figure 5-24. Variation of the average machining temperature (T) with the average resultant force (F) for pyramid LSM (P1) cutting inserts during semi-finishing

5.3.2. Analyses of insert tool life and wear performance of P1 cutting inserts

Table 5.6 shows the cutting insert life and wear performance results of P1 cutting inserts. Figure 5.25 depicts the variation of the maximum flank wear with the cutting time for pyramid LSM cutting edges during semi-finishing. The figure illustrates that the VB_{max} for all pyramid LSM cutting inserts, regardless of the sintering technique and composition, was under 70 µm. This value is approximately 8.6 times lower than the maximum allowable Vmax for semi-finishing. Similar to the shark skin modified LSM cutting inserts, the majority of pyramid LSM cutting inserts, including the R2MS-P1, T1ML-P1, R2S-P1, N2MS-P1, N2S-P1 and TCN1S-P1 achieved 20 minutes insert life performance (see Figure 5.25). As shown in Figure 5.25, the R2MS-P1 cutting insert had the lowest VB_{max} compared to all the other cutting inserts irrespective of the composition. The TCN1S-P1, had the highest maximum flank wear among all the cutting inserts which achieved 20 minutes of cutting time. From the figure, it can also be seen that the difference in the VB_{max} of T1ML-P1, R2S-P1, and N2MS-P1 was very small, therefore suggesting that the inserts had very similar life performance. The R2L-P1 had the highest VB_{max}, and the lowest insert life compared to the rest of the cutting inserts (see Figure 5.25). In general, the NbC-Ni based PECS produced cutting inserts had a better insert life performance than their LPS produced counterparts. From the figure, it can also be seen that the additions of Mo, TiC and TiC_7N_3 into NbC-12Ni (wt%) slightly reduced the VB_{max}.

Table 5.6. Cutting insert tool life, maximum flank wear, and flank wear rate results of P1 cutting inserts during semi-finishing at n = 800 rpm and a_p = 1.0 mm

Insert name	Insert life. I_l (min)	Maximum flank wear, VB_{max} (µm)	Flank wear rate, FWR (µm/min)
T1ML-P1	20	35.56	1.78
N2S-P1	20	41.11	2.06
N2ML-P1	17	44.45	2.61
N2MS-P1	20	38.89	1.94
R2L-P1	8	67.23	8.40
R2S-P1	20	36.67	1.83
R2MS-P1	20	28.89	1.44
TCN1L-P1	14	54.45	3.89
TCN1S-P1	20	60.56	3.03

The effects of pyramid LSM on the cutting insert life performance are shown in Figure 5.26. The figure shows the improvement or reduction of the insert life of pyramid LSM (P1) cutting inserts compared to the blank (B1) cutting inserts. Similar to the shark skin LSM, the pyramid LSM generally improved the insert life. The pyramid LSM (P1) had very similar effects on the insert life compared to those of shark skin LSM (S1). Figure 5.26 shows no improvement or reduction in insert life for the T1ML, N2S and R2MS. This is because both the T1ML and N2S achieved 20 minutes cutting duration, whilst the R2MS on the other hand, had no blank counterpart for comparison. From the figure, it can be seen that the N2MS-P1 had the highest insert life improvement compared to all the other P1 cutting inserts, irrespective of composition or sintering technique. The pyramid LSM improved the cutting insert's life of N2MS-P1 by 900% followed by TCN1S-P1, R2S-P1 and N2ML-P1 with insert life improvements of 233%, 150% and 55%, respectively. In addition, Figure 5.26 shows that similar to the shark skin LSM, the pyramid LSM technique also resulted in adverse effects on the insert life of R2L-P1 and TCN1L-P1. Thus, the pyramid LSM reduced the insert life of the two cutting inserts by 27% and 30% respectively.

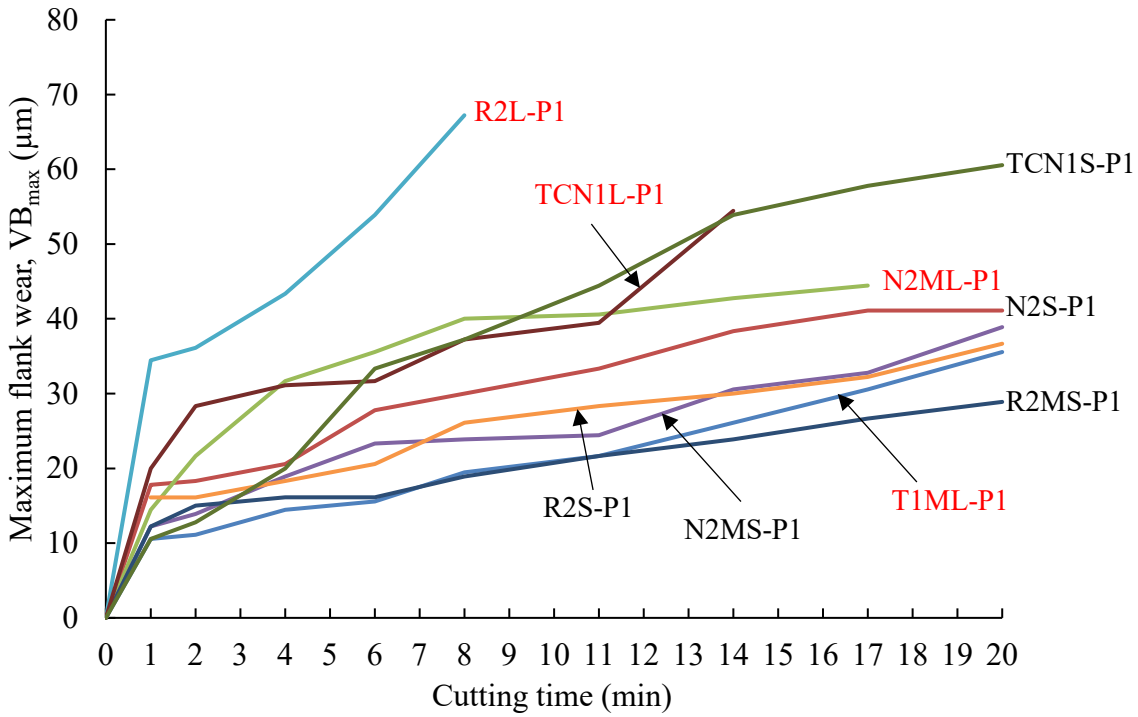


Figure 5-25. Variation of the maximum flank wear (VB_{max}) with cutting time (l_l) for pyramid LSM (P1) cutting inserts during semi-finishing at n = 800 rpm and a_p = 1.0 mm

Figure 5.27 shows the variation of the flank wear rate, FWR with the average resultant force, F for pyramid LSM (P1) cutting inserts. From the figure, it can be seen that the FWR increases slightly with increasing average resultant cutting force. As shown in the figure, the R2MS-P1 had the lowest combination of the FWR, and F compared to all the other cutting inserts. This observation is not surprising as the cutting insert exhibited the lowest VB_{max} whilst achieving the maximum allowable cutting duration. The figure also shows that there is no significant variation in FWR performances for R2S-P1, T1ML-P1, N2MS-P1 and N2S-P1 cutting inserts. Additionally, Figure 5.27 shows that the R2L-P1 had the highest FWR compared to all the cutting inserts irrespective of the composition. Similar to the shark skin LSM, the R2L-P1 and the TCN1L-P1 had the poorest FWRs performance. In general, the NbC-Ni based PECS produced cutting inserts had a better FWR performance than their LPS counterparts. When comparing the T1ML-P1 and the N2S-P1 cutting inserts, it could be seen that they had very similar FWRs.

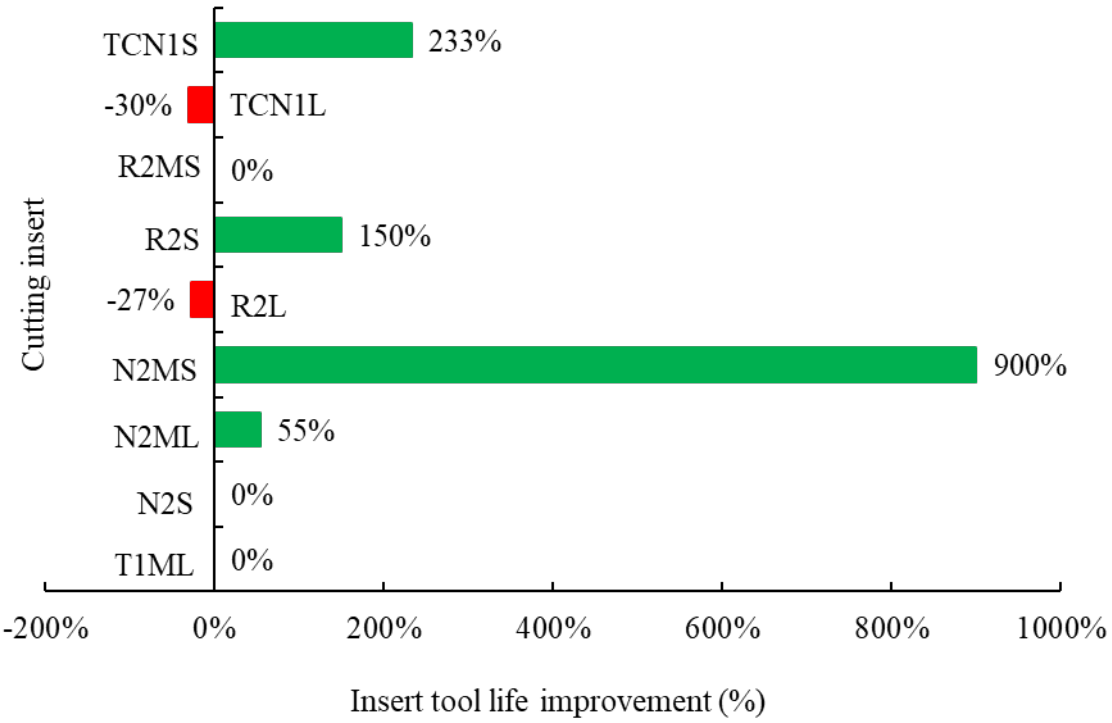


Figure 5-26. Effect of pyramid LSM technique on the cutting insert life performance benchmarked with the blank (B1) cutting inserts during semi-finishing at n = 800 rpm and a_p = 1.0 mm

Figure 5.28 depicts the comparison of the FWRs of B1 cutting inserts against P1 cutting inserts. As shown in the figure, the pyramid LSM reduced the FWR of the majority of cutting inserts. In fact, from the figure, it can be seen that the technique resulted in the reduction of FWR for all the cutting inserts except for the R2L-P1 and TCN1L-P1 cutting inserts whose FWRs were increased by 54% and 2%, respectively. Figure 5.28 shows that the N2MS-P1 cutting insert had the biggest improvement in FWR compared to all the other cutting inserts (i.e. the FWR of the insert was about 91% lower when compared to the N2MS-B1). This was followed by the TCN1S-P1 and R2S-P1 cutting inserts whose FWRs were lowered by 51% and 40%, respectively. The N2S-P1, N2ML-P1, and T1ML-P1 cutting inserts had FWR reductions of less than 24% with the inserts having reductions of 23%, 17%, and 10%, respectively.

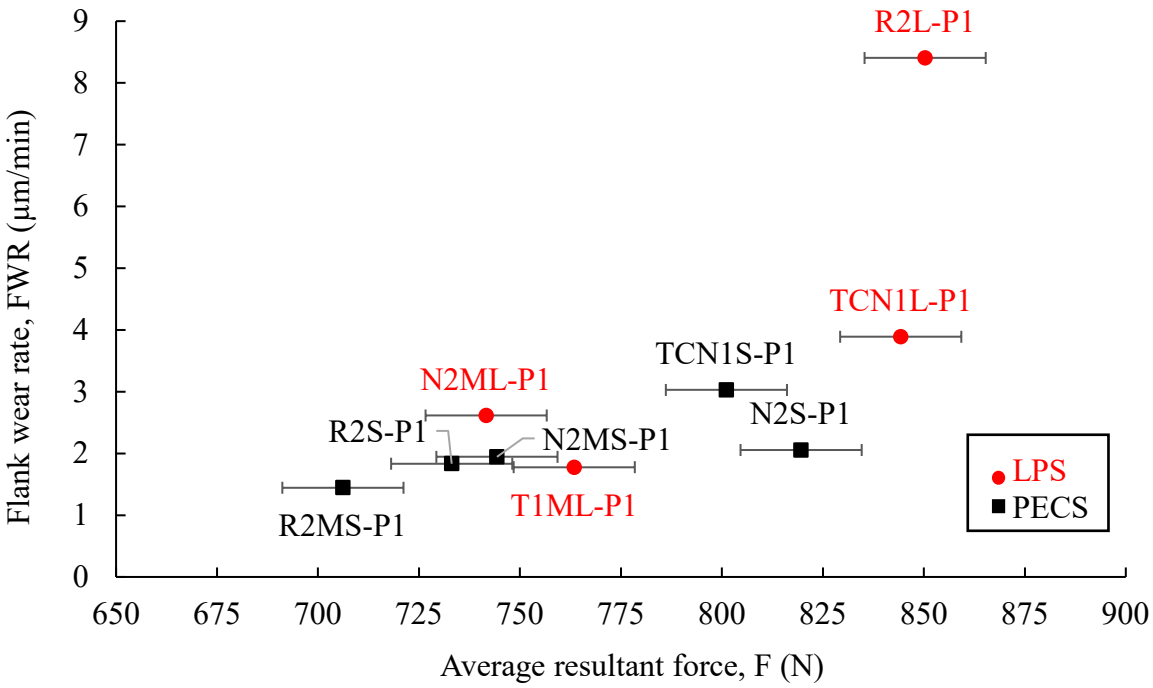


Figure 5-27. Variation of the flank wear rate (FWR) with the average resultant force (F) for pyramid LSM (P1) cutting inserts during semi-finishing

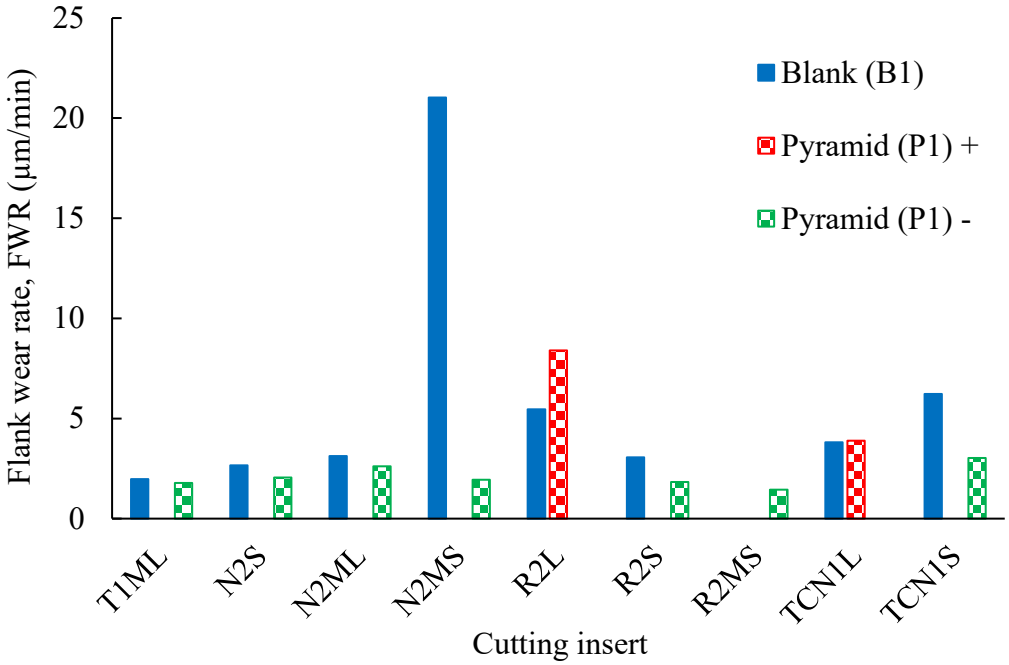


Figure 5-28. Comparison of the flank wear rate of blank vs. pyramid LSM cutting inserts during semi-finishing

5.3.3. Analyses of optical micrographs of the flank and rake faces of P1 cutting inserts

This subsection provides optical micrograph analyses of pyramid LSM (P1) cutting inserts. Figure 5.29 shows the optical micrographs of the flank and rake faces of (a) R2MS-P1, (b) T1ML-P1 and (c) R2S-P1 cutting inserts. As shown in the figure, the cutting edge of the R2MS-P1 cutting insert had the least wear compared to that of the T1ML-P1 and R2S-P1 cutting inserts. The R2MS-P1 cutting insert had the smallest wear land and very minimal abrasion grooves on the flank face of the insert. Additionally, a small degree of chipping was also observed on the rake face of the cutting insert. Similar to R2MS-P1, the T1ML-P1 and R2S-P1 cutting inserts exhibited small wear lands and minimal abrasion grooves. However, the rake face of the R2S-P1 exhibited slightly more chipping compared to the R2MS-P1 and T1ML-P1 cutting inserts (see Figure 5.29). In accordance with the (ISO) 3685:1993 insert tool life criteria, the three cutting inserts could possibly still continue with milling even after reaching the set 20 minutes of machining time. The analysis of the optical micrographs of the remaining P1 cutting inserts was also done. The optical micrographs of the flank and rake faces of N2MS-P1, N2S-P1 and TCN1S-P1 cutting inserts exhibited abrasion grooves on the flank face. The wear on N2MS-P1's cutting edge in terms of wear (both wear land and pattern of the abrasion grooves) was very similar to those of T1ML-P1 and R2S-P1 cutting inserts. The micrographs also showed that during machining, the cutting inserts experienced mechanical shock which was confirmed by the appearance of cracks on the rake face of the inserts. Some evidence of chipping was also observed on the rake face of N2MS-P1 cutting insert. Although there was evidence of wear on the cutting edge, the N2MS-P1 could still machine beyond the 20 minutes based on the insert tool life criteria. In addition to the abrasion grooves, the flank face of N2S-P1 cutting insert indicates that the wear on the insert's cutting edge was slightly more than that of the N2MS-P1. For example, the N2S-P1 has slightly thicker abrasion grooves on the flank face as well as more pronounced cracks and chipping on the rake face of the cutting insert Among the cutting inserts that achieved 20 minutes of cutting time, the TCN1S-P1 showed the worst wear of the cutting edge. The TCN1S-P1 cutting insert had the longest and thickest abrasion grooves on the flank face. Additionally, from the micrograph, it was observed that the cutting edge experienced mechanical fracture during machining. The flank face optical micrograph of N2ML-P1 had prominent abrasion grooves. The rake face on the other hand indicated that the cutting edge experienced cracking and chipping during machining. The cutting edge of the TCN1L-P1 cutting insert completely shattered during machining and multiple abrasion grooves were also formed on the flank face of the cutting insert. The rake face optical micrograph of TCN1L-P1 indicates that the cutting edge experienced mechanical fracture during the cutting process.

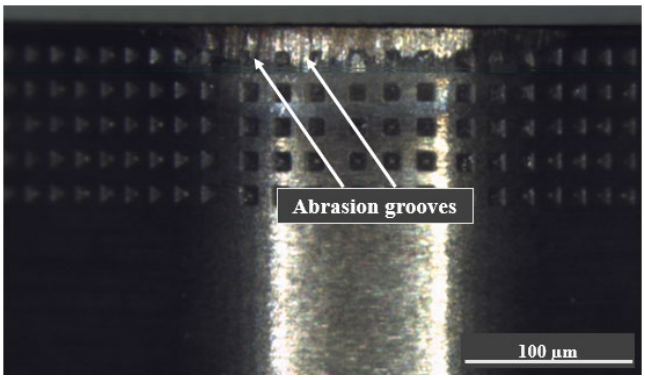
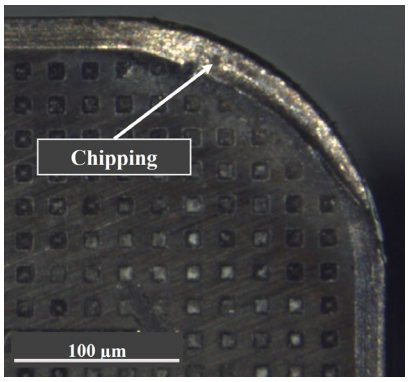
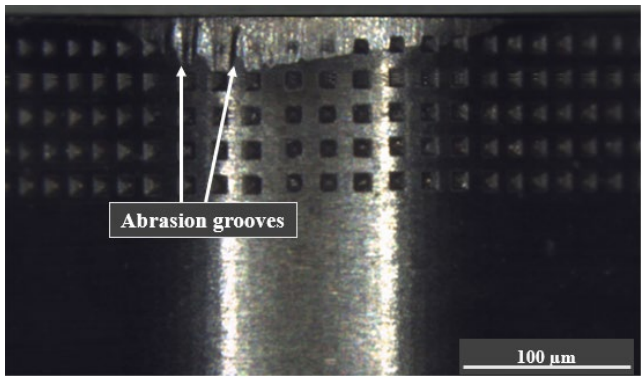
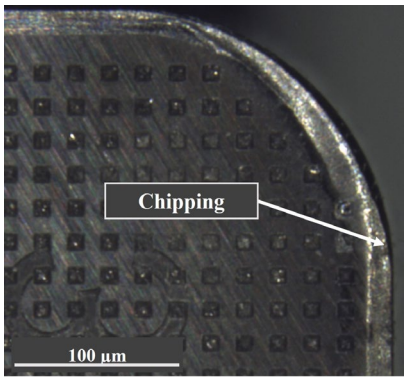
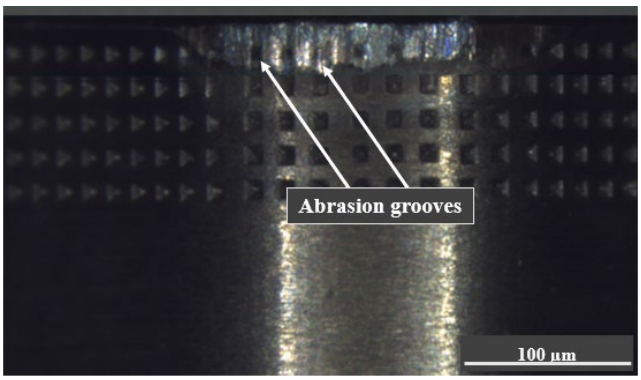
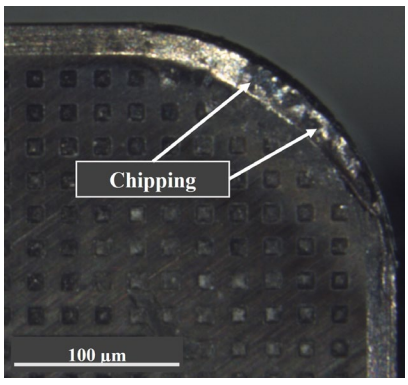
Insert	Flank face	Rake face
(a) R2MS-P1		
	VB_{max} = 28.89 µm Cutting time = 20 minutes	
(b) T1ML-P1		
	VB_{max} = 35.56 µm Cutting time = 20 minutes	
(c) R2S-P1		
	VB_{max} = 36.67 µm Cutting time = 20 minutes	

Figure 5-29. Optical micrographs of the flank and rake faces of (a) R2MS-P1, (b) T1ML-P1 and (c) R2S-P1 cutting edges during semi-finishing machining

Similar to the TCN1L-P1, the cutting edge of the R2L-P1 cutting insert was completely shattered during machining. Abrasion grooves and BUE were noted on the flank face of the cutting insert. Furthermore, the optical micrograph also showed that the rake face of the R2L-P1 cutting insert

experienced mechanical fracture as well. Like the shark skin LSM (S1) cutting inserts, the optical micrographs show that the pyramid LSM (P1) generally improved wear and mechanical shock resistance of the cutting edges of the cutting inserts.

5.3.1. Machining performance evaluation and analysis of P1 cutting inserts

Figure 5.30 shows the variation of specific cutting energy with the cutting time of the P1 cutting inserts. The figure shows that the R2MS-P1 cutting insert had the best combination of the machining performance criteria. Conversely, the R2L-P1 cutting insert had the poorest combination of the criteria. Similar to the S1 cutting inserts, the PECS produced P1 cutting inserts had better combinations of the machining performance criteria compared to their LPS produced counterparts. The effects of composition could be seen on the PECS produced cutting inserts. From the figure, it can be seen that the additions of TiC_7N_3, Mo, TiC and a combination of Mo and TiC to the N2S-P1, improved the overall machining performances of TCN1S-P1, N2MS-P1, R2S-P1, and R2MS-P1 cutting inserts respectively. The opposite observation was seen for the S1 cutting inserts.

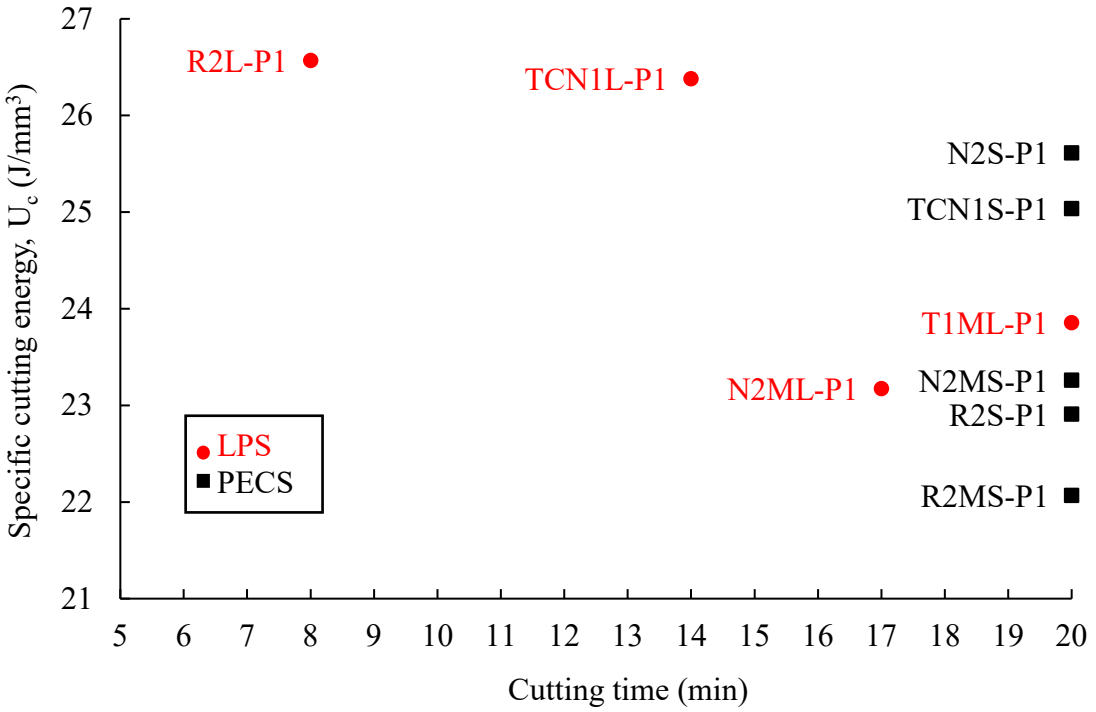


Figure 5-30. Variation of specific cutting energy (U_c) with cutting time (l_t) for pyramid LSM (P1) cutting inserts during semi-finishing at n = 800 rpm and a_p = 1.0 mm

Figure 5.31 shows the overall preference score (O_i) and rank of the pyramid LSM (P1) cutting inserts used during semi-finishing. From the figure, it can be seen that the top three ranked P1 cutting inserts were the R2MS-P1, R2S-P1, and N2MS-P1. The average performing P1 cutting inserts were the

T1ML-P1, TCN1L-P1 and N2S-P1. The N2ML-P1, TCN1L-P1 and R2L-P1 fell in the poor performing cutting inserts category.

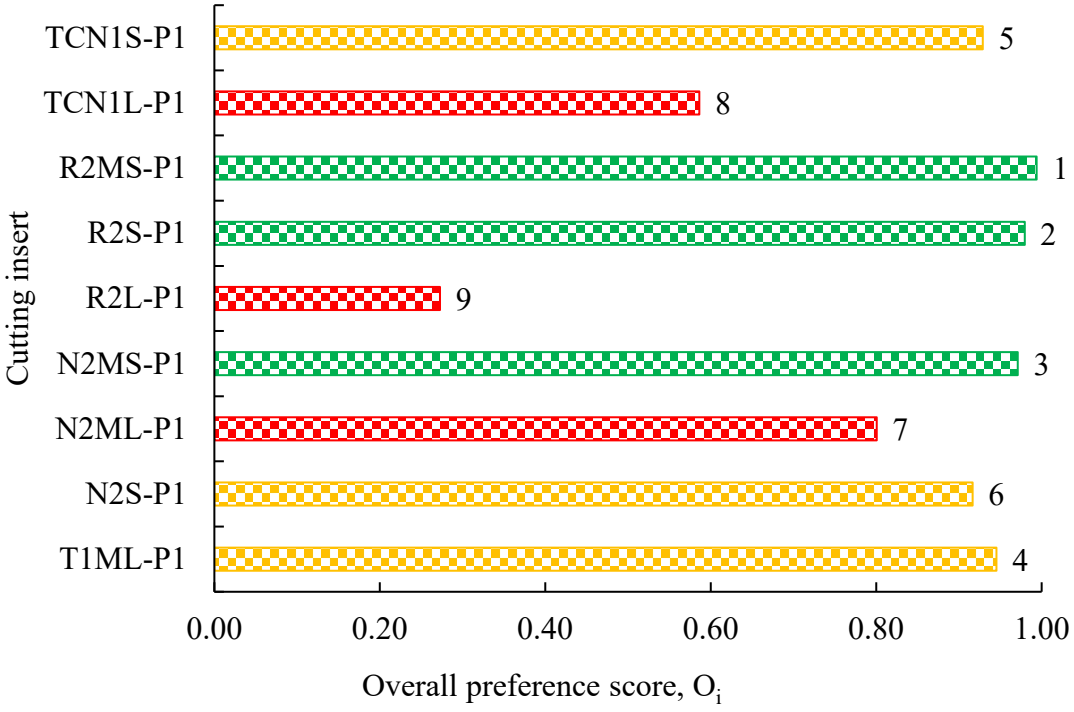


Figure 5-31. Overall preference score (O_i) and rank of P1 cutting inserts (alternatives)

5.4. Consolidated results for semi-finishing (Test 1)

This section summarises the overall results of the semi-finishing process. The overall analyses and comparisons of the machining performance of cutting inserts are made and presented here. The primary goal was to evaluate and rank the performance of all the cutting inserts used during semi-finishing. For this purpose, the TOPSIS methodology was employed on the 26 cutting inserts (edges) used during test 1 machining trials. Table 5.7 gives the machining performance criteria, the overall preference scores as well as the rank of cutting inserts used during semi-finishing. From the table, it can be seen that the best cutting insert for semi-finishing was the R2MS-P1 cutting insert. The cutting insert obtained an overall preference score of 0.953 with performance criteria values of I_l = 20 min, Fmax = 1087 N and U_c =22 J/mm^3. The poorest overall performing cutting insert on the other hand was determined to be the N2MS-B1 cutting insert with the relative closeness score of 0.038 and criteria values of 2 min, 1394 N, and 42 J/mm^3 for the I_l , Fmax, and U_c , respectively.

Table 5.7. Machining performance criteria, overall preference scores, and rank of all the cutting inserts used during semi-finishing.

Solution	Cutting insert	C1 (min)	C2 (J/mm^3)	C3 (N)	Overall preference score	Rank	Category
A24	R2MS-P1	20	22	1087	0.953	1	Best (1 – 9)
A23	R2S-P1	20	23	1066	0.941	2	
A1	T1ML-B1	20	21	1569	0.939	3	
A21	N2MS-P1	20	23	1053	0.935	4	
A9	T1ML-S1	20	24	1194	0.929	5	
A18	T1ML-P1	20	24	1131	0.926	6	
A10	N2S-S1	20	25	1200	0.915	7	
A11	N2ML-S1	20	25	1233	0.912	8	
A26	TCN1S-P1	20	25	1140	0.910	9	
A2	N2S-B1	20	24	1615	0.903	10	Average (10 – 18)
A19	N2S-P1	20	26	1132	0.902	11	
A7	TCN1L-B1	20	26	1104	0.894	12	
A14	R2S-S1	20	27	1243	0.886	13	
A15	R2MS-S1	20	28	1259	0.875	14	
A17	TCN1S-S1	20	29	1306	0.859	15	
A20	N2ML-P1	17	23	1057	0.832	16	
A25	TCN1L-P1	14	26	1322	0.669	17	
A16	TCN1L-S1	14	36	1462	0.605	18	
A3	N2ML-B1	11	26	1674	0.525	19	Poor (19 – 26)
A5	R2L-B1	11	33	1751	0.485	20	
A6	R2S-B1	8	19	1069	0.442	21	
A22	R2L-P1	8	27	1086	0.392	22	
A12	N2MS-S1	8	27	1245	0.390	23	
A8	TCN1S-B1	6	25	1302	0.326	24	
A13	R2L-S1	6	34	1437	0.248	25	
A4	N2MS-B1	2	42	1394	0.038	26	

6. Finishing (Test 2 and Test 3) Results

This chapter provides the results of finishing 1 (test 2) and finishing 2 (test 3) trials on a-GCI. Like in seme-finishing, each test was conducted as a singular experiment without any repetition of measurements

The machining conditions for the tests are listed as follows:

- Cutting speed (V_c): 400 mm/min,
- Spindle speed (n): 1600 rpm,
- Depth of cut (a_p): 0.5 mm (test 2) and 0.25 mm (test 3),
- Feed rate (V_f): 0.1 mm/tooth,
- Machining duration: 20 minutes (test 2) and 40 minutes (test 3).

6.1. Analyses of the blank (B2) cutting inserts

This subsection presents and analyses resultant cutting forces, specific cutting energy, insert life, wear, and machining temperature of the blank (B2) cutting inserts during the face milling of a-GCI under finishing conditions. The micrographs of cutting inserts showing the flank and rake sides are also presented in this section. Lastly, the machining performance evaluation of the B2 cutting inserts is done to rank the cutting inserts.

6.1.1. Analysis of the resultant forces, specific cutting energy, and temperature of the B2 cutting inserts

Table 6.1 shows the resultant forces, specific energy consumption, and the temperature of the blank cutting edges during finishing 1 machining. Figure 6.1 shows F and F_{max} experienced by B2 cutting inserts. As shown in Figure 6.1, the maximum resultant forces were significantly higher than the average resultant forces for all the cutting inserts except for the R2L-B2 which had similar F and F_{max}. The figure also shows that the F_{max} values of all the cutting inserts with the exception of R2L-B2, exceeded 1600 N. The TCN1S-B2 cutting insert exhibited the highest F_{max} (2222 N) in comparison to all the other B2 cutting inserts used during finishing 1 trials. This was followed by the R2MS-B2 and the TCN1L-B2 cutting inserts as shown in Table 6.1 and Figure 6.1. The R2S-B2 cutting insert had a F_{max} of 1324 N which was the same as its F. As shown in Figure 6.1, the T1ML-B2 cutting insert had the lowest F (918 N) compared to all the other cutting inserts irrespective of the sintering technique or

composition. From the figure, it can also be seen that the rest of the B2 cutting inserts experienced average resultant forces exceeding 1100 N. The TCN1L-B2 cutting insert exhibited the highest average resultant cutting force (1574 N) under finishing 1 conditions. Among the NbC-12Ni (wt%) based cutting inserts, the LPS produced cutting inserts had slightly higher F values compared to their PECS counterparts (see Table 6.1 and Figure 6.1).

Table 6.1. Machining forces, specific energy consumption, and temperature results of B2 cutting inserts during finishing at n = 1600 rpm and a_p = 0.5 mm

Insert name	Average resultant force, F (N)	Maximum resultant force, F_{max} (N)	Specific cutting energy, U_c (J/mm^3)	Average Temperature, T (°C)
T1ML-B2	918	1627	57.36	73.13 ± 0.67
N2S-B2	1215	1660	75.95	76.27 ± 0.70
N2ML-B2	1356	1715	84.72	84.61 ± 0.80
N2MS-B2	1277	1656	79.80	78.17 ± 0.72
R2L-B2	1324	1324	82.78	-
R2S-B2	1199	1658	74.95	89.55 ± 0.84
R2MS-B2	1280	1784	80.01	90.16 ± 0.85
TCN1L-B2	1574	1745	98.38	37.06 ± 0.25
TCN1S-B2	1397	2222	87.30	94.59 ± 0.89

*NB: The average and maximum resultant force have a fixed error of ±15 N from the Kistler.

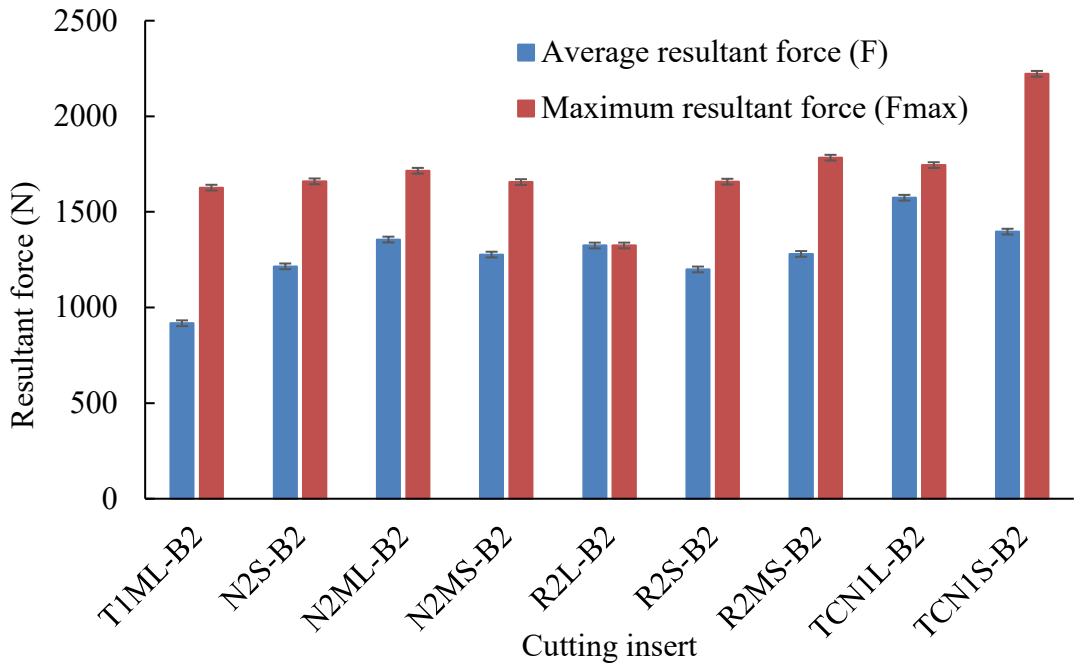


Figure 6-1. Average resultant force (F) and maximum resultant force (F_{max}) for B2 cutting inserts during finishing at n = 1600 rpm and a_p = 0.5 mm

Figure 6.2 shows the variation of specific cutting energy with the average resultant force of B2 cutting inserts. As shown in the figure, the T1ML-B2 cutting insert had the lowest specific cutting energy (~57 J/mm^3) and therefore lowest energy consumption compared to all the other cutting inserts. All the NbC-Ni based cutting inserts had U_c of >1.32 times that of T1ML-B2. This shows that irrespective of the composition or sintering technique, the NbC-Ni based cutting inserts consumed more energy than the WC-Co based T1ML-B2. Among the NbC-Ni based cutting inserts, the TCN1L-B2 had the highest specific cutting energy (~98 J/mm^3). From Figure 6.2 it can be observed that the LPS produced NbC-Ni based cutting inserts exhibited higher specific cutting energy than their PECS counterparts. When considering the PECS produced cutting inserts, the R2S-B2 had the lowest energy consumption (see Figure 6.2). This was followed by the N2S-B2, R2MS-B2 and N2MS-B2 which had very similar specific cutting energies, and then the TCN1S-B2 which had the highest energy consumption in comparison to all the PECS produced B2 cutting inserts.

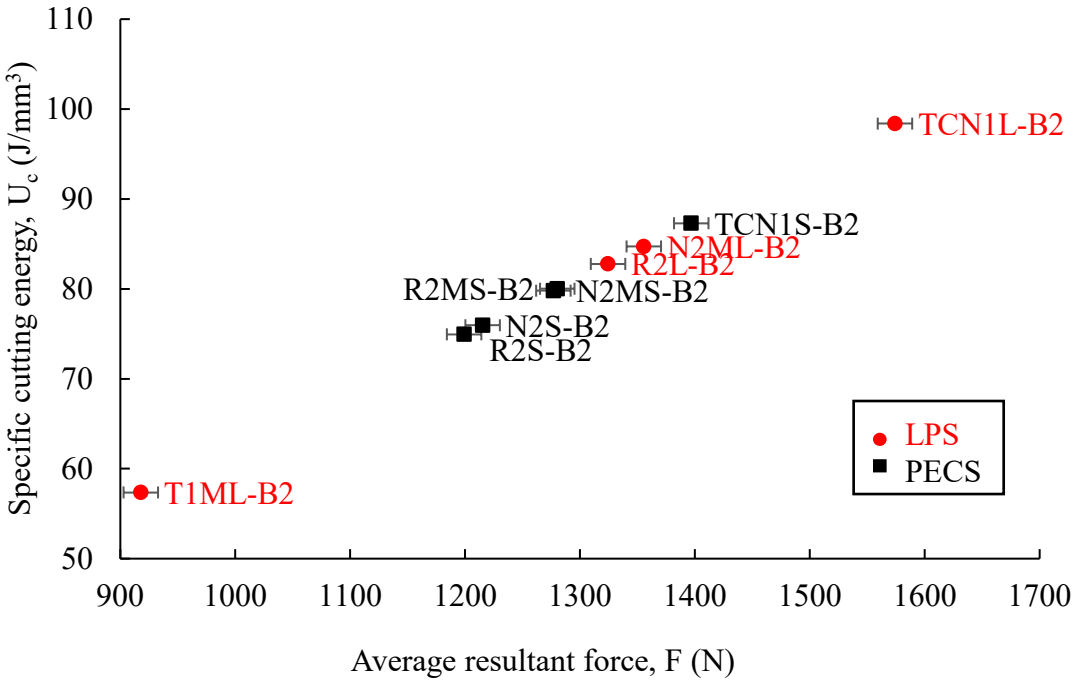


Figure 6-2. Variation of the specific cutting energy (U_c) with the average resultant force (F) for B2 cutting inserts during finishing 1 at n = 1600 rpm and a_p = 0.5 mm

Figure 6.3 shows the variation of machining temperature with the average resultant force for B2 cutting inserts during finishing 1. Despite experiencing the highest average cutting force among the B2 cutting inserts, the TCN1L-B2 cutting insert had the lowest T (37.06 ± 0.25 °C). Its PECS counterpart (TCN1S-B2) on the other hand, exhibited the highest average machining temperature among the B2 cutting inserts. From the figure it was also observed that there was no significant difference between the average machining temperatures of N2S-B2 and N2MS-B2 (~77 °C) as well as between those of R2S-B2 and R2MS-B2 (~90 °C). The effects of composition can be seen on the NbC-Ni based cutting inserts. The additions of TiC, a combination of Mo and TiC, and TiC_7N_3 to the N2S-B2 resulted in slight increases in average machining temperatures. For example, the R2S-B2, R2MS-B2, and TCN1S-B2 cutting inserts had slightly higher T values than the N2S-B2 cutting insert. As shown in the figure, generally, T values of B2 cutting inserts appear to increase with increasing F.

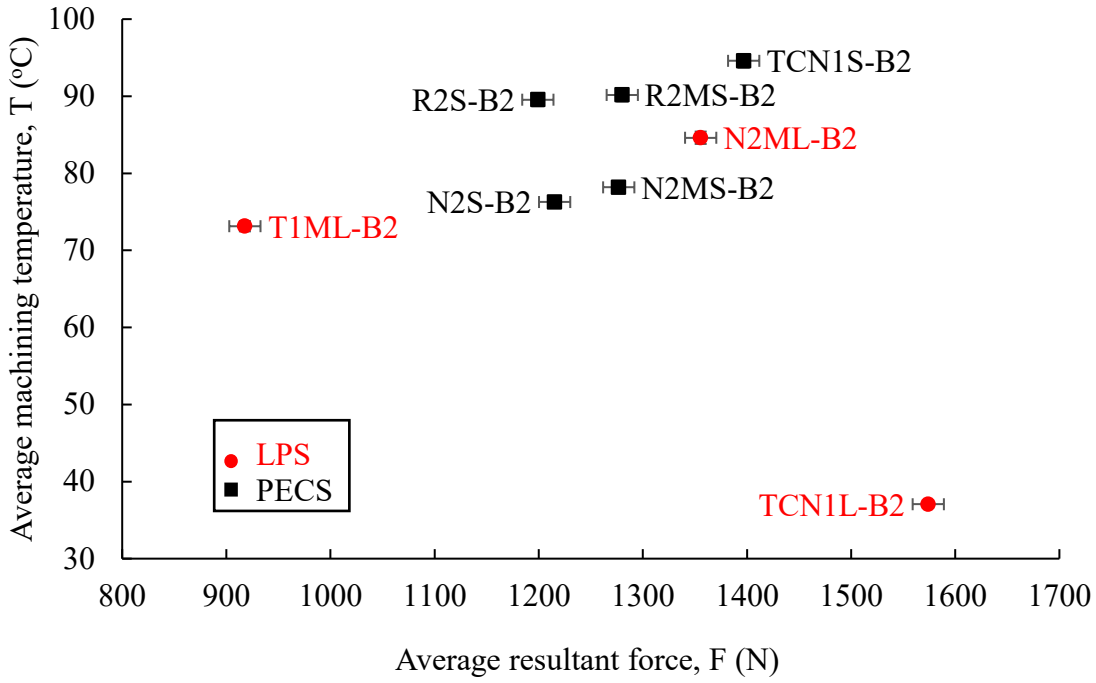


Figure 6-3. Variation of the average machining temperature (T) with the average resultant force (F) for blank (B2) cutting inserts during finishing 1

6.1.2. Analyses of insert life and wear performance of blank (B2) cutting inserts

Table 6.2 shows the cutting insert life and wear performance results of B2 cutting inserts. Figure 6.4 shows the variation of the maximum flank wear (VB_{max}) with the cutting time for blank cutting edges during finishing 1. As shown in the figure, T1ML-B2, R2MS-B2, R2S-B2 and TCN1S-B2 cutting inserts achieved the maximum cutting duration of 20 minutes. As such, the cutting inserts were regarded to have the best performance in terms of insert life under finishing 1 machining conditions. The T1ML-B2 had the lowest VB_{max} (45 µm) followed by the R2MS-B2 with the VB_{max} of ~78 µm. The R2S-B2 and the TCN1S-B2 cutting inserts had VB_{max} of ~101 µm and ~108 µm, respectively (see Table 6.2 and Figure 6.4). Figure 6.4 also shows that the N2S-B2 and the N2MS-B2 cutting inserts had average insert life as they failed after 11- and 8-minutes cutting durations and had VB_{max} of ~107 µm and ~94 µm, respectively. The N2ML-B2 had a VB_{max} of 71.67 µm and achieved only 6 minutes of cutting duration. The TCN1L-B2 failed after 4 minutes and had a VB_{max} of 39.45 µm which was the lowest in comparison to all the B2 cutting inserts. Lastly, as shown in both Table 6.2 and Figure 6.4, the R2L-B2 had the poorest insert life performance with the insert only managing to machine for a minute before failure.

Table 6.2. Cutting insert tool life, maximum flank wear, and flank wear rate results of B2 cutting inserts during finishing at n = 1600 rpm and a_p = 0.5 mm

Insert name	Insert tool life, I_l (min)	Maximum flank wear, VB_{max} (μm)	Flank wear rate, FWR (μm/min)
T1ML-B2	20	45.00	2.25
N2S-B2	11	107.23	9.75
N2ML-B2	6	71.67	11.95
N2MS-B2	8	94.45	11.81
R2L-B2	1	43.34	43.34
R2S-B2	20	101.12	5.06
R2MS-B2	20	77.78	3.89
TCN1L-B2	4	39.45	9.86
TCN1S-B2	20	108.34	5.42

From Figure 6.4, it can be seen that with the exception of the T1ML-B2, the LPS produced cutting inserts had poor insert life performance compared to PECS produced cutting inserts. Furthermore, all the PECS produced NbC-Ni based cutting inserts had better insert life than their LPS counterparts. The effects of composition on the insert life could be seen on the PECS produced cutting inserts. The additions of various compositions improved the insert life while reducing the VB_{max} of the base N2S-B2 cutting insert. For example, additions of a combination of Mo and TiC, TiC and TiC_7N_3 improved the machining performance of the NbC-12Ni (wt%). However, the addition of Mo only resulted in the reduction of the insert life (i.e. insert life of N2MS-B2 is less than that of N2S-B2 cutting insert).

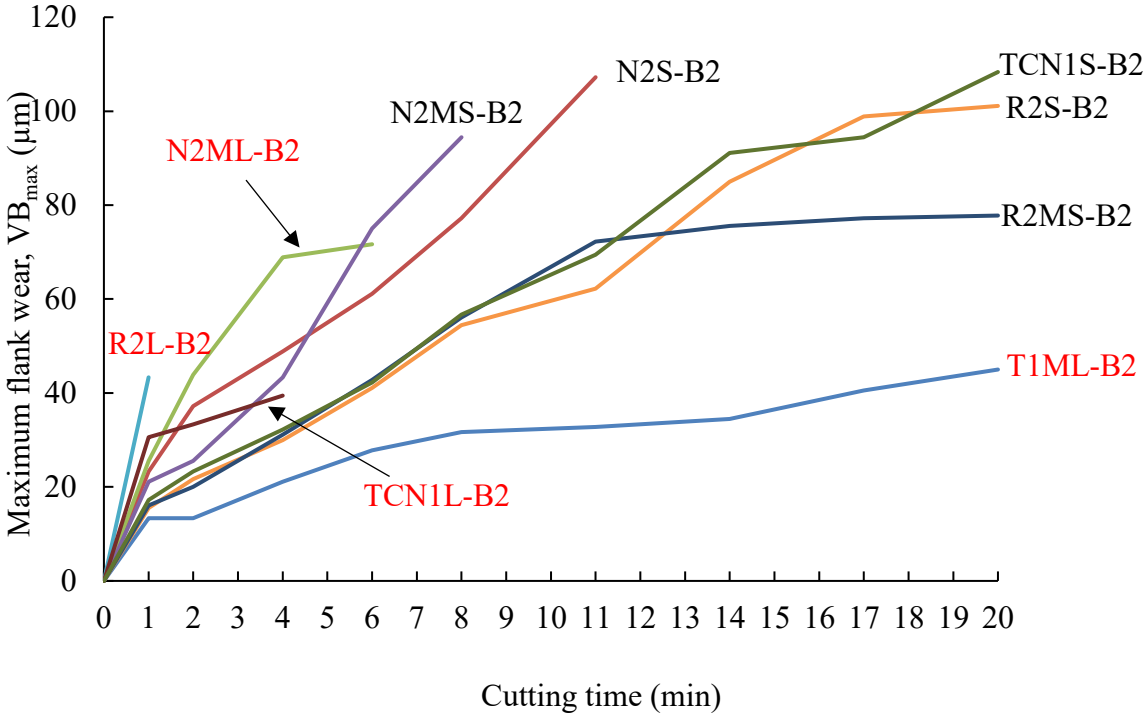


Figure 6-4. Variation of the maximum flank wear (VB_{max}) cutting time (l_l) for blank (B2) cutting inserts during finishing at n = 1600 rpm and a_p = 0.5 mm

Figure 6.5 depicts the relationship between the flank wear rate (FWR) and the average resultant force (F) for the blank (B2) cutting inserts during finishing. From the figure, it can be seen that the T1ML-B2 had the lowest FWR (2.25 µm/min) compared to all the other cutting inserts irrespective of composition and sintering technique. This was followed by the R2MS-B2 whose FWR was recorded to be 3.89 µm/min. With the exception of N2M based cutting inserts, the LPS produced NbC-Ni based cutting insert generally had slightly higher FWRs compared to their PECS counterparts as shown in Figure 6.5. The figure also shows that the R2L-B2 had the highest FWR (43.34 µm/min) compared to the rest of the B2 cutting inserts. When considering only the PECS produced NbC-Ni based cutting inserts, it can be seen from the figure that the additions of various constituents to the base N2S composition affected the FWR of the cutting inserts. For example, the addition of a combination of TiC and Mo, TiC, and TiC_7N_3 reduced FWR in R2MS-B2, R2S-B2, and TCN1S-B2 respectively. However, the addition of Mo slightly increased the FWR in N2MS-B2.

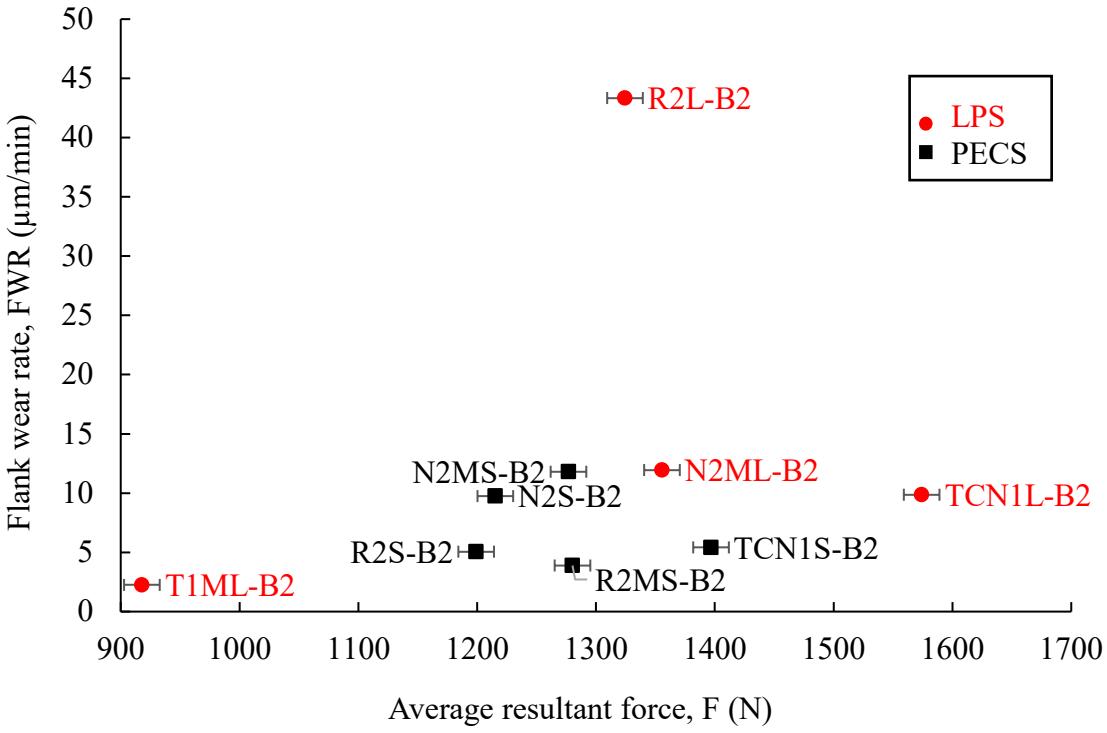


Figure 6-5. Variation of the flank wear rate, FWR with the average resultant force, F for blank (B2) cutting inserts during finishing at n = 1600 rpm and a_p = 0.5 mm

6.1.3. Analyses of micrographs of the flank and rake faces of the blank (B2) cutting inserts

This subsection provides optical micrograph analyses of blank (B2) cutting inserts Figure 6.6 shows the optical micrographs of the flank and rake faces of (a) T1ML-B2, (b) R2MS-B2 and (c) R2S-B2 cutting inserts. From the figure, the cutting edge of T1ML-B2 cutting insert had the least wear compared to those of R2MS-B2 and R2S-B2 cutting inserts. The flank face of T1ML-B2 shows that the cutting insert, experienced abrasion wear and minor chipping. The rake face, on the other hand, shows that there was an occurrence of crater wear on the cutting edge during the machining process. Based on the insert tool life criteria, the T1ML-B2 cutting insert could possibly continue with milling even after reaching the preset 20 minutes machining duration. As shown in the figure, the R2MS-B2 and R2S-B2 cutting inserts exhibited very similar cutting edge wear. Mechanical fracture and abrasion wear were observed on the flank faces of both cutting inserts. The rake faces of the cutting inserts exhibited mechanical fracture and non-uniform surface layer removal (see Figures 6.6 (b) and (c)).

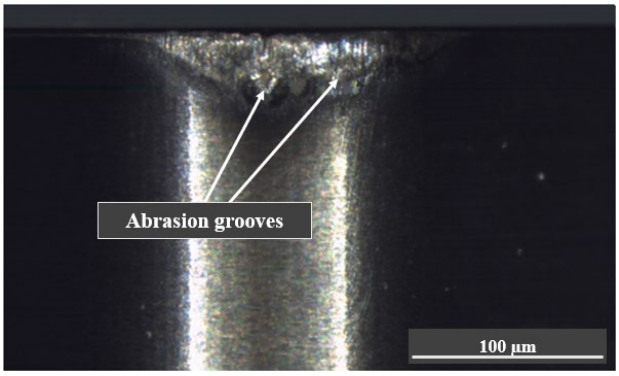
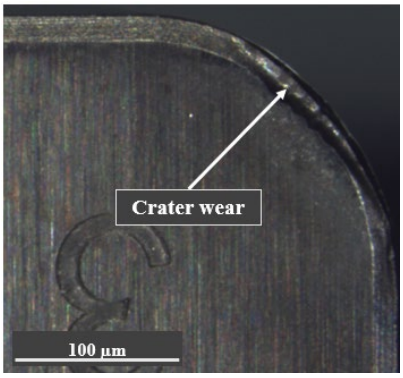
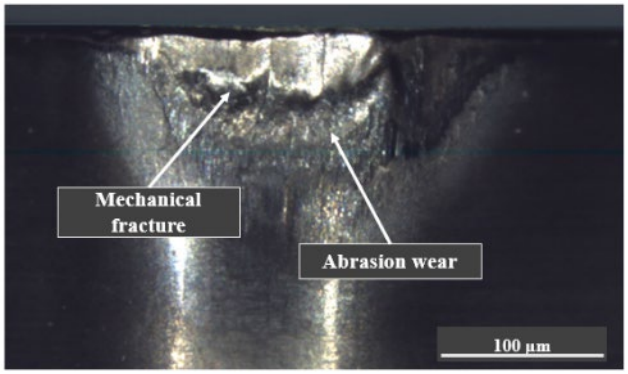
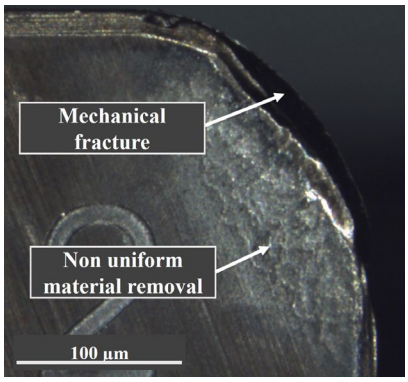
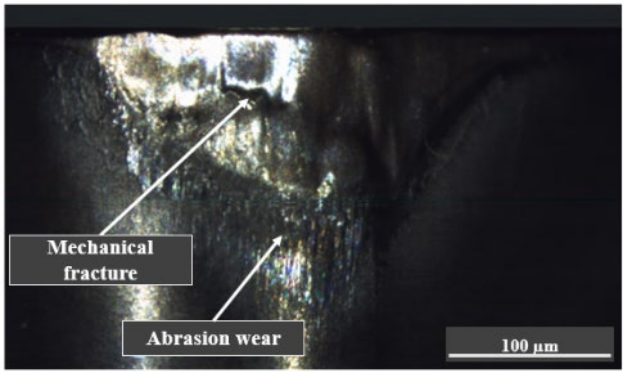
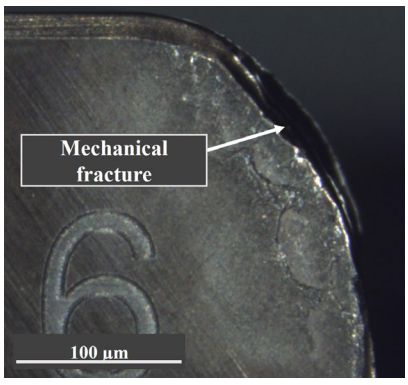
Insert	Flank face	Rake face
(a) T1ML-B2		
	VB_{max} = 45.00 µm Cutting time = 20 minutes	
(b) R2MS-B2		
	VB_{max} = 77.78 µm Cutting time = 20 minutes	
(c) R2S-B2		
	VB_{max} = 101.12 µm Cutting time = 20 minutes	

Figure 6-6. Optical micrographs of the flank and rake faces of (a) T1ML-B2, (b) R2MS-B2 and (c) R2S-B2 cutting edges during finishing 1 machining

The optical micrographs of the other B2 cutting inserts were also analysed. The TCN1S-B2 cutting insert exhibited similar cutting edge wear to those of the R2MS-B2 and R2S-B2 cutting inserts. The flank face of N2ML-B2 exhibited some built-up edge in addition to mechanical fracture and abrasion

wear. The N2S-B2, N2MS-B2 and N2ML-B2 cutting inserts also showed very similar cutting edge wear characteristics. Similarly, the R2L-B2 and TCN1L-B2 cutting inserts exhibited similar cutting edge wear mechanisms. In general, the main wear and failure mechanisms of the B2 cutting inserts were abrasion wear and mechanical fracture.

6.1.4. Machining performance evaluation and analyses of B2 cutting inserts

Figure 6.7 shows the variation of specific cutting energy with cutting time for B2 cutting inserts. The figure shows that the T1ML-B2 cutting insert had the best combination of the machining performance criteria. From the figure, the R2L-B2 cutting insert had the poorest combination as it failed within one minute of machining but is also among the inserts with the highest specific cutting energy. In general, the PECS produced B2 cutting inserts had better combinations of the machining performance criteria than their LPS counterparts. The figure also shows that the additions of TiC, a combination of TiC plus Mo, and TiC_7N_3 to the N2S-B2, improved the overall machining performances of R2S-B2, R2MS-B2 and TCN1S-B2 cutting inserts, respectively.

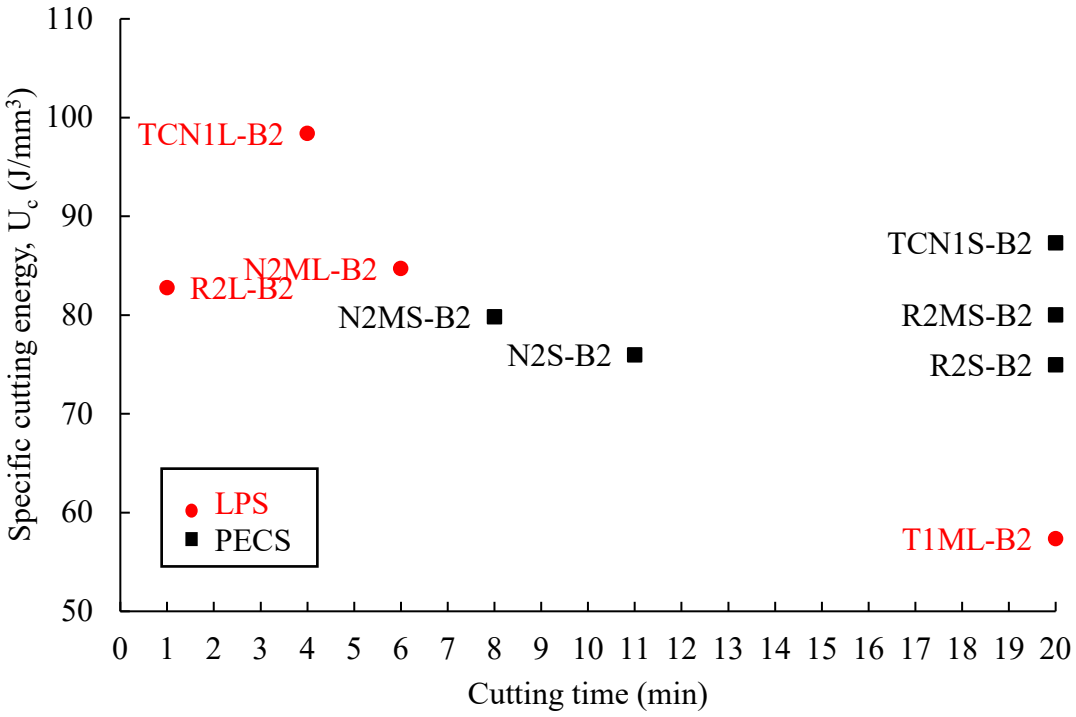


Figure 6-7. Variation of specific cutting energy (U_c) with cutting time (l_l) for blank (B2) cutting inserts during finishing 1 at n = 1600 rpm and a_p = 0.5 mm

Figure 6.8 shows the overall preference score (O_i) and rank of the blank (B2) cutting inserts during finishing 1. From the figure, it can be observed that according to the rankings, the best B2 cutting inserts were the T1ML-B2, R2S-B2 and TCN1S-B2. The TCN1S-B2, N2S-B2, and N2MS-B2 fell

into the average performing cutting inserts category. Lastly, the N2ML-B2, TCN1L-B2 and R2L-B2 cutting inserts had the poorest machining performance.

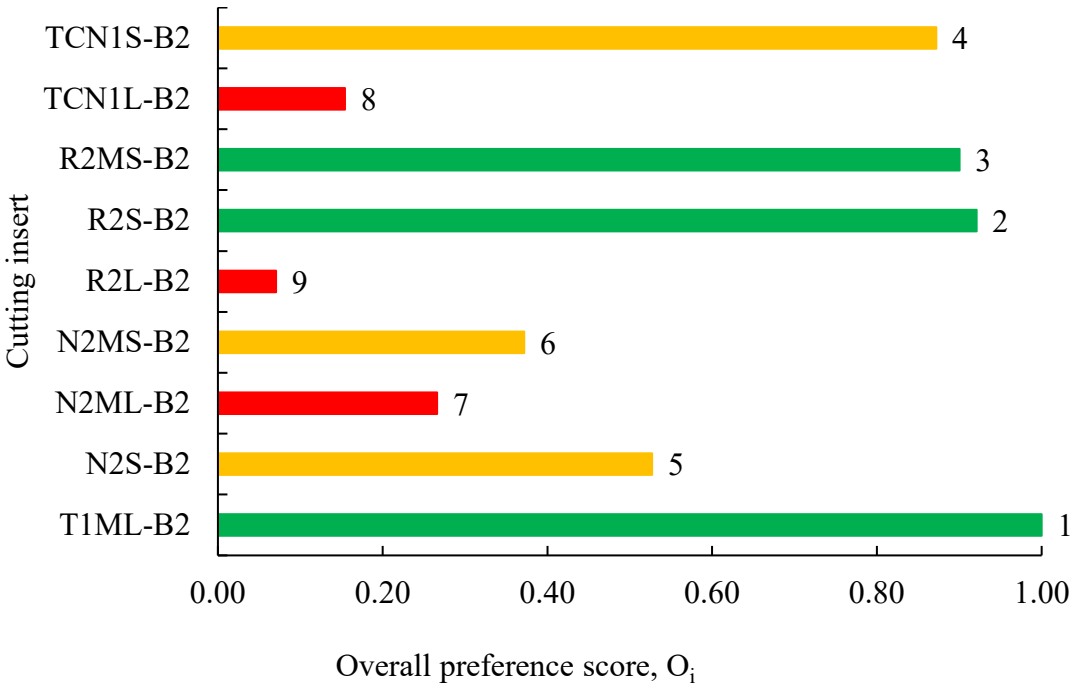


Figure 6-8. Overall preference score (O_i) and rank of B2 cutting inserts (alternatives)

6.2. Analysis of the shark skin LSM (S2) cutting inserts

This subsection presents and analyses the resultant cutting forces, specific cutting energy, insert tool life, wear and average machining temperature of the shark skin LSM cutting inserts during the face milling of a-GCI under finishing conditions. The micrographs of cutting inserts showing the flank and rake faces are also given in this section. Lastly, the machining performance evaluation of the cutting inserts is done to rank the cutting inserts.

6.2.1. Analysis of the resultant forces, specific cutting energy, and temperature of the S2 cutting inserts.

Table 6.3 shows the resultant forces, specific cutting energy, and the average machining temperature of the shark skin LSM (S2) cutting inserts during finishing 1 machining. Figure 6.9 shows the average resultant forces and maximum resultant forces experienced by S2 cutting inserts during finishing 1. As shown in the figure, the cutting inserts' F_{max} values were significantly higher than F values except for the R2L-S2 and TCN1L-S2 cutting inserts which had similar F and F_{max}. It is worth noting that these cutting inserts experienced the lowest resultant forces (i.e. ~ 256 N and 319 N for R2L-S2 and TCN1L-S2 respectively). From the figure, it can be observed that the N2S-S2 cutting insert experienced the

highest maximum resultant cutting force (~1621 N) compared to all the S2 cutting inserts (see Table 6.3 as well). This was followed by the N2ML-S2, T1ML-S2 and TCN1S-S2 cutting inserts whose F_{max} values were approximately 1400 N, 1369 N and 1361 N, respectively (see Table 6.3 and Figure 6.9). As shown in the figure, the average resultant forces experienced by the cutting inserts follow a similar trend exhibited by F_{max}.

Table 6.3. Machining forces, specific energy consumption, and temperature results of S2 cutting inserts during finishing at n = 1600 rpm and a_p = 0.5 mm

Insert name	Average resultant force, F (N)	Maximum resultant force, F_{max} (N)	Specific cutting energy, U_c (J/mm^3)	Average Temperature, T (°C)
T1ML-S2	689	1369	43.05	97.87 ± 0.94
N2S- S2	811	1621	50.68	78.13 ± 0.72
N2ML-S2	689	1400	43.03	73.41 ± 0.68
N2MS-S2	577	948	36.07	85.77 ± 0.80
R2L-S2	256	256	15.99	-
R2S-S2	648	1199	40.50	79.04 ± 0.72
R2MS-S2	366	517	22.90	64.83 ± 0.59
TCN1L-S2	319	319	19.92	-
TCN1S-S2	694	1361	43.39	109.82 ± 1.06

*NB: The average and maximum resultant forces have a fixed error of ±15 N from the Kistler.

Figure 6.10 shows the variation of specific cutting energy with average resultant force for S2 cutting inserts. As expected, it can be seen from the figure that the R2L-S2 and TCN1L-S2 cutting inserts had the lowest specific cutting energies. The N2S-S2 cutting insert on the other hand exhibited the highest specific cutting energy (~51 J/mm^3) among the S2 cutting inserts. There was no notable difference in the U_c values of the N2ML-S2, T1ML-B2, and TCN1S-S2 cutting inserts (i.e., the specific cutting energies of these cutting inserts were approximately 43 J/mm^3). Generally, the LPS produced NbC-Ni based cutting inserts had the lowest energy consumption (specific cutting energy) compared to their PECS produced counterparts except for the N2ML-S2 cutting insert. The additions of Mo, TiC, of Mo, TiC, a combination of Mo plus TiC, and TiC_7N_3 to the base N2S-S2 resulted in the reduction of the energy consumption in all S2 PECS produced cutting inserts during finishing 1 machining (see Figure 6.10).

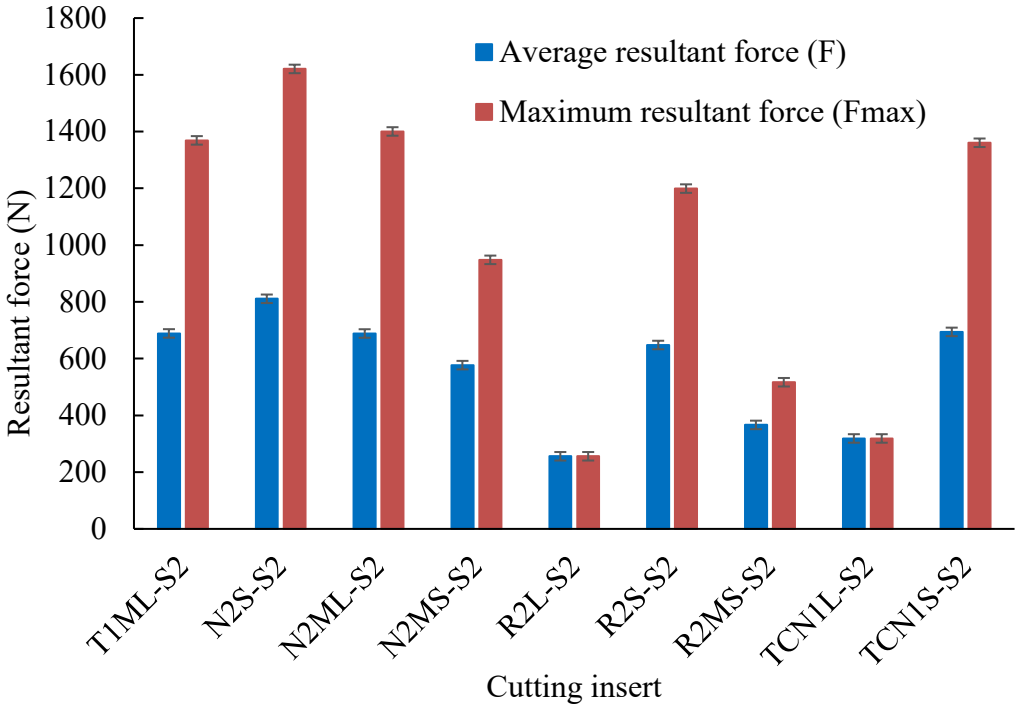


Figure 6-9. Average resultant force (F) and maximum resultant force (F_{max}) for S2 cutting inserts during finishing at n = 1600 rpm and a_p = 0.5 mm

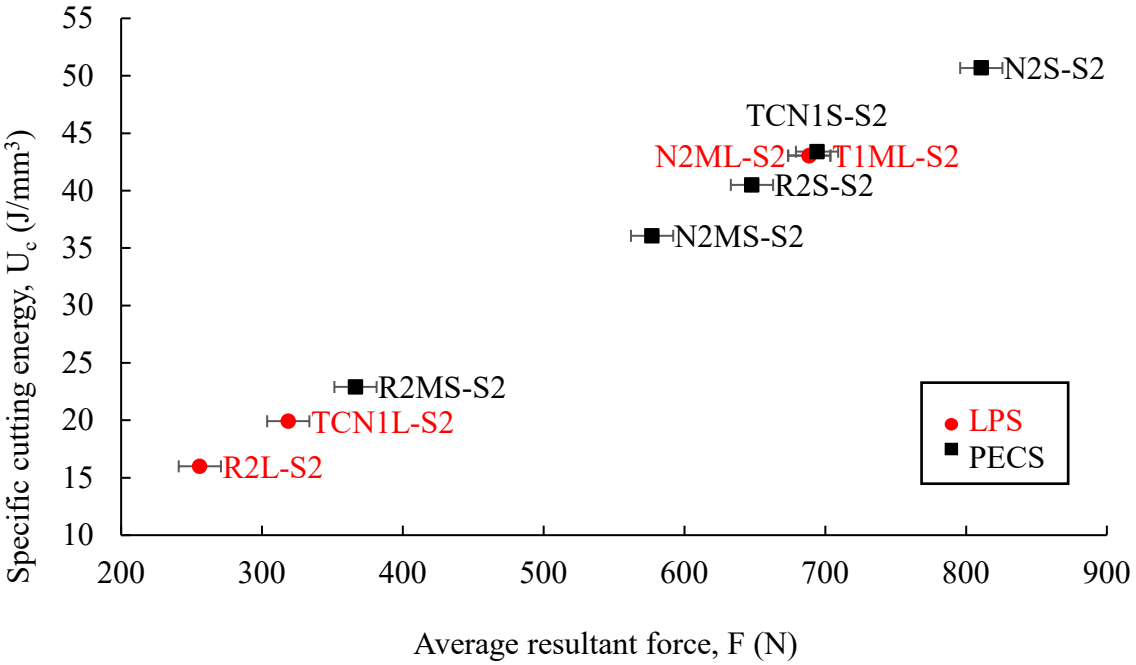


Figure 6-10. Variation of the specific cutting energy (U_c) with the average resultant force (F) for S2 cutting inserts during finishing 1 at n = 1600 rpm and a_p = 0.5 mm

Figure 6.11 shows the variations of average machining temperature with the average resultant force for the shark skin LSM (S2) cutting inserts during finishing 1. As shown in the figure, there was no obvious trend between the T and F values of S2 cutting inserts. From the figure, it can be seen that the

R2MS-S2 cutting insert had the lowest average machining temperature (64.83 ± 0.59 °C) among the S2 cutting inserts. The TCN1S-S2 cutting insert, on the other hand, exhibited the highest average machining temperatures. The figure shows that there was a significant difference in the machining temperatures of TCN1S-S2, T1ML-S2 and N2ML-S2 cutting inserts, despite having similar average resultant cutting forces. The average machining temperature of R2S-S2 and N2S-S2 cutting inserts were similar even though the average resultant cutting force of the latter was slightly higher than that of the former.

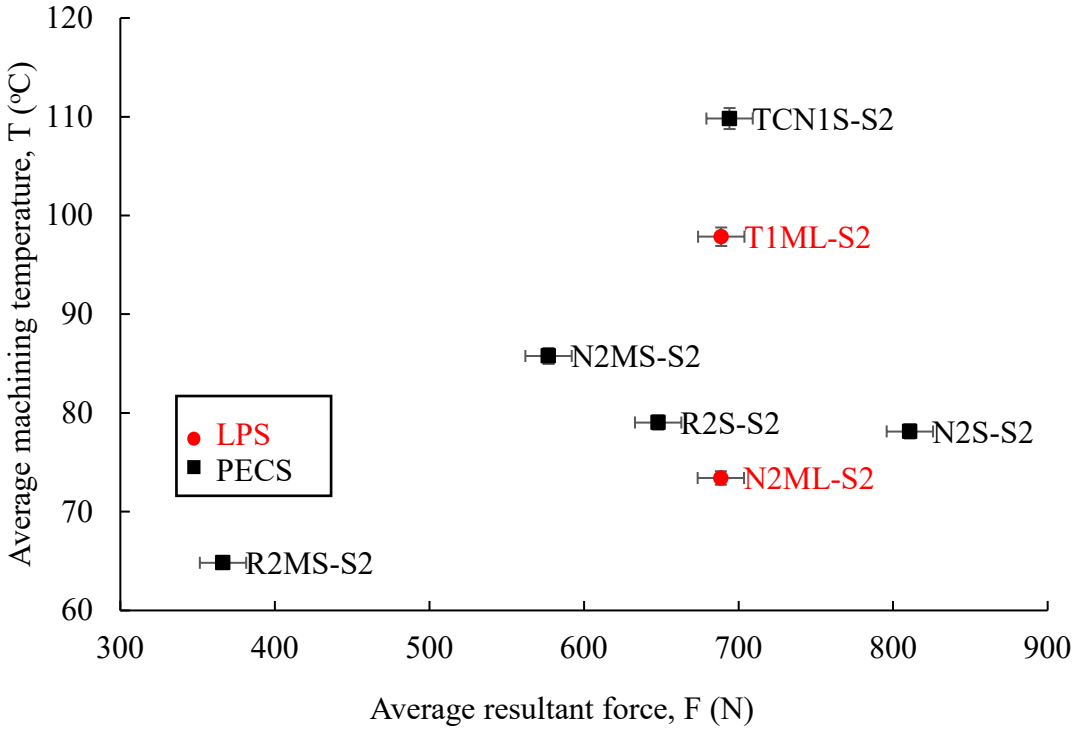


Figure 6-11. Variation of the average machining temperature (T) with the average resultant force (F) for shark skin (S2) cutting inserts during finishing 1

6.2.2. Analyses of insert tool life and wear performance of S2 cutting inserts.

Table 6.4 shows the cutting insert tool life and wear performance results of S2 cutting inserts. Figure 6.12 depicts the variation of the maximum flank wear rate with the cutting duration for the S2 cutting edges during finishing 1. From Figure 6.12, it can be observed that the T1ML-S2 cutting insert is the only one that managed to reach 20 minutes duration of machining. The insert had a VB_{max} of 78.34 µm after the 20 minutes of machining. The N2S-S2 cutting had the highest VB_{max} (i.e., 134.45 µm after 11 minutes) among the S2 cutting inserts. The R2MS-S2 cutting insert had the lowest maximum flank wear. However, the cutting insert was among those that exhibited poor tool life performance. The TCN1S-S2 and R2S-S2 cutting inserts had very similar insert tool life and wear performances. As

shown in the figure, both cutting inserts exhibited VB_{max} of 69.45 µm and 72.23 µm after 14 minutes of machining respectively. In general, the PECS produced NbC-Ni based cutting inserts had better insert tool life performance than their LPS produced counterparts.

Table 6.4. Cutting insert tool life, maximum flank wear, and flank wear rate results of S2 cutting inserts during finishing at n = 1600 rpm and a_p = 0.5 mm

Insert name	Insert tool life, I_l (min)	Maximum flank wear, VB_{max} (µm)	Flank wear rate, FWR (µm/min)
T1ML-S2	20	78.34	3.92
N2S- S2	11	134.45	12.22
N2ML-S2	8	101.12	12.64
N2MS-S2	11	86.67	7.88
R2L-S2	1	82.23	82.23
R2S-S2	14	72.23	5.16
R2MS-S2	6	57.78	9.63
TCN1L-S2	1	77.23	77.23
TCN1S-S2	14	69.45	4.96

Figure 6.13 depicts the effects of shark skin LSM on the cutting insert tool life performance of S2 cutting inserts. The figure shows the improvement or reduction of insert tool life of S2 cutting inserts in comparison to the B2 cutting inserts. There was neither improvement nor reduction in the insert tool life performances of the T1ML-S2, N2S-S2 and R2L-S2 cutting inserts due to shark skin LSM. Figure 6.13 shows that the only improvement in the insert tool life performance was observed on the N2M based cutting inserts whereby the N2ML-S2 and the N2MS-S2 cutting inserts' tool life performance improved by 33% and 38% respectively. As shown in the figure, the shark skin LSM decreased the cutting duration (tool life) of the majority of the cutting inserts. The TCN1L-S2 cutting insert had the highest tool life performance reduction. From the figure, it can be seen that the cutting insert exhibited about 75% insert tool life reduction. This was followed by the R2MS-S2, and R2S-S2 and TCN1S-S2 cutting inserts with insert tool life reductions of 70% and 30%, respectively.

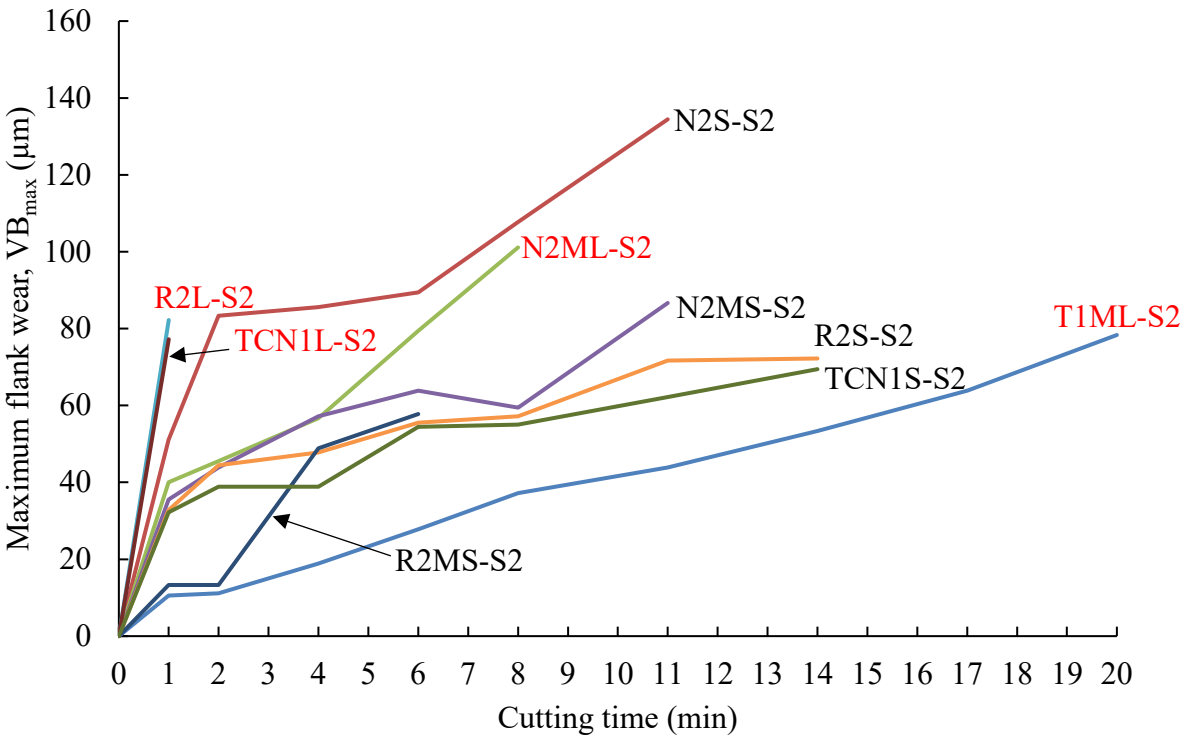


Figure 6-12. Variation of the maximum flank wear (VB_{max}) cutting time (l_l) for shark skin LSM (S2) cutting inserts during finishing at n = 1600 rpm and a_p = 0.5 mm

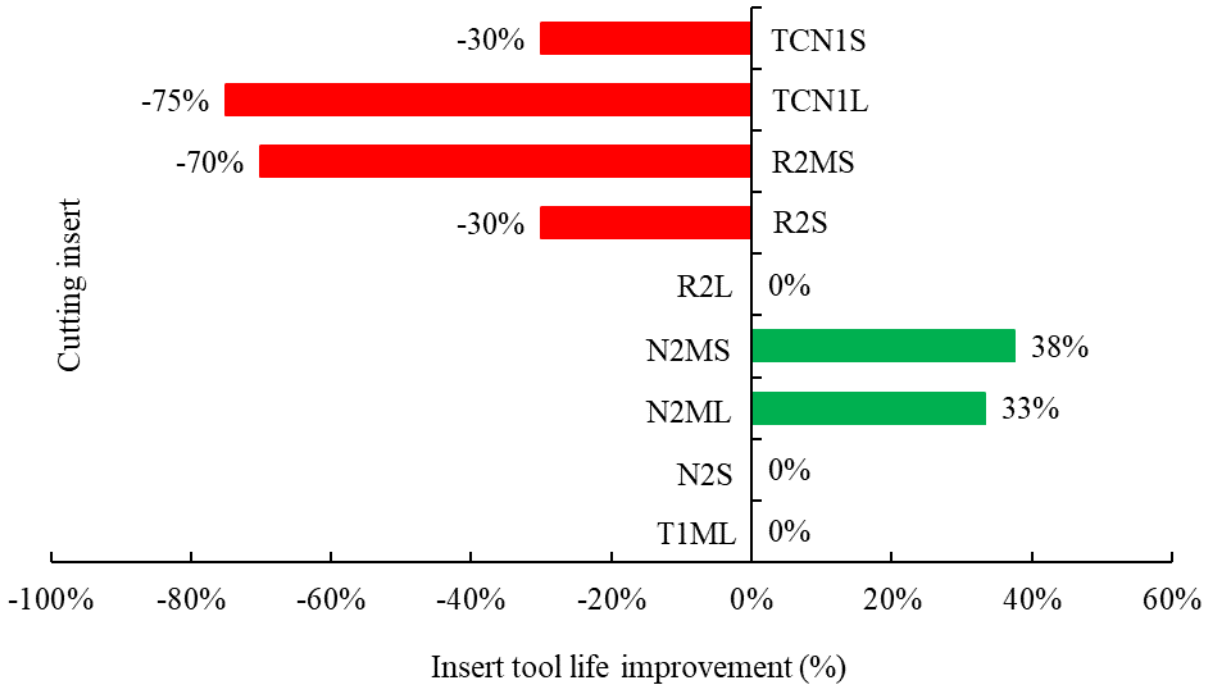


Figure 6-13. Effects of shark skin LSM technique on the S2 cutting inserts tool life performance benchmarked against B2 cutting inserts during finishing at n = 1600 rpm and a_p = 0.5 mm

Figure 6.14 shows the variation of the flank wear rate with the average resultant force for shark skin LSM (S2) cutting inserts. The expected linear relationship between FWR and F was not observed on the S2 cutting inserts. For example, the T1ML-S2 cutting insert had lower FWR compared to R2L-S2, TCN1L-S2, and R2MS-S2 and yet the average resultant cutting forces of these cutting inserts are significantly lower than that of the T1ML-S2. Another example is on the N2S-S2 and N2ML-S2 cutting inserts whose FWR are similar (~12 µm/min) even though the former has a slightly higher F value than the latter. From the figure, it can be observed that in general, the NbC-Ni based LPS produced cutting inserts had higher FWR compared to their PECS produced counterparts.

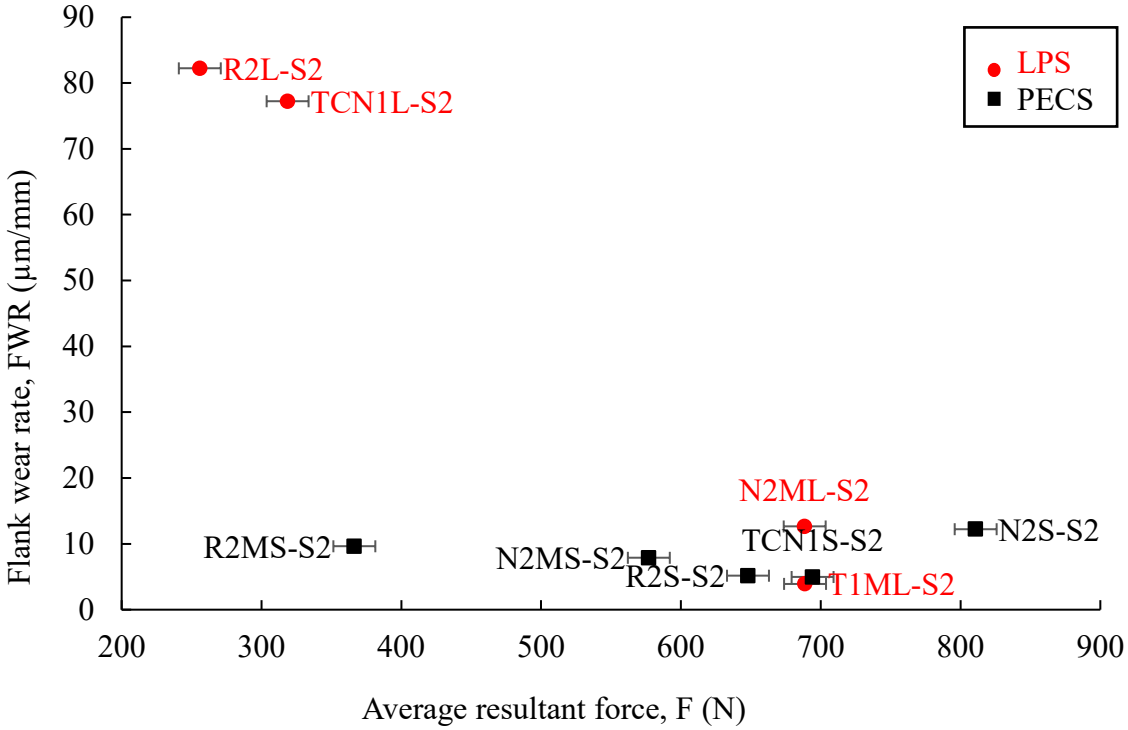


Figure 6-14. Variation of the flank wear rate (FWR) with the average resultant force (F) for shark skin LSM (S2) cutting inserts during finishing 1

Figure 6.15 shows the comparison of the FWR of B2 cutting inserts against S2 cutting inserts. From the figure, it can be seen that during machining under the finishing 1 conditions, the shark skin LSM technique increased the FWR of the majority of the cutting inserts. The shark skin LSM (S2) technique increased FWR of all the cutting inserts except for the N2MS-S2 and TCN1S-S2 cutting inserts whose FWRs were reduced by 33% and 8%, respectively. The TCN1L-S2 and R2MS-S2 had the highest increase in the FWRs with the cutting inserts increasing the FWR by 683% and 148% respectively. The R2L-S2 and T1ML-S2 cutting inserts had increases of approximately 90% and 74% in the FWRs respectively. Lastly, from the figure, it can be seen that there was no significant change in the FWR of the N2ML-S2 and R2S-S2 cutting inserts.

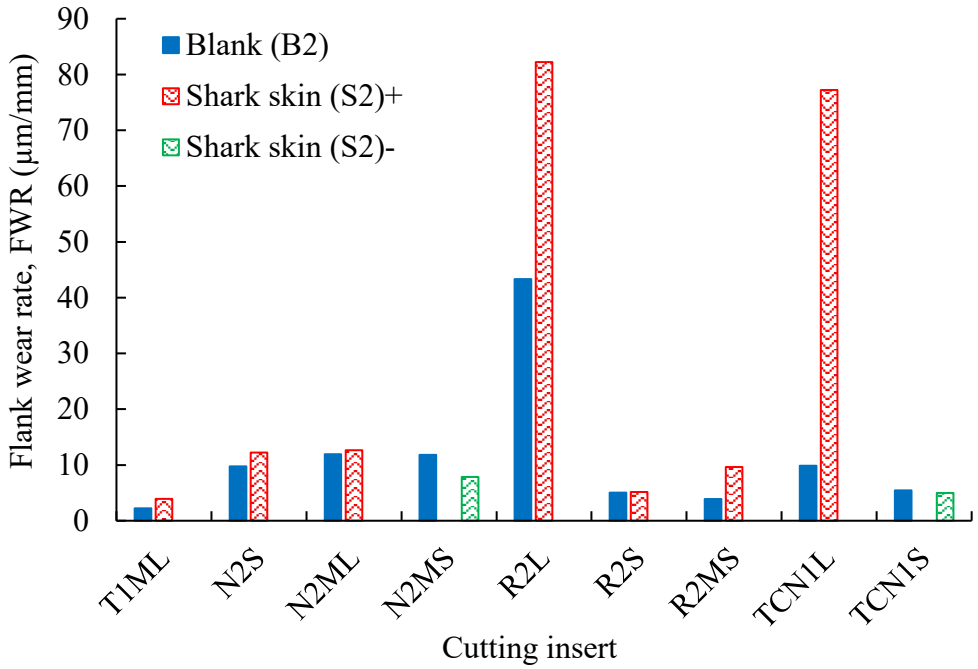


Figure 6-15. Comparison of the flank wear rate of blank (B2) vs. shark skin LSM (S2) cutting inserts during finishing 1

6.2.3. Analyses of micrographs of the flank and rake faces of S2 cutting inserts

This subsection provides optical micrograph analyses of shark skin LSM (S2) cutting inserts. Figure 6.16 shows the optical micrographs of the flank and the rake faces of (a) T1ML-S2, (b) TCN1S-S2, and (c) R2S-S2 cutting inserts. As observed in the figure, abrasion wear was the main wear mechanism on the flank of the T1ML-S2 cutting insert. The cutting edge of the insert also exhibited chipping as shown on the flank face in Figure 6.16 (a). Mechanical fracture, chipping and crater wear were also observed on the rake face of T1ML-S2 cutting insert. The insert tool life of T1ML-S2 was 20 minutes as indicated in the figure. However, unlike its B2 counterpart, the cutting insert could not be used to machine beyond the preset 20 minutes machining duration. Mechanical fracture, abrasion wear (grooves), and removed surface layer of shark skin patterns were observed on the flank faces of the TCN1S-S2 and R2S-S2 cutting inserts (see Figures 6.16 (b) and (c), respectively). The TCN1S-S2 and the R2S-S2 cutting inserts had very similar wear performances on the flank and the rake faces as shown in the figure. Figure 6.16 (b) also shows that there was welding of the workpiece material on the rake face of the TCN1S-S2 during machining. The optical micrographs of the other S2 cutting inserts were analysed and the micrographs showed that the cutting inserts exhibited very similar cutting edge wear behaviour. The cutting edge wear on the flank faces was mainly characterised by abrasion wear (grooves and ridges) and mechanical fracture. The rake faces of the cutting inserts, on the other hand,

exhibited major mechanical fracture, chipping and cracking. Similar to B2 cutting inserts, the main wear and failure mechanisms of S2 cutting inserts were abrasion wear and mechanical fracture.

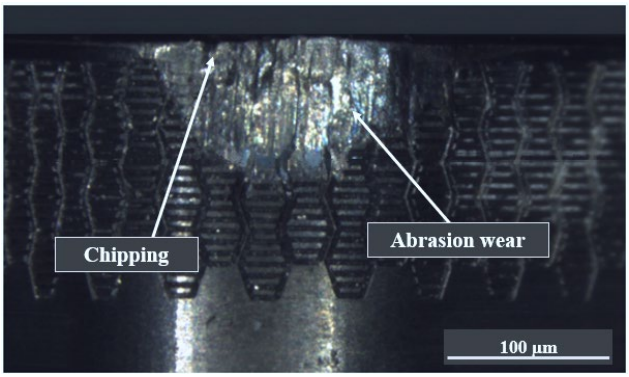
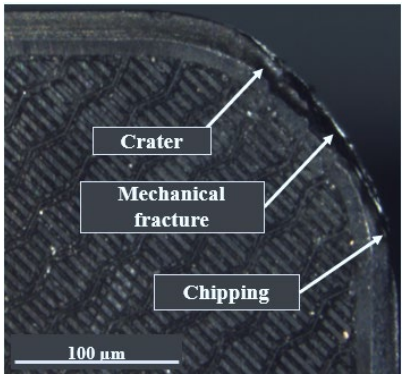
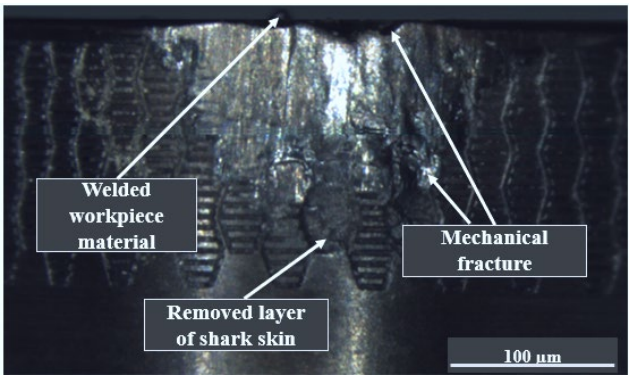
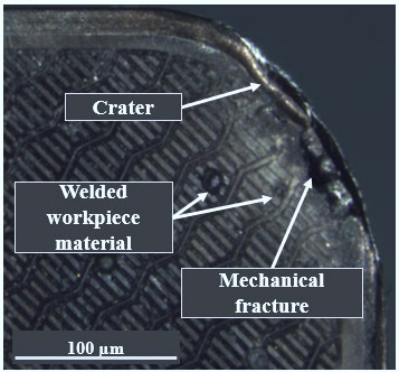
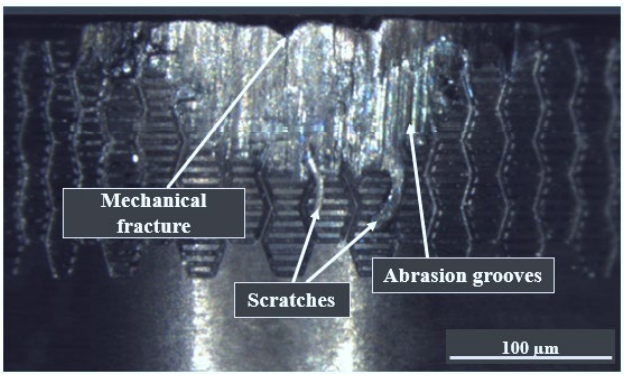
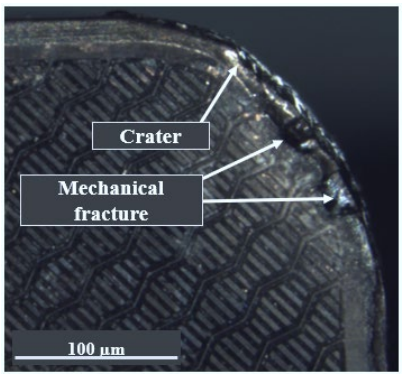
Insert	Flank face	Rake face
(a) T1ML-S2		
	VB_{max} = 78.34 µm Cutting time = 20 minutes	
(b) TCN1S-S2		
	VB_{max} = 69.45 µm Cutting time = 14 minutes	
(c) R2S-S2		
	VB_{max} = 72.23 µm Cutting time = 14 minutes	

Figure 6-16. Optical micrographs of the flank and rake faces of (a) T1ML-S2, (b) TCN1S-S2 and (c) R2S-S2 cutting edges during finishing 1 machining

6.2.4. Machining performance evaluation and analyses of S2 cutting inserts

Figure 6.17 shows the variation of specific cutting energy with the cutting time of the S2 cutting inserts. As shown in the figure, the T1ML-S2 cutting insert had a better combination of the machining performance criteria. Even though the cutting insert was among the inserts with high energy consumption, it was able to reach the tool life of 20 minutes (i.e. the longest among S2 cutting inserts). The R2L-S2 cutting insert had the lowest specific cutting energy and the shortest insert tool life, as such the cutting insert had the poorest combination of the machining performance criteria. From the figure, it can also be observed that the PECS produced S2 cutting inserts had better combinations of the machining performance criteria than their LPS produced counterparts. Additionally, the figure indicates that the additions of Mo, TiC and TiC_7N_3 to the N2S-S2 improved the overall machining performances of N2MS-S2, R2S-S2 and TCN1S-S2 respectively. For instance, U_c was reduced in these cutting inserts while the insert tool life was increased in R2S-S2 and TCN1S-S2, respectively.

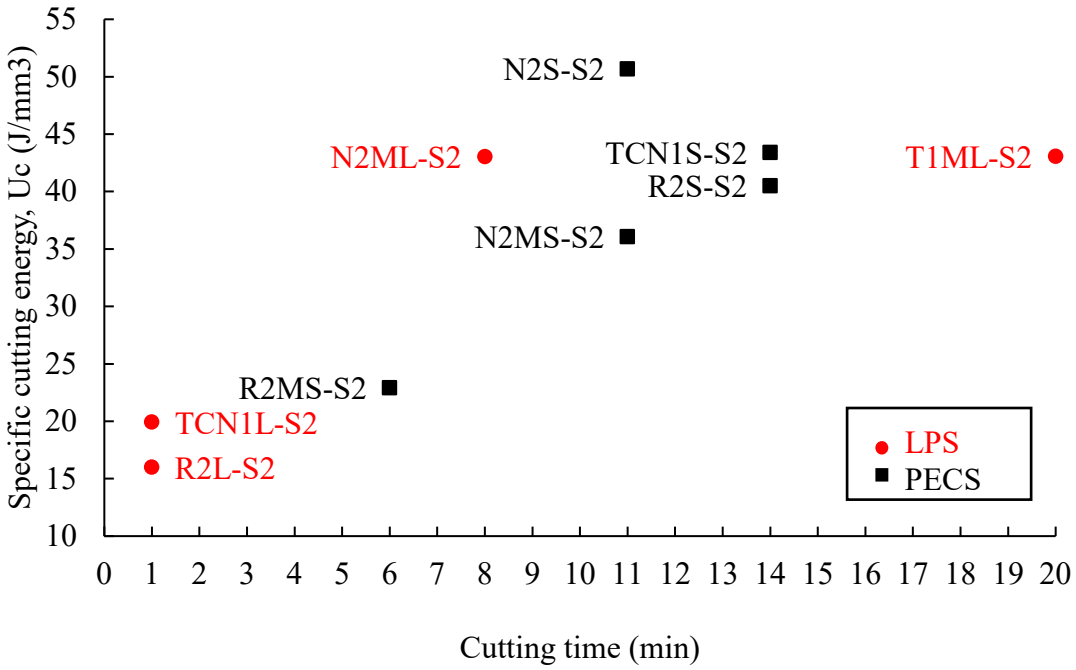


Figure 6-17. Variation of specific cutting energy (U_c) with cutting time (I_t) for shark skin LSM (S2) cutting inserts during finishing 1 at n = 1600 rpm and a_p = 0.5 mm

Figure 6.18 shows the overall preference score (O_i) and rank of the shark skin LSM (S2) cutting inserts used during finishing 1. The cutting inserts are coded according to rank (best top three ranked cutting inserts in green, average, and worst ranked in amber and red respectively). From the figure, it can be seen that the top three ranked S2 cutting inserts were T1ML-S2, R2S-S2 and TCN1S-S2 cutting inserts. The average performing ones were the N2MS-S2, N2S-S2 and N2ML-S2 cutting inserts. Lastly, the R2MS-S2, R2L-S2 and TCN1L-S2 fell under the poor performing cutting inserts category.

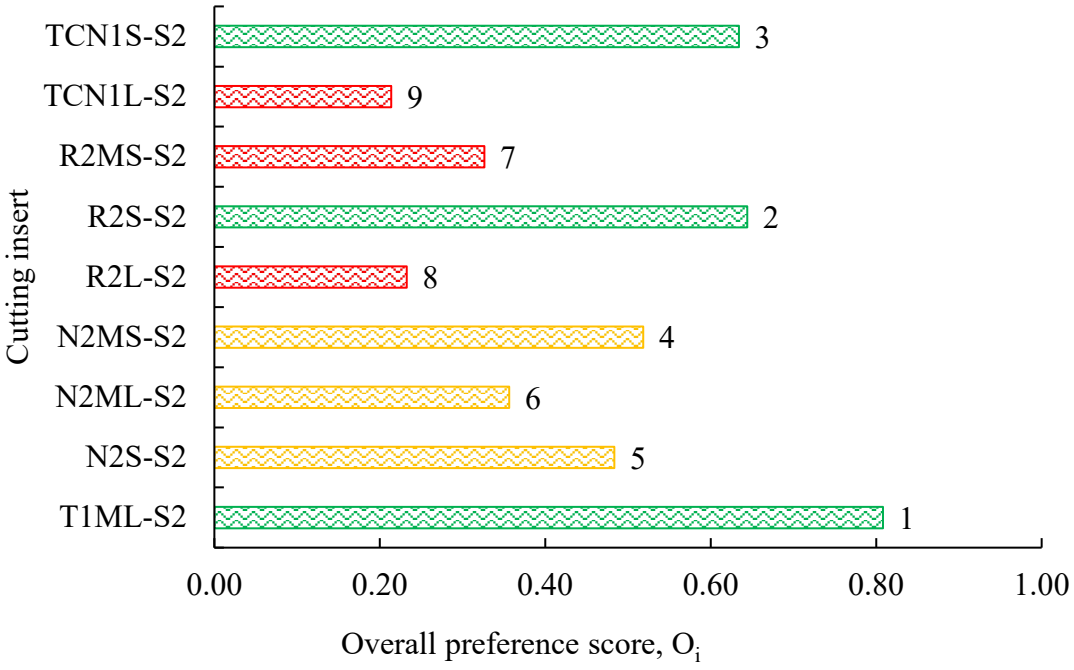


Figure 6-18. Overall preference score (O_i) and rank of S2 cutting inserts (alternatives)

6.3. Analyses of the pyramid LSM (P2) cutting inserts

This subsection presents and analyses resultant cutting forces, specific cutting energy, insert life, wear and temperature of the pyramid LSM cutting inserts during the face milling of a-GCI under finishing 1 conditions. The micrographs of the cutting inserts showing the flank and rake sides are also presented in this section. Lastly, the machining performance evaluation of the pyramid LSM cutting inserts is done to rank the cutting inserts.

6.3.1. Analysis of the resultant forces, specific cutting energy, and temperature of the P2 cutting inserts

Table 6.5 gives the resultant forces, specific cutting energy (energy consumption) and the average machining temperature of the pyramid LSM (P2) cutting edges during finishing 1. Figure 6.19 shows the average resultant forces and the maximum resultant forces experienced by P2 cutting inserts during machining. As shown in the figure, the F_{max} of the P2 cutting inserts (with the exception of R2MS-P2), exceeded 1500 N. From the figure, it can also be seen that in general, the maximum resultant cutting forces experienced by the cutting inserts were significantly higher than the average resultant forces. The R2MS-P2 cutting insert had the lowest F_{max}, followed by the TCN1L-P2. It is worth noting that for these two cutting inserts, the value of F_{max} was the same as that of the average resultant cutting force (see Table 6.5). The cutting insert which experienced the highest F_{max} was the R2S-P2 (2332 N),

followed by the N2MS-P2 cutting insert as shown in Table 6.5 and Figure 6.19. As shown in the figure, the T1ML-P2, N2S-P2, and TCN1S-P2 had very similar F_{max} values. The average resultant force of the P2 cutting inserts exhibited a similar trend to that of the maximum resultant force (see Figure 6.19). The N2ML-P2 had the lowest average resultant force among the P2 cutting inserts, whilst the R2L-P2 had the highest respectively. In general, the NbC-Ni based LPS produced cutting inserts had slightly lower cutting forces compared to their PECS produced counterparts.

Table 6.5. Machining forces, specific energy consumption, and temperature results of P2 cutting inserts during finishing at n = 1600 rpm and a_p = 0.5 mm

Insert name	Average resultant force, F (N)	Maximum resultant force, F_{max} (N)	Specific cutting energy, U_c (J/mm^3)	Average Temperature, T (ºC)
T1ML-P2	1294	1789	80.85	93.88 ± 0.50
N2S- P2	1305	1797	81.56	87.10 ± 0.83
N2ML-P2	1097	1725	68.54	73.02 ± 0.67
N2MS-P2	1256	2068	78.53	106.98 ± 1.04
R2L-P2	1573	1573	98.29	-
R2S-P2	1307	2332	81.66	96.75 ± 0.93
R2MS-P2	1427	1427	89.16	-
TCN1L-P2	1525	1525	95.30	-
TCN1S-P2	1265	1796	79.05	91.40 ± 0.80

*NB: The average and maximum resultant force have a fixed error of ±15 N from the Kistler.

Figure 6.20 shows the relationship between the specific cutting energy and the average resultant cutting force of P2 cutting inserts. As expected, the figure shows that the N2ML-P2 had the lowest U_c (~69 J/mm^3) per volume of material removed during machining. With the exception of the N2ML-P2, the specific cutting energy of the P2 cutting inserts exceeded 78 J/mm^3. As shown in the figure, the cutting insert that had the highest energy consumption was the R2L-P2 which had U_c of ~98 J/mm^3. The figure also shows that there were no significant differences in the energy consumption between the T1ML-P2, R2S-P2 and N2S-P2 cutting inserts. A similar observation was also made between the N2MS-P2 and TCN1S-P2 cutting inserts.

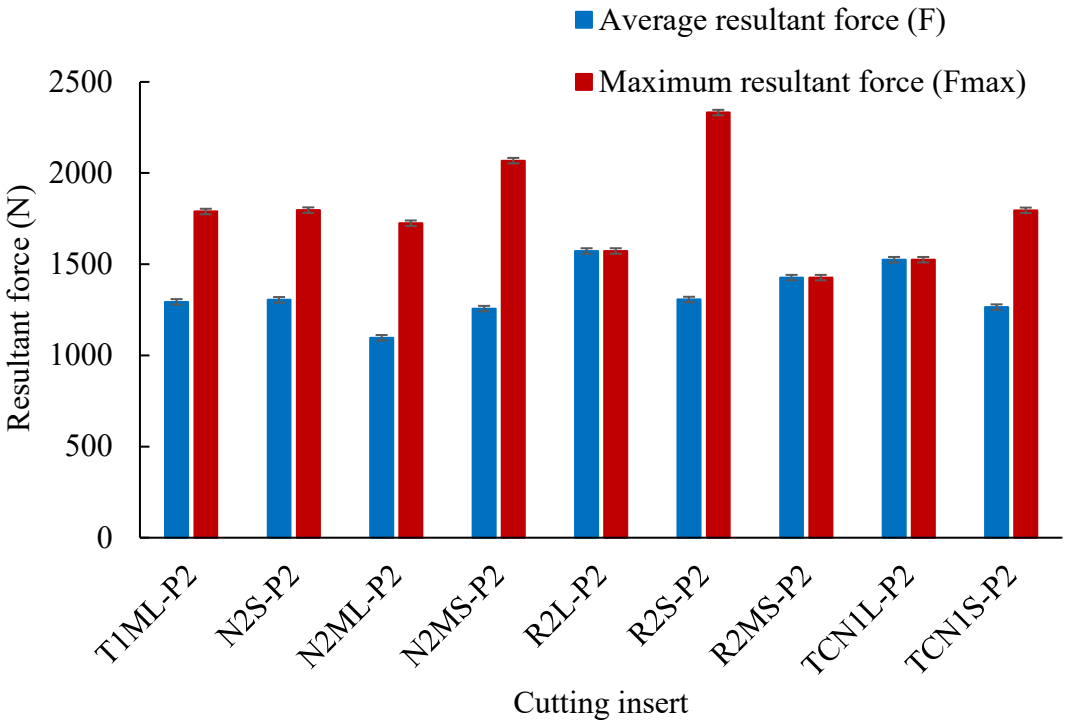


Figure 6-19. Average resultant force (F) and maximum resultant force (F_{max}) for P2 cutting inserts during finishing at n = 1600 rpm and a_p = 0.5 mm

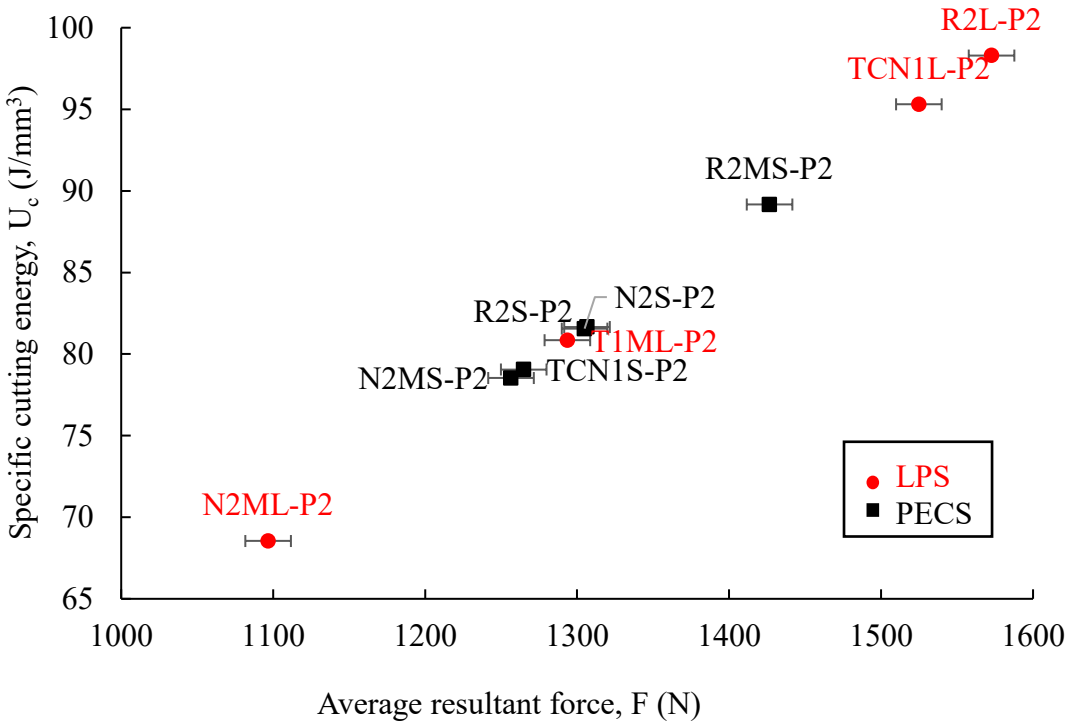


Figure 6-20. Variation of the specific cutting energy (U_c) with the average resultant force (F) for P2 cutting inserts during finishing 1 at n = 1600 rpm and a_p = 0.5 mm

Figure 6.21 shows the variations of the average machining temperature with the average resultant cutting force of the pyramid LSM (P2) cutting inserts during finishing 1. From the figure, it can be seen that there was no obvious trend between the two variables. The N2ML-P2 cutting insert had the lowest average machining temperature (73.02 ± 0.67 °C), whereas its PECS produced counterpart (N2MS-P2) exhibited the highest machining temperature (106.98 ± 1.04 °C) (see Table 6.5 and Figure 6.21). As shown in the figure, the additions of Mo, TiC, and TiC_7N_3 into N2S-P2 resulted in an increase of T in N2MS-P2, R2S-P2 and TCN1S-P2 cutting inserts.

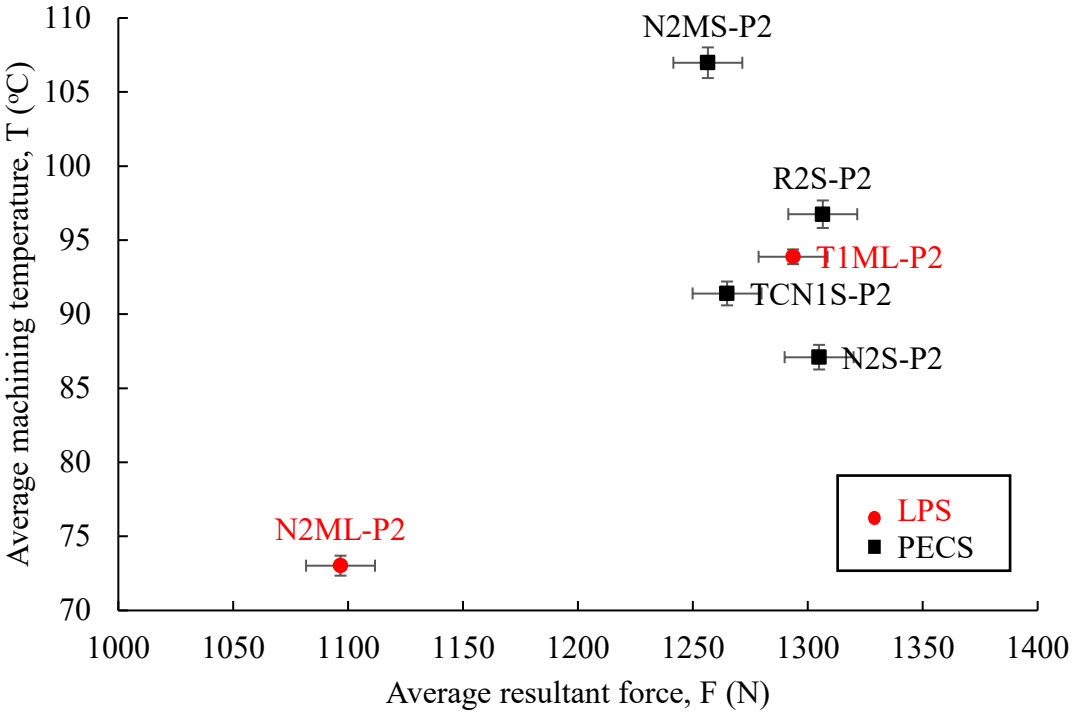


Figure 6-21. Variation of the average machining temperature (T) with the average resultant force (F) for pyramid (P2) cutting inserts during finishing 1

6.3.2. Analyses of insert tool life and wear performance of P2 cutting inserts

Table 6.6 shows the cutting insert tool life and wear performance results of P2 cutting inserts. Figure 6.22 depicts the variation of the maximum flank wear with the cutting time for pyramid LSM (P2) cutting inserts during finishing 1. From the figure, it can be seen that the VB_{max} of all the P2 cutting inserts irrespective of the sintering technique or composition was less than 140 µm. As shown in the figure, only T1ML-P2 and R2S-P2 cutting inserts achieved the insert tool life performance of 20 minutes. Although they had similar machining duration, it was observed that the latter had a higher VB_{max} than the former (see Table 6.6 and Figure 6.22). The figure shows that the R2MS-P2 cutting insert had the lowest VB_{max} (17.78 µm). However, the cutting insert was among the poor performing

cutting inserts in terms of insert tool life. The N2MS-P2 exhibited the highest VB_{max} among the P2 cutting inserts, with the inserts having VB_{max} of 130.56 µm after 17 minutes of machining. From the figure, it can be seen that the addition of Mo, TiC, and TiC_7N_3 into N2S-P2 improved the insert tool life performances of N2MS-P2, R2S-P2 and TCN1S-P2 cutting inserts. In general, the PECS produced NbC-Ni based cutting inserts had better insert tool life performance than their LPS produced counterparts.

Table 6.6. Cutting insert tool life, maximum flank wear, and flank wear rate results of P2 cutting inserts during finishing at n = 1600 rpm and a_p = 0.5 mm

Insert name	Insert tool life, I_l (min)	Maximum flank wear, VB_{max} (µm)	Flank wear rate, FWR (µm/min)
T1ML-P2	20	48.34	2.42
N2S- P2	11	85.56	7.78
N2ML-P2	6	70.56	11.76
N2MS-P2	17	130.56	7.68
R2L-P2	1	53.89	53.89
R2S-P2	20	118.89	5.94
R2MS-P2	1	17.78	17.78
TCN1L-P2	1	39.45	39.45
TCN1S-P2	17	85.56	5.03

Figure 6.23 shows the effects of pyramid LSM on the cutting insert tool life performance. The figure shows the percentage improvement (green) or reduction (red) of the insert tool life of P2 cutting inserts compared to the blank (B2) cutting inserts. As shown in the figure, the majority of the cutting inserts had a 0% improvement. The figure shows that only the N2MS had an improvement in insert tool life performance of 115%. From the figure, it was also observed that the pyramid LSM technique reduced the insert tool life of R2MS-P2, TCN1L-P2 and TCN1S-P2 cutting inserts by 95%, 75% and 15% respectively.

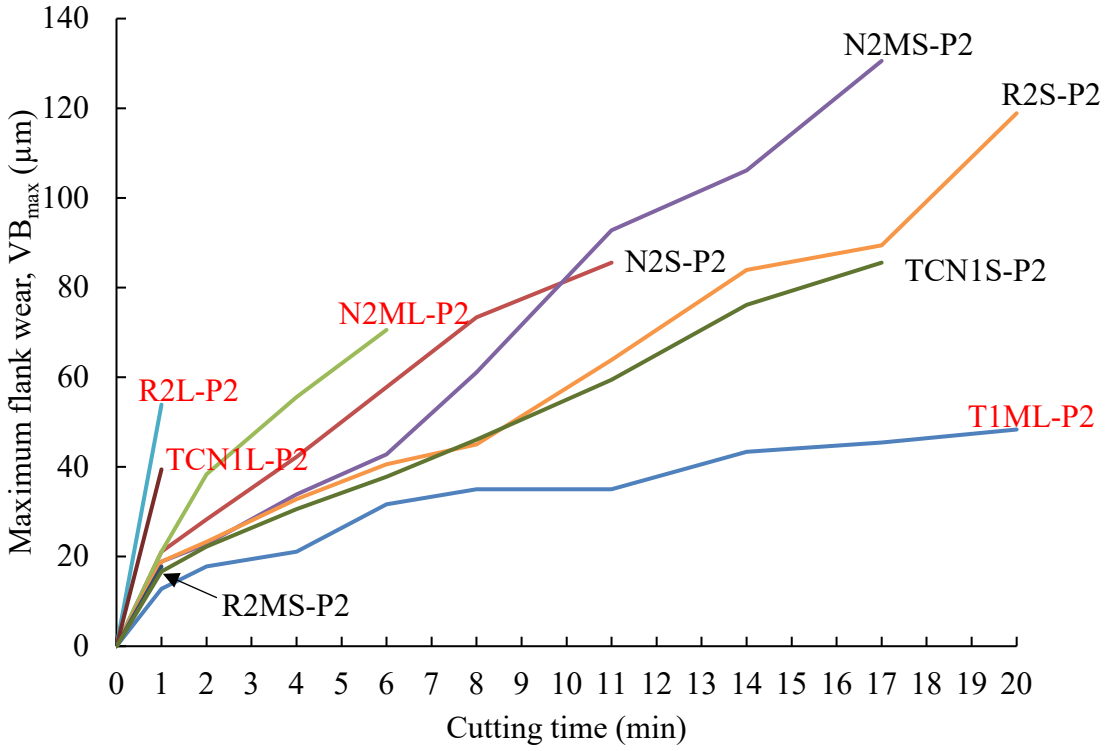


Figure 6-22. Variation of the maximum flank wear (VB_{max}) cutting time (l_l) for pyramid LSM (P2) cutting inserts during finishing at n = 1600 rpm and a_p = 0.5 mm

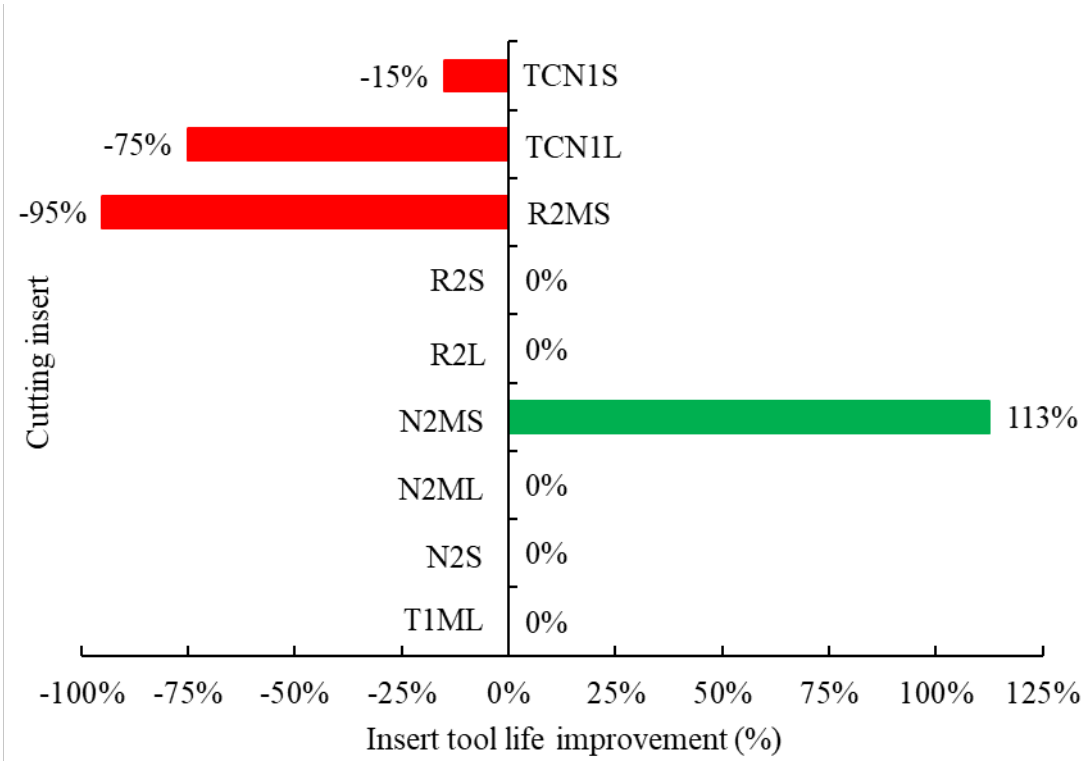


Figure 6-23. Effects of pyramid LSM technique on the P2 cutting inserts tool life performance benchmarked against B2 cutting inserts during finishing at n = 1600 rpm and a_p = 0.5 mm

Figure 6.24 depicts the variation of the FWR with F for the P2 cutting inserts. Similar to both B2 and S2 cutting inserts, the expected linear relationship between the two variables was not deductible from the figure. For example, the T1ML-P2 cutting insert had the lowest FWR (2.42 µm/min) among the P2 cutting inserts, although the inserts exhibited slightly higher average resultant cutting force compared to the N2ML-P2, N2MS-P2 and TCN1S-P2 cutting inserts respectively. Another example could be drawn from the T1ML-P2, R2S-P2 and N2S-P2 cutting inserts whose F values were similar, but the cutting inserts had slightly different FWR as shown in the figure. From the figure, it can be seen that there was no significant difference in FWRs of TCN1S-P2 and R2S-P2 as well as those of N2MS-P2 and N2S-P2 respectively. The figure also shows that the R2L-P2 cutting insert had the highest FWR (53.89 µm/min) among the P2 cutting inserts. In general, the PECS produced NbC-Ni based cutting inserts had lower FWR compared to their LPS produced cutting inserts.

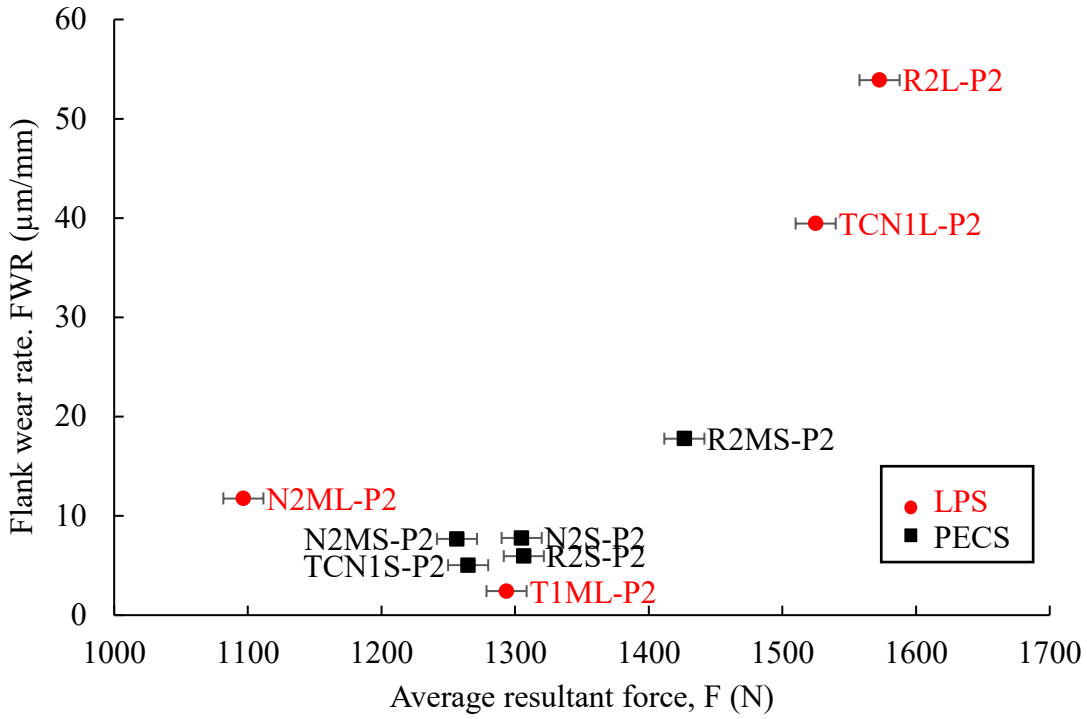


Figure 6-24. Variation of the flank wear rate (FWR) with the average resultant force (F) for pyramid LSM (P2) cutting inserts during finishing 1

Figure 6.25 shows the comparison of the FWR of B2 cutting inserts against P2 cutting inserts. From the figure, it can be observed that during machining under the finishing 1 conditions, the pyramid LSM technique improved (reduced) the FWR of some inserts while at the same time increasing the FWR of others. The increase in FWR is denoted by red while the reduction is denoted by green. As shown in the figure, there were no significant differences in the FWRs between the respective blank and pyramid LSM T1ML, N2ML, and TCNS cutting inserts. The pyramid LSM technique reduced the FWRs of

N2S-P2 and N2MS-P2 cutting inserts by 20% and 35% respectively. From the figure, it was observed that the technique increased the FWRs of the R2L-P2, R2S-P2, R2MS-P2 and TCN1L-P2 cutting inserts. The R2MS-P2 and TCN1L-P2 had approximately 357% and 300% increases in FWRs while those of the R2L-P2 and R2S-P2 were 25% and 18% respectively.

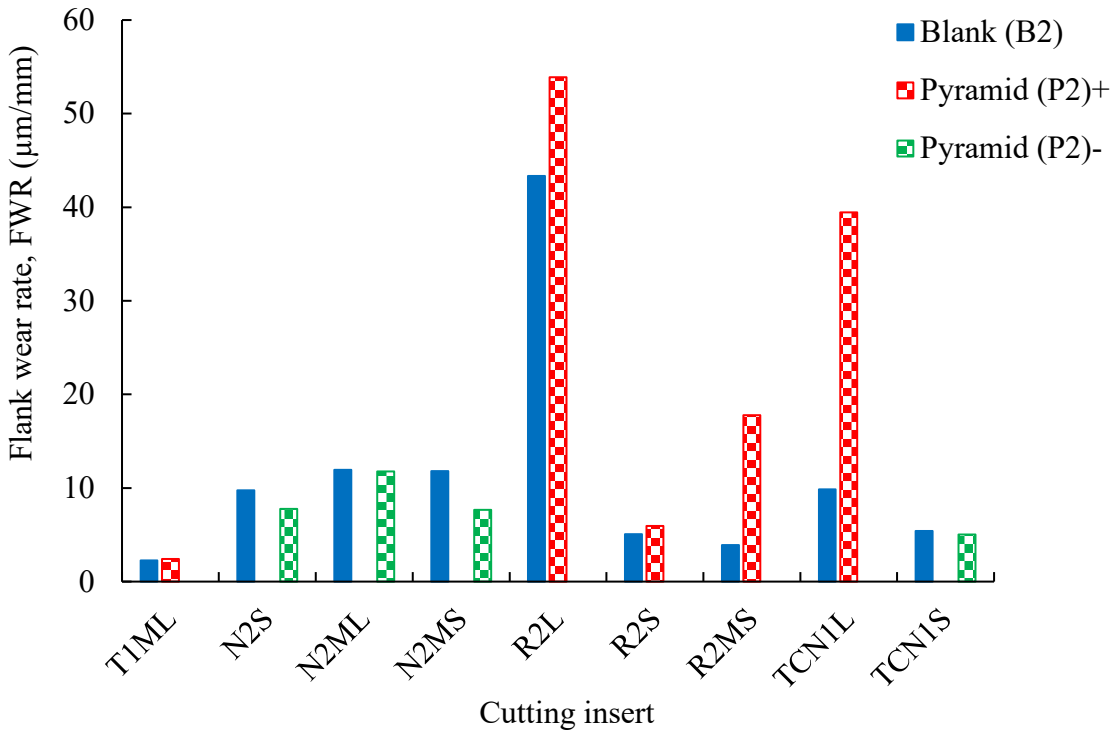


Figure 6-25. Comparison of the flank wear rate of blank (B2) vs. pyramid LSM (P2) cutting inserts during finishing 1

6.3.3. Analyses of micrographs of the flank and rake faces of P2 cutting inserts

This subsection provides optical micrographs analyses of pyramid LSM (P2) cutting inserts Figure 6.26 shows the optical micrographs of the flank and the rake faces of (a) T1ML-P2, (b) R2S-P2 and (c) TCN1S-P2 cutting inserts. The figure shows that the T1ML-P2 cutting insert experienced abrasive wear and chipping on the flank face of the insert. Crater wear was also observed on the rake face of the T1ML-P2 cutting insert. The insert tool life of T1ML-P2 was 20 minutes, however, similar to the S2 counterpart, the wear on the cutting edge prohibited the possibility of machining beyond 20 minutes. The R2S-P2 and TCN1S-P2 cutting inserts exhibited abrasion wear and mechanical fracture on the flank faces as shown in the figure. The rake faces of the two cutting inserts show that the cutting edges experienced mechanical fracture and major chipping (see Figures 6.26 (b) and (c)). Figure 6.26 (b) further shows that the rake face of the R2S-P2 cutting insert experienced some crater wear during machining.

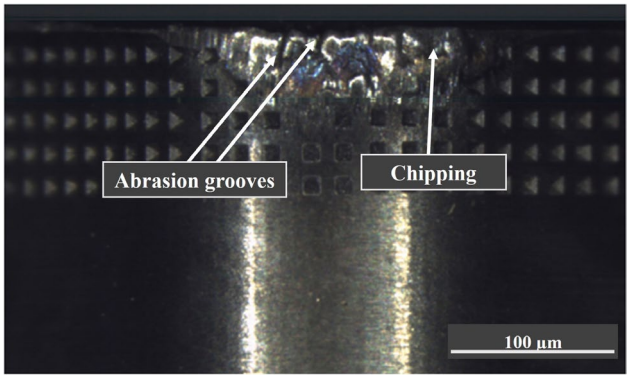
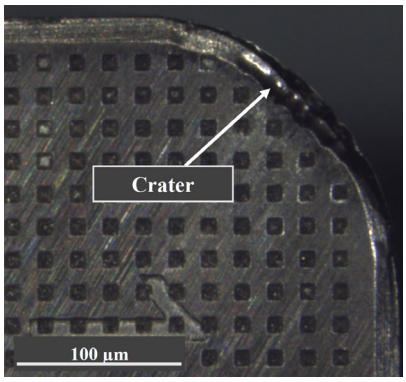
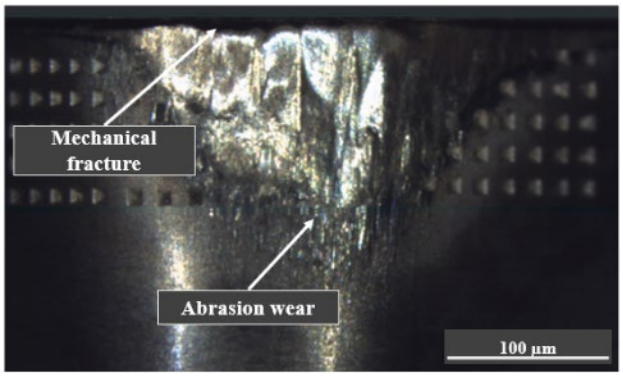
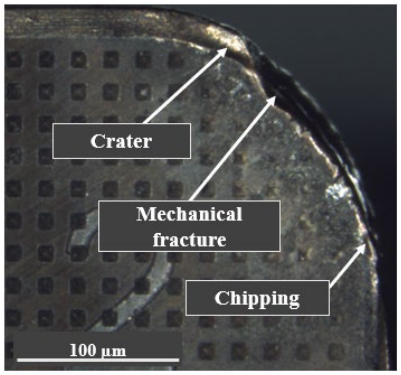
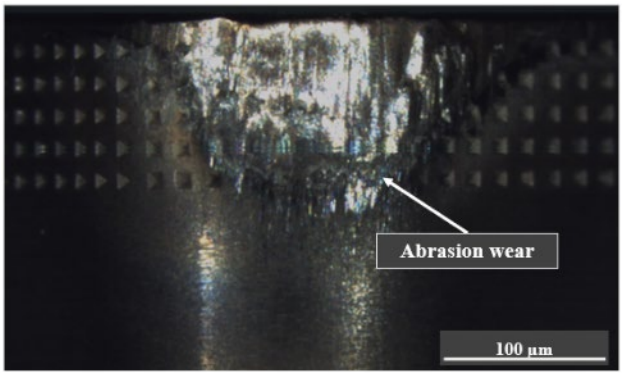
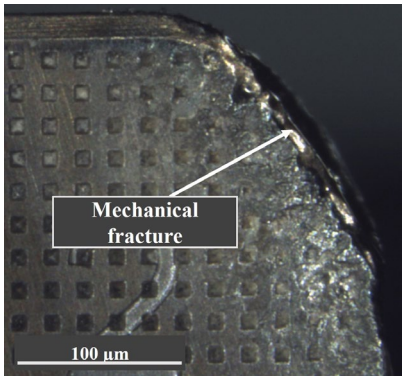
Insert	Flank face	Rake face
(a) T1ML-P2		
	VB_{max} = 48.34 µm Cutting time = 20 minutes	
(b) R2S-P2		
	VB_{max} = 118.89 µm Cutting time = 20 minutes	
(c) TCN1S-P2		
	VB_{max} = 85.56 µm Cutting time = 17 minutes	

Figure 6-26. Optical micrographs of the flank and rake faces of (a) T1ML-P2, (b) R2S-P2 and (c) TCN1S-P2 cutting edges during finishing 1 machining

The optical micrographs of the rest of P2 cutting inserts were also analysed. Similar to their S2 counterparts, the flank and rake faces of N2S-P2, N2ML-P2 and N2MS-P2 revealed very similar cutting edge wear characteristics. A similar observation was made for the TCN1L-P2 and R2L-P2

cutting inserts, respectively. In general, the main cutting edge wear was characterised by abrasion wear, and mechanical fracture.

6.3.4. Machining performance evaluation and analyses of P2 cutting inserts

Figure 6.27 shows the variation of specific cutting energy with the cutting time of the P2 cutting inserts. As shown in the figure, the T1ML-P2 and R2S-P2 had very similar machining performance. The two cutting inserts had the best combinations of the machining performance criteria with both inserts obtaining 20 minutes insert tool life while consuming a similar amount of energy. The N2ML-P2 cutting insert had the lowest specific cutting energy among the P2 cutting inserts. However, it can be seen from the figure that the cutting insert had poor to average insert tool life. The figure shows that there was no significant difference between the machining performances of the N2MS-P2 and TCN1S-P2 cutting inserts. Similar to their B2 and S2 counterparts, the R2L-P2 and TCN1L-P2 cutting inserts had the poorest combinations of the machining performance criteria. Generally, the PECS produced P2 cutting inserts had better combinations of the machining performance criteria than their LPS counterparts. In addition, the overall machining performances of R2S-P2, N2MS-P2 and TCN1S-P2 improved due to the respective additions of TiC, Mo and TiC_7N_3 to the composition of N2S-P2 cutting insert. Figure 6.28 depicts the overall preference score (O_i) and rank of the pyramid LSM (P2) cutting inserts used during finishing 1. In the figure, the cutting inserts are colour coded according to their rank with the top three being green, average coded amber and the poorly ranked being red, respectively. As expected, the T1ML-P2, R2S-P2, and N2MS-P2 were the top ranked cutting inserts, while the R2MS-P2, TCN1L-P2 and R2L-P2 were the poorly ranked cutting inserts, respectively.

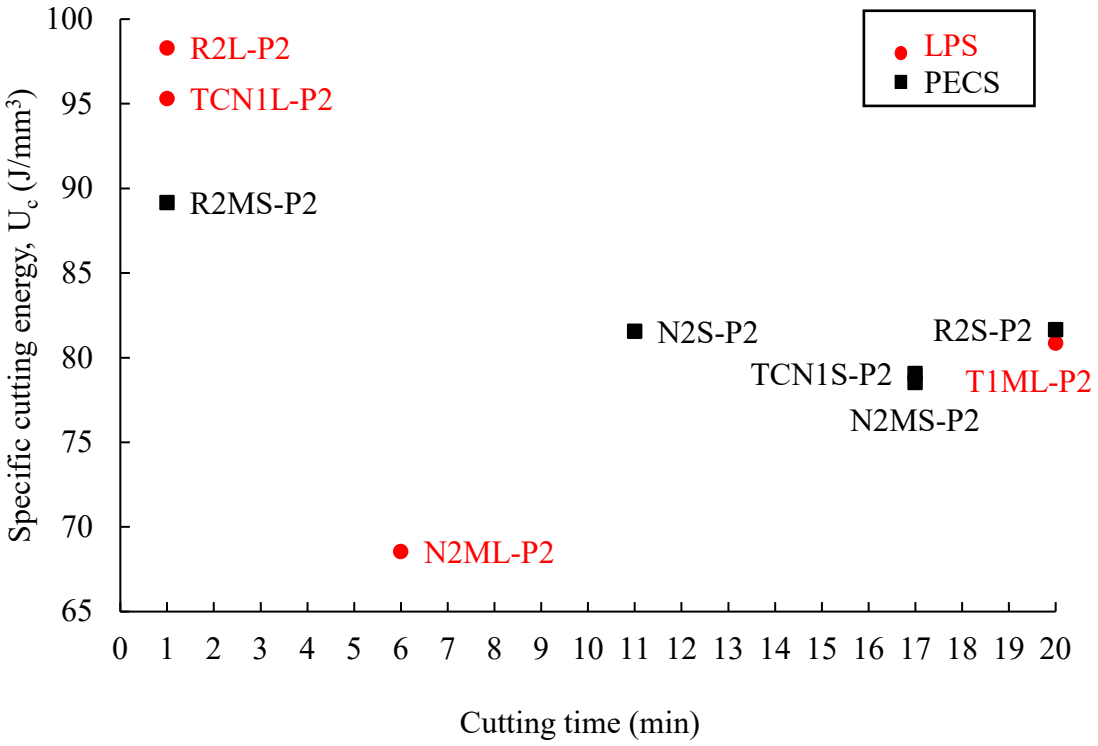


Figure 6-27. Variation of specific cutting energy (U_c) with cutting time (l_l) for pyramid LSM (P2) cutting inserts during finishing 1 at n = 1600 rpm and a_p = 0.5 mm

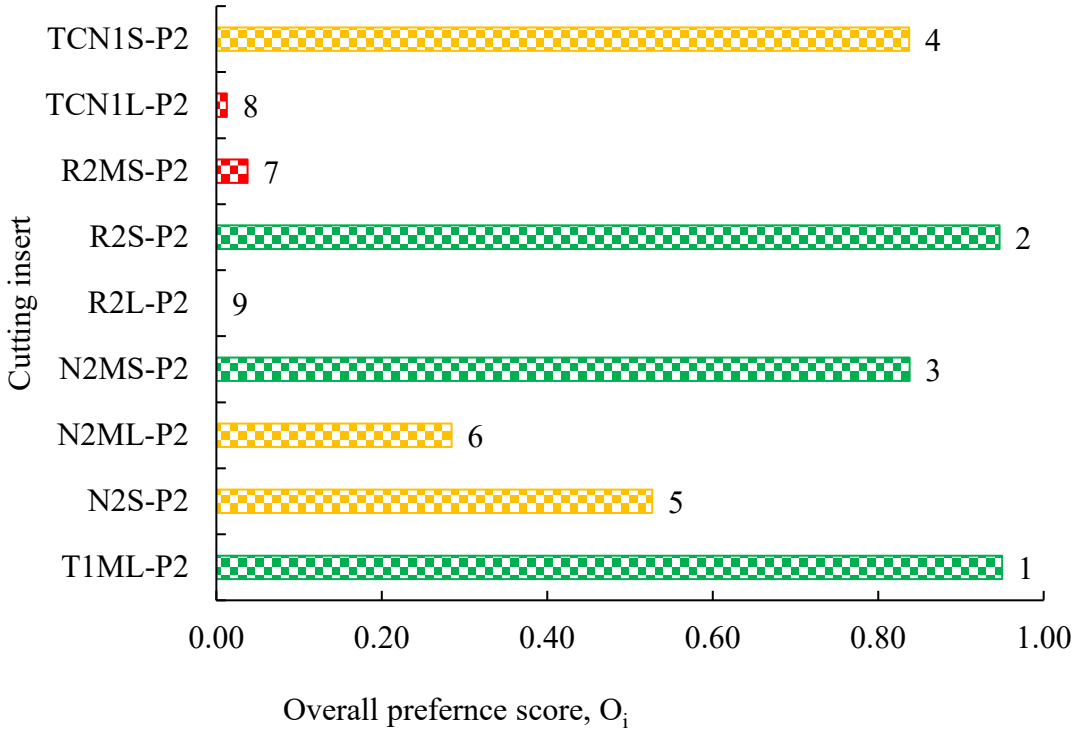


Figure 6-28. Overall preference score (O_i) and rank of P2 cutting inserts (alternatives)

6.4. Consolidated results for finishing 1 (Test 2)

This section summarises the overall machining results of the finishing 1 process. The overall analyses and comparisons of the machining performance of the finishing 1 cutting inserts are made and presented in this section. The primary objective was to evaluate and rank the performance of all the cutting inserts used during finishing 1 machining. For this purpose, the TOPSIS methodology was employed on the 27 cutting inserts used during the machining trials under finishing 1 conditions. Table 6.7 provides the machining performance criteria, the overall preference scores, and the rank of all the cutting inserts used during finishing 1 machining trials. From the table, it can be seen that the T1ML-S2 had the best overall machining performance. The cutting insert obtained an overall preference score of 0.863 with performance criteria values of I_l = 20 min, F_{max} = 1369 N and U_c = 43 J/mm^3. The top ranked NbC-based cutting inserts under finishing 1 conditions was the R2S-B2 which obtained position 3 in terms of ranking with performance criteria values of I_l = 20 min, F_{max} = 1199 N and U_c =75 J/mm^3. The poorest performing insert, on the other hand, was the LPS produced R2L-P2 which secured the last position with an overall performance score of 0.004 and machining performance criteria values of 1 min, 98 J/mm^3, and 1573 N, for C1, C2 and C3, respectively.

Table 6.7. Machining performance criteria, overall preference scores, and rank of combined cutting inserts used during finishing 1

Solution	Cutting insert	C1 (min)	C2 (J/mm^3)	C3 (N)	Overall preference score	Rank	Category
A10	T1ML-S2	20	43	1369	0.863	1	Best (1 – 9)
A1	T1ML-B2	20	57	918	0.831	2	
A6	R2S-B2	20	75	1199	0.773	3	
A7	R2MS-B2	20	80	1280	0.757	4	
A19	T1ML-P2	20	81	1294	0.755	5	
A24	R2S-P2	20	82	1307	0.752	6	
A9	TCN1S-B2	20	87	1397	0.736	7	
A22	N2MS-P2	17	79	1256	0.707	8	
A27	TCN1S-P2	17	79	1265	0.705	9	
A15	R2S-S2	14	40	1199	0.680	10	Average (10 – 18)
A18	TCN1S-S2	14	43	1361	0.673	11	
A13	N2MS-S2	11	36	948	0.555	12	
A11	N2S-S2	11	51	1621	0.526	13	
A2	N2S-B2	11	76	1215	0.490	14	
A20	N2S-P2	11	82	1305	0.480	15	
A12	N2ML-S2	8	43	1400	0.411	16	
A16	R2MS-S2	6	23	517	0.384	17	
A4	N2MS-B2	8	80	1277	0.349	18	
A14	R2L-S2	1	16	256	0.294	19	Poor (19 – 27)
A17	TCN1L-S2	1	20	319	0.284	20	
A21	N2ML-P2	6	69	1097	0.279	21	
A3	N2ML-B2	6	85	1356	0.251	22	
A8	TCN1L-B2	4	98	1574	0.144	23	
A5	R2L-B2	1	83	1324	0.070	24	
A25	R2MS-P2	1	89	1427	0.043	25	
A26	TCN1L-P2	1	95	1525	0.016	26	
A23	R2L-P2	1	98	1573	0.004	27	

6.5. Analyses of the blank (B3) cutting inserts

This subsection presents and analyses resultant cutting forces, specific cutting energy, machining temperature, insert life, wear and surface roughness of the blank cutting inserts during the face milling of a-GCI under finishing 2 conditions. The micrographs of the cutting inserts showing the flank and rake faces are also presented in this section. Lastly, the machining performance evaluation of the blank cutting inserts is done to obtain the overall ranking of the cutting inserts.

6.5.1. Analyses of the resultant forces, specific cutting energy, and temperature of the B3 cutting inserts

Table 6.8 shows the resultant forces, specific cutting energy, and the average machining temperature of the blank cutting inserts during finishing 2 (test 3) machining. Figure 6.29 depicts the average and maximum resultant cutting forces experienced by B3 cutting inserts during machining. As shown in the figure, the maximum resultant force experienced by B3 cutting inserts exceeded 1000 N, except for the N2S-B3 which had the lowest F_{max}' (575 N). The cutting insert which exhibited the highest F_{max}' was observed to be the TCN1S-B3 (see Figure 6.29).

Table 6.8. Machining forces, specific energy consumption, and temperature results of B3 cutting inserts during finishing 2 at n = 1600 rpm and a_p = 0.25 mm

Insert name	Average resultant force, F′ (N)	Maximum resultant force, F_{max}' (N)	Specific cutting energy, U_c' (J/mm^3)	Average Temperature, T′ (°C)
T1ML-B3	719	1111	44.93	59.87 ± 0.52
N2S-B3	575	575	35.92	72.95 ± 0.67
N2ML-B3	749	1045	46.78	53.47 ± 0.19
N2MS-B3	697	1395	43.53	66.91 ± 0.58
R2L-B3	673	1073	42.08	51.49 ± 0.43
R2S-B3	919	1317	57.46	84.98 ± 0.81
R2MS-B3	729	1028	45.53	75.78 ± 0.70
TCN1L-B3	913	1084	57.05	68.31 ± 0.63
TCN1S-B3	957	1551	59.80	76.96 ± 0.72

*NB: The average and maximum resultant forces have a fixed error of ±15 N from the Kistler.

Figure 6.29 shows that the LPS produced cutting inserts experienced lower F_{max}' compared to their PECS produced counterparts. With the exception of N2ML-B3, the average resultant cutting forces of the other B3 cutting inserts appear to follow a trend similar to that of the F_{max}' as shown in Figure 6.29. The F' values of B3 cutting inserts were significantly lower than the F_{max}' values. As shown in the figure, the B3 cutting inserts exhibited average resultant cutting forces of below 960 N.

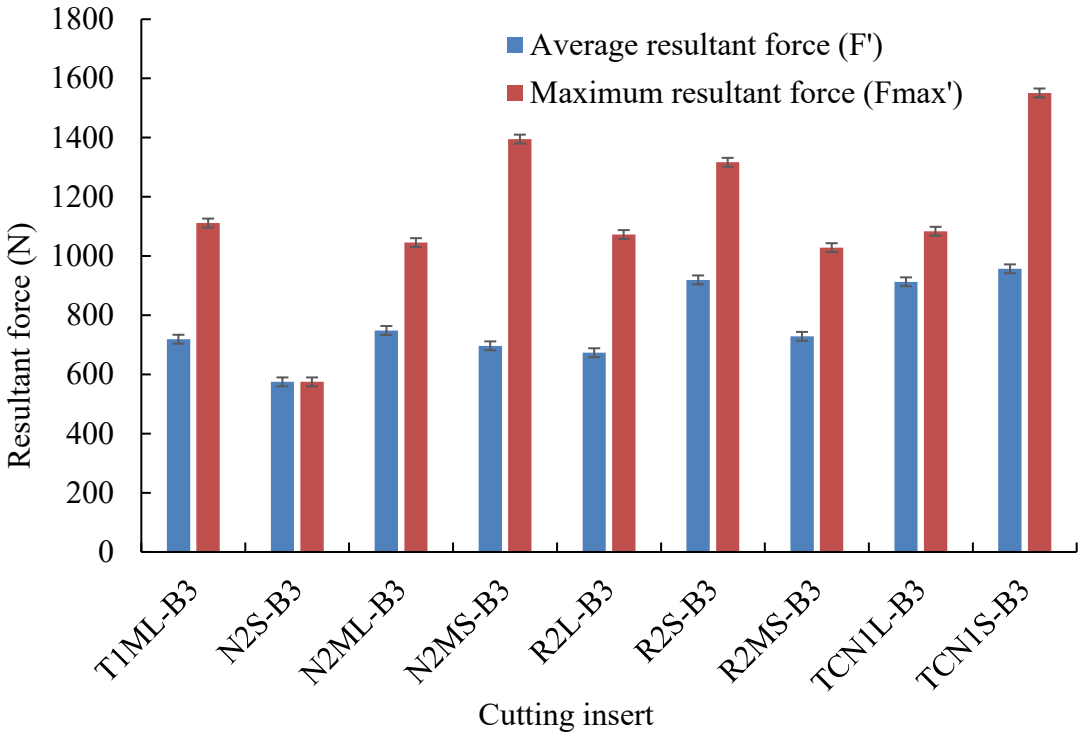


Figure 6-29. Average resultant force (F') and maximum resultant force (F_{max}') for B3 cutting inserts during finishing at n = 1600 rpm and a_p = 0.25 mm

Figure 6.30 shows the variation of the specific cutting energy with the average resultant cutting force of B3 cutting inserts. As expected, the TCN1S-B3 had the highest specific cutting energy (~60 J/mm^3) per volume of material removed during machining. The cutting insert with the lowest specific cutting energy was the N2S-B3 which had U_c' of ~36 J/mm^3. This was followed by the R2L-B3 with U_c' of approximately 42 J/mm^3 as shown in the figure and Table 6.8. From the figure, it can be deduced that there were no significant differences in the energy consumption between the T1ML-B3 and R2MS-B3 cutting inserts whose specific energies were in the range of approximately 45 – 46 J/mm^3. A similar observation was made for the TCN1L-B3 and R2S-B3 cutting inserts whose U_c' values were in the range of approximately 57 – 58 J/mm^3. With the exception of the N2ML-B3, the LPS produced cutting inserts had lower specific cutting energy compared to their PECS produced counterparts.

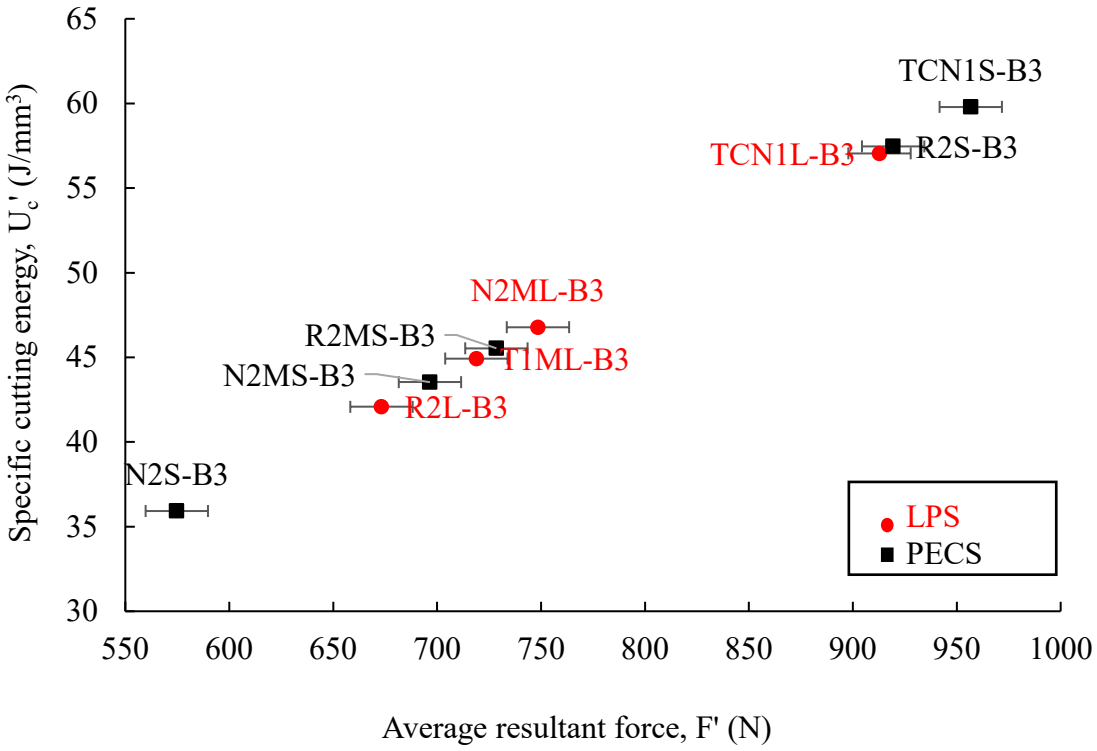


Figure 6-30. Variation of the specific cutting energy (U_c') with the average resultant force (F′) for B3 cutting inserts during finishing 2 at n = 1600 rpm and a_p = 0.25 mm

Figure 6.31 shows the variations of the average machining temperature with the average resultant force for the B3 cutting inserts during finishing 2. From the figure, it can be deduced that the average machining temperature of the B3 cutting inserts appears to slightly increase with increasing average resultant cutting force. As shown in the figure, the R2L-B3 had the lowest average machining temperature (51.49 ± 0.43 °C) among the rest of the B3 cutting inserts. In contrast, the R2S-B3 cutting insert had the highest average machining temperature (84.98 ± 0.81 °C) as shown in the figure. The figure also shows that in general, the LPS produced cutting inserts had lower average machining temperatures compared to their PECS produced counterparts.

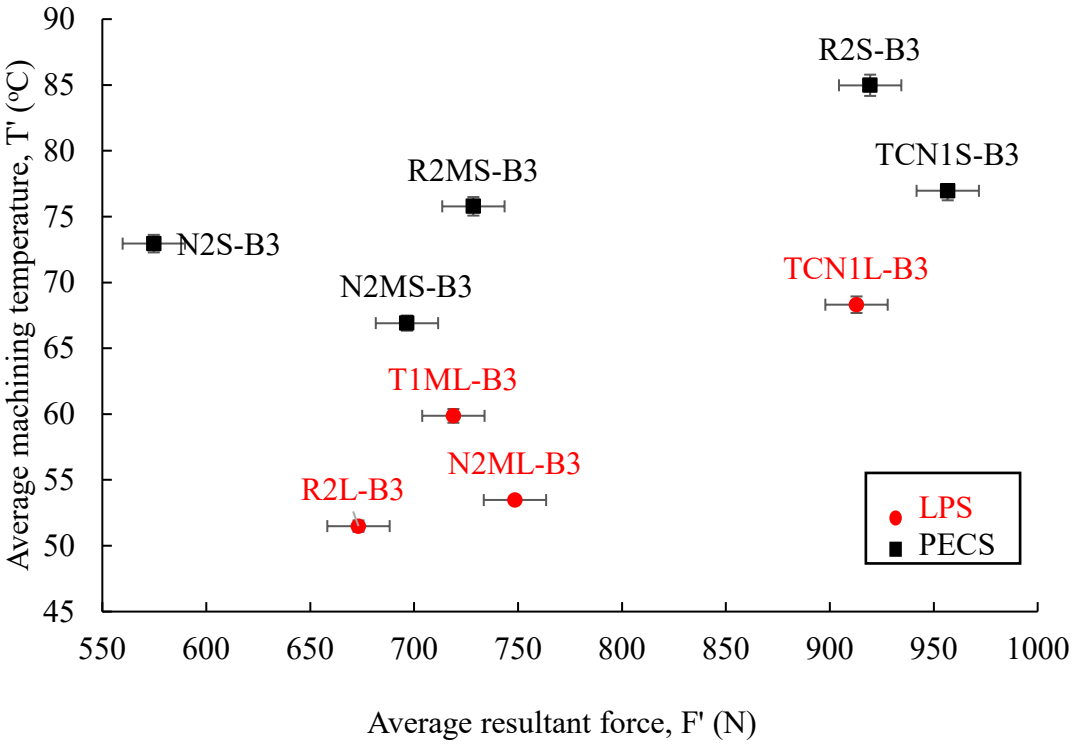


Figure 6-31. Variation of the average machining temperature (T′) with the average resultant force (F′) for blank (B3) cutting inserts during finishing 2

6.5.2. Analyses of insert tool life and wear performance of B3 cutting inserts

Table 6.9 shows the effective insert tool life, wear performance and surface roughness results of B3 cutting inserts. Figure 6.32 gives the variation of the maximum flank wear with the cutting time for B3 cutting inserts during finishing 2 machining. As indicated in the figure, the T1ML-B3 cutting insert had the lowest VB_{max}' among the B3 cutting inserts which had the longest cutting time (effective insert tool life when Ra ≤ 2.5µm) during machining. For instance, the VB_{max}' of T1ML-B3 was determined to be ~33 µm after 20 minutes cutting time while that of TCN1S-B3 and R2S-B3 cutting inserts was ~107 µm and ~116 after 20 minutes, respectively. The maximum flank wear of R2S-B3 was the highest in comparison to the rest of B3 cutting inserts. Conversely, N2S-B3 cutting insert had the lowest VB_{max}'. However, the insert failed just after one minute of machining (see Table 6.9). In general, the PECS produced NbC-Ni based cutting inserts had better insert tool life performance than their LPS produced counterparts. From the figure, the LPS produced NbC-Ni based cutting inserts had an insert tool life of 6 minutes and below. The additions of Mo, TiC, TiC_7N_3 and a combination of Mo plus TiC to the N2S-B3 composition significantly improved the effective insert tool life of N2MS-B3, R2S-B3, TCN1S-B3, and R2MS-B3, respectively. The effective tool life of TCN1S-B3 and R2S-B3 cutting inserts were increased by 1900% whilst those of N2MS-B3 and R2MS-B3 were improved by 1300% and 700%, respectively.

Table 6.9. Effective insert tool life, maximum flank wear, flank wear rate, and surface roughness results of B3 cutting inserts during finishing at n = 1600 rpm and a_p = 0.25 mm

Insert name	Insert tool life, I_l' (min)	Maximum flank wear, VB_{max}' (µm)	Flank wear rate, FWR′ (µm/min)	Surface roughness Ra (µm)
T1ML-B3	20	33.33	1.67	2.34 ± 0.57
N2S-B3	1	25.00	25.00	1.06 ± 0.07
N2ML-B3	6	52.78	8.80	2.39 ± 0.65
N2MS-B3	14	103.89	7.42	1.80 ± 0.43
R2L-B3	4	58.89	14.72	1.61 ± 0.27
R2S-B3	20	115.56	5.78	2.00 ± 0.30
R2MS-B3	8	41.67	5.21	2.02 ± 0.06
TCN1L-B3	4	46.11	11.53	1.53 ± 0.56
TCN1S-B3	20	106.67	5.33	1.75 ± 0.20

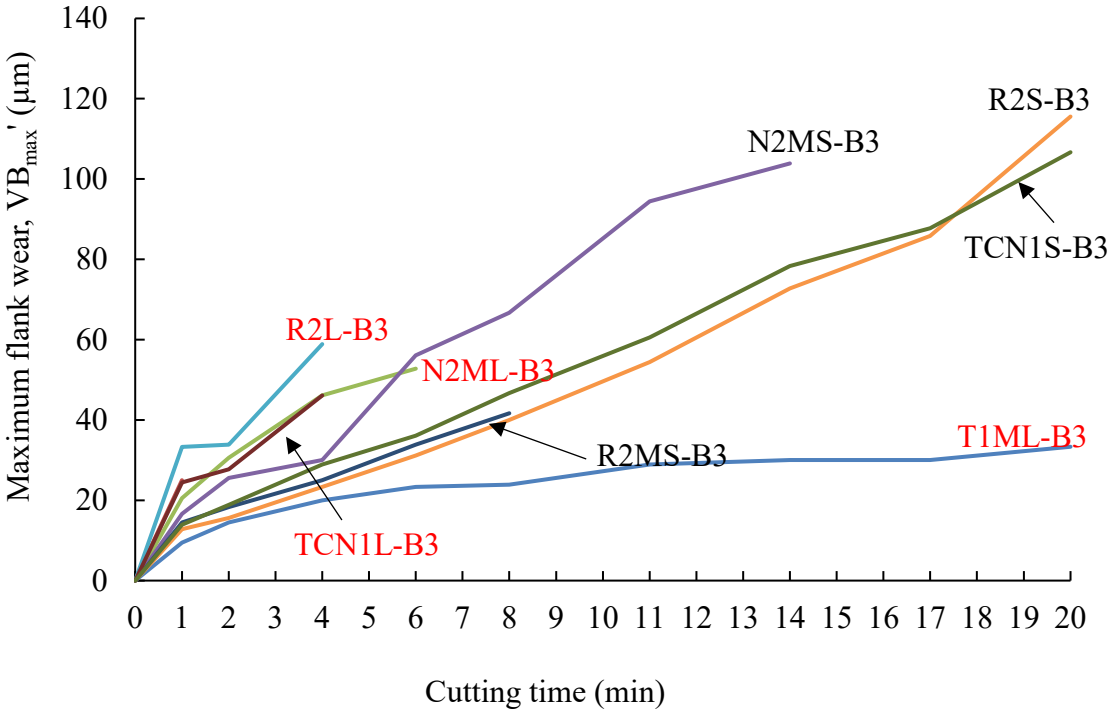


Figure 6-32. Variation of the maximum flank wear (VB_{max}') cutting time (I_l') for blank (B3) cutting inserts during finishing 2 at n = 1600 rpm and a_p = 0.25 mm

Figure 6.33 depicts the variation of the flank wear rate and the average resultant force of the blank (B3) cutting inserts during finishing 2. From the figure, there was no obvious relationship between the two variables. The T1ML-B3 had the lowest FWR′ compared to the other B3 cutting inserts. As shown

in the figure, the R2MS-B3, R2S-B3 and TCN1S-B3 cutting inserts had similar FWRs even though they had different average resultant cutting forces. Figure 6.33 also shows that the LPS produced NbC-Ni based cutting inserts had higher FWRs compared to their PECS produced counterparts. The additions of Mo, TiC, TiC_7N_3, and a combination of Mo plus TiC to the N2S-B3 composition significantly reduced the FWR of N2MS-B3, R2S-B3, TCN1S-B3, and R2MS-B3 cutting inserts, respectively.

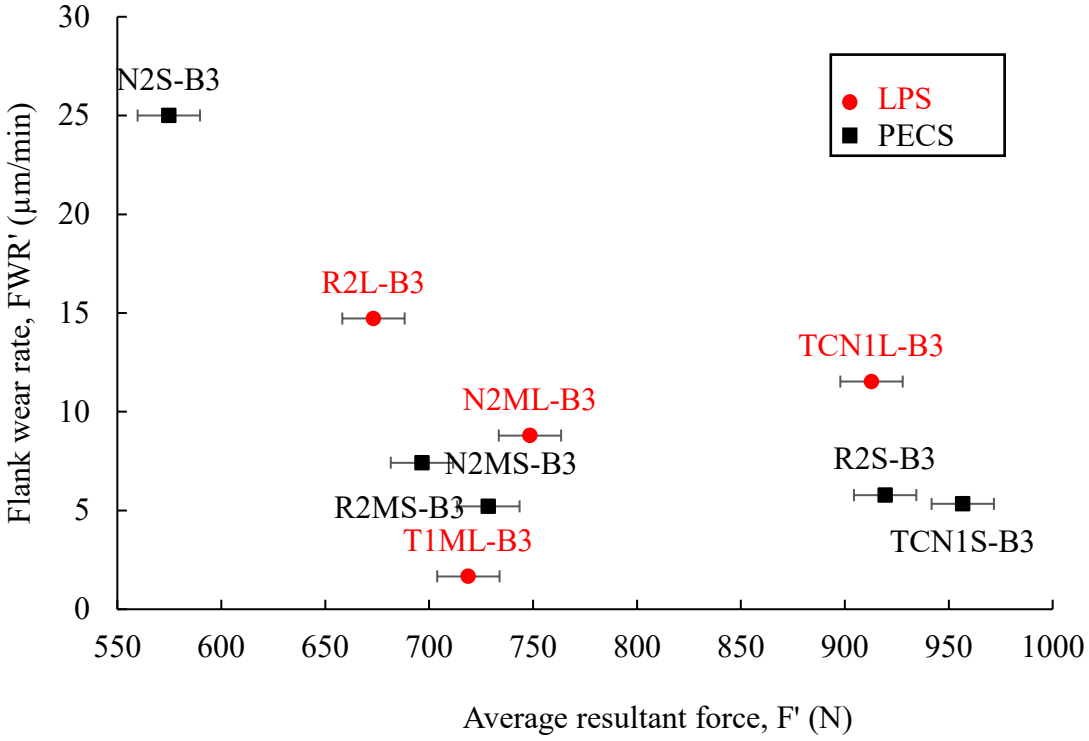


Figure 6-33. Variation of the flank wear rate (FWR′) with the average resultant force (F′) for blank (B3) cutting inserts during finishing 2

6.5.3. Analyses of micrographs of the flank and rake faces of B3 cutting inserts

Figure 6.34 shows the optical micrographs of the flank and the rake faces of (a) T1ML-B3, (b) TCN1S-B3 and (c) R2S-B3 cutting inserts. As shown in the figure, the flank of T1ML-B3 exhibited a smaller wear land compared to the TCN1S-B3 and R2S-B3 cutting inserts. The flank faces of the cutting inserts show that abrasion wear and mechanical fracture were the main mechanisms of cutting edge failure. From Figure 6.34 (b) and (c), the TCN1S-B3 and R2MS-B3 exhibited very similar wear and cutting edge wear characteristics on both the flank and rake faces. The rake face of T1ML-B3 shows that there was the presence of crater wear on the cutting edge. This feature was not observed on the rake face of TCN1S-B3 and R2S-B3 cutting inserts, which experienced mechanical fracture instead. The rest of the B3 cutting inserts were also analysed and similar wear and cutting edge failure mechanisms were

observed on the flank and rake faces. The flank faces exhibited abrasion wear, whereas the rake faces showed failure through mechanical fracture. In general, LPS produced cutting inserts exhibited more cutting edge wear compared to their PECS counterparts.

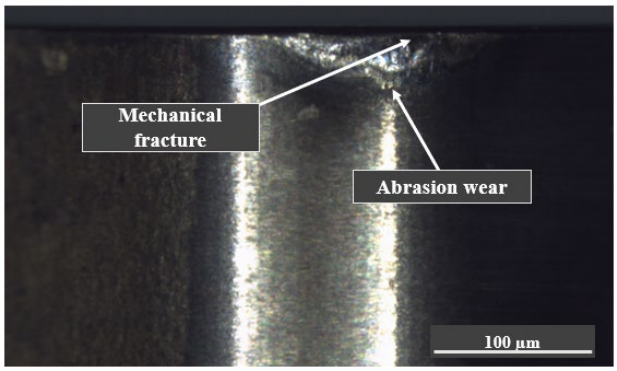
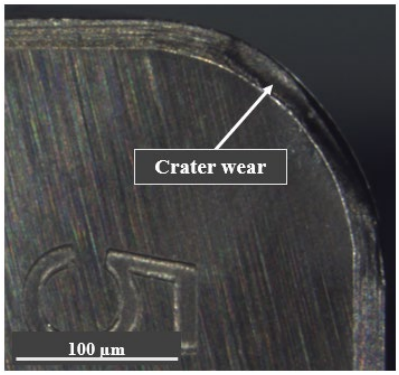
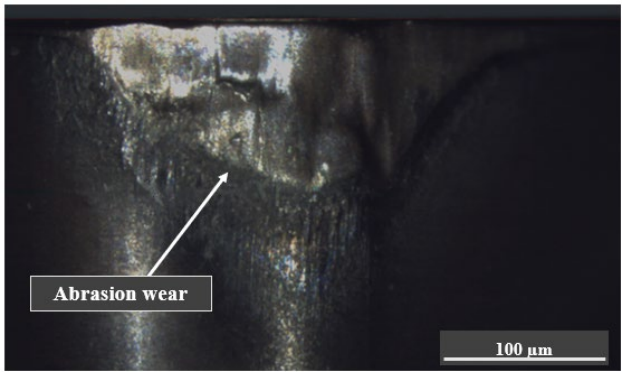
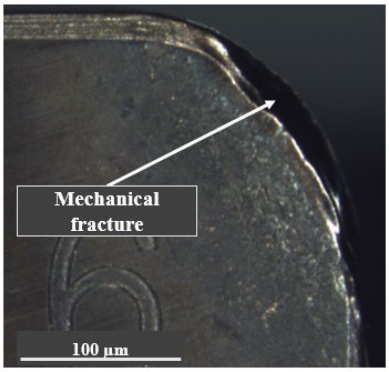
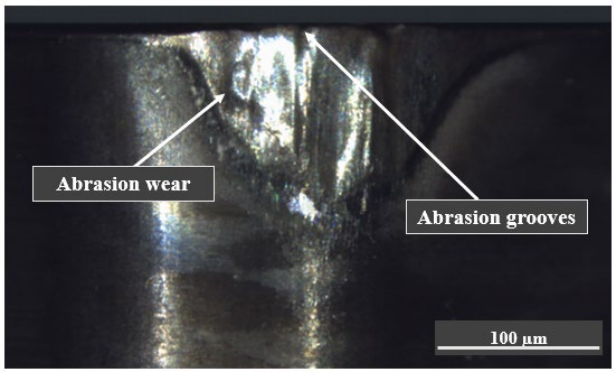
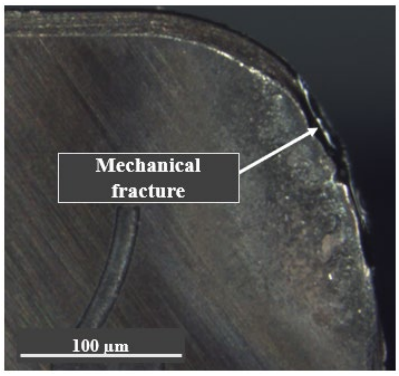
Insert	Flank face	Rake face
(a) T1ML-B3		
	VB_{max}' = 33.33 µm Cutting time = 20 minutes	
(b) TCN1S-B3		
	VB_{max}' = 106.67 µm Cutting time = 20 minutes	
(c) R2S-B3		
	VB_{max}' = 115.56 µm Cutting time = 20 minutes	

Figure 6-34. Optical micrographs of the flank and rake faces of (a) T1ML-B3, (b) TCN1S-B3 and (c) R2S-B3 cutting edges during finishing 2 machining

6.5.4. Machining performance evaluation and analyses of B3 cutting inserts

This subsection provides machining performance evaluation and analyses of blank (B3) cutting inserts during finishing 2 machining trials. Table 6.10 shows the values of criteria C1-C4 used for evaluating and assessing the machining performance of B3 cutting inserts. Figure 6.35 depicts the variation of specific cutting energy with effective insert tool life of B3 cutting inserts. From Table 6.10 and Figure 6.35, the TCN1S-B3, R2S-B3, T1ML-B3 cutting inserts had the highest effective insert tool life (20 minutes) among B3 cutting inserts. From the figure, the T1ML-B3 had the lowest specific cutting energy among the B3 cutting inserts with the highest insert tool life. However, as shown in the table, TCN1S-B3 and R2S-B3 had lower surface roughness values (i.e. 1.75 ± 0.20 µm and 2.00 ± 0.30 µm, respectively) than T1ML-B3 (2.34 ± 0.57 µm). The N2S-B3 cutting insert had the lowest specific cutting energy and surface roughness among the B3 cutting inserts. However, the most critical criterion (the effective insert tool life) was only 1 minute which is on the poor spectrum of machining performance. As shown in the figure, there was no significant difference in the specific cutting energy of T1ML-B3, N2MS-B3, and R2MS-B3 cutting inserts, even though the inserts had different effective insert tool lives.

Table 6.10. Machining performance evaluation criteria for B3 cutting inserts

Insert name	Effective insert tool life, I_l' (min) [C1]	Specific cutting energy, U_c' (J/mm^3) [C2]	Surface roughness, Ra (µm) [C3]	Maximum resultant cutting force, F_{max}' (N) [C4]
T1ML-B3	20	44.93	2.34 ± 0.57	1111
N2S-B3	1	35.92	1.06 ± 0.07	575
N2ML-B3	6	46.78	2.39 ± 0.65	1045
N2MS-B3	14	43.53	1.80 ± 0.43	1395
R2L-B3	4	42.08	1.61 ± 0.27	1073
R2S-B3	20	57.46	2.00 ± 0.30	1317
R2MS-B3	8	45.53	2.02 ± 0.06	1028
TCN1L-B3	4	57.05	1.53 ± 0.56	1084
TCN1S-B3	20	59.80	1.75 ± 0.20	1551

In general, both Table 6.10 and Figure 6.35 indicates that LPS produced cutting inserts exhibited poorer combinations of machining performance criteria than their PECS produced counterparts. Considering the PECS produced cutting inserts, the N2S-B3 had the poorest combinations of

machining performance criteria. From Figure 6.35, the overall machining performance of N2S-B3 cutting insert was improved by the additions of TiC, TiC_7N_3 and simultaneous addition of Mo and TiC to the N2S-B3 composition, respectively. For example, the machining performances of R2S-B3, TCN1S-B3 and R2MS-B3 cutting inserts were better than that of N2S-B3.

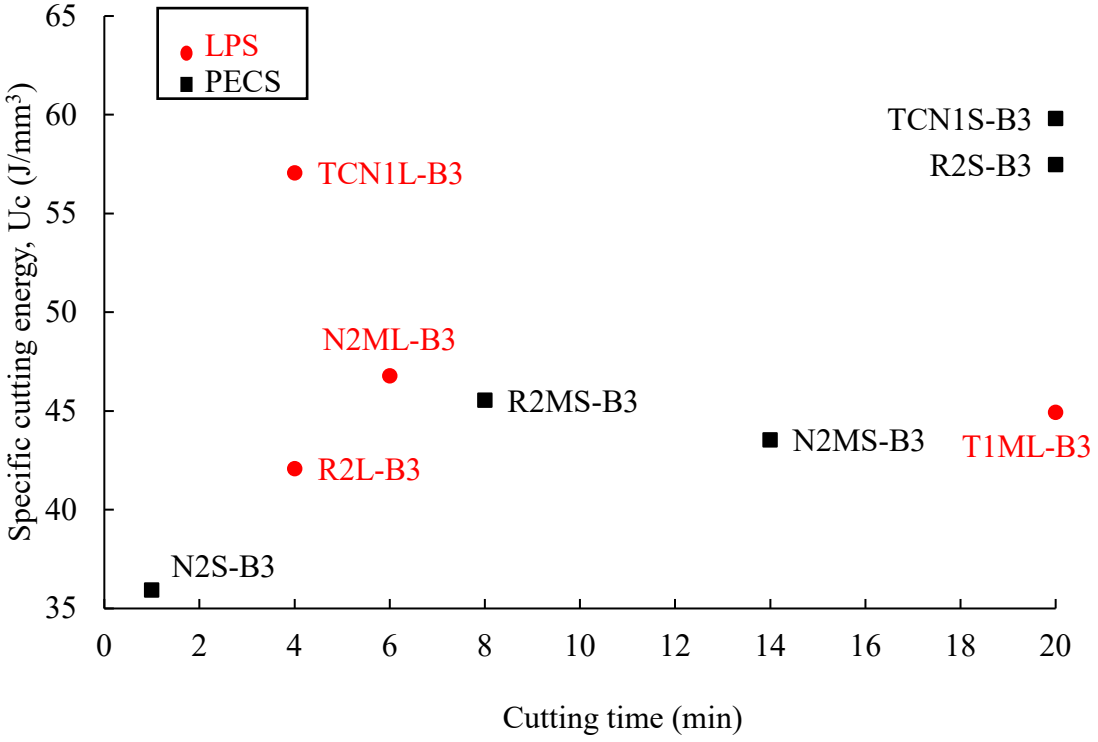


Figure 6-35. Variation of specific cutting energy (U_c') with effective cutting time (I_l') for blank (B3) cutting inserts during finishing 2 at n = 1600 rpm and a_p = 0.25 mm

Figure 6.36 shows the overall preference score and rank of the blank (B3) cutting inserts used during finishing 2 machining trials. The green colour code signifies the best cutting inserts while amber and red indicate average and poorly ranked cutting inserts, respectively. Accordingly, the T1ML-B3, R2S-B3 and, TCN1S-B3 cutting inserts were top ranked with overall preference scores of 0.79, 0.77 and 0.76, respectively. As shown in the figure, besides N2MS-B3 cutting insert, the remaining B3 cutting inserts obtained overall preference scores of below 0.4. Figure 6.36 also shows that there was no significant difference in the overall preference scores of N2ML-B3, N2S-B3, R2L-B3 and TCN1L-B3 cutting inserts.

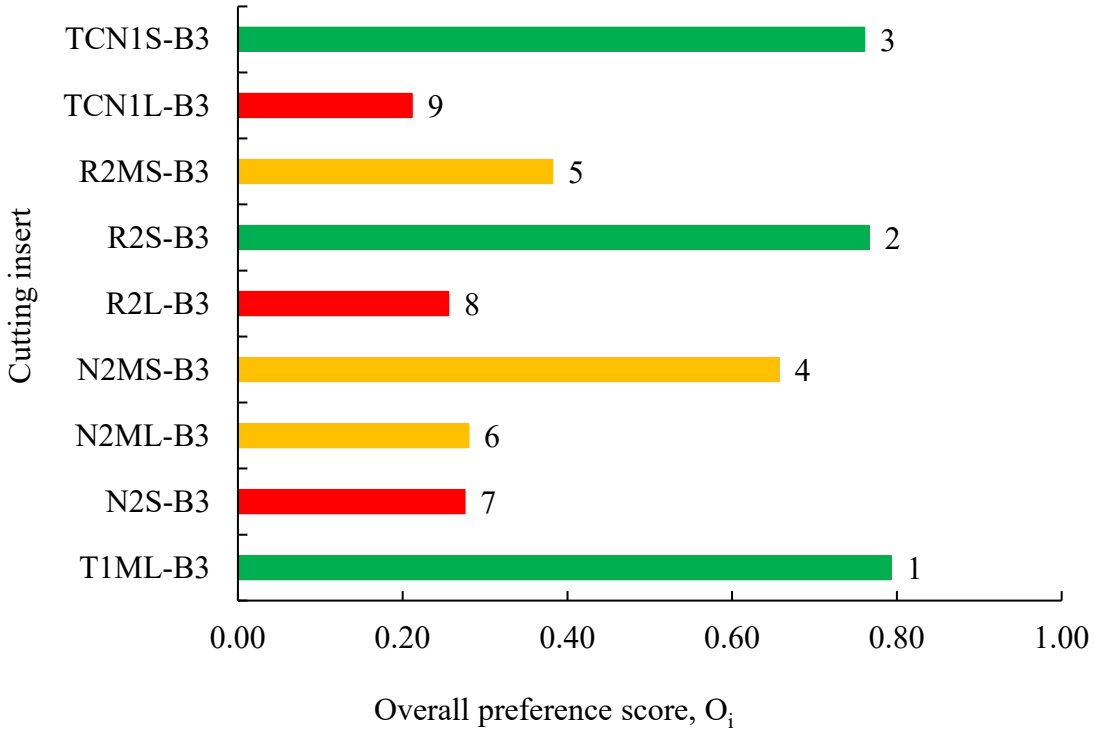


Figure 6-36. Overall preference score (O_i) and rank of B3 cutting inserts (alternatives)

6.6. Analyses of the shark skin LSM (S3) cutting inserts

This subsection presents and analyses resultant cutting forces, specific cutting energy, machining temperature, insert life, wear and surface roughness of the shark skin LSM cutting inserts during the face milling of a-GCI under finishing 2 conditions. The micrographs of the cutting inserts showing the flank and rake faces are also presented in this section. Lastly, the machining performance evaluation of the shark skin LSM cutting inserts is done to obtain the overall ranking of the cutting inserts

6.6.1. Analysis of the resultant forces, specific cutting energy, and temperature of the S3 cutting inserts

Table 6.11 shows the resultant forces, specific cutting energy and the average machining temperature of the shark skin cutting inserts during finishing 2 machining trials. Figure 6.37 depicts the average and maximum resultant cutting forces experienced by S3 cutting inserts during machining. As shown in the figure, the maximum resultant cutting forces experienced by the S3 cutting inserts during machining trials were between the range of 1430 N and 1560 N, respectively. From Figure 6.37, the N2ML-S3 had the highest F_{max}' (1565 N) among S3 cutting inserts while the R2S-S3 had the lowest F_{max}' (1436 N), respectively.

Table 6.11. Machining forces, specific energy consumption, and temperature results of S3 cutting inserts during finishing 2 at n = 1600 rpm and a_p = 0.25 mm

Insert name	Average resultant force, F′ (N)	Maximum resultant force, F_{max}′ (N)	Specific cutting energy, U_c' (J/mm^3)	Average Temperature, T′ (°C)
T1ML-S3	1079	1522	67.41	83.17 ± 0.78
N2S-S3	1232	1540	76.99	68.24 ± 0.61
N2ML-S3	1213	1565	75.84	53.28 ± 0.45
N2MS-S3	1180	1541	73.76	74.25 ± 0.69
R2L-S3	1500	1500	93.72	NA
R2S-S3	1054	1436	65.86	73.93 ± 0.68
R2MS-S3	1016	1441	63.52	70.71 ± 0.64
TCN1L-S3	1515	1515	94.65	NA
TCN1S-S3	1086	1463	67.85	72.15 ± 0.65

*NB: The average and maximum resultant forces have a fixed error of ±15 N from the Kistler.

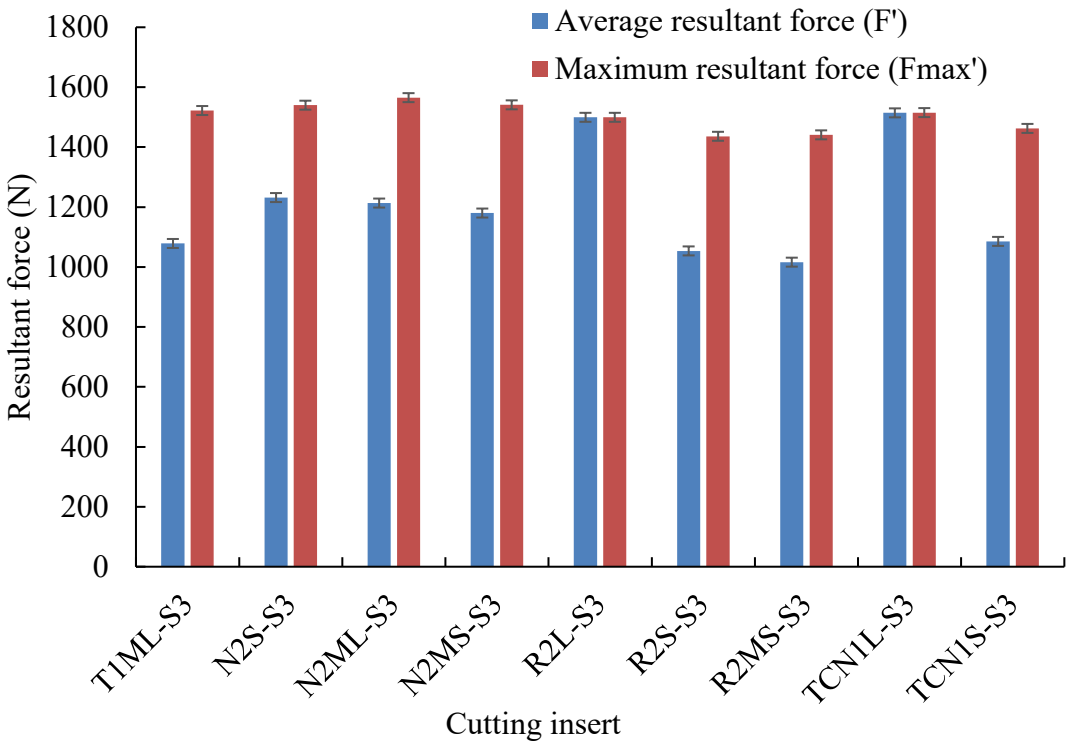


Figure 6-37. Average resultant force (F′) and maximum resultant force (F_{max}′) for S3 cutting inserts during finishing at n = 1600 rpm and a_p = 0.25 mm

With the exception of R2L-S3 and TCNL-S3 cutting inserts, the average resultant cutting forces of S3 cutting inserts were significantly lower than the maximum resultant cutting inserts. As shown in Figure 6.37, the R2MS-S3 cutting insert had the lowest F′ (1016 N) among the S3 cutting inserts, whereas the TCN1L-S3 had the highest F′ (1514 N) respectively. In general, the LPS produced cutting inserts had higher average resultant cutting forces compared to their PECS counterparts.

Figure 6.38 shows the variation of the specific cutting energy with the average resultant cutting force of S3 cutting inserts. The figure shows that the R2MS-S3 cutting insert had the lowest specific cutting energy (~64 J/mm^3) per volume of material removed during machining. The cutting insert that exhibited the highest specific energy among S3 cutting inserts was the TCN1L-S3 (~95 J/mm^3), and this was followed by the R2L-S3 which had a slightly lower specific cutting energy or consumption (~94 J/mm^3) as shown in the figure. From the figure, there was no significant difference between the specific cutting energy of TCN1S-S3 and T1ML-S3 cutting inserts. Furthermore, Figure 6.38 indicates that the LPS produced cutting inserts had higher specific cutting energy than their PECS produced counterparts.

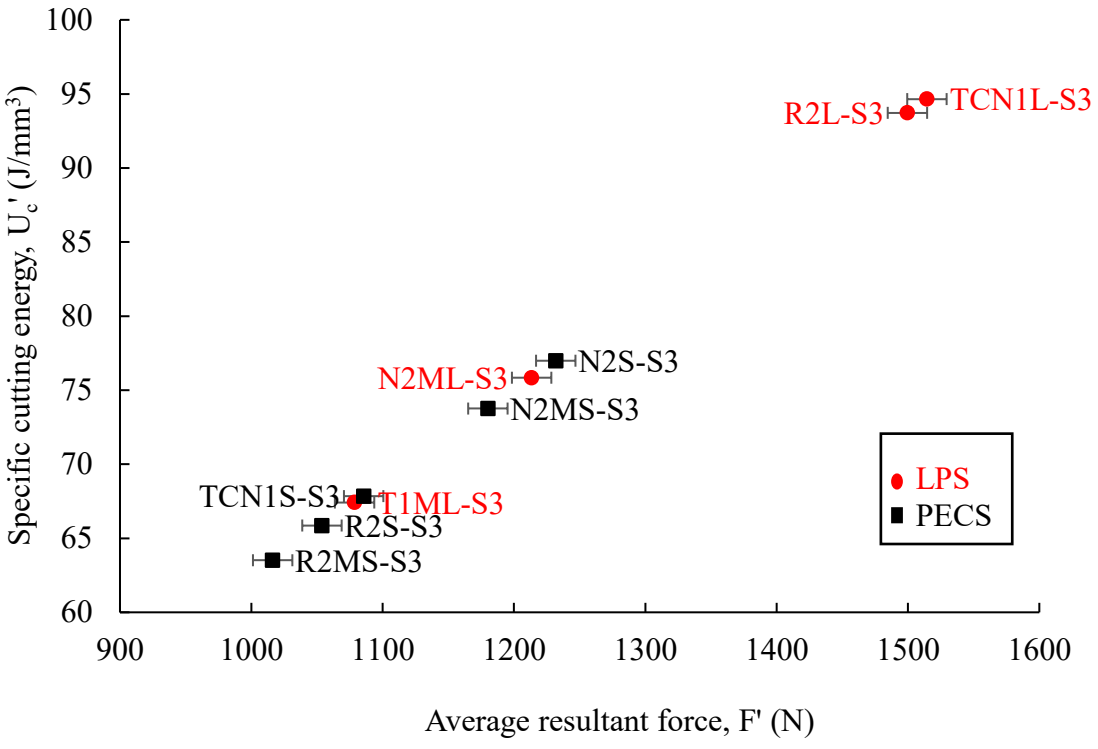


Figure 6-38. Variation of the specific cutting energy (U_c') with the average resultant force (F') for S3 cutting inserts during finishing 2 at n = 1600 rpm and a_p = 0.25 mm

Figure 6.39 shows the variations of the average machining temperature with the average resultant cutting force of the shark skin LSM (S3) cutting inserts during finishing 2. Similar to the blank (B3)

cutting inserts, there is no obvious trend between F′ and T′. The N2ML-S3 cutting insert had the lowest average machining temperature (53.28 ± 0.45 °C) despite exhibiting the second highest average resultant cutting force among S3 cutting inserts. The T1ML-S3 cutting insert had the highest average machining temperature compared to all the S3 cutting inserts. There was no significant difference in the average machining temperatures of the PECS produced cutting inserts as shown in the figure. It is worth noting however, that the additions of Mo, TiC, TiC_7N_3 and a combination of Mo plus TiC to the N2S-S3 composition slightly increased the average machining temperatures in N2MS-S3, R2S-S3, TCN1S-S3 and R2MS-S3 cutting inserts, respectively.

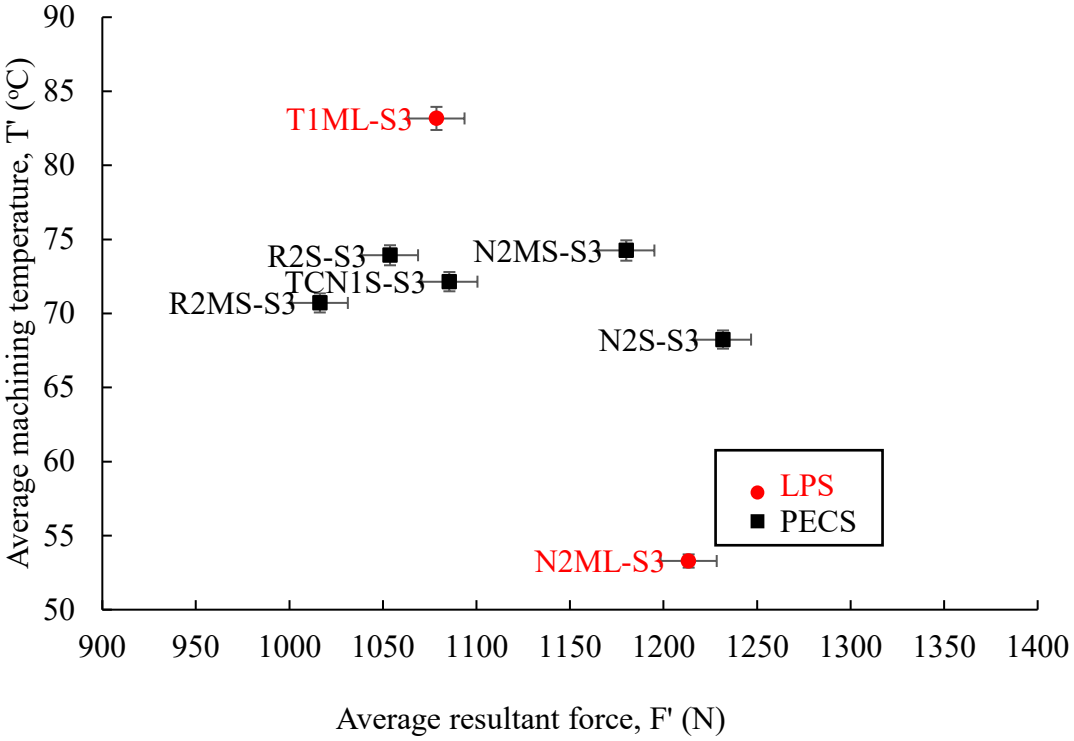


Figure 6-39. Variation of the average machining temperature (T′) with the average resultant force (F′) for shark skin LSM (S3) cutting inserts during finishing 2

6.6.2. Analyses of insert tool life and wear performance of S3 cutting inserts.

Table 6.12 gives the effective insert tool life, wear performance and surface roughness of S3 cutting inserts. Figure 6.40 shows the variation of the maximum flank wear with the cutting time for shark skin LSM (S3) cutting inserts during finishing 2 machining trials. The figure shows that the VB_{max}' of all the S3 cutting inserts was below 90 µm. The T1ML-S3 had the lowest VB_{max}' among the S3 cutting inserts (i.e., the cutting insert had a VB_{max}' of 51.11 µm after 17 minutes of machining). The R2S-S3, R2MS-S3 and TCN1S-S3 cutting inserts also achieved an effective insert tool life of 17 minutes. However, the VB_{max}' values of these inserts were higher than that of T1ML-B3. The VB_{max}' of the

R2S-S3 cutting insert was slightly lower than that of TCN1S-S3 and R2MS-S3 cutting inserts respectively (see Table 6.12). Similar to the observations on B3 cutting inserts, the NbC-Ni based PECS produced cutting inserts generally had better effective insert tool life performance than their LPS produced counterparts. The addition of Mo to the N2S-S3 composition resulted in a reduction in VB_{max}' of N2MS-S3 cutting insert. The additions of TiC, TiC_7N_3, and a combination of Mo plus TiC to the N2S-S3 composition resulted in a reduction of VB_{max}' and tool life improvement of R2S-S3, TCN1S-S3 and R2MS-S3 cutting inserts, respectively.

Table 6.12. Effective insert tool life, maximum flank wear, flank wear rate, and surface roughness results of S3 cutting inserts during finishing at n = 1600 rpm and a_p = 0.25 mm

Insert name	Insert tool life, I_l' (min)	Maximum flank wear, VB_{max}' (µm)	Flank wear rate, FWR′ (µm/min)	Surface roughness Ra (µm)
T1ML-S3	17	51.11	3.01	2.31 ± 0.24
N2S-S3	4	81.11	20.28	1.62 ± 0.19
N2ML-S3	8	84.45	10.56	2.44 ± 0.09
N2MS-S3	11	52.78	4.80	1.88 ± 0.11
R2L-S3	1	81.67	81.67	1.08 ± 0.16
R2S-S3	17	74.45	4.38	2.09 ± 0.19
R2MS-S3	17	81.11	4.77	1.00 ± 0.26
TCN1L-S3	1	66.11	66.11	1.00 ± 0.13
TCN1S-S3	17	82.23	4.84	1.92 ± 0.45

Figure 6.41 shows the effects of shark skin LSM on the cutting insert tool life performance. The figure shows the percentage improvement (in green) and reduction (in red) of the insert tool life of S3 cutting inserts compared to the blank (B3) cutting inserts. From Figure 6.41, the application of LSM resulted in insert tool life improvements of N2S-S3, R2MS-S3 and N2ML-S3 cutting inserts. The N2S-S3 had the highest improvement (75%) followed by R2MS-S3 and then N2ML-S3 cutting inserts with improvements of 53% and 25% respectively. As shown in the figure, the majority of the cutting inserts (6 out of 9) had their insert tool life reduced by shark skin LSM application. The TCN1L-S3 and R2L-S3 cutting inserts had the highest reductions in insert tool life (i.e. 300%), followed by the N2MS-S3 with insert tool life reduction of 27%. The remaining cutting inserts (T1ML-S3, TCN1S-S3 and R2S-S3 cutting inserts had similar reductions in insert tool life as shown in the figure, respectively.

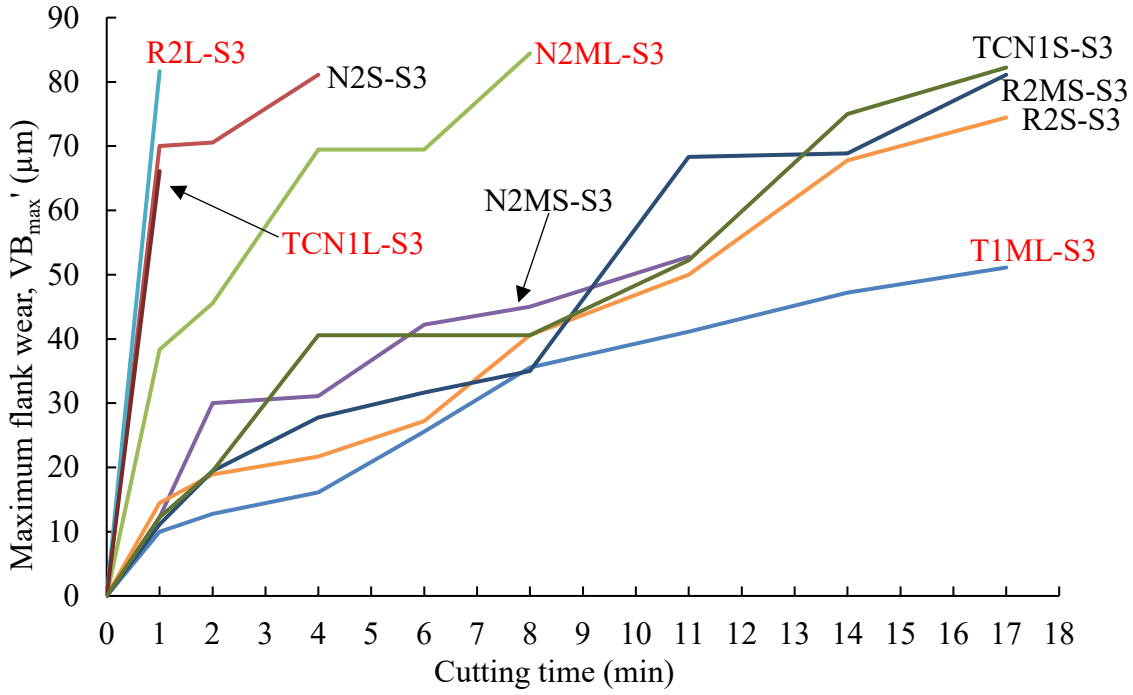


Figure 6-40. Variation of the maximum flank wear (VB_{max}') cutting time (l_l') for shark skin LSM (S3) cutting inserts during finishing 2 at n = 1600 rpm and a_p = 0.25 mm

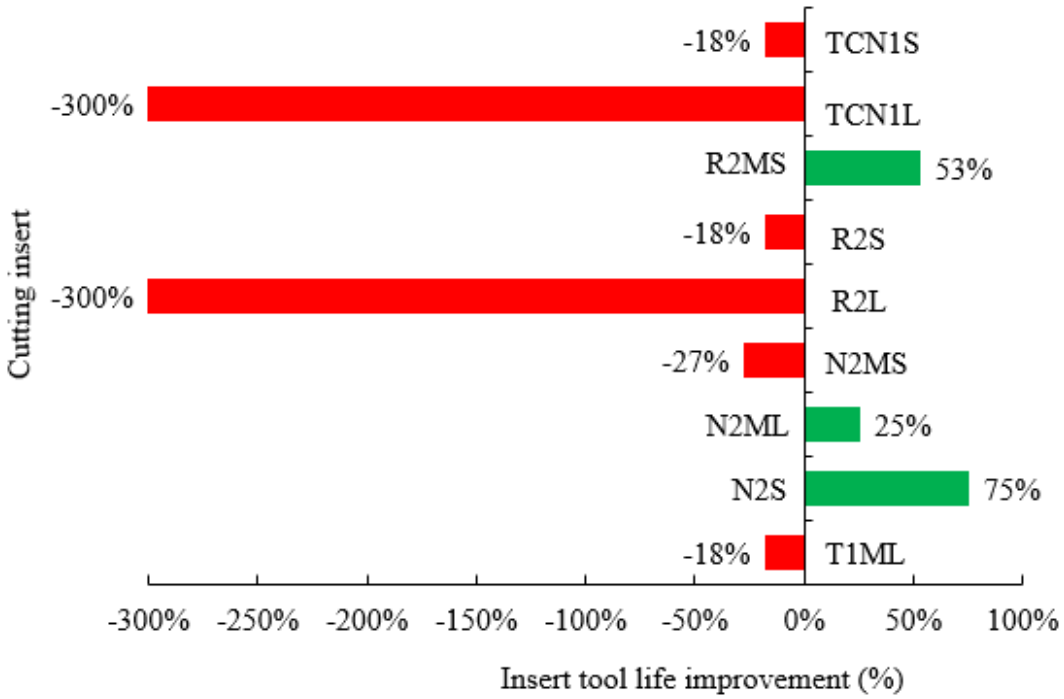


Figure 6-41. Effects of shark skin LSM technique on the S3 cutting inserts tool life performance benchmarked against B3 cutting inserts during finishing at n = 1600 rpm and a_p = 0.25 mm

Figure 6.42 shows the variation of flank wear rate against the average resultant cutting force S3 cutting inserts. As shown in the figure, there is a slight direct proportionality relationship between FWR' and

F’. It should be noted, however, that this connection is not immediately apparent. The T1ML-S3 cutting insert had the lowest FWR′ (3.01 µm/min) compared to all the other S3 cutting inserts. There was no significant difference between the FWR’s of R2MS-S3, R2S-S3, TCN1S-S3, and N2MS-S3 cutting inserts despite the inserts having slightly different average resultant cutting forces (see Figure 6.42 and Table 6.12). The R2L-S3 and TCN1L-S3 cutting inserts exhibited high values of FWR′ and average resultant cutting forces, with the former having the highest FWR′ (81.67 µm/min) among the S3 cutting inserts. In general, the LPS produced cutting inserts exhibited higher FWR’ than their PECS produced counterparts.

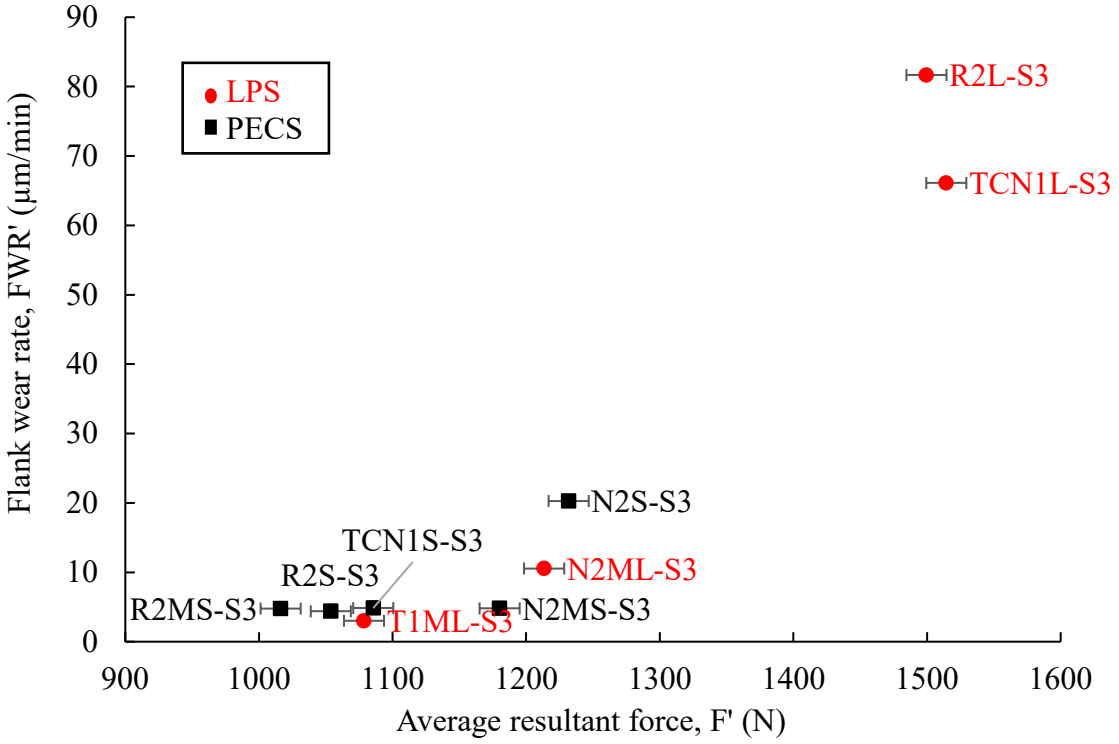


Figure 6-42. Variation of the flank wear rate (FWR’) with the average resultant force (F’) for shark skin LSM (S3) cutting inserts during finishing 2

Figure 6.43 shows the comparison of FWR′ of B3 cutting inserts against S3 cutting inserts. As shown in the figure, the FWR’s of the majority of S3 cutting inserts were slightly lower than those of B3 cutting inserts. It is worth noting that for some inserts, the difference is very minimal (i.e. the FWR’ values of R2MS-S3 and TCN1S-S3 were determined to be 8% and 9% lower than their B3 counterparts). Figure 6.43 also shows that the shark skin LSM (S3) technique increased the FWR′ of all the LPS produced cutting inserts irrespective of the composition. Among the cutting inserts that exhibited increased FWRs, the TCN1L-S3 was the highest with an increase of 473%, followed by R2L-S3 cutting insert with an increased percentage of 455%. In contrast to LPS produced cutting

inserts, the application of the technique to the PECS produced cutting inserts resulted in the reduction of the FWR′ respectively.

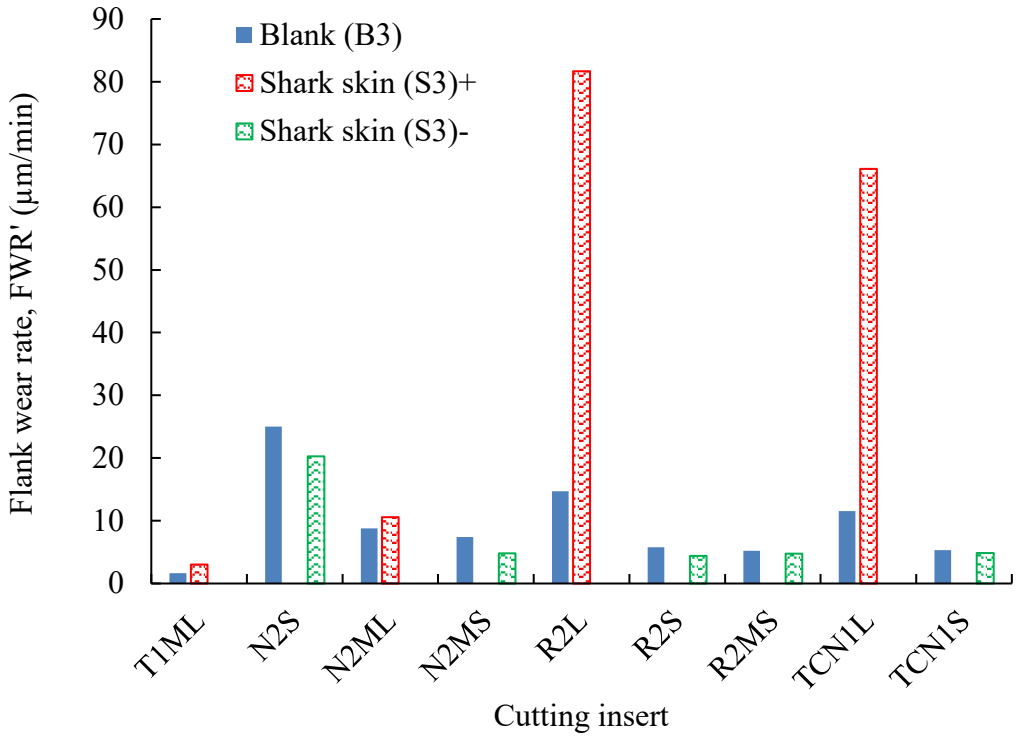


Figure 6-43. Comparison of the flank wear rate of blank (B3) vs. shark skin LSM (S3) cutting inserts during finishing 2

6.6.3. Analyses of micrographs of the flank and rake faces of S3 cutting inserts

Figure 6.44 shows the optical micrographs of the flank and the rake faces of the (a) T1ML-S3, (b) R2S-S3, and (c) R2MS-S3 cutting inserts. From the figure, the cutting inserts experienced abrasion wear on the flank faces. It could also be observed that the wear land on the cutting edges for these cutting inserts was very similar. In addition to abrasion wear, the flank face of R2S-S3 shows that the insert also experienced mechanical fracture (see Figure 6.44 (b)). The rake face of T1ML-S3 exhibited a small degree of crater wear. A similar observation was made on the rake of R2MS-S3 cutting insert whereby the cutting edge experienced a combination of crater wear and chipping. Only mechanical fracture was observed on the rake face of the R2S-S3 cutting insert. The rest of the S3 cutting inserts were also analysed and similar wear behaviour and cutting edge failure mechanisms were observed on the flank and rake faces. The flank faces exhibited abrasion wear whereas the rake faces showed failure through mechanical fracture. In general, LPS produced cutting inserts exhibited more cutting edge wear compared to their PECS counterparts.

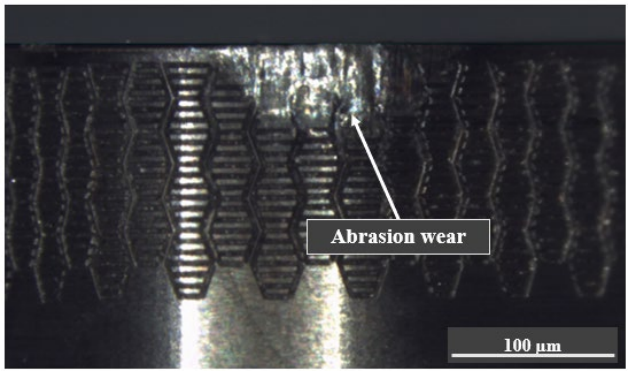
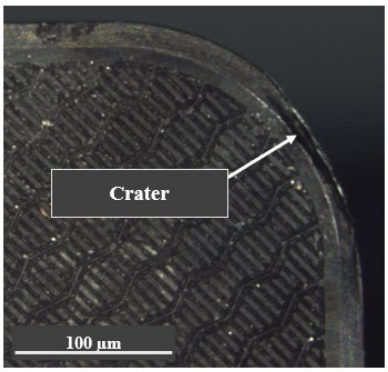
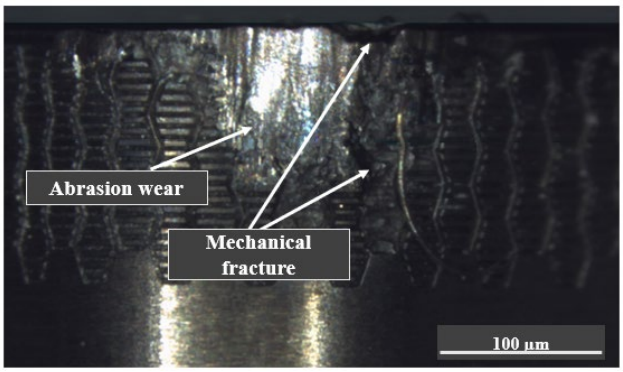
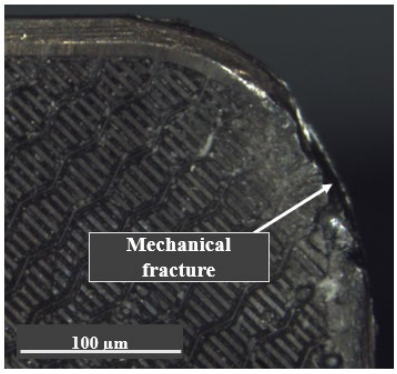
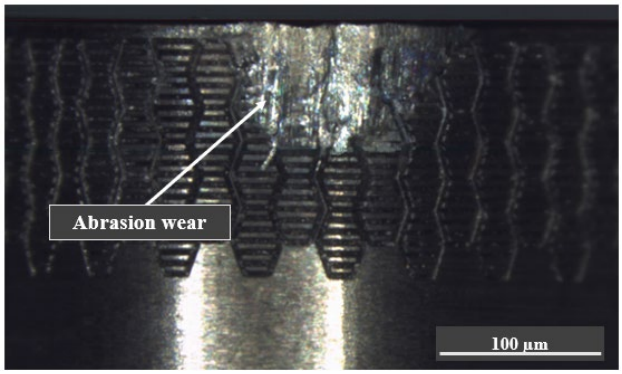
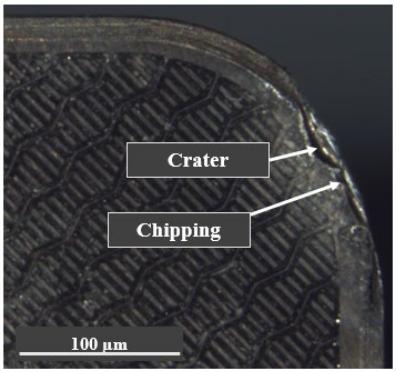
Insert	Flank face	Rake face
(a) T1ML-S3		
	$VB_{max}' = 51.11$ µm Cutting time = 17 minutes	
(b) R2S-S3		
	$VB_{max}' = 74.45$ µm Cutting time = 17 minutes	
(c) R2MS-S3		
	$VB_{max}' = 81.11$ µm Cutting time = 17 minutes	

Figure 6-44. Optical micrographs of the flank and rake faces of (a) T1ML-S3, (b) R2S-S3 and (c) R2MS-S3 cutting edges during finishing 2 machining

6.6.4. Machining performance evaluation and analyses of S3 cutting inserts

This subsection provides machining performance evaluation and analyses of shark skin LSM (S3) cutting inserts during finishing 2 machining trials. Table 6.13 shows the values of criteria C1-C4 used for evaluating and assessing the machining performance of S3 cutting inserts. Figure 6.45 depicts the variation of specific cutting energy with the effective insert tool life of S3 cutting inserts. From Table 6.13 and Figure 6.45, the R2MS-S3, R2S-S3, T1ML-S3 and TCN1S-S3 cutting inserts had the best combinations of machining performance criteria. The inserts had the highest effective insert tool life (17 minutes) and lower specific cutting energies among the S3 cutting inserts. Table 6.13 shows that R2MS-S3 and TCN1L-S3 cutting inserts produced the lowest surface roughness (1.00 ± 0.26 µm and 1.00 ± 0.13 µm, respectively) compared to other S3 cutting inserts. However, as was discussed previously, the latter failed just after 1 minute of machining. The T1ML-S3 cutting insert exhibited the highest surface roughness among the S3 cutting inserts, with the insert having a Ra of 2.31 ± 0.24 µm after 17 minutes of effective insert tool life. As shown in both Table 6.13 and Figure 6.45, the R2L-S3 and TCN1L-S3 cutting inserts had the poorest combinations of the machining performance criteria with both inserts having the highest specific cutting energy and the least effective insert tool life.

Table 6.13. Machining performance evaluation criteria for S3 cutting inserts

Insert name	Effective insert tool life, I_l' (min) [C1]	Specific cutting energy, U_c' (J/mm^3) [C2]	Surface roughness, Ra (µm) [C3]	Maximum resultant cutting force, F_{max}' (N) [C4]
T1ML-S3	17	67.41	2.31 ± 0.24	1522
N2S-S3	4	76.99	1.62 ± 0.19	1540
N2ML-S3	8	75.84	2.44 ± 0.09	1565
N2MS-S3	11	73.76	1.88 ± 0.11	1541
R2L-S3	1	93.72	1.08 ± 0.16	1500
R2S-S3	17	65.86	2.09 ± 0.19	1436
R2MS-S3	17	63.52	1.00 ± 0.26	1441
TCN1L-S3	1	94.65	1.00 ± 0.13	1515
TCN1S-S3	17	67.85	1.92 ± 0.45	1463

Similar to the B3 cutting inserts, the S3 PECS produced cutting inserts exhibited better combinations of machining performance criteria than the LPS produced cutting inserts. In addition, the machining

performance of N2S-S3 was improved by the additions of Mo, TiC_7N_3, TiC, and a combination of TiC plus Mo.

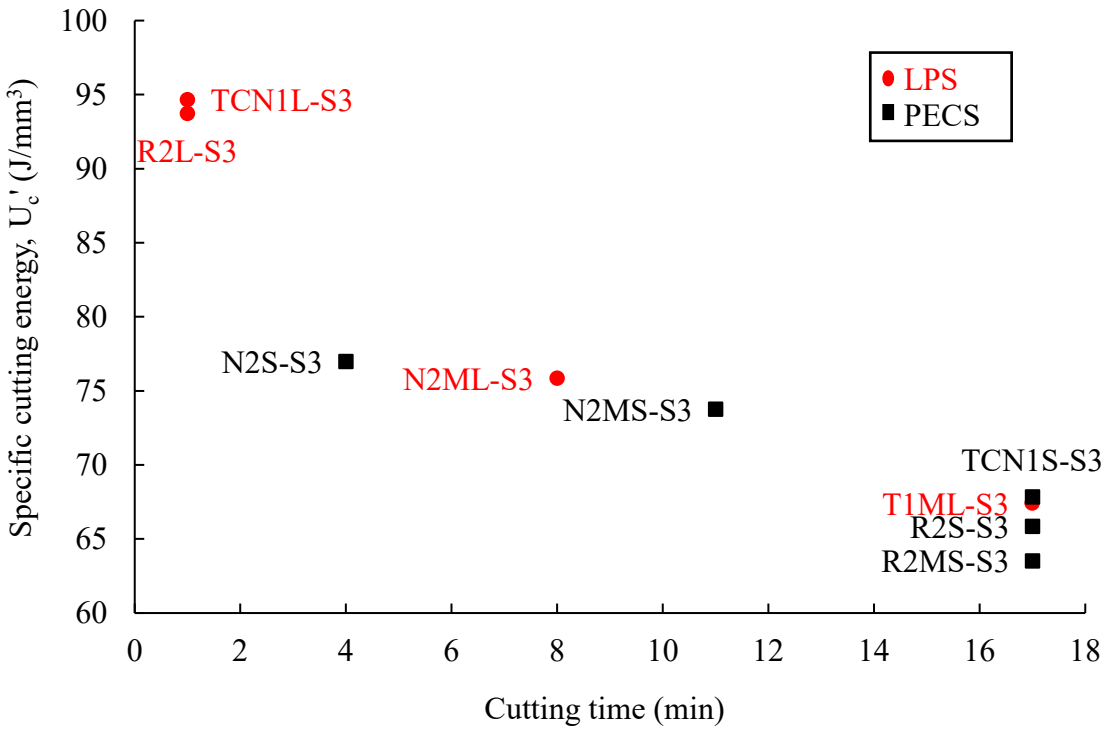


Figure 6-45. Variation of specific cutting energy (U_c') with effective cutting time (I_l') for shark skin (S3) cutting inserts during finishing 2 at n = 1600 rpm and a_p = 0.25 mm

Figure 6.46 shows the overall preference score and rank of the shark skin (S3) cutting inserts used during finishing 2 machining trials. The green colour code signifies the best cutting inserts while amber and red indicate average and poorly ranked cutting inserts, respectively. As shown in the figure, the most ideal solution for the S3 cutting inserts was the R2MS-S3 cutting insert with an overall preference score of 0.999 and it was followed by TCN1S-S3 and R2S-S3 with scores of 0.84 and 0.81, respectively. The average performing cutting inserts had overall preference scores of between 0.4 and less than 0.8. From Figure 6.46, it can be seen that the poorly ranked cutting inserts (N2S-S3, R2L-S3 and TCN1L-S3) had overall preference scores of below 0.3.

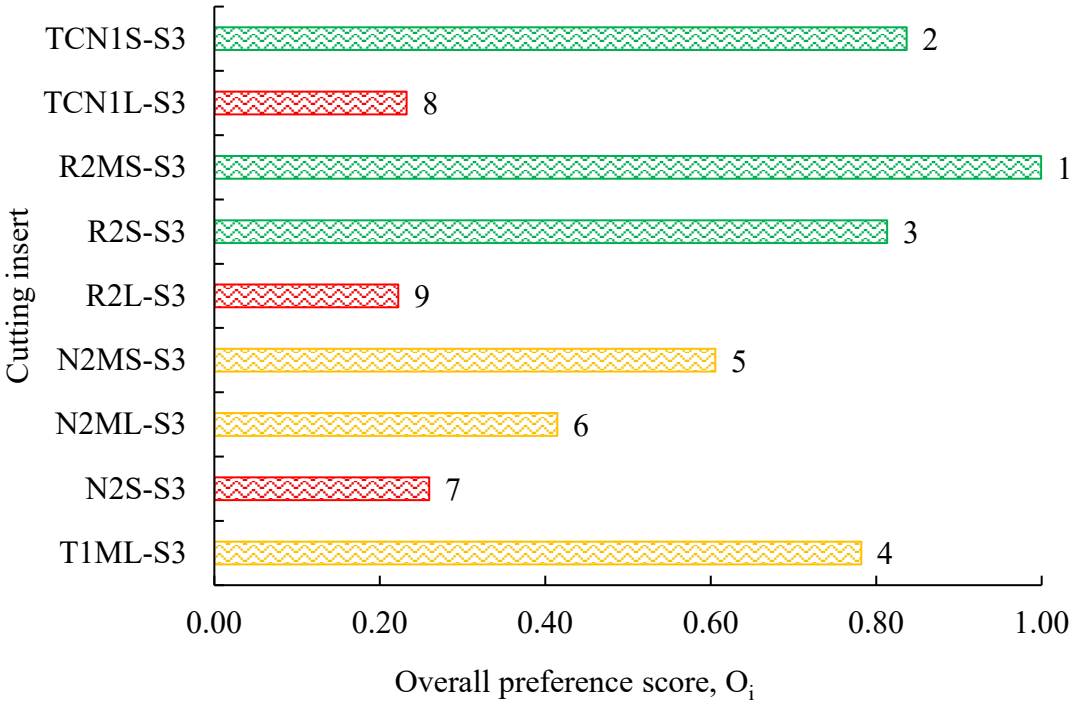


Figure 6-46. Overall preference score (O_i) and rank of S3 cutting inserts (alternatives)

6.7. Analyses of the pyramid LSM (P3) cutting inserts

This subsection presents and analyses resultant cutting forces, specific cutting energy, machining temperature, insert life, wear, and surface roughness of the pyramid LSM (P3) cutting inserts during the face milling of a-GCI under finishing 2 conditions. The micrographs of the cutting inserts showing the flank and rake faces are also presented in this section. Lastly, the machining performance evaluation of the pyramid LSM cutting inserts is done to obtain the overall ranking of the cutting inserts.

6.7.1. Analysis of the resultant forces, specific cutting energy, and temperature of the P3 cutting inserts

Table 6.14 gives the resultant forces, specific cutting energy (energy consumption), and the average machining temperature of the pyramid LSM (P3) cutting inserts during finishing 2. Figure 6.47 depicts the average resultant and the maximum resultant forces experienced by P3 cutting inserts during finishing2 machining operations. From the figure, the majority of P3 cutting inserts experienced maximum resultant forces of above 1500 N. The figure also shows that the R2L-P3 and TCN1L-P3 cutting inserts experienced the highest F_{max}' among the P3 cutting inserts. The cutting insert which exhibited the lowest F_{max}' was observed to be the T1ML-P3 with F_{max}' of 1577 N (see Table 6.14 and

Figure 6.47). As shown in the figure, there were generally no significant differences in F_{max}' experienced by the majority of the P3 cutting inserts. In addition, Figure 6.47 shows that the maximum resultant forces were significantly higher than the average resultant forces for P3 cutting inserts except for R2L-P3 and TCN1L-P3 cutting inserts which shared the same values for the two variables. The average resultant forces appear to follow a similar trend to that F_{max}'. Irrespective of composition and sintering technique, the T1ML-P3 cutting insert exhibited the lowest F' compared to the other P3 cutting inserts (see Figure 6.47). The LPS produced NbC-Ni based cutting inserts had slightly higher F' values than their PECS produced counterparts. There were no significant differences in the average resultant cutting forces of the R2S-P3 and the R2MS-P3 cutting inserts.

Table 6.14. Machining forces, specific energy consumption, and temperature results of P3 cutting inserts during finishing 2 at n = 1600 rpm and a_p = 0.25 mm

Insert name	Average resultant force, F' (N)	Maximum resultant force, F_{max}' (N)	Specific cutting energy, U_c' (J/mm^3)	Average Temperature, T' (^{o}C)
T1ML-P3	793	1577	49.54	71.17 ± 0.65
N2S-P3	822	1587	51.37	55.08 ± 0.47
N2ML-P3	894	1606	55.90	69.29 ± 0.63
N2MS-P3	838	1628	52.40	65.49 ± 0.59
R2L-P3	1703	1703	106.43	NA
R2S-P3	889	1642	55.56	83.59 ± 0.78
R2MS-P3	902	1649	56.36	78.63 ± 0.73
TCN1L-P3	1698	1698	106.13	NA
TCN1S-P3	966	1670	60.37	70.43 ± 0.64

*NB: The average and maximum resultant force have a fixed error of ±15 N from the Kistler.

Figure 6.48 shows the variation of the specific cutting energy with the average resultant cutting force of P3 cutting inserts. The T1ML-P3 had the lowest U_c' (~50 J/mm^3) per volume of material removed during the machining process. Besides, the TCN1L-P3 and R2L-P3, the specific cutting energies of the majority of P3 cutting inserts were below 61 J/mm^3. As shown in the figure, TCN1L-P3 and R2L-P3 had U_c' of ~106 J/mm^3. Generally, the LPS produced NbC-Ni based cutting inserts had higher U_c' values compared to their PECS counterparts.

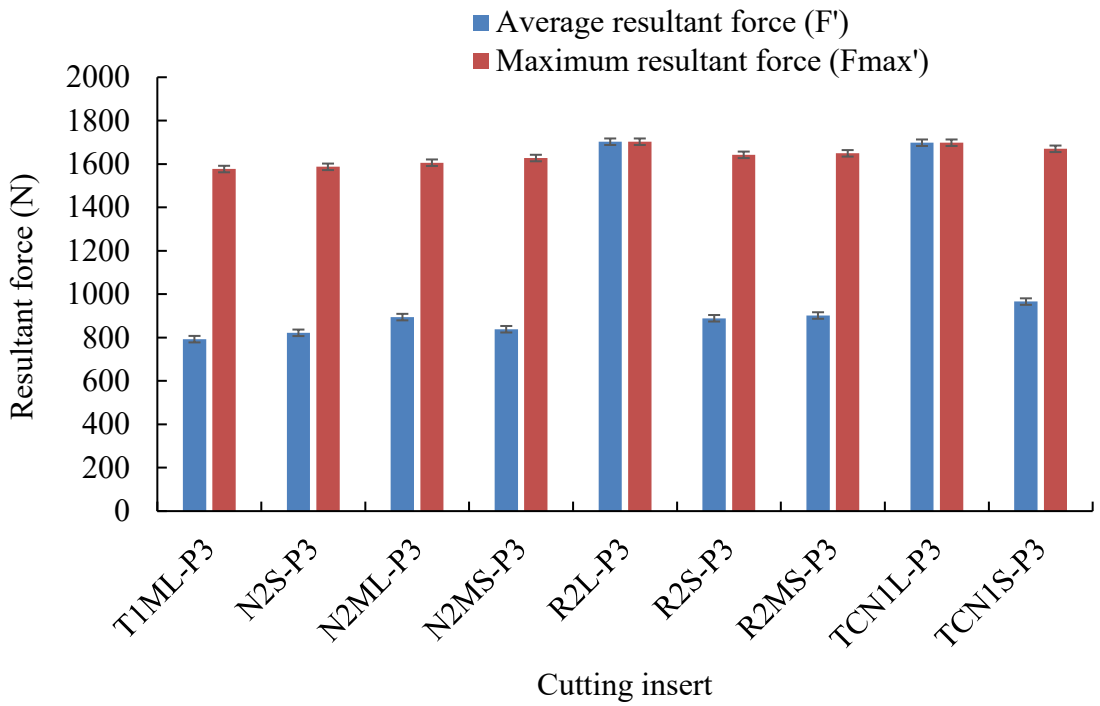


Figure 6-47. Average resultant force (F′) and maximum resultant force (F_{max}') for P3 cutting inserts during finishing at n = 1600 rpm and a_p = 0.25 mm

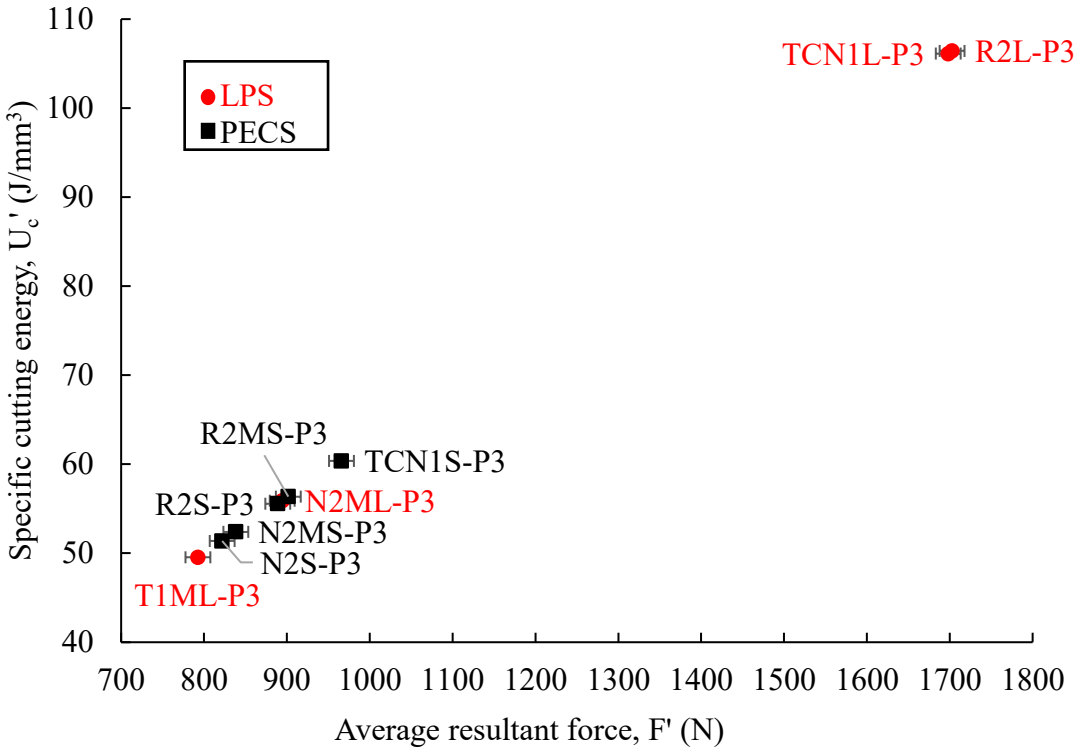


Figure 6-48. Variation of the specific cutting energy (U_c') with the average resultant force (F′) for P3 cutting inserts during finishing 2 at n = 1600 rpm and a_p = 0.25 mm

Figure 6.49 shows the average machining temperature with the average resultant cutting force of the pyramid LSM (P3) cutting inserts during finishing 2. Unlike B3 and S3 cutting inserts, T′ of P3 cutting inserts appears to increase with increasing F'. However, it should be highlighted that this relationship is not immediately apparent as indicated in Figure 6.49. The N2S-P3 cutting insert had the lowest average machining temperature (55.08 ± 0.47 °C) (see Figure 6.49). The cutting insert which exhibited the highest average machining temperature was the R2S-P3. Furthermore, Figure 6.49 also shows that the additions of Mo, TiC, TiC_7N_3, and a combination of Mo plus TiC, to the N2S-P3 composition resulted in increased average machining temperature in N2MS-P3, R2S-P3, TCN1S-P3 and R2MS-P3 cutting inserts respectively.

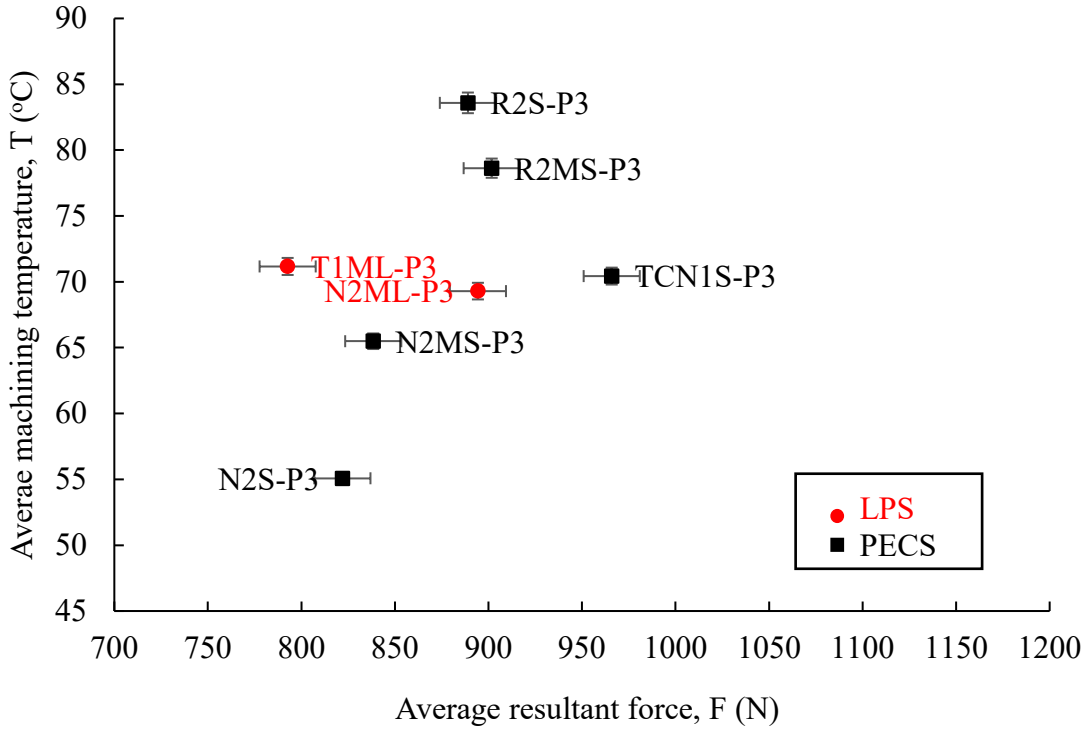


Figure 6-49. Variation of the average machining temperature (T′) with the average resultant force (F′) for pyramid LSM (P3) cutting inserts during finishing 2

6.7.2. Analyses of insert tool life and wear performance of P3 cutting inserts

Table 6.15 gives the cutting insert tool life, wear performance and surface roughness of P3 cutting inserts. Figure 6.50 shows the variation of the maximum flank wear with the cutting time for pyramid LSM (P3) cutting inserts during finishing 2 machining trials. According to the figure, the VB_{max}' of all P3 cutting inserts did not exceed 85 µm. The TCN1S-P3 cutting insert exhibited the highest VB_{max}' (82.23 µm) after 11 minutes of cutting time which was the longest among the P3 cutting inserts (see Table 6.15 and Figure 6.50). The insert tool life of the majority of P3 cutting inserts was 8 minutes

and below as indicated in Figure 6.50. The T1ML-P3, R2MS-P3, R2S-P3 and N2MS-P3 exhibited similar I_l' values. Among these cutting inserts, the T1ML-P3 had the lowest VB_{max}' (28.89 µm), followed by the R2MS-P3, R2S-P3 and N2MS-P3 with VB_{max}' values of 38.89 µm, 45.00 µm and 51.67 µm, respectively. Similar to in B3 and S3 cutting inserts, the TCN1L-P3 and R2L-P3 cutting inserts had the shortest I_l' values among the P3 cutting inserts. In general, the PECS produced NbC-Ni based cutting inserts had better insert tool life performance than their LPS produced counterparts. Furthermore, Figure 6.50 shows that the additions of Mo, TiC, TiC_7N_3, and a combination of Mo plus TiC, to the N2S-P3 composition resulted in improved insert tool life performance of N2MS-P3, R2S-P3, TCN1S-P3 and R2MS-P3 cutting inserts respectively.

Table 6.15. Effective insert tool life, maximum flank wear, flank wear rate, and surface roughness results of P3 cutting inserts during finishing at n = 1600 rpm and a_p = 0.25 mm

Insert name	Insert tool life, I_l' (min)	Maximum flank wear, VB_{max}' (µm)	Flank wear rate, FWR′ (µm/min)	Surface roughness Ra (µm)
T1ML-P3	8	28.89	3.61	1.68 ± 0.28
N2S-P3	4	36.67	9.17	1.22 ± 0.06
N2ML-P3	6	60.00	10.00	1.64 ± 0.21
N2MS-P3	8	51.67	6.46	1.76 ± 0.58
R2L-P3	1	50.56	50.56	2.34 ± 0.83
R2S-P3	8	45.00	5.63	1.81 ± 0.28
R2MS-P3	8	38.89	4.86	1.39 ± 0.17
TCN1L-P3	1	32.78	32.78	1.68 ± 0.35
TCN1S-P3	11	82.23	7.48	1.56 ± 0.39

Figure 6.51 shows the effects of pyramid LSM on the cutting insert tool life performance. The figure shows the percentage improvement (in green) and reduction (in red) of the insert tool life of P3 cutting inserts compared to the blank (B3) cutting inserts. From the figure, the application of pyramid LSM resulted in insert tool life improvement of N2S-P3 cutting insert only, with the insert achieving an increase of 75% (the same as N2S-S3). The N2ML-P3 and R2MS-P3 cutting inserts had neither improvement nor reduction in insert tool life performance. The remaining P3 cutting inserts had their insert tool life reduced by the pyramid LSM application, with the TCN1L-P3 and R2L-P3 having 300% reductions respectively (an observation noted on their S3 counterparts). The insert tool life performance of R2S-P3 and T1ML-P3 cutting inserts were reduced by 150%, and the reductions of TCN1S-P3 and N2MS-P3 were 82% and 75%, respectively.

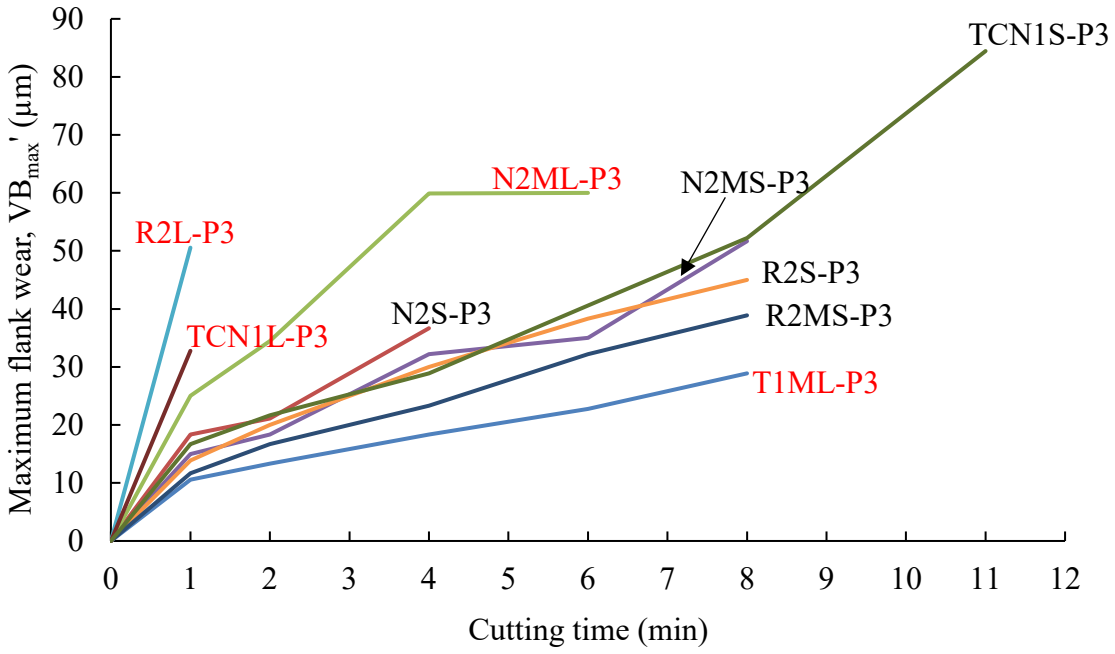


Figure 6-50. Variation of the maximum flank wear (VB_{max}') cutting time (l_l') for pyramid LSM (P3) cutting inserts during finishing 2 at n = 1600 rpm and a_p = 0.25 mm

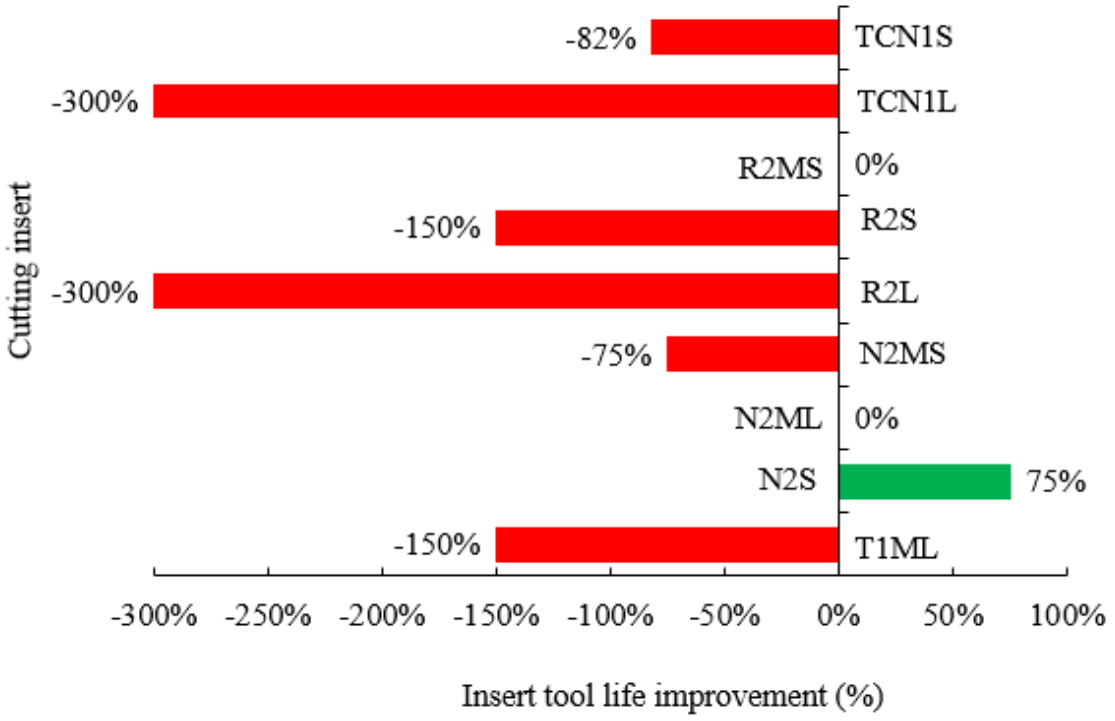


Figure 6-51. Effects of pyramid LSM technique on the P3 cutting inserts tool life performance benchmarked against B3 cutting inserts during finishing at n = 1600 rpm and a_p = 0.25 mm

Figure 6.52 shows the variation of flank wear rate against the average resultant cutting force of P3 cutting inserts. Similar to the observations in S3 cutting inserts, there is a slight direct proportionality relationship between FWR′ and F′ of P3 cutting inserts. However, this connection is not immediately apparent. From the figure, the majority of the P3 cutting inserts had FWR's of below 10.00 µm/min. Similar to its S3 counterpart, the T1ML-P3 exhibited the lowest FWR′ (3.61 µm/min) among the P3 cutting inserts. The R2L-P3 and TCN1L-P3 cutting inserts exhibited high values of FWR and average resultant cutting forces, with the former having the highest FWR′ (50.56 µm/min) among the P3 cutting inserts. In general, the LPS produced cutting inserts exhibited higher FWR' than their PECS produced counterparts.

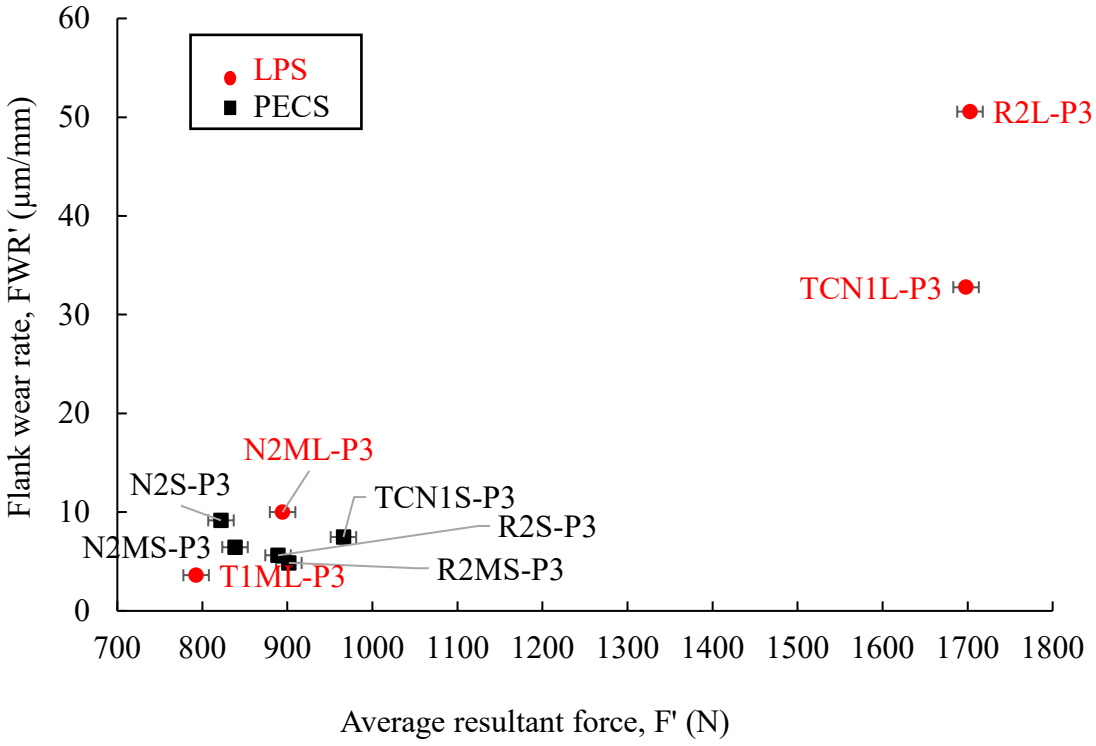


Figure 6-52. Variation of the flank wear rate (FWR′) with the average resultant force (F′) for pyramid LSM (P3) cutting inserts during finishing 2

Figure 6.53 shows the comparison of FWR of B3 cutting inserts against P3 cutting inserts. From the figure, all LPS produced P3 cutting inserts irrespective of composition and sintering technique had higher FWR' compared to their B3 counterparts. A contrasting observation was made on the PECS produced cutting inserts, whereby the PECS produced P3 cutting inserts had slightly lower FWR′ than the B3 counterparts as shown in the figure. It is worth noting that the increase in FWR′ of LPS produced cutting inserts was significant in the majority of the cutting inserts. For instance, the R2L-P3 and TCN1L-P3 had FWR′ increments of 243% and 184% respectively, while the increment of FWR′ in N2ML-P3 was 14%. Considering the PECS produced cutting inserts, the N2S-P3 had the highest

reduction in FWR′ with the cutting insert having a reduction of 63%. The N2MS-P3 had an FWR′ reduction of 13% and the FWR′ reductions in R2MS-P3 and R2S-P3 were below 10%.

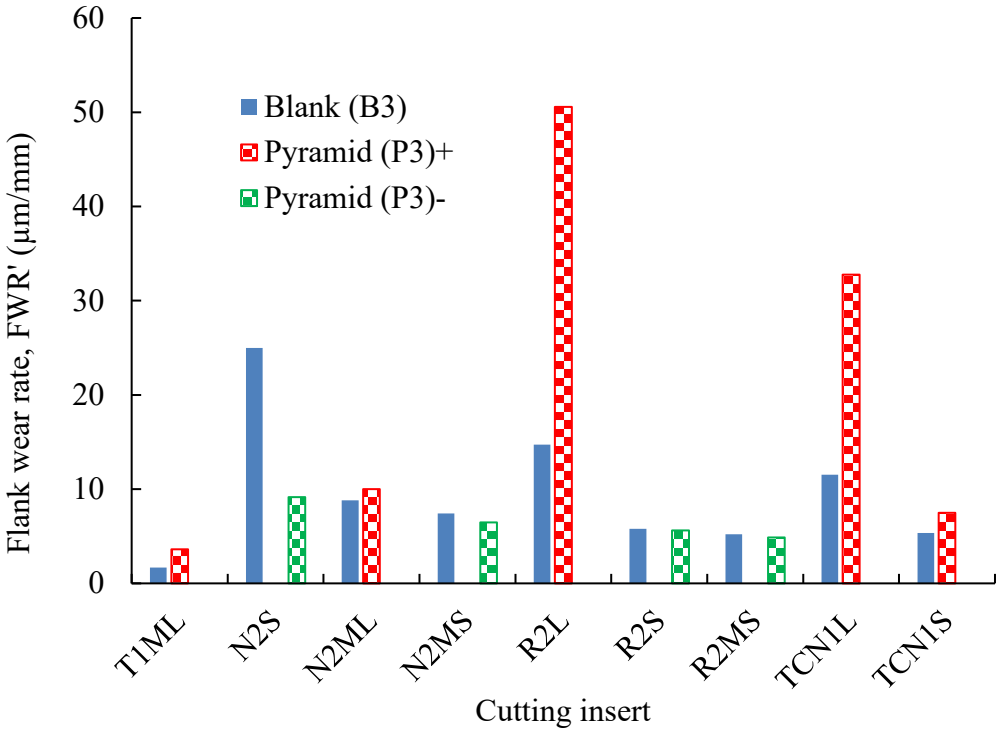


Figure 6-53. Comparison of the flank wear rate of blank (B3) vs. pyramid LSM (P3) cutting inserts during finishing 2

6.7.3. Analyses of micrographs of the flank and rake faces of P3 cutting inserts

Figure 6.54 shows the optical micrographs of the flank and the rake faces of the (a) TCN1S-P3, (b) T1ML-P3, and (c) R2MS-P3 cutting inserts. From the figure, the cutting inserts experienced abrasion wear on the flank faces. The wear land on the flank face of TCN1S-P3 cutting insert was slightly more pronounced than on the T1ML-P3 and R2MS-P3 cutting inserts. The rake face of the TCN1S-P3 exhibited mechanical fracture (see Figure 6.54 (a)). Very similar cutting edge wear characteristics were observed on the rake faces of T1ML-P3 and R2MS-P3. The rake faces of these cutting inserts exhibited chipping of the cutting edge. The rest of the P3 cutting inserts were also analysed and similar wear behaviour and cutting edge failure mechanisms were observed on the flank and rake faces. The flank faces exhibited abrasion wear whereas the rake faces showed failure through chipping and mechanical fracture. In general, LPS produced cutting inserts exhibited more cutting edge wear compared to their PECS counterparts.

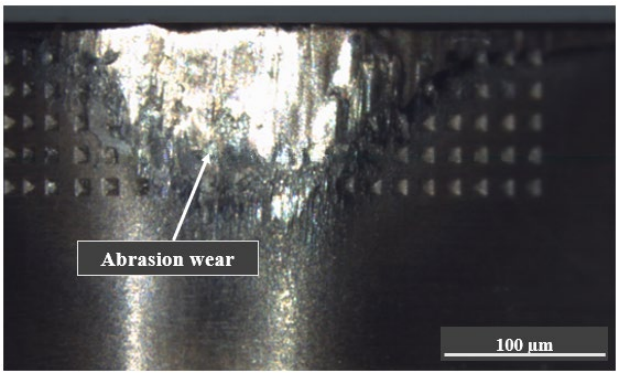
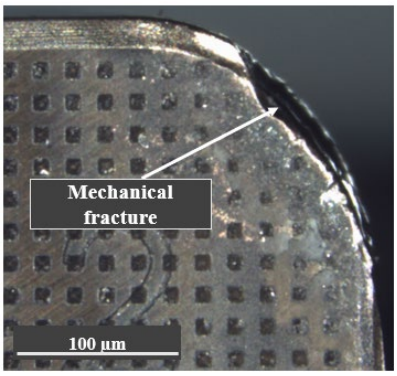
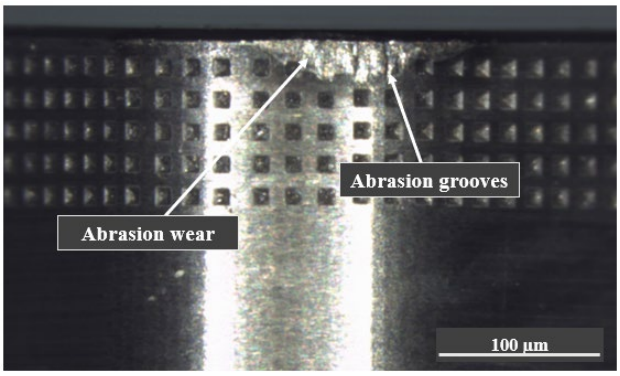
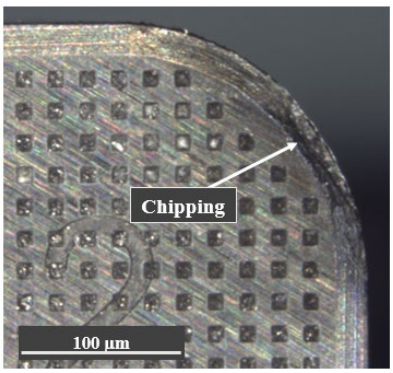
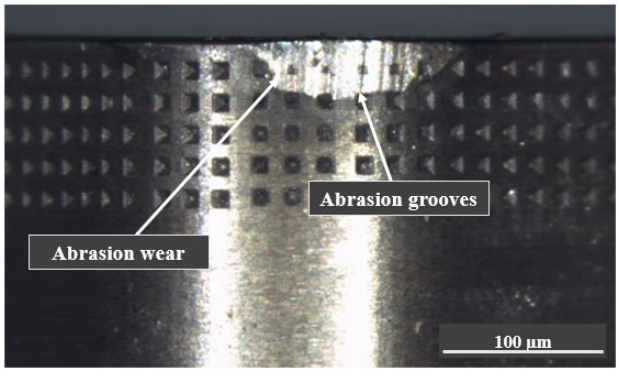
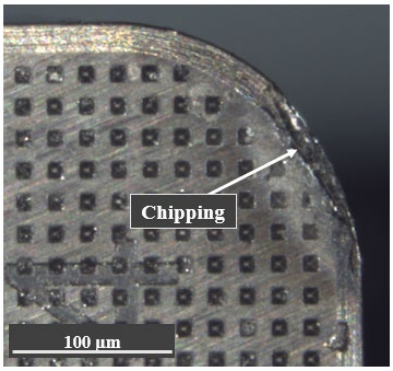
Insert	Flank face	Rake face
(a) TCN1S-P3		
	VB_{max}' = 82.23 µm Cutting time = 11 minutes	
(b) T1ML-P3		
	VB_{max}' = 28.89 µm Cutting time = 8 minutes	
(c) R2MS-P3		
	VB_{max}' = 38.89 µm Cutting time = 8 minutes	

Figure 6-54. Optical micrographs of the flank and rake faces of (a) TCN1S-P3, (b) T1ML-P3 and (c) R2MS-P3 cutting edges during finishing 2 machining

6.7.4. Machining performance evaluation and analyses of P3 cutting inserts

This subsection provides machining performance evaluation and analyses of pyramid LSM (P3) cutting inserts during finishing 2 machining trials. Table 6.16 shows the values of criteria C1-C4 used for evaluating and assessing the machining performance of P3 cutting inserts. Figure 6.55 depicts the variation of specific cutting energy with the effective insert tool life of P3 cutting inserts. From Table 6.16 and Figure 6.55, the TCN1S-P3 cutting insert had the best combinations of the machining performance criteria. This performance was followed by that of T1ML-P3, N2MS-P3, R2S-P3 and R2MS-P3 cutting inserts which achieved 8 minutes of cutting time and had slightly lower specific cutting energy than TCN1S-P3 cutting insert (see Figure 6.55). The T1ML-P3 exhibited the lowest energy consumption, however, its Ra was slightly higher than the TCN1S-P3 cutting insert. There was no significant difference between the machining performances of R2S-P3 and R2MS-P3 as shown in both Table 6.16 and Figure 6.55. Table 6.16 also shows that the N2S-P3 cutting insert had the lowest surface roughness among P3 cutting inserts. However, the insert only managed a cutting time of 4 minutes. Similar to the observations in B3 and S3 cutting inserts, the R2L-P3 and TCN1L-P3 cutting inserts exhibited the poorest machining performance among the P3 cutting inserts. In general, Table 6.16 and Figure 6.55 indicate that the LPS produced cutting inserts exhibited poorer combinations of machining performance criteria than their PECS produced counterparts.

Table 6.16. Machining performance evaluation criteria for P3 cutting inserts

Insert name	Effective insert tool life, I_l' (min) [C1]	Specific cutting energy, U_c' (J/mm^3) [C2]	Surface roughness, Ra (µm) [C3]	Maximum resultant cutting force, F_{max}' (N) [C4]
T1ML-P3	8	49.54	1.68 ± 0.28	1577
N2S-P3	4	51.37	1.22 ± 0.06	1587
N2ML-P3	6	55.90	1.64 ± 0.21	1606
N2MS-P3	8	52.40	1.76 ± 0.58	1628
R2L-P3	1	106.43	2.34 ± 0.83	1703
R2S-P3	8	55.56	1.81 ± 0.28	1642
R2MS-P3	8	56.36	1.39 ± 0.17	1649
TCN1L-P3	1	106.13	1.68 ± 0.35	1698
TCN1S-P3	11	60.37	1.56 ± 0.39	1670

Considering the PECS produced cutting inserts, the N2S-P3 had the poorest combinations of machining performance criteria. From Figure 6.55, the overall machining performance of the N2S-P3 cutting insert was improved by the additions of Mo, TiC, TiC_7N_3 and a simultaneous addition of Mo and TiC to the N2S-P3 composition, respectively. For example, the machining performances of N2MS-P3, R2S- P3, TCN1S- P3 and R2MS-P3 cutting inserts were better than that of N2S-P3.

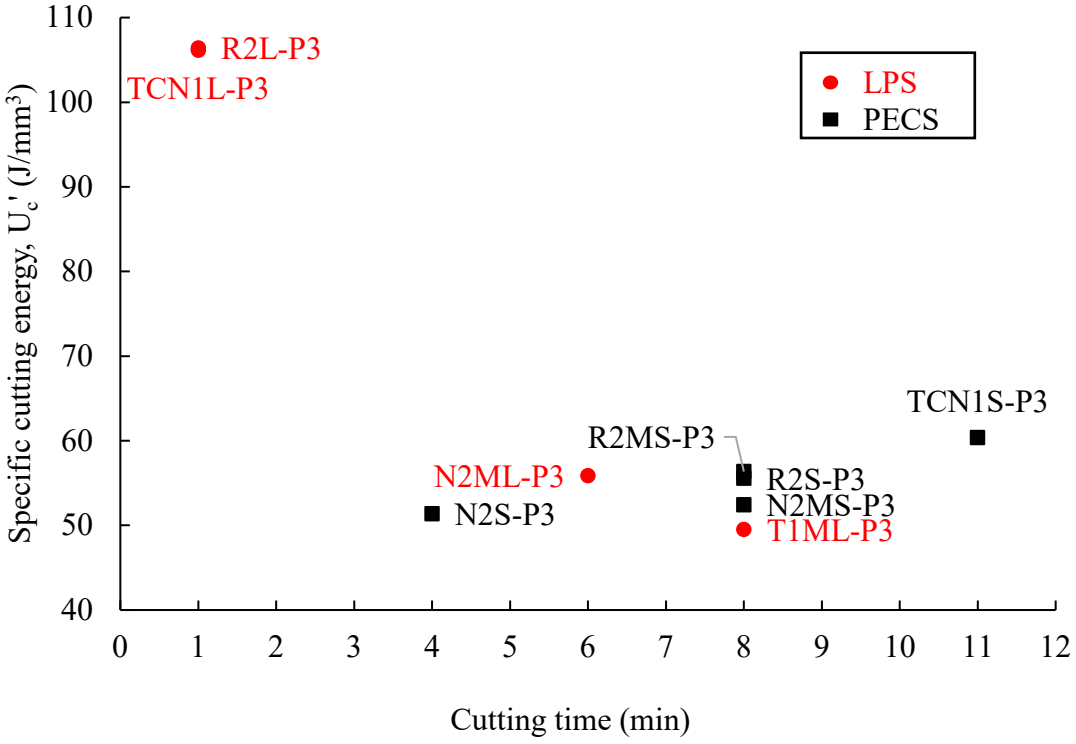


Figure 6-55. Variation of specific cutting energy (U_c') with effective cutting time (I_l') for pyramid LSM (P3) cutting inserts during finishing 2 at n = 1600 rpm and a_p = 0.25 mm

Figure 6.56 shows the overall preference score and rank of the pyramid LSM (P3) cutting inserts used during finishing 2 machining trials. The green colour code signifies the best cutting inserts while amber and red indicate average and poorly ranked cutting inserts, respectively. As a result, the top ranked cutting inserts were the TCN1S-P3, T1ML-P3 and N2MS-P3, with overall preference scores of 0.91, 0.73, and 0.72. From the figure, there was no significant difference between the overall preference scores of N2MS-P3 and R2S-P3 cutting inserts. As expected, the TCN1L-P3 and R2L-P3 had the lowest overall preference scores among the P3 cutting inserts, with the inserts having scores of 0.11 and 0.01.

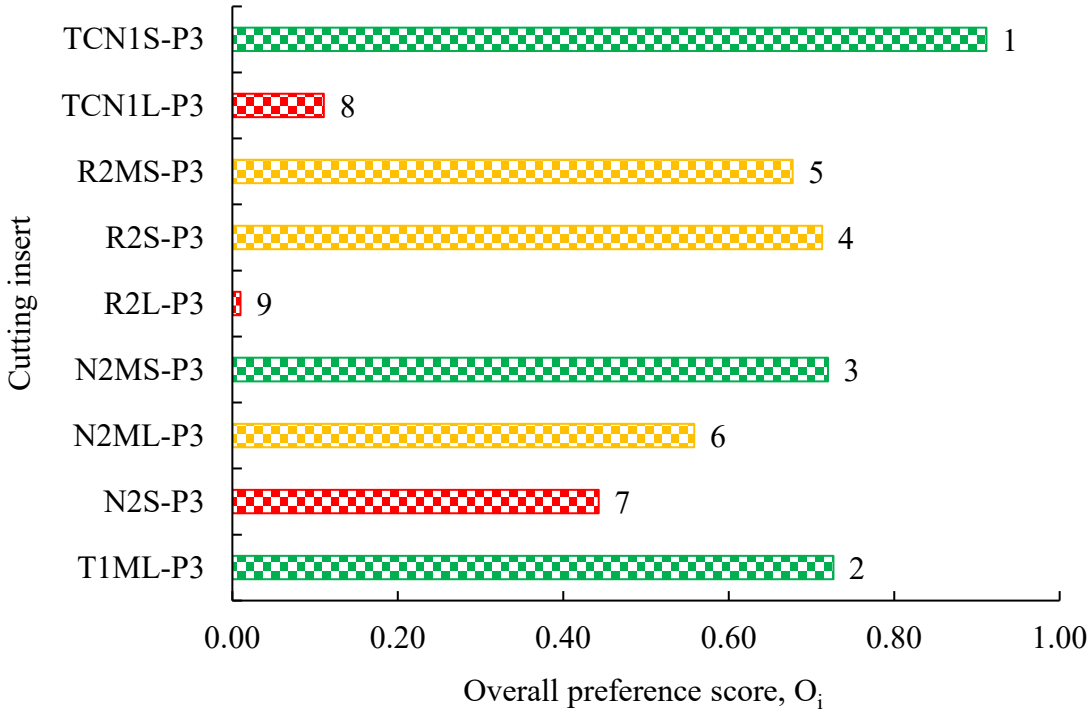


Figure 6-56. Overall preference score (O_i) and rank of P3 cutting inserts (alternatives)

6.8. Consolidated results for finishing 2 (Test 3)

This section summarises the overall machining results of the finishing 2 trials. The overall analyses and comparisons of the machining performance of the finishing 2 cutting inserts are made and presented in this section. The primary objective was to evaluate and rank the performance of all the cutting inserts used during finishing 2 machining. For this purpose, the TOPSIS model was employed on the 27 cutting inserts (B3, S3 and P3 inserts) used during the machining trials under finishing 2 conditions. Table 6.17 provides the machining performance criteria, the overall preference scores, and the rank of all the cutting inserts used during finishing 2 machining trials. From the table, it can be seen that the TCN1S-B3 and T1ML-B3 inserts had the best overall machining performance. Both cutting inserts obtained an overall preference score of 0.826 respectively. The TCN1S-B3 had performance criteria values of I_l' = 20 min, U_c' = 59.80 J/mm^3, Ra = 1.75 µm, and F_{max}' = 1551 N, whereas those of T1ML-B3 were 20 min, 44.93 J/mm^3, 2.34 µm and 1111 N, respectively.

Table 6.17. Machining performance criteria, overall preference scores, and rank of combined cutting inserts used during finishing 2

Solution	Cutting insert	C1 (min)	C2 (J/mm^3)	C2 (N)	C4 (μm)	Overall preference score	Rank	Category
A9	TCN1S-B3	20	60	1.75	1551	0.826	1	Best (1 – 9)
A1	T1ML-B3	20	45	2.34	1111	0.826	2	
A6	R2S-B3	20	57	2.00	1317	0.822	3	
A16	R2MS-S3	17	64	1.00	1441	0.781	4	
A18	TCN1S-S3	17	68	1.92	1463	0.737	5	
A15	R2S-S3	17	66	2.09	1436	0.735	6	
A10	T1ML-S3	17	67	2.31	1522	0.716	7	
A4	N2MS-B3	14	44	1.80	1395	0.695	8	
A27	TCN1S-P3	11	60	1.56	1670	0.546	9	
A13	N2MS-S3	11	74	1.88	1541	0.506	10	Average (10 – 18)
A7	R2MS-B3	8	46	2.02	1028	0.458	11	
A19	T1ML-P3	8	50	1.68	1577	0.453	12	
A22	N2MS-P3	8	52	1.76	1628	0.443	13	
A24	R2S-P3	8	56	1.81	1642	0.434	14	
A25	R2MS-P3	8	56	2.40	1649	0.418	15	
A3	N2ML-B3	6	47	2.39	1045	0.383	16	
A21	N2ML-P3	6	56	1.64	1606	0.369	17	
A12	N2ML-S3	8	76	2.44	1565	0.366	18	
A5	R2L-B3	4	42	1.61	1073	0.360	19	Poor (19 – 27)
A2	N2S-B3	1	36	1.06	575	0.347	20	
A20	N2S-P3	4	51	1.22	1587	0.342	21	
A8	TCN1L-B3	4	57	1.53	1084	0.316	22	
A11	N2S-S3	4	77	1.62	1540	0.241	23	
A17	TCN1L-S3	1	95	1.00	1515	0.185	24	
A14	R2L-S3	1	94	1.08	1500	0.179	25	
A26	TCN1L-P3	1	106	1.68	1698	0.098	26	
A23	R2L-P3	1	106	2.34	1703	0.015	27	

7. Discussion

This chapter provides the analysis, interpretation and implications of the findings presented in the previous chapters.

7.1. Densification

All the sintered samples irrespective of the sintering technique achieved densification of ≥ 97%. With the exception of N2ML, the LPS produced samples had slightly higher densification than the PECS produced samples. This was attributed to the presence of the wetting liquid phase, which enhances diffusion, facilitating material transport by capillary forces which pull the grains together and densification during the LPS process [13]. The T1ML sample exhibited the highest densification compared to all the other samples used due to the good solubility and wettability of WC in the Co liquid phase [13] compared to that of NbC in Ni. The PECS produced samples had comparable densities to LPS produced samples, even though the former were sintered at significantly lower temperatures as shown in Table 3.2 and Table 3.3. This is because when the sample is heated during the PECS process, every particle is heated spontaneously, and the sample quickly approaches the sintering temperatures [181]. Furthermore, the sample is sintered from the surface to the inner core at the same time, resulting in fast densification [181]. In contrast, in conventional LPS, the sample's surface initially reaches the sintering temperature and is sintered, while the centre is not sintered because heat cannot be transferred quickly enough through the sample's thickness. The addition of Mo as a binder phase to the N2S sample composition (NbC-12Ni) did not have a significant effect on the densification of the N2MS sample. However, a contrasting observation was observed in the R2S and R2MS samples, whereby the addition of Mo to the R2S composition (NbC-10TiC-12Ni) slightly improved the densification. Mo addition improved the wettability of the binder phase to the hard phase by the formation (Nb, Ti, Mo) C solid solution which is wetted easier by Ni liquid than TiC [182]. Similar observations were made in independent studies by Wang et al. [182] and Genga et al. [183]. The additions of TiC and TiC_7N_3 to the N2S sample composition (NbC-12Ni (wt.%)) slightly inhibited the densification of PECS produced R2S and TCN1S samples at 1285 °C and 30 MPa, respectively. These additions have relatively higher melting points than NbC, thus their presence adversely impacted densification during the sintering process [13], [184]. As a result, higher sintering temperatures and pressures were required [58].

7.2. Microstructure

7.2.1. Microstructure of WC-10TiC-10[Co/Mo] (wt%.) (T1ML) sample

The microstructure of the liquid phased sintered T1ML sample had fine WC platelet shaped grains (light phase) with homogeneously distributed Co binder pools (light grey phase), dark grey phase is the (W, Ti, Co) C solid solution and TiC rich solid solutions (dark phase) (see Figure 4.1 and Table 4.2). This observation was in contrast to the conventional (or straight) WC-Co alloys produced by LPS which typically consist of relatively larger carbide grains within their microstructure [58]. The fine WC grains obtained in T1ML were due to the addition of TiC and the partial substitution of Co by Mo which resulted in the restriction of grain growth [13, 44]. This is attributed to the formation of a solid solution (W, Ti, Mo, Co) C which limited grain boundary migration and thus inhibited grain growth during the sintering process [13]. Molybdenum was added to also improve the wettability between the TiC and the metallic Co phase by the formation of the (W, Ti, Mo, Co) C solid solution [182], which slowed down the aggregation of WC grains. Thus, a finer microstructure was obtained [44]. The good distribution of the Co binder pools was due to the formation of the Co liquid phase during sintering which enhanced the solubility of WC, and the capillarity action of the binder phase between pores during the secondary rearrangement stage of sintering [12]. Although Mo improves the wettability between the ceramic phase and the metallic phase, it also reduces the solubility of TiC in the binder, thus limiting grain growth by the solution-precipitation mechanism during sintering [44]. This effect is confirmed by the presence of a dark undissolved TiC phase as shown in the SEM-BSE micrograph of T1ML sample (see Figure 4.1). Furthermore, as expected, the additives also resulted in the change of shape of the WC grains, yielding a microstructure that has a mixture of thin platelets (elongated rectangular), faceted and near-spherical smaller grains as opposed to truncated trigonal prism shaped found in the WC-Co alloys [185]. Molybdenum was not detected in EDS due to the small amount but was found to be all over the microstructure of T1ML by HAADF-STEM mapping (Figure 4.1 and Figure 4.2). The HAADF-STEM mapping indicated that the TiC phase was isolated from the WC-Co composition. This was mainly due to the lower sintering temperatures and pressures which prevented a complete dissolution of TiC, leading to the formation of Ti-rich regions [14]. In other areas of the microstructure, the fine TiC precipitated into WC-Co phase leading to the formation of the (W, Co, Ti) C solid solution [14]. These observations were confirmed by the HAADF-STEM mapping of the sample (Figure 4.2). The mapping also revealed that the Co binder phase typically coincided with the WC grains, especially along the boundaries of the carbide. This was due to the good solubility of WC in Co and the good wetting of WC by Co [13].

7.2.2. Microstructure of NbC-12Ni based sintered samples

The microstructure of the PECS produced N2S (NbC-12Ni) (wt%) sample showed medium-sized grains, fairly distributed Ni binder pools (dark phase) and a higher degree of NbC grains (light phase) contiguity. This was because of the PECS shorter sintering time and lower sintering temperatures which promoted rapid solidification and prevented Ostwald ripening [58]. The sub-micrometre dark spherical spots visible inside the carbide grains (Figure 4.3 (a)) were pores [47, 186]. The LPS produced N2ML (NbC-12[Ni/Mo]) (wt%) sample exhibited relatively larger NbC grains and better binder pool distribution than its PECS produced N2MS counterpart. The larger NbC grains in N2ML sample were due to the grain growth by coalescence and Ostwald ripening [187]. The better Ni pool distribution was attributed to the formation of a liquid phase during LPS, unlike in PECS where the Ni liquid only formed momentarily and then followed by rapid solidification during PECS [12]. Similar to the N2S sample microstructure, the N2ML and N2MS samples also exhibited dark spots/phases (pores) inside the NbC grains. These phases were slightly more pronounced in the N2ML sample than in the N2S and N2MS samples. In general, porosity in the microstructure typically suggests that the densification process was adversely impacted [29]. Furthermore, the presence of pores in the samples was due to the low solubility of NbC in Ni, and the poor wetting behaviour of the Ni liquid during sintering [13, 186]. Unlike in T1ML, Mo was detected by EDS in both N2ML and N2MS samples. This was attributed to the low concentration (i.e. less than 10 wt%) of the added Mo in samples [188]. In T1ML, Mo completely precipitated in the carbide phase during the formation of the (W, Ti, Mo, Co) C solid solution which made its detection difficult during EDS. In N2ML and N2MS samples, Mo was only detected as a trace element due to the low concentration [188]. As a result, its exact location was not detected in EDS analysis but was confirmed to be mainly inside the NbC grains, therefore suggesting the formation of the (Nb, Mo) C solid solution [47] by HAADF-STEM mapping. The effect of Mo addition in the N2ML sample could not be observed since there was not an LPS produced NbC-12Ni sample. However, it has been reported in other studies that the addition of Mo or Mo_2C can improve the wettability of NbC and inhibit NbC grain growth in the solid state during the sintering of NbC-Ni alloy grades [13, 47]. Furthermore, an investigation by Genga et al. [20] reported that Mo was able to reduce the grain size through the formation of (Nb, Mo) C solid solution which delayed aggregation of fine NbC grains during sintering, and thus inhibiting coalescence grain growth. Lin et al. [189] also reported the dissolution and re-precipitation grain growth inhibition effect of Mo addition in WC-Co alloys. The addition of Mo to the N2S composition had no significant influence on the microstructure of N2MS (Figures 4.3 (a) and (c)). However, there was a slight clustering of Ni binder (poor Ni binder distribution) in the microstructure of N2MS than in N2S, suggesting that sintering at

1285 °C partially occurred in the solid state. Therefore, higher sintering temperatures and pressures were required [190]

The light, medium grey and dark phases in the microstructure of LPS produced R2L (NbC-10TiC-12Ni) (wt%) sample were determined to be NbC grains, Ni binder and TiC rich phases by the EDS mapping. The microstructure of the R2L sample exhibited a mixture of abnormally large faceted and slightly smaller spherical NbC grains compared to its PECS produced R2S counterpart (Figure 4.4). The large NbC grains in R2L were attributed to the grain growth due to Ostwald ripening and coalescence during the sintering process [54]. It must be noted that the abnormal grain growth observed in the R2L sample was unexpected since the composition consisted of TiC which is known to inhibit grain growth during sintering [13, 191]. However, the microstructure exhibited a sparsely distributed undissolved TiC, indicating that the majority of TiC was dissolved and precipitated in NbC resulting in the formation of (Nb, Ti) C solid solution during sintering [20, 190]. This was attributed to the high sintering temperature and longer sintering time during the LPS process [13]. The microstructure of the R2L sample also exhibited pores and/or impurities [186] and carbide pullouts due to the abrasive effect of grinding and polishing during sample preparation [192] (see Figure 4.4 (a)). The PECS produced R2S and R2MS samples exhibited very similar microstructural characteristics (Figure 4.4). The micrographs of both samples revealed a continuous NbC skeleton with isolated or clustered Ni binder phase. This was attributed to the shorter sintering time and lower sintering temperature associated with PECS sintering [193]. The micrographs of the samples also exhibited very bright Nb-rich phases inside the carbide grains, and patches of undissolved TiC (darkest phase) as confirmed by EDS. It is worth noting that the undissolved TiC phases were more pronounced in the R2MS sample than in R2S. The presence of the undissolved TiC phases was attributed to shorter sintering times and lower sintering temperatures as a result of PECS [58]. The undissolved TiC as well as the poor distribution of TiC suggests that higher sintering temperatures and pressures were required [183]. Similar to the N2MS sample, Mo in R2MS was detected by EDS and confirmed to be within the NbC grains by HAADF-STEM mapping even though it was added into the composition as a partial substitution to the binder. The mapping also revealed that some of the TiC also precipitated in NbC during sintering, resulting in the formation of (Nb, Mo, Ti) C solid solution as shown in Figure 4.5 [190]. These observations were consistent with a different study by Genga et al. [20]. The non-uniform (poor) distribution of undissolved TiC in R2MS compared to T1ML was attributed to the lower sintering temperatures and shorter dwelling time during PECS compared to LPS.

The microstructure of LPS produced TCN1L (NbC-10TiC_7N_3-12Ni) (wt%.) sample exhibited larger spherical grains than its PECS produced TCN1S counterpart. In both samples, the NbC was

represented by the light phase, Ni by the medium dark and TiCN-rich regions by the darkest phase as confirmed by EDS mapping, respectively. The Ni binder pool was fairly distributed in TCN1L due to the melting of Ni as a result of high sintering temperatures and longer sintering durations during LPS process [13, 54]. However, due to the shorter sintering times and lower sintering temperatures including rapid solidification during the PECS process, the Ni phase was not easily detectable in the TCN1S sample's microstructure [58, 68]. The microstructure of TCN1L showed Nb-rich core and TiCN-rich rim grains with bright contrast core (spots) towards the centre of the grains, a feature that was not easily detectable on the microstructure of the TCN1S sample. In general, the formation of core/rim structure is attributed to the difference in surface energies of the carbide constituents during sintering, which is closely related to the solubility of the carbides in molten metal [194]. The solubility of NbC in Ni is lower than that of TiC and TiN [195], therefore the surface energy of NbC in Ni is higher. Hence, the core of undissolved NbC particles acted as nucleation sites for the TiCN rim structure during sintering [194]. Furthermore, the presence of pores, and undissolved TiCN in the microstructure of TCN1L was observed and this was attributed to low solubility NbC in Ni and the poor wettability of the binder and carbide phase during sintering [13, 186]. Similar to the observations in the R2L sample, the undissolved TiCN phase was sparsely distributed in TCN1L compared to TCN1S which exhibited a more homogeneous distribution. This observation is consistent with the observations in a different study conducted by Huang et al. [196] which provides a detailed explanation of microstructural evolution during the sintering of NbC-Ni based cermets doped with TiCN. The carbide pull-outs were attributed to the abrasive effect of grinding and polishing during sample preparation (Figure 4.6) [192]. In general, the LPS produced NbC-Ni based cermets had larger NbC grains due to Ostwald ripening and coalescence and better Ni binder pool distribution due to longer sintering times and temperatures than the PECS produced cermets. Molybdenum addition was more effective in grain growth inhibition than TiC and TiC_7N_3 as shown by the smaller NbC grains in N2ML than in R2L and TCN1L, respectively. However, it should be noted that the sintering temperature of N2ML was lower (1390 °C) compared to that of R2L and TCN1L (1450 °C). The higher sintering temperatures in R2L and TCN1L could have led to the increased grain growth observed in the samples. The three samples showed the formation of respective solid solutions. In the case of N2ML, Mo dissolved completely inside NbC grains whereas R2L and TCN1L exhibited small amounts of sparsely distributed undissolved TiC and TiC_7N_3. This shows the higher temperature applied was necessary to allow the dissolution of these phases, however, it resulted in undesired grain growth. The PECS produced NbC-Ni based cermets had fine grains with NbC skeleton and poorly distributed Ni binder due to shorter sintering time and lower sintering temperature. Elemental Mo completely precipitated inside NbC grains in both N2MS and R2MS samples (confirmed by HAADF-STEM mapping). This

was despite the fact that it was introduced into both compositions as a metal rather than a secondary carbide phase. The samples R2S, R2MS, and TCN1S exhibited undissolved TiC and TiC_7N_3 phases. This was again attributed to the lower sintering temperature (1285 °C) and shorter sintering dwell times during PECS. The undissolved TiC phases in R2MS were slightly bigger than those in R2S due to the presence of Mo which could have influenced the wetting behaviour of the binder and solubility in R2MS.

7.3. Mechanical properties

7.3.1. Hardness properties

The LPS produced T1ML sample had the highest Vickers hardness (HV_{30}) (~14.5 GPa) compared to all the other samples irrespective of the composition or sintering technique. This was mainly due to the higher hardness of WC (22.5 GPa) compared to NbC (19.6 GPa) [42], Ni's lower hardness (or higher plasticity) than Co [13], and the finer WC grains within the T1ML microstructure [12, 13]. Furthermore, the fine WC grains resulted in increased hardness whilst the WC platelet (thin elongated) grains improved the fracture toughness due to a higher aspect ratio [197]. In general, the hardness and fracture toughness of WC-Co alloys can be influenced by the WC grain sizes (i.e. hardness is inversely proportional to the WC grain size meaning it increases with decreasing WC grain size whereas fracture toughness increases with increasing WC grain size) [198]. The PECS produced N2S and the LPS produced R2L samples exhibited similar hardness properties (~11 GPa), despite N2S having significantly smaller NbC grains than R2L (Table 4.2). Typically, the LPS produced NbC-12Ni (wt%.) sintered grades exhibit lower hardness properties than PECS produced grades of a similar composition due to slightly larger grains in LPS compared to PECS [58]. For example, Genga et al. [20] recorded hardness (HV_{30}) values of 9.73 ± 0.11 GPa and 12.47 ± GPa for LPS and PECS produced NbC-12Ni (wt%) samples in their investigations. In this study, the slightly higher hardness observed in R2L was attributed to the influence of the addition of a hard TiC as a secondary carbide [190]. Similar to R2L, the N2ML and TCN1L samples which had relatively larger carbide grain sizes (Table 4.2) also exhibited slightly higher hardness (i.e. 12.81 ± 0.12 GPa and 12.77 ± 0.13 GPa) than fine grained N2S (Table 4.3). The improved hardness in N2ML was attributed to the formation of (Nb, Mo) C solid solution, whereas the hardness in TCNL was attributed to the formation of (Nb, Ti) (C, N) solid solution [48]. These observations demonstrated that the hardness properties of conventionally sintered NbC-Ni cermets can be improved by composition manipulation, i.e. the addition of Mo as a partial binder substitution and TiC_7N_3 as a secondary carbide addition in N2ML and TCN1L, respectively. Furthermore, the slightly higher hardness in N2ML and TCN1L samples than R2L suggests that Mo

and TiC_7N_3 additions are more effective in improving the hardness properties of conventionally produced NbC-12Ni (wt%) cermets than TiC. This observation is consistent with the findings of a study by Genga et al. [20] where the addition of Mo_2C to NbC-12Ni (wt.%) yielded slightly higher hardness than the TiC addition to a similar composition. With the exception of N2MS, all the PECS produced NbC-12Ni (wt%.) based samples had slightly higher hardness than their LPS counterparts and this was attributed to the smaller fine grains as a result of lower sintering temperatures and shorter sintering times in PECS than LPS [58]. Furthermore, additions of Mo, TiC, TiC_7N_3 and a combination of Mo plus TiC to the N2S composition significantly improved the hardness properties in N2MS, R2S, TCN1S and R2MS. The PECS produced R2MS sample exhibited the highest. This observation was attributed to the combined effect of PECS's grain refinement and the formation of respective solid solutions [48]. In addition, TiC, and Ti (CN) have hardness of ~ 30 GPa and ~17.5 GPa respectively [16]. As a result, the presence of hard undissolved TiC in R2S and R2MS, and TiC_7N_3 in TCN1S contributed to the increased hardness of the samples [16]. The R2MS sample exhibited the highest hardness (14.11 ± 0.22 GPa) among the NbC-Ni based samples. The individual additions of Mo and TiC resulted in improved hardness, thus the combined effect of the two additions is expected to be higher.

7.3.2. Fracture toughness properties

The LPS produced samples exhibited higher fracture toughness (K_{IC}) than samples with similar compositions produced by PECS. This was due to the better distribution of the binder phase during LPS than in PECS which improved the carbide solubility, and the capillary action of the liquid during the secondary re-arrangement stage of sintering [26]. The more homogeneous distribution of binder in LPS results in lower contiguity and hence reduces the amount of carbide/carbide interface fracture which is considered the most critical fracture in cemented carbides [199]. During the PECS process, considerable inhomogeneous temperature distribution occurs from the centre to the surface of the conducting Ni particles when the pulsed current is carried through [69]. The contacting particles reached very high temperatures, melting momentarily, followed by rapid solidification [69], leading to poor binder distribution [45]. Furthermore, the fracture toughness property of cermets is directly proportional to the carbide grain sizes as mentioned previously [196]. Thus, generally, LPS produced samples are typically expected to exhibit relatively higher fracture toughness than PECS samples. The TCN1L sample had the highest fracture toughness (9.31 ± 0.53 $MPa \cdot m^{1/2}$) compared to all the samples in this study irrespective of composition and sintering technique. Comparable fracture toughness values of cermets containing TiCN additions were obtained by Huang et al. [196]. The high fracture

toughness in TCN1L was attributed to the more homogeneously distributed thicker and tougher Ni binder pools which acted as layers that inhibited crack propagation [199]. Conversely, the fine grained T1ML sample exhibited the second highest fracture toughness after TCN1L. The relatively higher fracture toughness of TCN1L when compared to T1ML can be attributed to the higher plasticity of the more homogeneously distributed Ni binder compared to Co [13]. It is worth noting, however, that this observation is somewhat unexpected considering the porosity and contiguity in the microstructure of the TCN1L sample. The relatively high fracture toughness of the T1ML sample was attributed to the thick Co pools and a more homogeneous distribution of the Co binder between the carbide grains which prevented WC/WC interface (trans-granular) fracture. The N2ML sample had the lowest fracture toughness (~7.0 MPa.m$^{1/2}$) among the LPS produced samples. This was attributed to the slightly smaller grains and the presence of pores in the N2ML microstructure. The fracture toughness values of the PECS produced samples were between the range of approximately 5.5 – 6.5 MPa.m$^{1/2}$ (Figure 4.7). This observation indicated that the different composition additions (i.e., Mo, TiC or TiC_7N_3) did not result in any significant changes to the fracture toughness. Thus, these additions increased the hardness without significantly affecting the fracture toughness [58].

7.3.3. Elastic modulus and shear modulus

The PECS produced samples had relatively higher modulus of elasticity (E) and rigidity (G) than the LPS samples. The relatively poor E and G in LPS samples could be attributed to the presence of larger and slightly pronounced pores in the microstructure of LPS samples than in PECS [20]. The N2ML sample exhibited the lowest E (372.47 ± 1.84 GPa) and G (149.85 ± 0.32 GPa) compared to all the other samples irrespective of the sintering technique and composition. The lower E and G in N2ML were attributed to the formation of (Nb, Mo) C solid solution which are considered as “weak functions” of the alloy content [200] due to Mo addition and porosity in the microstructure. Genga et al. [20] also reported a decrease in the elastic modulus of NbC-Ni alloys due to the weak bonding strength between the elements of the (Nb, Mo) C solid solutions formed through the addition of Mo_2C. This observation was also confirmed when comparing the PECS produced N2S and N2MS samples as well as R2S and R2MS samples (see Figure 4.8) whereby the samples containing Mo exhibited slightly lower E and G properties. There was no significant difference in the elastic modulus and shear modulus of the R2MS and N2MS samples. This observation suggested that the presence of TiC in R2MS had a negligible effect on the modulus properties of the material. A similar observation was reported by an investigation by Genga et al. [20]. The LPS produced TCN1L sample also had a relatively lower modulus property compared LPS produced R2L and T1ML samples. The difference in the modulus properties of TCN1L

and R2L could not be explained since the samples had similar microstructures, a characteristic that was observed in their PECS produced counterparts (TCN1S and R2S) which exhibited very similar modulus properties. The TCN1S and R2S samples exhibited the highest elastic modulus (549.60 ± 1.15 GPa for TCN1S and 547.54 ± 2.06 GPa for R2S) and shear modulus (216.24 ± 0.21 GPa and 216.18 ± 0.12 GPa, respectively), compared the other samples used in this study. This was due to the undissolved hard TiCN and TiC phases within the respective microstructures. The relatively higher E and G of TCN1S and R2S than N2S suggests that the respective solid solutions formed due to the additions of TiCN and TiC have stronger bonding strength than those containing Mo. The T1ML sample exhibited very similar elastic modulus properties and lower shear modulus to the porous grained R2L sample. Similar to the N2ML, the relatively low modulus properties of T1ML were attributed to the presence of Mo which resulted in the formation of (W, Ti, Mo) C solid solution.

7.4. Semi-finishing face milling

This subsection provides a discussion of the B1, S1 and P1 cutting inserts machining trials during semi finishing at a spindle speed of 800 rpm and a depth of cut of 1 mm.

7.4.1. Blank (B1) cutting inserts

7.4.1.1. Resultant cutting forces, specific cutting energy, and temperature of B1 cutting inserts

The maximum resultant cutting forces (F_{max}) experienced by the blank (B1) cutting inserts were significantly higher than the average resultant cutting forces (F) except for the N2MS-B1 cutting insert. The F_{max} of all B1 cutting inserts (irrespective of composition and sintering technique) exceeded 1000 N. The relatively high values of F_{max} were attributed to the increased loading experienced by the cutting inserts when chips are formed. During machining trials, the cutting forces indicated a fluctuating behaviour, varying between very high forces and relatively lower forces. This force behaviour was attributed to the discontinuous nature of a-GCI chips, with the higher cutting forces “peaks” signifying the formation of the chips and the lower forces “ridges” indicating the breaking off of chips as they stop being in contact with the rake or cutting edge thereof [201]. In addition, the GCI workpiece, the chips, and the cutting inserts created three body abrasion systems during machining, resulting in increased forces [201]. The average resultant cutting forces (F) of B1 cutting inserts followed the trend of F_{max} (Figure 5.1). The R2S-B1 had the lowest resultant cutting forces (both F_{max} and F) amongst B1 cutting inserts whilst its LPS produced counterpart (R2L-B1) exhibited the highest cutting forces,

respectively. In general, the PECS produced B1 cutting inserts exhibited lower resultant cutting forces than their LPS counterparts. This observation indicated that PECS improved the cutting insert's hardness which increased resistance to abrasion wear [17]. The effects of composition on the resultant cutting forces were observed on the NbC-Ni based PECS cutting inserts. The addition of TiC to the N2S-B1 composition reduced the average resultant cutting force in R2S-B1 by ~168 N (Figure 4.7) due to the improved hardness and abrasion wear resistance [12]. However, there was no significant difference between the average resultant forces of N2S-B1 and TCN1S-B1, suggesting that the addition of TiC_7N_3 had minimal effects on the cutting forces. The N2MS-B1 had a higher F than N2S-B1. Thus, the increase in average resultant force due to the addition of Mo could not be explained since N2MS had slightly higher hardness and fracture toughness than N2S (Table 4.3). The specific cutting energy (U_c) had a linear relationship with the average resultant cutting force. As such, the inserts with the lowest and highest energy consumptions among the B1 cutting inserts were the R2S-B1 and N2MS-B1 with U_c of ~19 J/mm^3 and ~42 J/mm^3, respectively. The machining temperatures of B1 cutting inserts were below 126 ^{0}C. The T1ML-B1 exhibited the lowest machining temperatures (92.51 ± 0.88 °C) whilst the N2MS-B1 had the highest temperature (124.79 ± 1.22 °C) among the B1 cutting inserts. Similar temperatures were recorded by Da Silva et al. [202] during milling of compacted graphite iron (CGI) with similar hardness properties to a-GCI at comparable cutting speeds and feed rates. The graph of the temperature against the average resultant force exhibited a linear trend which was not readily apparent or easy to see (Figure 5.3). This could be due to the low range of temperatures experienced by the cutting inserts during the machining process.

7.4.1.2. Insert tool life and wear performance of B1 cutting inserts

The T1ML-B1, N2S-B1 and TCN1L-B1 cutting inserts achieved 20 minutes insert tool life among the blank (B1) cutting inserts. The T1ML-B1 had the lowest FWR (1.97 µm/min), with a maximum flank wear (VB_{max}) of 39.45 µm after 20 minutes, followed by the N2S-B1 cutting insert (Table 5.2 and Figure 5.4). The N2MS-B1 cutting insert failed after 2 minutes, resulting in the highest FWR (21.04 µm/min), followed by the TCN1S-B1 and R2S-B1 inserts which failed after 6 minutes and 8 minutes, respectively (Table 5.2 and Figure 5.4). The N2ML-B1 and R2L-B1 cutting inserts failed after 11 minutes, with the inserts having FWRs of 3.13 µm/min and 5.45 µm/min, respectively. In general, cutting insert wear and (or) failure can mainly be due to mechanical wear (including abrasion, attrition, and fracture) and chemical wear (diffusion) [17, 203]. The primary cause of flank wear is rubbing at the interface between the insert cutting edge and the workpiece, which can lead to abrasive and/or adhesive wear at high temperatures including chemical wear [13, 203]. The main flank wear

mechanism is abrasion which is typically characterised by grooves in the direction in which the insert moves against the surface of the workpiece [203]. The main wear mechanisms during the machining of grey cast iron are attrition and abrasion [204]. The lower FWR in T1ML-B1 was attributed to the good combination of hardness and fracture toughness which improved impact resistance and abrasion wear resistance [26]. With the exception of R2L-B1, the LPS produced N2ML and TCN1L cutting inserts had better insert tool life performance than the PECS produced counterparts (N2MS and TCN1S, see Figure 5.4). This was attributed to the relatively higher K_{IC} of LPS produced inserts which improved impact resistance and prevented cutting edge wear and failure by mechanical fracture during machining at a depth of cut of 1 mm [26]. During interrupted machining such as face-milling, the cutting edges experience shear, tensile and compressive stresses from cyclic impact and loading as machining progresses [26]. As a result, cutting inserts used for roughing and semi-finishing should have better impact resistance and a higher K_{IC} since these properties offer resistance to mechanical fracture, which has been reported to increase with increasing depths of cuts [152].

The optical micrographs of the B1 cutting inserts confirmed that the cutting edge wear mechanisms were mainly due to abrasion and mechanical fracture (Figure 5.6). The T1ML-B1 cutting insert exhibited the smallest wear land and fewer abrasion grooves compared to N2S-B1 and TCN1L-B1 due to its good combinations of physical (density and elastic modulus) and mechanical (hardness and fracture toughness) properties [17]. In addition, some cracks were also observed on the rake face of T1ML-B1. The cutting edge wear on the N2S-B1 and TCN1L-B1 characterised by cracks, chipping, fracture and thicker abrasion grooves was more pronounced compared to the T1ML-B1 cutting insert (Figure 5.6). Edge cracking, chipping and mechanical fracturing were attributed to the large resultant cutting forces generated during interrupted machining whereby the inserts are subjected to alternating stresses or loading [205]. Furthermore, due to lower semi-finishing cutting speed, the N2S-B1 experienced some BUE formation [152, 158]. However, due to attrition, welded (adhered) workpiece material broke off from the cutting edge due to the continuous motion during machining, carbide pull-out and creating cavities as well as abrasion grooves in the process [17, 152]. Although there was the presence of wear on the cutting edges of T1ML-B1 and N2S-B1 cutting inserts, the wear was minimal, and the inserts could still continue with machining as per the ISO 3685:1993 tool life criteria [159]. Conversely, the TCN1L-B1 insert whose cutting edge was completely shattered after 20 minutes of machining. The optical micrographs of the other NbC-Ni based B1 cutting inserts revealed similar cutting edge failure, mirroring the mechanical fractures and shattering observed in TCN1L-B1. Crater wear on the rake face was not detected in any of the B1 cutting inserts during semi-finishing. This was due to the fine texture of the GCI chips, derived from the brittle graphite flakes within the GCI

microstructure [133]. The formation of these chips played a crucial role in preventing material transport on the rake face, thus reducing, or restricting crater [17]. The HAADF-STEM map of the T1ML-B1 flank face cutting edge/workpiece interface cross section (Figure 5.7) revealed fracturing of WC grains close to the cutting edge, pull-out of the carbide grains and cracks on the interface of TiC and WC grains close to the cutting edge. The carbide pull-out resulted in exposure of the Co binder due to attrition wear leading to slight rounding of WC grains [17]. This observation confirms the chemical instability of WC-Co based inserts during machining of cast irons. Genga et al. [17] performed HAADF-STEM analyses on NbC-Ni based inserts and reported a straight cutting edge/workpiece interface with slight cracks of the NbC-Ni based inserts during the face-milling of GCI, thus demonstrating the good chemical stability of NbC during machining of cast irons. In this study, the optical micrographs of NbC-Ni based B1 cutting inserts irrespective of composition or sintering technique, revealed worn flank faces which had grooves from abrasion wear by hard particles and surface asperities and cavities due to attrition. The inserts also showed cracks, chipping, and mechanical fracture on both the flank and rake faces of the cutting edges [17].

7.4.1.3. Machining performance evaluation of B1 cutting inserts

In this study (Chapter 3), a model based on TOPSIS (Technique for Order of Preference by Similarity to an Ideal Solution) was developed to evaluate the machining performance of cutting inserts for face-milling of a-GCI. This model not only assessed machining performance but also facilitated the ranking and selection of the most suitable cutting inserts for various face-milling regimes, such as semi-finishing and finishing. To the author's knowledge, there is currently no existing literature model capable of simultaneously evaluating machining performance and providing a systematic ranking and selection process for cutting inserts across roughing, semi-finishing and finishing face-milling operations. Further, the developed model optimised face-milling machining of a-GCI process by providing the best (optimal) cutting inserts (solutions) for both semi-finishing and finishing. For semi-finishing processes, the model incorporated criteria such as insert tool life (I_l) which is considered the most important factor in machining, specific cutting energy (U_c) or energy consumption which is critical for sustainable manufacturing, and the maximum resultant cutting force (F_{max}) which is used to monitor machining conditions. The criteria were assigned performance weight indexes (PWIs) of 0.6, 0.3 and 0.1, respectively as outlined in Table 3.12. The TOPSIS technique determined the T1ML-B1 to be the best cutting insert among B1 cutting inserts with the overall preference score (O_i) of 0.953. Expectedly, the N2S-B1 and TCN1L-B1 cutting inserts were ranked 2nd and 3rd with O_i of 0.922 and 0.912, respectively. The relatively high overall preference scores obtained by these inserts were

attributed to the good combinations of the criteria used for machining performance evaluations and ranking. Thus, indicating that during semi-finishing, the cutting inserts were able to achieve longer tool life whilst consuming relatively less cutting energy and experiencing relatively lower maximum resultant cutting forces. The moderately ranked and average performing cutting inserts such as N2ML-B1, R2L-B1 and R2S-B1 achieved overall preference scores (O_is) between 0.40 and 0.52, whereas the lowly ranked and poor performing TCN1S-B1 and N2MS-B1 cutting inserts had O_i of less than 0.30. As opposed to the optimal (best) cutting inserts, the average and poor performing inserts exhibited lower insert tool life, higher levels of energy consumption and higher maximum resultant cutting forces. Thus, the outputs of the TOPSIS model were consistent with the microstructural, physical, and mechanical properties of the B1 cutting inserts as well as the overall observations of the machining analyses during semi-finishing.

7.4.2. Shark skin LSM (S1) cutting inserts

7.4.2.1. Resultant cutting forces, specific cutting energy, and temperature of S1 cutting inserts

The maximum resultant cutting forces experienced by shark skin LSM (S1) cutting inserts were significantly higher than the average resultant cutting forces. The F_{max} of all S1 cutting inserts, irrespective of composition and sintering technique exceeded 1100 N. The T1ML-S1 cutting insert had the lowest F_{max} (1194 N) amongst the S1 cutting inserts, and the insert with the highest F_{max} was the TCN1L-S1 (1306 N) (Table 5.3 and Figure 5.10). The average resultant force of S1 cutting inserts followed the trend of F_{max} (Figure 5.10). The T1ML-S1 had the lowest F whilst TCN1L-S had the highest F (i.e. 756 N and 1141 N, respectively). With the exception of N2MS-S1, the PECS produced S1 cutting inserts showed lower average resultant cutting forces than their LPS counterparts due to the improved hardness and resistance to abrasion wear by PECS [17]. For instance, R2S-S1 and TCN1S-S1 had average resultant cutting forces of approx. 674 N and 223N lower than R2L-S1 and TCN1L-S1, respectively. The T1ML-S1 had the lowest specific cutting energy (~24 J/mm^3) among S1 cutting inserts due to the lower average resultant cutting force. The majority of S1 cutting inserts exhibited specific cutting energy of between ~25 – 28 J/mm^3 (Figure 5.11). Only R2L-S1 and TCN1L-S1 cutting inserts had U_c of above 30 J/mm^3, with the TCN1L-S1 having the highest energy consumption with U_c of above 35 J/mm^3, respectively. Accordingly, the LPS produced NbC-Ni based cutting inserts had higher U_c than their PECS counterparts except for the N2ML-S1 cutting insert. The N2S-S1 cutting insert exhibited the lowest average machining temperature (93.71 ± 0.90 °C) compared to other S1

cutting inserts. The cutting insert with the highest machining temperature among S1 cutting inserts was noted to be N2MS-S1 (165.20 ± 1.61 °C). In general, the machining temperatures of S1 cutting inserts were slightly higher than those observed in their B1 counterparts. The slightly higher temperatures observed in S1 cutting inserts were attributed to the entrapment of some GCI workpiece chips on the shark skin micro-grooves [206]. This resulted in increased friction between the chips and micros-grooves as well as delaying heat dissipation, leading to increased machining temperatures during the machining process (Figure 5.18) [206].

7.4.2.2. Insert tool life and wear performance of S1 cutting inserts

The R2MS-S1 cutting insert had the lowest FWR (1.33 µm/min), with a VB_{max} of 26.67 µm after 20 minutes of machining, followed by R2S-S1 and TCN1S-S1 cutting inserts which exhibited FWRs of 2.33 µm/min after 20 minutes machining duration, respectively (Table 5.4 and Figure 5.13). With the exception of N2MS-S1, the PECS produced cutting inserts exhibited slightly lower FWRs and better insert tool life compared to their LPS produced counterparts. The lower FWRs were due to the higher hardness and improved resistance to abrasion wear in the cutting inserts through LSM application [17], [207]. The shark skin LSM technique improved the insert tool life performance of the majority of S1 cutting inserts including N2MS-S1, TCN1S-S1 and R2S-S1 which had insert tool life improvements of 300%, 233% and 150%, compared to their B1 counterparts, respectively (Figure 5.14). Consequently, the increased insert tool life resulted in reduced FWRs as indicated in Figure 5.16. Denkena et al. [140] and Alagan et al. [208] also independently recorded an increase in the insert tool life of laser surface modified cutting inserts. Both authors attributed the increase to the improved surface hardness and abrasive wear resistance. The T1ML-S1 and N2S-S1 cutting inserts had 0% improvement in insert tool life as they achieved 20 minutes machining duration as their B1 counterparts. For these inserts, the shark skin LSM technique resulted in FWR increases of 5% and less (Figure 5.14). It is worth noting that while the shark skin LSM technique improved the insert tool life of several inserts, it also led to reductions in the insert tool life and consequently slightly higher FWRs of R2L-S1 and TCN1L-S1 cutting inserts. This could be attributed to the porosity of the sample whereby the application of LSM could have further exposed some of the pores (crack initiation points) within the microstructure during texturing (patterning). The different effects of shark skin LSM on the inserts highlight the nuanced impact of the technique, thus emphasising the need for a comprehensive understanding of the material-specific interactions to optimise its application. Similar to B1 inserts, the optical micrographs of the S1 cutting inserts revealed that the main wear mechanisms were abrasion, attrition and mechanical fracture (chipping and complete edge shattering) (Figure 5.17). Due

to the increased hardness by PECS and shark skin LSM, the R2MS-S1 cutting insert exhibited the smallest wear land on the flank and minor cracking and chipping on both the flank and rake faces compared to other S1 cutting inserts [17, 205]. The R2MS-S1 and T1ML-S1 had minimal cutting edge wear. Thus, the cutting inserts did not reach the failure criteria (ISO 3685:1993 standard) for semi-finishing after 20 minutes [159]. The R2S-S1 exhibited some BUE due to the adhesion of the workpiece onto the cutting edge [209]. However, due to attrition, BUE was not prevalent on S1 cutting inserts during semi-finishing [152], [158]. The flank faces of S1 cutting inserts revealed that the top-most layers of shark skin micro-grooves towards the cutting edge (or at the point of contact with the workpiece) were removed due to abrasion wear (Figure 5.17) [209]. The other NbC-Ni based S1 cutting inserts exhibited comparable cutting edge failure mechanisms. However, the optical micrographs revealed that these features, in particular the mechanical fracture and edge shattering were more pronounced in these inserts. Due to the brittle graphite flakes within the GCI workpiece, crater wear was not detected on the rake faces of S1 cutting inserts, just like in B1 cutting inserts [133].

The HAADF-STEM map of R2MS-S1 cross section of the flank face showed that Nb, TiC and Mo coincided on the top-most (shark skin) layer with ~ 1.3 µm thickness (Figure 5.19). Thus, suggesting that the surface of the cutting edge was composed mostly of an (Nb, Mo, Ti) C solid solution. In addition, the TiC appeared to be completely dissolved in this layer, unlike in the sample microstructure, thus further increasing the surface hardness of the cutting edge, improving abrasion wear resistance, and resulting in lower FWR [13, 17]. This observation was consistent with the findings by Genga et al. [17] who reported that femtosecond LSM technique produced a hard ~2.5 µm thick "self-carbide" coating. The slightly thinner surface layer observed in this study could be due to abrasion wear on the flank. The map also showed a good distribution of the nano-sized Ni binder pools. Some of the Ni binder appeared to be exposed towards the cutting edge and was distributed in patches within the microstructure and this facilitated NbC pull-out, and fragmentation as shown in Figure 5.19 [12, 17]. The HAADF-STEM map of the R2MS-S1 further showed a lighter contrast layer at the insert cutting edge/workpiece interface, and the adherence of Fe (workpiece) on the cutting edge, which confirmed the formation of BUE during semi-finishing.

7.4.2.3. Machining performance evaluation of S1 cutting inserts

According to the TOPSIS model, the top six ranked S1 cutting inserts comprising the best and average performing cutting inserts, had overall preference scores (O_is) between 0.90 and 1.00 (Figure 5.21). The T1ML-S1 cutting insert obtained O_i of 1.00 (i.e., the highest among the S1 cutting inserts). This was followed by N2S-S1 and N2ML-S1 with O_i of 0.979 for both cutting inserts, respectively. The

R2S-S1, R2MS-S1 and TCN1S-S1 were determined to be the average performing S1 cutting inserts with overall preference scores of 0.938, 0.922 and 0.900, respectively. It is worth noting that these cutting inserts were designated as "average" simply due to the demarcation of using the top three ranked inserts as best, 4-6 as average and the last three as poor performers as indicated by green, amber, and red colour codes (Figure 5.21). The relatively high O_is obtained by S1 cutting inserts underpins the effectiveness of LSM technique in improving the surface hardness and resistance to abrasive wear of the cutting edges, and reducing the cutting forces [17, 210]. Thus, improving the overall machining performance of S1 cutting inserts (i.e. better insert tool life, lower specific cutting energy and reduced cutting forces).

7.4.3. Pyramid LSM (P1) cutting inserts

7.4.3.1. Resultant cutting forces, specific cutting energy, and temperature of P1 cutting inserts

The maximum resultant cutting forces experienced by the pyramid LSM (P1) cutting inserts were significantly higher than the average resultant forces. The F_{max} of all P1 cutting inserts irrespective of composition and sintering technique exceeded 1038 N. There was no significant difference between the F_{max} of P1 cutting inserts except for TCN1L-P1 which experienced the highest maximum resultant force (i.e. in excess of ~182 N as shown in Figure 5.22). The average resultant cutting forces followed a similar trend to the F_{max}, with the R2MS-P1 insert experiencing the lowest F (706 N) and the R2L-P1 the highest average resultant cutting forces, respectively. Similar to the S1 cutting inserts, the LPS produced NbC-Ni based cutting inserts exhibited slightly higher average resultant cutting forces than their PECS counterparts due to their slightly lower hardness and resistance to abrasive and attrition wear [17], [26]. The specific cutting energy of all the P1 cutting inserts (irrespective of composition and sintering technique) was below 27 J/mm^3. The R2MS-P1 had the lowest specific cutting energy (~22 J/mm^3) among the P1 cutting inserts due to the lower average resultant cutting force. Similar to the observations in S1 cutting inserts, the LPS produced R2L-P1 and TCN1L-P1 cutting inserts exhibited the highest U_c (~27 J/mm^3 and ~26 J/mm^3, respectively) amongst P1 cutting inserts (Figure 5.23). Accordingly, the PECS produced cutting inserts (with the exception of N2MS-P1) had slightly lower cutting energy consumption due to improved hardness, and resistance to abrasion and attrition wear [17], [209]. P1 cutting inserts exhibited slightly lower machining temperatures compared to B1 and S1 cutting inserts. The machining temperatures for the majority of P1 cutting inserts were within the range of 107 - 119 °C. The TCN1L-P1 had the lowest machining temperature (80.73 ± 0.76 °C)

compared to the other P1 cutting inserts. This observation could not be explained considering that the cutting insert exhibited the highest resultant cutting forces (F and F_{max}) among P1 cutting inserts. The lower machining temperatures in P1 cutting inserts could be attributed to the reduced friction due to decreased contact area (or reduced tribological interactions) between the cutting edge and a-GCI chips [210].

7.4.3.2. Insert tool life and wear performance of P1 cutting inserts

Similar to its S1 counterpart, the R2MS-P1 exhibited the lowest FWR (1.44 µm/min), with a VB_{max} of 28.89 µm after 20 minutes of machining, followed by T1Ml-P1 and R2S-P1 cutting inserts which had FWRs of 1.78 µm/min and 1.83 µm/min after 20 minutes of machining, respectively (Table 5.6 and Figure 5.25). Just like in S1, all the PECS produced P1 cutting inserts (irrespective of composition) had slightly lower FWRs and better insert tool life compared to their LPS produced counterparts due to improved hardness and resistance to abrasion wear and attrition [17, 207]. The pyramid LSM technique improved the insert tool life performance of the majority of P1 cutting inserts including N2MS-P1, TCN1S-P1 and R2S-P1 which had insert tool life improvements of 900%, 233% and 150%, compared to their B1 counterparts, respectively (Figure 5.26). These observations mirror the observations in S1 cutting inserts with the difference being on the N2MS-P1 which had an additional 600% improvement compared to N2MS-S1. The improvements in insert tool life led to a significant reduction in FWRs of P1 cutting inserts compared to their B1 counterparts, with the N2MS-P1 having about 91% reduction in FWR and inserts such as TCN1S-P1 and R2S-P1 having reductions of 51% and 40% respectively (Figure 5.28). The pyramid LSM (P1) technique, like S1, increased the FWRs of R2L-P1 and TCN1L-P1 cutting inserts. This was attributed to the further exposure of pores with the microstructures of the inserts during pyramid LSM application. The optical micrographs of P1 cutting inserts also revealed that the main wear and cutting edge failure mechanisms were abrasion, attrition, and mechanical fracture which was characterised by cracks, chipping and complete edges shattering as shown in Figure 5.29. The PECS produced P1 cutting inserts exhibited relatively small wear lands due to hardness and resistance to abrasion wear resulting from combined effects of the sintering technique and pyramid LSM [17], [205]. Similar to their S1 counterparts, the R2MS-P1 and T1ML-P1 cutting inserts had minimal cutting edge failure and had therefore not yet reached failure criteria in accordance with ISO 3685:1993 standard after 20 minutes of machining [159]. BUE and crater wear were not observed on the optical micrographs of P1 cutting inserts. It is worth noting that the abrasion grooves on the flank face of the majority of P1 cutting were thicker and appeared to originate from the micro pyramidal patterns (or “pits”). This suggests that the chips would occasionally be trapped inside

the “pits” and then get dragged along during a machining revolution till they exit the cutting insert-workpiece interface. Similar wear patterns were observed by Alagan et al. [208] in their investigations.

7.4.3.3. Machining performance evaluation of P1 cutting inserts

The pyramid LSM (P1) cutting inserts obtained relatively higher overall preference scores compared to B1 and S1 cutting inserts. With the exception of R2L-P1, the P1 inserts irrespective of composition and sintering technique had O_is of above 0.590. The R2MS-P1 cutting insert obtained the highest O_i (0.994), followed by R2S-P1 and N2MS-P1 with O_i of 0.979 and 0.971, respectively (Figure 5.31). It is important to note that unlike in B1 and S1 cutting inserts, these NbC-Ni based PECS produced cutting inserts obtained higher overall performance scores than the WC-Co based (conventional) T1ML-P1 cutting insert which had an O_i of 0.945. This shows that the pyramid LSM technique was more effective than the shark skin LSM in improving the machining performance [17, 209].

7.4.4. Consolidated overall semi-finishing machining performance

The TOPSIS model was applied on the combined 26 cutting inserts used during semi-finishing machining trials to evaluate and rank all the cutting inserts during machining at a spindle speed of 800 rpm, depth of cut of 1.0 mm and feed of 0.1 mm/tooth. Since the model inputs were of all the cutting inserts, the overall preference scores were different to those obtained during the evaluations of respective cutting edges (i.e. B1, S1 and P1). The evaluation of the cutting inserts revealed notable variations in machining performance. The R2MS-P1 emerged as the top performer with the highest overall preference score (0.953) through machining performance criteria values of 20 min, 22 J/mm^3, and 1087 N for C1, C2 and C3, respectively (Table 5.7). As a result, the insert was rendered as the most suitable cutting insert for face-milling of a-GCI during semi-finishing. The R2S-P1 and T1ML-B1 followed closely in the second and third positions with O_i of 0.941 and 0.939, respectively (Table 5.7). The P1 cutting inserts were the better performers with 5 inserts in the best performer category, followed by the S1 (3 inserts), and then B1 with only one (T1ML-B1) cutting insert, as shown in Table 5.7. The better performance displayed by LSM based cutting inserts underpins the effectiveness of the technique in improving the physical and mechanical properties of inserts. In particular, improving the surface hardness, resistance to wear (abrasion and attrition), and cutting edge strength of inserts for semi-finishing conditions. It must be highlighted that all WC-Co based (T1ML) cutting inserts were within the best performer category. However, the application of LSM slightly reduced the machining performance of the T1ML grade since the blank had a slightly higher overall preference score than both shark skin and pyramid laser surface modifications. The N2S-B1 and N2S-P1 cutting inserts

represent the average performers, securing the tenth and eleventh ranks with O_is of 0.903 and 0.902, respectively. Notably, the overall preference scores of these inserts are above 0.90 even though they are designated as "average". This observation further underpins the remarkable machining performance of the majority of cutting inserts (especially the LSM inserts) during semi-finishing. Some inserts, however, including the N2ML-B1 and N2MS-B1, fell into the poor performer category, ranking nineteenth and twenty-sixth, respectively with overall preference scores of 0.525 and 0.038. In this category, the inserts are mainly characterised by poor insert tool life and higher values of specific cutting energy and maximum resultant cutting forces when compared to the best performers. For instance, the R2MS-P1 had up to 10 times the insert tool life, almost half the specific cutting energy, and about 28% less maximum resultant cutting force than the N2MS-B1. In general, the consolidated overall machining performance evaluation of semi-finishing cutting inserts using the TOPSIS based model, highlighted the effectiveness of the model as a tool for assessing cutting inserts and their intrinsic properties. Especially, considering that the input criteria of the model included insert tool life, specific cutting energy, and resultant cutting forces. Furthermore, the overall machining performance for semi-finishing machining trials revealed that the NbC-Ni based cutting inserts can potentially replace conventional WC-Co based cutting inserts. This can be achieved through composition manipulation (additions of Mo as a partial binder and TiC as a secondary carbide phase), rapid sintering (PECS) and laser surface modification (micro-pyramid surface texturing).

7.5. Finishing-1 face milling

This subsection provides a discussion for finishing-1 machining trials at a spindle speed of 1600 rpm and depths of cut of 0.5 mm.

7.5.1. Blank (B2) cutting inserts

7.5.1.1. Resultant cutting forces, specific cutting energy, and temperature of B2 cutting inserts.

Similar to semi-finishing machining trials, the maximum resultant cutting forces experienced by the blank (B2) cutting inserts were significantly higher than the average resultant cutting forces except for R2L-B2 and TCN1L-B2. The F_{max} of the majority of B2 cutting inserts exceeded 1600 N. In general, the resultant cutting forces for B2 cutting inserts were higher than those observed in B1 due to increased spindle speed (cutting speed) [17]. The TCN1S-B2 cutting insert exhibited the highest F_{max} (2222 N), followed by R2MS-B2 and TCN1L-B2 with F_{max} of 1784 N and 1745 N, respectively (Table

6.1 and Figure 6.1). With the exception of TCN1S-B2, the average resultant cutting force of the rest of the B2 cutting inserts followed a similar trend to F_{max}. The T1ML-B2 insert exhibited the lowest average resultant cutting forces (918 N) amongst the other B2 cutting inserts due to its good combination of physical and mechanical properties [26]. Additionally, due to slightly lower hardness and resistance to abrasion wear, the LPS produced B2 cutting inserts, exhibited slightly higher resultant cutting forces than their PECS produced counterparts. Considering the specific cutting energy, the T1ML-B2 cutting insert had the lowest U_c (~57 J/mm^3) while TCN1L-B2 had the highest (~98 J/mm^3) among B2 cutting inserts. Generally, the specific cutting energy of B2 cutting inserts was more than double those observed in their respective B1 cutting inserts during semi-finishing (Table 6.1). However, it is worth noting that the specific cutting energy of B2 cutting inserts follows similar trends to B1 cutting inserts. The significant increase in specific cutting energy was attributed to the increased resultant cutting forces due to increased cutting speeds [211]. This observation suggests that machining operations with higher cutting speeds have higher energy consumption than those with relatively low cutting speeds while cutting for the same period of time or having the same material removal rate. Despite experiencing the highest average resultant cutting force among B2 cutting inserts, the TCN1L-B2 exhibited the lowest machining temperature (37.06 ± 0.25 °C). This could be attributed to the short insert tool life (4 minutes) of the cutting insert, meaning there was not enough time for the temperature to rise. The machining temperatures of the majority of B2 cutting inserts were between 72 °C and 95 °C. These temperatures were slightly lower than those observed in semi-finishing (irrespective of the cutting edge). The slightly lower machining temperatures could be attributed to the reduction of the depth of cut (a_p) [211]. In general, the machining temperatures of the B2 cutting inserts appear to increase with increasing average resultant cutting forces (Figure 6.3). This observation was attributed to the increasing friction between the inserts and workpiece due to increased impact (i.e. increased collisions of the insert with the workpiece), as well as blunting of the cutting edge due to wear [211].

7.5.1.2. Insert tool life and wear performance of B2 cutting inserts.

The T1ML-B2 cutting insert had the lowest FWR (2.25 µm/min), with a VB_{max} of 45.00 µm after 20 minutes, followed by the R2MS-B2 cutting insert with a FWR of 3.89 µm/min and VB_{max} of 77.78 µm after 20 minutes of machining (Table 6.2). The T1ML-B2, R2S-B2, R2MS-B2, and TCN1S-B2 cutting inserts achieved 20 minutes of insert tool life. The relatively higher insert tool life of the WC-Co based T1ML-B2 is attributed to the good combination of hardness and fracture toughness [13]. When compared to their B1 counterparts, the R2S-B2, R2MS-B2 and TCN1S-B2 cutting inserts had better insert tool life. This was attributed to the reduced depth of cut and resistance to abrasive wear which

is critical during finishing [152, 211]. The importance of the hardness properties of a cutting insert during finishing conditions is further highlighted by the slightly higher FWR of T1ML-B2 compared to its B1 counterpart. This observation suggests that at higher cutting speeds, greater resistance to abrasion wear in cermet-based cutting inserts is more significant than the fracture toughness provided by the "soft" binder phase at high cutting speeds [17]. The additions of TiC, TiC_7N_3, and a combination of Mo and TiC, to the N2S-B2 composition led to increased insert tool life due to improved hardness and resistance to abrasion wear [26]. However, a contrasting observation was made with the addition of Mo (Table 6.2 and Figure 6.4). Similar to observations in B1, due to relatively low hardness and resistance to abrasive and attrition wear, the LPS produced cutting inserts exhibited slightly higher FWR than their PECS produced counterparts [26]. The optical micrographs of B2 cutting inserts revealed that the main cutting edge wear mechanisms were abrasion wear and mechanical fracture (Figure 6.6). Amongst the B2 cutting inserts that achieved 20 minutes, the T1ML-B2 exhibited the least wear land and cutting edge wear due to its good combination of hardness and fracture toughness. Furthermore, the rake face of the cutting insert exhibited the occurrence of crater wear (Figure 6.6 (a)). The presence of crater was attributed to the increased high-speed collisions of GCI chips against the rake face of T1ML-B2 and the chemical instability of WC-Co based cutting inserts during the machining of cast irons [12]. Although the T1ML-B2 cutting edge exhibited some wear, the insert showed the ability to continue machining beyond the 20 minutes as per ISO 3685:1993 standard for machining [159]. Just like in semi-finishing, the NbC-Ni based cutting inserts had very similar cutting edge wear mechanisms. As shown in Figure 6.6 (b) and (c), the R2S-B2 and R2MS-B2 cutting inserts exhibited mechanical fracture and abrasion wear [148]. Wear was attributed to ploughing resulting from a series of abrasion grooves. During this process, material was displaced from the grooves to the sides of the inserts without being removed. Only after the surface has been ploughed multiple times does material removal occur due to the low-cycle fatigue mechanism. Following this, ridges form along the edges of the ploughed grooves, which flatten and eventually fracture following repeated cycle stress [148]. Due to chemical stability during machining of steels and cast irons, crater wear was not observed on any of the NbC-Ni based cutting inserts. However, the optical micrographs of the rake faces of R2S-B2 and R2MS-B2 revealed removal of some of the surface layer of the insert closer to the cutting edge. This could be attributed to the high-speed impact of GCI chips as they collide against the insert, leading to fracturing of the surface layer due to poor fracture toughness [17]. As a result, an appreciable level of fracture toughness in cutting inserts is still required for finishing.

7.5.1.3. Machining performance evaluation of B2 cutting inserts

The TOPSIS model determined T1ML-B2 as the best cutting insert among the other B2 cutting inserts with an overall preference score of 1.00, followed by the R2S-B2 and R2MS-B2 in 2nd and 3rd positions with O_i of 0.921 and 0.900, respectively (Figure 6.8). The high O_i obtained by the T1ML-B2 shows that the insert had a good combination of mechanical properties leading to longer insert tool life, reduced energy consumption and resultant cutting forces. The TCN1S-B2 had the highest O_i (0.872) among the average B2 performers. All the LPS produced NbC-Ni based cutting inserts had O_i's of less than 0.300 as in shown in Figure 6.8. The relatively high overall preference scores obtained by R2S-B2 and R2MS-B2 indicate the possibility of NbC-Ni based cutting inserts as potential replacements for conventional WC-Co based cutting inserts for the machining of a-GCI.

7.5.2. Shark skin LSM (S2) cutting inserts

7.5.2.1. Resultant cutting forces, specific cutting energy, and temperature of S2 cutting inserts

Similar to B2 cutting inserts, the maximum resultant cutting forces experienced by the shark skin LSM (S2) cutting inserts were significantly higher than the average resultant cutting forces except for the LPS produced R2L-S2 and TCN1L-S2 which had the same values for their respective F_{max} and F (Figure 6.9). The inserts (R2L-S2 and TCN1L-S2) exhibited the lowest resultant cutting forces among S2 cutting inserts. It is worth noting, however, that the cutting edges of the R2L-S2 and TCN1L-S2 inserts completely shattered within one minute of machining. Thus, although the hardness of the inserts may have been improved by shark skin LSM, the technique could also have initiated cracks within the pores in the microstructure of the inserts during texturing [138], leading to a premature failure. The average resultant cutting forces of S2 cutting inserts followed a trend similar to that of the maximum resultant cutting forces (Figure 6.9). Due to higher average resultant cutting forces, the PECS produced N2S-S2 cutting insert exhibited the highest specific cutting energy (~51 J/mm^3) among S2 cutting inserts. With the exception of N2ML-S2, the NbC-Ni based LPS produced cutting inserts had lower U_c than their PECS counterparts. This was attributed to the longer insert tool life of the PECS cutting inserts than LPS inserts. The machining temperatures of S2 cutting inserts were in the range of 65 °C and 110 °C. Thus, unlike the observations in semi-finishing, there was no significant difference between the temperatures in B2 and S2 respectively. This could be attributed to the higher cutting speeds during finishing-1 whereby the chips flew past the insert quickly without being trapped inside the shark skin micro grooves, leading to higher heat dissipation rates. It is worth noting that there was

a significant difference in the machining temperatures of TCN1S-S2, T1ML-S2 and N2ML-S2 cutting inserts, despite the fact that the inserts exhibited similar average resultant forces (Figure 6.11). This observation could not be readily explained since the inserts had varying insert tool life as well.

7.5.2.2. Insert tool life and wear performance of S2 cutting inserts

The T1ML-S2 cutting insert had the lowest FWR (3.92 µm/min) among the S2 cutting inserts, with a VB_{max} of 78.34 µm after 20 minutes of machining. This FWR was slightly higher compared to the blank T1ML-B2 cutting edge, indicating that the shark skin LSM slightly lowered resistance to abrasion wear of the T1ML-B2 insert during finishing. Although the T1ML-S2 insert achieved an insert tool life of 20 minutes, the insert displayed major chipping and cutting edge wear and thus, could not be used beyond the 20 minutes like its B2 counterpart. After 14 minutes of machining, the FWRs of the TCN1S-S2 and R2S-S2 cutting inserts were 4.96 µm/min and 5.16 µm/min, respectively (Table 6.4 and Figure 6.12). These inserts had lower insert tool life when compared to their B2 counterparts (i.e. 30% reduction as shown in Figure 6.13). However, there was no discernible change in FWR between these cutting inserts. It can be deduced from this observation that, although the shark skin LSM improved the hardness of the cutting edges, it also compromised the fracture toughness. This led to chipping and mechanical fracture as shown by the optical micrographs of the flank and rake faces of both TCN1S-S2 and R2S-S2 (Figure 6.16).

The shark skin LSM technique also reduced the insert tool life of TCN1L-S2 and R2MS-S2 by 75% and 70% respectively, therefore increasing the FWRs of the inserts by 683% and 148% (Figure 6.13 and Figure 6.15). The reduction in insert tool life in TCN1L-S2 was attributed to the crack initiations in pores of the cutting insert's microstructure due to shark skin LSM application [138] whilst in R2MS-S2, it was due to the increased hardness and consequent reduction of fracture toughness. Similar to B2 cutting inserts, the optical micrographs of the flank and rake faces of S2 cutting inserts showed that the main cutting edge wear was abrasion wear (characterised by abrasion grooves), chipping, and mechanical fracture. In addition, similar to S1 cutting inserts, the optical micrograph of the flank faces of S2 cutting inserts revealed shark skin LSM pattern layer removal along the cutting edges of inserts due to abrasion wear (Figure 6.16). The rake face of T1ML-S2 cutting insert exhibited crater wear due to poor chemical stability of WC-Co based cutting inserts during machining of cast irons.

7.5.2.3. Machining performance evaluation of S2 cutting inserts

According to the TOPSIS model, the T1ML-S2 was the best among the S2 cutting inserts with an overall preference score of 0.808. This was followed by R2S-S2 and TCN1S-S2 cutting inserts with

O_is of 0.644 and 0.634, respectively (Figure 6.18). The majority of S2 cutting inserts had O_i of below 0.50. This suggests that generally, the S2 cutting inserts had relatively poor machining performances. It is worth noting, however, that similar to B2 inserts, the additions of Mo, TiC and TiC_7N_3 to the N2S-S2 composition improved the overall machining performances of N2MS-S2, R2S-S2 and TCN1S-S2. Although this was the case, unlike with B2 cutting inserts, the NbC-Ni based S2 cutting inserts could still not compete with the WC-Co based T1ML-S2 during finishing-1 machining.

7.5.3. Pyramid (P2) cutting inserts

7.5.3.1. Resultant cutting forces, specific cutting energy, and temperature of S2 cutting inserts

The maximum resultant cutting forces experienced by the pyramid LSM (P2) cutting inserts were significantly higher than the average resultant cutting forces, and this observation was noted in B2 and S2 cutting inserts. The F_{max} of all P2 cutting inserts exceeded 1500 N. The R2MS-P2 insert exhibited the lowest F_{max} (1427 N) amongst the P2 cutting inserts due to its higher hardness and resistance to abrasion wear [26] (Figure 6.19). The average resultant cutting forces followed a similar trend to that of F_{max}, with the exceptions of R2L-P2, TCN1L-P2 and R2MS-P2 inserts which exhibited the same values of F and F_{max}, respectively. With the exception of N2MS-P2, the PECS produced P2 cutting inserts showed slightly lower average resultant cutting forces compared to their LPS produced counterparts due to a slightly higher hardness and resistance to abrasion wear [26]. In general, the P2 cutting inserts exhibited slightly higher machining forces than both B2 and S2 inserts. The relatively higher resultant cutting forces in P2 inserts were attributed to the entrapment of chips (or debris) inside the micro-pyramidal pits which intensified the abrasive action, resulting in increased friction and vibrations at high machining speeds, and thus leading to higher cutting forces. Due to higher average resultant cutting forces, the P2 cutting inserts exhibited slightly higher specific cutting energy compared to B2 and S2 cutting inserts. With the exception of N2ML-P2, the LPS produced cutting inserts, had slightly higher U_c than their PECS produced cutting inserts (Table 6.5 and Figure 6.20). This is consistent with the observation in B2 and S2 cutting inserts, and similarly, it was attributed to the higher hardness and resistance to abrasion wear in PECS cutting inserts than LPS [26]. The machining temperatures for P2 cutting inserts were similar to those observed in B2 and S2 cutting inserts (Figure 6.21).

7.5.3.2. Insert tool life and wear performance of P2 cutting inserts

Similar to both B2 and S2 cutting inserts, the WC-Co based T1ML-P2 exhibited the lowest FWR among the P2 cutting inserts. The insert had a FWR of 2.42 µm/min with a VB_{max} of 48.34 µm after 20 minutes of machining, and it was followed by TCN1S-P2 and R2S-P2 with FWRs of 5.03 µm/min and 5.94 µm/min after 17 minutes and 20 minutes, respectively. These inserts exhibited very similar insert tool life and wear performance to their B2 counterparts (Figure 6.25), although the TCN1S-P2 cutting insert had a slight reduction in insert tool life (by 15% as shown in Figure 6.23). Similar to S2 cutting inserts, the pyramid (P2) LSM improved the insert tool life of N2MS-P2 cutting insert by 113%. However, there was no significant difference in the insert tool life of the majority of cutting inserts (indicated by the 0% improvement in Figure 6.23). Accordingly, this observation underpins the suggestion that irrespective of the type of surface texturing the LSM techniques had adverse effects than improvements during finishing in contrast to semi-finishing. Just like in B2 cutting inserts, the optical micrographs of the flank and rake faces of P2 cutting inserts revealed that the main cutting edge wear were abrasion wear (characterised by abrasion grooves), chipping and mechanical fracture (Figure 6.26).

7.5.3.3. Machining performance evaluation of P2 cutting inserts

The T1ML-P2 and R2S-P2 obtained the overall preference scores of 0.950 and 0.947 respectively, and thus, the two inserts were the best performers among the P2 cutting inserts. The TCN1S-P2 and N2MS-P2 cutting inserts also demonstrated excellent machining performance achieving respective O_is of 0.838 and 0.837 and securing third and fourth positions respectively (Figure 6.28). However, notably, the R2MS-P2, TCN1L-P2, and R2L-P2 had overall preference scores of below 0.100, suggesting potential limitations in their machining capabilities under finishing-1 conditions.

7.5.4. Consolidated overall finishing-1 machining performance

Similar to semi-finishing, the TOPSIS model was applied on all the 27 cutting inserts used during finishing-1 machining trials to evaluate and rank the cutting inserts during machining at a spindle speed of 1600 rpm, depth of cut of 0.5 mm and feed of 0.1 mm/tooth. Accordingly, the overall preference scores obtained would be different to those obtained for the cutting edge specific machining evaluations. Notably, all the T1ML based cutting inserts fell in the best category, with T1ML-S2 and T1ML-B2 securing positions one and two with overall preference scores of 0.863 and 0.831, respectively (Table 6.7). The top ranked T1ML-S2 insert had the machining performance criteria values of 20 min for C1, 43 J/mm^3 for C2 and 1369 N for C3, respectively. The highest ranked NbC-

Ni based insert was the R2S-B2 which secured the third position during finishing-1 with an overall performance score of 0.773 and machining performance values of 20 min, 75 J/mm^3 and 1199 N. Following closely was the R2MS-B2 insert at position four with an O_i of 0.757. It is crucial to highlight that the top-ranked T1ML-S2 outperformed these cutting inserts based on the energy consumption per unit volume of material removed during machining. Specifically, the R2S-B2 insert consumed more than 0.667 times the energy of the T1ML-S2 insert. As shown in the table, the best performer category was led by B2 and P2 cutting inserts, with S2 making only one appearance. Even though, P2 matched B2 in terms of the number of inserts within the "best" category, the B2 cutting inserts exhibited slightly higher O_is than P2 inserts, and thus indicating their better performance at finishing-1 machining conditions. It is worth mentioning that these observations are different to those in semi-finishing whereby the LSM based cutting inserts led the best performer category. The R2S-S2 cutting insert represents the average performers, securing the tenth position with an O_i of 0.680. Some of the inserts in this category exhibited comparable specific energies and maximum resultant cutting forces to the best performers. However, the inserts had relatively lower insert tool life which had the highest PWI among the performance evaluation criteria, leading to lower overall preference scores. All inserts in the poor performer category exhibited overall preference scores below 0.30. This category was led by the LPS produced inserts which exhibited poor hardness and resistance to abrasion wear properties. Similar to semi-finishing results, the overall machining performance evaluation for finishing-1 machining trials revealed that the NbC-Ni based cutting inserts can potentially replace or compete with conventional WC-Co based cutting inserts in high-speed machining of cast irons. This can be achieved through composition manipulation and rapid sintering techniques. For instance, in this particular case, PECS sintering and the addition of TiC as a secondary carbide phase to develop R2S-B2 insert as well as the combined additions of Mo as a partial binder plus TiC in developing R2MS-B2, led to inserts that could offer good machining performance. The use of laser surface modification on the other hand appears to be yielding adverse effects on the cutting inserts during high-speed machining, thus emphasising the importance of aligning cutting insert designs with specific machining requirements for optimal performance.

7.6. Finishing-2 face milling

This subsection provides a discussion for finishing-2 machining trials at a spindle speed of 1600 rpm and depths of cut of 0.25 mm. As previously mentioned, the values of the machining variables obtained by the cutting inserts used during finishing-2 are surface roughness dependent and the reader is referred to Chapter 3 (page 86) for a detailed explanation and rationale on this.

7.6.1. Blank (B3) cutting inserts

7.6.1.1. Resultant cutting forces, specific cutting energy, and temperature of B3 cutting inserts

The maximum resultant cutting forces of blank (B3) cutting inserts were significantly higher than the average resultant cutting forces (Table 6.8 and Figure 6.29). This has been a consistent observation throughout the face milling tests, irrespective of the conditions. As seen in Figure 6.29, both F′ and F_{max}' of B3 inserts also showed comparable patterns. The resultant cutting forces of B3 cutting inserts were lower than those of B2 because of the reduced depth of cut [17]. For instance, the F_{max}' of T1ML-B3 and R2S-B3 were 1111 N and 1317 N, respectively, while the corresponding F_{max}' of their B2 counterparts were 1627 N and 1658 N. It is worth noting that the insert tool life of these cutting inserts was 40 minutes). The TCN1S-B3 cutting insert had the highest specific cutting energy (~60 J/mm^3), whereas the N2S-B3 had the lowest (~36 J/mm^3) amongst the B3 cutting inserts. The low specific energy of N2S-B3 is attributed to the premature failure (within the first minute of machining) of the insert at an average resultant cutting force (575 N). There was no significant difference in the specific cutting energies of the majority of B3 inserts, and this was due to the similar average resultant cutting forces the inserts experienced (Table 6.8). The machining temperatures for B3 cutting inserts were between the range of ~51 °C and ~85 °C. Similar to the resultant cutting forces, the T′ values of B3 cutting inserts were slightly lower than those of B2 inserts. The slightly lower machining temperatures observed in B3 inserts were also attributed to the reduction of the depth of cut by 0.25 mm.

7.6.1.2. Effective insert tool life and wear performance of B3 cutting inserts

The T1ML-B3, TCN1S-B3 and R2S-B3 cutting inserts achieved an effective insert tool life (I_l') of 20 minutes. The T1ML-B3 had the lowest FWR′ (1.67 µm/min), with a VB_{max}' of 33.33 µm after 20 minutes of machining. This was followed by R2MS-B3 and TCN1S-B3 with FWR′s of 5.21 µm/min and 5.33 µm/min, although the former had an effective insert tool life of 8 minutes. With the exception of R2MS-B3, the effective insert tool life and FWR of T1ML-B3, TCN1S-B3 and R2S-B3 inserts were comparable to their B2 counterparts. As discussed in the previous sections, the lower FWR and longer insert tool life observed in these inserts were due to high hardness and resistance to abrasion wear [17, 26]. However, it must be highlighted that the maximum duration of B3 cutting inserts was set at 40 minutes due to the reduction of depth of cut in finishing-2 compared to finishing-1. This means that these B3 cutting inserts showed the ability to continue with machining if only the ISO 3685:1993 tool life criteria were used instead of surface roughness which is a critical criterion when assessing the

quality of machining during finishing [212]. In general, the LPS produced NbC-Ni based B3 cutting inserts had relatively low surface roughness compared to their PECS counterparts (Table 6.9). However, the LPS inserts exhibited higher FWR′s and lower I_l' (i.e., below 6 minutes) due to the poor hardness and resistance to abrasive wear. Thus, albeit having better surface roughness, the inserts had relatively short effective insert tool life and high flank wear rate, respectively. The additions of Mo, TiC, TiC_7N_3, and a combination of Mo plus TiC to the N2S-B3 composition improved I_l' in all the PECS produced inserts as a result of increased hardness and resistance to abrasive wear. The R2S-B3 and TCN1S-B3 cutting inserts had the highest effective insert tool life improvements which increased by 1900%, whereas those of N2MS-B3 and R2MS-B3 were increased by 1300% and 700%, respectively. Similar to finishing-1 trials, these observations also confirm the importance of hardness of cutting inserts at finishing conditions. Similar to observations in semi-finishing and finishing-1 trials, the main cutting edge wear mechanisms of B3 cutting inserts were mechanical fracture (chipping) and abrasion wear as indicated by the optical micrographs (Figure 6.34). Crater wear was observed only on the rake face of T1ML-B3 cutting insert due to its chemical instability when machining cast irons [12]. The flank faces of NbC-Ni based B3 inserts which had longer I_l's exhibited pronounced abrasion wear, for similar reasons outlined for B2 cutting inserts. On the other hand, the B3 inserts with shorter effective tool life exhibited excessive chipping and mechanical fracture due to high machining speeds.

7.6.1.3. Machining performance of B3 cutting inserts

The TOPSIS model determined T1ML-B3 as the best cutting insert among the B3 alternatives. The insert achieved position one with an overall preference score of 0.793, followed by the R2S-B3 and TCN1S-B3 in positions two and three respectively, with O_is of 0.766 and 0.760 (Figure 6.36). The overall preference scores of TCN1S-B3 and R2S-B3 inserts are very close to that of T1ML-B3. The T1ML-B3 had a slightly higher surface roughness compared to TCN1S-B3 and R2S-B3 (Table 6.10) and thus the slightly better performance of T1ML-B3 was attributed to its lower U_c' and F_{max}' as result of the good combination of hardness and fracture toughness. The relatively lower surface roughness exhibited by the TCN1S-B3 and R2S-B3 cutting inserts was attributed to the slightly higher stiffness (elastic modulus) which can help in maintaining dimensional accuracy during machining [213]. The N2MS-B3 insert had the highest O_i (0.657) among the average B3 performers, and the rest of the inserts obtained the overall preference scores of below 0.4. As with previous tests, the average and poor performers are mainly the LPS produced NbC-Ni based inserts due to their relatively poor combinations of hardness and fracture toughness properties. It is worth mentioning that although

slightly different machining performance criteria were used for finishing-2, the performance of B3 cutting inserts mirrors that of B2 inserts.

7.6.2. Shark skin LSM (S3) cutting inserts

7.6.2.1. Resultant cutting forces, specific cutting energy, and temperature of S3 cutting inserts

The maximum resultant cutting forces experienced by the shark skin LSM (S3) were significantly higher than the average resultant cutting forces (Table 6.11). The average resultant cutting forces followed a similar trend to that of F_{max}'. Due to its slightly higher hardness and abrasion wear resistance, the R2MS-S3 insert exhibited the lowest F′ (1016 N) among the S3 inserts. This was followed by the R2S-S3, TCN1S-S3 and T1ML-S3 cutting inserts. In general, the PECS produced S3 inserts had slightly lower average resultant cutting forces than their LPS produced counterparts. This observation is consistent with the results observed throughout the results of the machining trials. Due to the slightly lower F′ of PECS than LPS inserts, the PECS inserts exhibited slightly lower specific cutting energies (Table 6.11). The machining temperatures of the majority of S3 cutting inserts were between the range of 70 °C and 75 °C. In contrast to B3 inserts, where T′ values exhibited significant variation (Figure 6.31), the T′ values of S3 cutting inserts were closely grouped within the mentioned range (see Figure 6.39). Notably, the inserts with longer cutting duration appeared to have slightly higher machining temperatures due to prolonged insert-workpiece contact which led to temperature rise.

7.6.2.2. Effective insert tool life and wear performance of S3 cutting inserts

The T1ML-S3 cutting insert exhibited the lowest FWR′ (3.01 µm/min) compared to other S3 cutting inserts, with the insert having a VB_{max}' of 51.11 µm after 17 minutes of machining. This was followed by the R2S-S3, R2MS-S3 and TCN1S-S3 cutting inserts which also achieved an effective insert tool life of 17 minutes and slightly higher FWR′s than the T1ML-S3 (Table 6.12). Notably, none of the S3 cutting inserts had I_t' of above 17 minutes. As shown in Figure 6.41, the shark skin LSM technique resulted in a reduction of effective insert tool life of the majority of S3 cutting inserts, with the TCN1L-S3 and R2L-S3 having the highest reductions (300 %) whereas T1ML-S3, TCN1S-S3 and R2S-S3 exhibiting reductions of only 18% respectively. Similar to observations in finishing-1, the reductions in effective tool life of S3 inserts compared to their B3 counterparts could be attributed to the entrapment of chips during machining which led to a non-smooth interaction between the inserts and

workpiece. Resulting in increased abrasion action, chipping, and mechanical fracture. However, contrasting effects of shark skin LSM technique were detected on inserts such as N2S-S3, R2MS-S3 and N2ML-S3 inserts, where the application of the technique improved the effective insert tool life of these inserts by 75%, 53% and 25%, respectively. The improvement was attributed to the increased hardness, resistance to abrasive wear and cutting edge strengthening by shark skin LSM. These observations suggest that although the resultant cutting forces in these inserts were increased, the hard carbide layer produced by the shark skin LSM slightly improved the properties of the cutting edges [17]. Similar to previous tests (irrespective of cutting conditions, cutting edge, or sintering technique), the main cutting edge wear mechanisms observed on the optical micrographs of the flank and rake faces were abrasion wear, chipping, and mechanical fracture (Figure 6.44).

7.6.2.3. Machining performance of S3 cutting inserts

According to TOPSIS model, the R2MS-S3 cutting insert had the best performance with an overall preference score of 0.999, followed by TCN1S-S3 and R2S-S3 inserts with O_is of 0.837 and 0.813, respectively. Notably, the top three ranked cutting inserts were NbC-Ni based inserts, which means that they outperformed the conventional T1ML-B3, which had an O_i of 0.782 in position four. As shown in Table 6.13, these inserts exhibited similar effective insert tool life and comparable specific cutting energy. However, the T1ML-S3 had slightly higher surface roughness and F_{max}' than the other top ranked inserts. Consistent with the results from the previous machining trials, the LPS produced inserts had poor performance compared to the PECS produced inserts. Similarly, the additions of Mo, TiC, TiC_7N_3, and a combination of Mo plus TiC to the N2S-S3 composition resulted in improved machining performances of N2MS-S3, R2S-S3, TCN1S-S3 and R2MS-S3.

7.6.3. Pyramid LSM (P3) cutting inserts

7.6.3.1. Resultant cutting forces, specific cutting energy, and temperature of P3 cutting inserts

Similar to B3 and S3 inserts, the maximum resultant cutting forces of the pyramid LSM (P3) inserts were significantly higher than the average resultant cutting forces (Table 6.14). The average resultant cutting forces of P3 cutting inserts also followed the trend of F_{max}'. Due to its good combination of physical and mechanical properties, the T1ML-P3 insert exhibited the lowest F′ (793 N) among the P3 inserts. Similar to previous tests, the LPS produced P3 cutting inserts exhibited slightly higher resultant cutting forces than their PECS produced counterparts. Due to the good combinations of hardness and

abrasion wear resistance, the T1ML-P3 exhibited the lowest specific cutting energy (~49.5 J/mm^3) among the P3 cutting inserts. Besides TCN1L-P3 and R2L-P3 cutting inserts, the specific cutting energy of P3 inserts was below 60 J/mm^3 (Table 6.14 and Figure 6.48). The machining temperatures of P3 cutting inserts were comparable to those of S3 and B3 cutting inserts. In addition, similar to S3 cutting inserts, P3 inserts with longer machining times exhibited slightly higher T′ than those with shorter cutting times.

7.6.3.2. Effective insert tool life and wear performance of P3 cutting inserts

Similar to its S3 counterpart, the T1ML-P3 cutting insert had the lowest FWR′ (3.61 µm/min) among the P3 inserts with a VB_{max}' of 28.89 µm after 8 minutes of machining. The same observations were made for R2MS-P3 and R2S-P3 inserts which exhibited FWR′ of 4.86 µm/min and 5.63 µm/min after 8 minutes of machining respectively. The TCN1S-P3 insert exhibited the highest effective insert tool life (11 minutes) among P3 inserts. However, the insert obtained a slightly higher FWR′ compared to the aforementioned inserts. Notably, the P3 cutting inserts generally exhibited lower effective insert tool life than B3 and S3 inserts. This was attributed to the poor surface roughness quality associated with the pyramidal LSM technique. As previously indicated, the trapped debris (hard abrasive particles in the form of GCI chips) was noted to be the main contributor to the relatively higher surface roughness of P3 inserts at relatively low machining durations (Table 6.15). Thus, the inserts quickly reached the 2.5 µm surface roughness limit, leading to premature failure. As a result, the pyramid LSM technique reduced the effective tool life of the majority of P3 inserts compared to B3 inserts (Figure 6.51). The highest reductions were detected in TCN1L-P3 and R2S-P3 (about 300% reduction), as well as in T1ML-P3 and TCN1S-P3 with reductions of 150% and 82%, respectively. The cutting edge wear mechanisms were similar to those observed in S3 and B3 as shown in Figure 6.54, respectively.

7.6.3.3. Machining performance of P3 cutting inserts

The TCN1S-P3 cutting insert was ranked first among the P3 cutting inserts with an overall preference score of 0.911 from the TOPSIS model. This was followed by T1ML-P3 and N2MS-P3 inserts in positions two and three with O_is of 0.726 and 0.720, respectively (Figure 6.56). As shown in the figure, there was no significant difference in the machining performance of P3 inserts ranked between positions two and five. Consistent with the results from the previous machining trials (including S3), the LPS produced inserts had poor performance compared to the PECS produced inserts. Similarly, the additions of Mo, TiC, TiC_7N_3, and a combination of Mo plus TiC to the N2S-P3 composition resulted in improved machining performances of N2MS-P3, R2S-P3, TCN1S-P3 and R2MS-P3.

7.6.4. Consolidated overall finishing-2 machining performance

Similar to semi-finishing and finishing-1, the TOPSIS model was applied on all the 27 cutting inserts used during finishing-2 machining trials to evaluate and rank the cutting inserts during machining at a spindle speed of 1600 rpm, depth of cut of 0.25 mm and feed of 0.1 mm/tooth. The TCN1S-B3 and T1ML-B3 obtained the highest overall preference score (0.826) among the finishing-2 inserts (Table 6.17), rendering them the best inserts for machining a-GCI at finishing conditions. The TCN1S-B3 had performance criteria values of 20 min, 60 J/mm^3, 1.75 µm and 1551 N for C1, C2, C3 and C4, whereas those of T1ML-B3 were 20 min, 45 J/mm^3, 2.34 µm, and 1111 N, respectively. Although these inserts had similar overall preference scores, the TCN1S-B3 insert produced significantly lower surface roughness than the T1ML-B3 insert. As shown in Table 6.17, the surface roughness of the T1ML-B3 insert was very close to the limit of 2.5 µm as prescribed by Auto Industrial Group, thus making the insert less suitable compared to the TCN1S-B3. These results further indicate that cermets (or ceramic) cutting inserts were advantageous over conventional cemented carbide when higher levels of surface finish are prioritised [212], [214]. The R2S-B3 followed TCN1S-B3 and T1ML-B3, obtaining the third rank with an O_i of 0.822 and performance evaluation criteria values of 20 min, 57 J/mm^3, 2.00 µm, and 1317 N. As shown in Table 6.17, the best performing inserts were mainly the B3 inserts followed by S3 and then P3 with only one entry (i.e., TCN1S-P3 with the lowest O_i (0.546) in the category). The N2MS-S3 and R2L-B3 cutting inserts represents the average and poor performers with O_is of 0.506 and 0.360 at positions ten and nineteen, respectively. Notably, the results of finishing-2 were similar to those of finishing-1 indicating that the "best" insert category where the blank cutting inserts. This observation, therefore, suggests that the blank cutting edges as opposed to the laser surface modified ones, were ideal for finishing processes, especially during machining operations where surface roughness quality is a critical consideration. This argument holds even for cutting inserts in the poor performing category in Table 6.17, whereby the laser surface modified cutting inserts obtained even lower overall preference scores than the blanks. When considering the inserts by composition, the TCN1S (NbC-10TiC_7N_3-12Ni (wt.%)) based inserts had the best machining performance with all three TCN1S cutting inserts being represented in the best category. This was followed by the R2S (NbC-10TiC-12Ni (wt%)) and T1ML (WC-10TiC-10[Co/Mo]) (wt%)) inserts with two entries each made of the B3 and S3 cutting edges, respectively. The good performance exhibited by TCN1S and R2S based inserts could be explained by the slightly higher elastic modulus [213] as well as the hardness and impact to abrasion wear due to respective additions of TiC_7N_3 and TiC secondary carbide phases [26], whereas that of T1ML inserts could be attributed to a good combination of hardness and fracture toughness properties [17]. Similar to finishing-1, the overall

machining performance evaluation for finishing-2 machining trials revealed that the NbC-Ni based cutting inserts can potentially replace or compete with conventional WC-Co based cutting inserts in high-speed machining of cast irons.

8. Conclusions and recommendations

This chapter synthesises the key findings of this study and proposes actionable recommendations aimed at the following:

- Advancing design and fabrication of cutting inserts (in particular, composition manipulation and sintering techniques),
- Understanding the use of femtosecond laser surface modification technology for cutting edge strengthening, and
- Developing a machining performance evaluation model for sustainable manufacturing of a-GCI components.

The culmination of this research not only contributes to the current body of knowledge within science and engineering of hard materials but also offers practical insights that can inform decision-making processes and shape future developments. By navigating through the following conclusions and recommendations, readers will gain a comprehensive understanding of the implications of the current study and the avenues for advancing this area of research in both academic and practical domains.

8.1. Conclusions

All samples irrespective of composition and sintering technique achieved densification of 97% and above. The LPS produced samples had slightly higher densification than the PECS produced samples. Additions of Mo to the N2S (NbC-12Ni (wt.%)) composition did not have a significant effect on densification. However, additions of TiC and TiC_7N_3 to a similar composition inhibited densification. The presence of TiC and a partial substitution of Co by Mo inhibited grain growth in T1ML sample due to the formation of (W, Ti, Mo, Co) C solid solutions, resulting in a fine-grained microstructure. The sample also exhibited good distribution of the Co binder pools due to relatively high sintering temperatures and longer sintering duration associated with LPS. In addition, the T1ML sample had traces of undissolved TiC within the microstructure, thus suggesting the need for slightly higher sintering temperatures and pressure. The PECS produced NbC-Ni based samples had relatively smaller grains compared to the LPS samples irrespective of composition, due to the shorter sintering times and lower sintering temperatures which prevented grain growth by coalescence and Ostwald ripening. For similar reasons, the PECS samples had poorer Ni binder pool distributions than the LPS samples. Molybdenum was detected to have dissolved and fully reprecipitated inside the carbide phases in all samples containing the element during sintering, irrespective of the composition, because of its carbide

forming properties. Similar to T1ML sample, traces of undissolved TiC and TiCN were detected respectively in R2S, R2MS and TCN1S samples. In contrast, these phases were not easily apparent in the LPS samples due to higher sintering temperatures and longer sintering durations. The T1ML sample had a good combination of physical and mechanical properties compared to the other samples due to the fine WC grains and good Co binder pool distribution. The LPS produced NbC-Ni based samples exhibited lower hardness but slightly higher fracture toughness than PECS produced samples of identical composition due to larger carbide grains and better distribution of the binder phase during LPS than PECS. The additions of Mo, TiC, TiC_7N_3 and a combination of Mo plus TiC to the N2S composition improved the hardness in N2MS, R2S, TCN1S and R2MS samples due to the formation of carbide solid solutions and the presence of undissolved TiC and TiCN in respective samples. The LPS produced NbC-Ni samples exhibited relatively lower elastic modulus and modulus of rigidity than PECS samples due to the presence of slightly pronounced pores within the microstructures. The TCN1S and R2S samples had the highest elastic modulus and modulus of rigidity compared to all the samples due to the hard undissolved TiCN and TiC secondary carbide phases.

The cutting forces during face-milling machining of a-GCI fluctuate between the "peaks" of very high forces (F_{max}), which represent the formation of chips, and moderate forces, indicating the breaking off of the chips. These high forces were significantly higher than the average resultant cutting forces and were mostly responsible for fracture and chipping of the cutting edges during machining, leading to the failure of the cutting inserts. Due to a slightly higher depth of cut, the machining temperatures for semi-finishing were slightly higher compared to those observed during finishing conditions. The femtosecond LSM technique improved the surface hardness and resistance to abrasion and attrition wear of the cutting inserts. The laser surface modified cutting inserts led the best performer category during semi-finishing. The PECS produced R2MS-P1 (NbC-10TiC-12[Ni/Mo] (wt%)) pyramid LSM insert being the most suitable cutting insert for semi-finishing due to high hardness, good abrasion and attrition wear resistance, and the presence of undissolved TiC. The LSM technique was noted to be advantageous during semi-finishing but had adverse effects for the majority of inserts during finishing-1 and finishing-2 machining conditions. These contrasting observations between semi-finishing and finishing machining performance results emphasise the importance of aligning cutting insert designs with specific machining requirements for optimal performance. The most suitable cutting insert for finishing-1 was the conventional T1ML-S2 (WC-10TiC-10[Co/Mo] (wt%)) shark skin LSM insert. However, the PECS produced R2S-B2 (NbC-10TiC-12Ni (wt%)) blank insert exhibited comparable machining performance to that of T1ML-S2 due to high hardness, resistance to abrasion wear, presence of undissolved TiC, and a relatively higher elastic modulus. The TCN1S-B3 (NbC-10TiC_7N_3-12Ni

(wt%)) blank insert produced by PECS was found to be the most ideal insert for finishing-2 because of its comparatively high hardness, resistance to abrasion wear, relatively higher elastic modulus, and the presence of undissolved TiCN. The overall machining results demonstrated the successful application of the "newly" developed TOPSIS based model for machining performance evaluation as well as showing that the model could be a brilliant tool for assessing cutting inserts and their intrinsic properties.

8.2. Recommendations

The recommendations for future work are as follows:

- Optimisation of the sintering parameters to improve densification so that the density of samples could be increased to more than 99%, therefore improving the mechanical properties of the cutting inserts.
- The use of PECS and additions of TiC and TiC_7N_3 improved the hardness and resistance to abrasion wear resistance properties. However, to further improve these properties as well as improve the fracture toughness, slightly higher sintering temperatures and pressure must be explored.
- The PECS produced R2MS-P1 (NbC-10TiC-12[Ni/Mo] (wt%)) pyramid LSM insert was found to be the most suitable cutting insert for semi-finishing, while the PECS TCN1S-B3 (NbC-10TiC_7N_3-12Ni (wt%)) blank insert found to be the most ideal insert for finishing operations. Both inserts. Both inserts should be optimised and further developed to enhance their performance.
- Due to time constraints and the unavailability of equipment, the residual stress measurements could not be done to fully understand the effect of LSM application on the cutting edges. This would be vital for the comprehension of the cutting edge strengthening mechanisms including the mechanical properties as a result of LSM technique.
- The force behaviour during machining of a-GCI should be further studied. This could provide additional information on chip formation and the variation of forces that were observed in this study.
- Use the various multi-criteria decision-making models to benchmark and test the developed TOPSIS-based model for robustness.
- Consider testing other types of machining (i.e. turning, wood cutting, etc) using the newly developed grades used in this work since their fracture toughness values were relatively low.

9. Research outputs

This chapter provides the research outputs of this work in the form of conference papers as listed below:

1. M.S Rabothata, R. Genga, N.P Phasha, K. Phaka, N. B Nelwalani, S. Ngongo, C. Polese, S. Huang, J. Vleugels, *Effect of Femtosecond Laser Surface Modified WC and NbC Based Inserts During the Face-milling of Automotive Grey Cast Iron (GCI)*, 12th International Conference on the Science of Hard Materials (ICSHM12) (2024)

   This paper has been presented at the 12th International Congress on the Science of Hard Materials held on 11 – 15 March 2024 in Bentota, Sri Lanka. A journal paper based on this to be published in the special issue of the International Journal of Refractory Metals and Hard Materials in October 2024 is currently being prepared.

2. M Rabothata, N Mphasha, K Phaka, P Zeman, R Genga, C Polese S Huang and J Vleugels, *Tool Life of NbC-Based Cermets During Face-Milling of Automotive GCI*, 57th Congress of the Microscopy Society of Southern Africa (MSSA) 49 (2022)

   This paper was presented at the 57th Congress of the Microscopy Society of Southern Africa held on 05 – 08 December 2022 in Gold Reef City Theme Park Hotel, Johannesburg, South Africa.

3. N Mphasha, M Rabothata, P Zeman, R Genga, C Polese, S Huang, J Vleugels, A Janse van Vuuren and N Nelwalani*, Effects of TiC_7N_3 Additions and Sintering Technique on the Microstructural Properties of NbC-Based Cermets*, 57th Congress of the Microscopy Society of Southern Africa (MSSA) 49 (2022)

   This paper was presented at the 57th Congress of the Microscopy Society of Southern Africa held on 05 – 08 December 2022 in Gold Reef City Theme Park Hotel, Johannesburg, South Africa.

4. M Rabothata, N Mphasha, N Nelwalani, A Janse van Vuuren, R Genga, C Polese, S Huang and J Vleugels, *Physical, Microstructure, and Mechanical Property Effects of Molybdenum Additions to NbC-TiC-Ni and WC-TiC-Co Cemented Carbide Binders*, 20th Plansee Seminar HM 125 (2022)

This paper was presented at the 20th Plansee Seminar held on 30 May – 03 June 2022 in Reutte, Austria.

5. M.S Rabothata, R.M Genga, N.P Mphasha, K Phaka, P Zeman, C Polese, S. Huang, J Vleugels, S Ngongo, *Energy consumption of NbC based inserts during face milling of automotive GCI*.

   This paper has been accepted for oral presentation at the 58th Congress of the Microscopy Society of Southern Africa (MSSA).

References

[1] "Africa: total population forecast 2020-2050 | Statista." Accessed: Dec. 13, 2022. [Online]. Available: https://www.statista.com/statistics/1224205/forecast-of-the-total-population-of-africa/

[2] B. Tchanche, "A view of road transport in Africa," *Afr J Environ Sci Tech*, vol. 13, no. 8, pp. 296–302, Aug. 2019, doi: 10.5897/ajest2018.2575.

[3] "Top 10 Fastest Growing Industries in Africa - Arise IIP." Accessed: Apr. 28, 2023. [Online]. Available: https://www.ariseiip.com/top-10-fastest-growing-industries-in-africa/

[4] "South Africa's Manufacturing industry - South African Market Insights." Accessed: Jul. 07, 2022. [Online]. Available: https://www.southafricanmi.com/south-africas-manufacturing-industry.html

[5] J. O'Hara and F. Fang, "Advances in micro cutting tool design and fabrication," *International Journal of Extreme Manufacturing*, vol. 1, no. 3, p. 032003, 2019, doi: 10.1088/2631-7990/ab3e7f.

[6] M. O. Genç and Ç. Imer, "Graphite flake size effects to thermal durability of automobile flywheel under forced slippage," *Proceedings of the World Congress on Mechanical, Chemical, and Material Engineering*, pp. 1–8, 2017, doi: 10.11159/icmie17.121.

[7] A. Rizzo *et al.*, "The critical raw materials in cutting tools for machining applications: A review," *Materials*, vol. 13, no. 6, pp. 1–48, 2020, doi: 10.3390/ma13061377.

[8] J. García, V. Collado Ciprés, A. Blomqvist, and B. Kaplan, "Cemented carbide microstructures: a review," *International Journal of Refractory Metals and Hard Materials*, vol. 80. Elsevier Ltd, pp. 40–68, Apr. 01, 2019. doi: 10.1016/j.ijrmhm.2018.12.004.

[9] S. Lay, J. Thibault, and S. Hamar-Thibault, "Structure and role of the interfacial layers in VC-rich WC-Co cermets," *Philosophical Magazine*, vol. 83, no. 10, pp. 1175–1190, Apr. 2003, doi: 10.1080/1478643031000075759.

[10] P. J. Blau *et al.*, "Metals Handbook Desk Edition," 1998.

[11] K. Plucknett, “Cermets and hardmetals,” *Metals (Basel)*, vol. 8, no. 11, pp. 4–6, 2018, doi: 10.3390/met8110963.

[12] R. M. Genga, L. A. Cornish, M. Woydt, A. Janse van Vuuren, and C. Polese, “Microstructure, mechanical and machining properties of LPS and SPS NbC cemented carbides for face-milling of grey cast iron,” *Int J Refract Metals Hard Mater*, vol. 73, no. January, pp. 111–120, 2018, doi: 10.1016/j.ijrmhm.2017.12.036.

[13] G. S. Upadhyaya, D. R. Tobergte, and S. Curtis, *Cemented Tungsten Carbides: Production, Properties, and Testing*. Kanpur, India: Indian Institute of Technology, 1998. doi: http://dx.doi.org/10.1016/B978-081551417-6.50015-0.

[14] G. Andersson and B. Jansson, “The solubility of cubic carbide formers in liquid cobalt,” in *15th International Plansee Seminar*, G. Kneringer, P. Rodhammer, and H. Wildner, Eds., Reutte: Plansee Holding AG, 2001.

[15] M. Woydt and H. Mohrbacher, “The use of niobium carbide (NbC) as cutting tools and for wear resistant tribosystems,” *Int J Refract Metals Hard Mater*, vol. 49, no. 1, pp. 212–218, 2015, doi: 10.1016/j.ijrmhm.2014.07.002.

[16] K. Sarin, Vinod, D. Mari, and L. Llanes, *Comprehensive Hard Materials*. Oxford UK: Elsevier, 2014.

[17] R. M. Genga *et al.*, “Roughing, semi-finishing and finishing of laser surface modified nickel bonded NbC and WC inserts for grey cast iron (GCI) face-milling,” *Int J Refract Metals Hard Mater*, vol. 86, no. June 2019, 2020, doi: 10.1016/j.ijrmhm.2019.105128.

[18] S. G. Huang, K. Vanmeensel, H. Mohrbacher, M. Woydt, and J. Vleugels, “Microstructure and mechanical properties of NbC-matrix hardmetals with secondary carbide addition and different metal binders,” *Int J Refract Metals Hard Mater*, vol. 48, pp. 418–426, 2015, doi: 10.1016/j.ijrmhm.2014.10.014.

[19] S. G. Huang, O. Van der Biest, L. Li, and J. Vleugels, “Properties of NbC-Co cermets obtained by spark plasma sintering,” *Mater Lett*, vol. 61, no. 2, pp. 574–577, Jan. 2007, doi: 10.1016/J.MATLET.2006.05.011.

[20] R. M. Genga *et al.*, “High-temperature sliding wear, elastic modulus and transverse rupture strength of Ni bonded NbC and WC cermets,” *Int J Refract Metals Hard Mater*, vol. 87, p. 105143, Feb. 2020, doi: 10.1016/j.ijrmhm.2019.105143.

[21] G. Casalino, A. M. Losacco, A. Arnesano, F. Facchini, M. Pierangeli, and C. Bonserio, "Statistical Analysis and Modelling of an Yb: KGW Femtosecond Laser Micro-drilling Process," *Procedia CIRP*, vol. 62, pp. 275–280, Jan. 2017, doi: 10.1016/J.PROCIR.2016.06.111.

[22] S. Fang, R. Lima, D. Sandoval, D. Bähre, and L. Llanes, "Ablation Investigation of Cemented Carbides Using Short-Pulse Laser Beams," *Procedia CIRP*, vol. 68, no. April, pp. 172–177, 2018, doi: 10.1016/j.procir.2017.12.042.

[23] A. Kumar and M. C. Gupta, "Laser machining of micro-notches for fatigue life," *Opt Lasers Eng*, vol. 48, no. 6, pp. 690–697, 2010, doi: 10.1016/j.optlaseng.2010.01.008.

[24] W. M. Da Silva, M. P. Suarez, A. R. Machado, and H. L. Costa, "Effect of laser surface modification on the micro-abrasive wear resistance of coated cemented carbide tools," *Wear*, vol. 302, no. 1–2, pp. 1230–1240, 2013, doi: 10.1016/j.wear.2013.01.035.

[25] A. Tayal, N. Singh, and M. Kumar, "Machining of superalloys : A review on machining parameters , cutting tools , and cooling methods," *Mater Today Proc*, no. xxxx, 2020, doi: 10.1016/j.matpr.2020.10.815.

[26] R. M. Genga, G. Akdogan, C. Polese, J. C. Garrett, and L. A. Cornish, "Abrasion wear, thermal shock and impact resistance of WC-cemented carbides produced by PECS and LPS," *Int J Refract Metals Hard Mater*, vol. 49, no. 1, pp. 133–142, 2015, doi: 10.1016/j.ijrmhm.2014.07.031.

[27] A. Stephenson, David and S. Agapiou, John, *Metal Cutting Theory and Practice*, Third Edit. CRC Press, 2016. [Online]. Available: http://library1.nida.ac.th/termpaper6/sd/2554/19755.pdf

[28] Z. Z. Fang, M. C. Koopman, and H. Wang, "Cemented Tungsten Carbide Hardmetal-An Introduction," in *Comprehensive Hard Materials*, vol. 1, Elsevier Ltd., 2014, pp. 123–137. doi: 10.1016/B978-0-08-096527-7.00004-0.

[29] R. M. Genga, "Microstructure and Properties of Selected Wc-Cemented Carbides Manufactured By Sps Method," University of Witwatersrand, 2014.

[30] C. W. Li, K. C. Chang, and A.-C. Yeh, "On the microstructure and properties of an advanced cemented carbide system processed by selective laser melting," *J Alloys Compd*, vol. 782, pp. 440–450, Apr. 2019, doi: 10.1016/j.jallcom.2018.12.187.

[31] K. J. A. Brookes, “Half a century of hardmetals,” *Metal Powder Report*, vol. 50, no. 12, pp. 22–28, Dec. 1995, doi: 10.1016/0026-0657(95)80019-0.

[32] S. George, *Cutting Tools Application*. 2002.

[33] P. Schwarzkopf, “Deutsche Edelstahl Werke AG,” German Patent 720502, 1942

[34] H. Fukui, “Evolutional history of coating technologies for cemented carbide inserts - Chemical vapor deposition and physical vapor deposition,” *SEI Technical Review*, no. 82, pp. 39–45, 2016.

[35] M. Kobayashi and Y. Doi, “TiN and TiC coating on cemented carbides by ion plating,” *Thin Solid Films*, vol. 54, no. 1, pp. 67–74, Oct. 1978, doi: 10.1016/0040-6090(78)90278-X.

[36] R. Haubner, M. Lessiak, R. Pitonak, A. Köpf, and R. Weissenbacher, “Evolution of conventional hard coatings for its use on cutting tools,” *Int J Refract Metals Hard Mater*, vol. 62, pp. 210–218, Jan. 2017, doi: 10.1016/j.ijrmhm.2016.05.009.

[37] G. E. Spriggs, “A history of fine grained hardmetal,” *Int J Refract Metals Hard Mater*, vol. 13, no. 5, pp. 241–255, Jan. 1995, doi: 10.1016/0263-4368(95)92671-6.

[38] W. D. Schubert, A. Bock, and B. Lux, “General aspects and limits of conventional ultrafine WC powder manufacture and hard metal production,” *Int J Refract Metals Hard Mater*, vol. 13, no. 5, pp. 281–296, 1995, doi: 10.1016/0263-4368(95)92674-9.

[39] Z. Fang and J. W. Eason, “Study of nanostructured WC-Co composites,” *Int J Refract Metals Hard Mater*, vol. 13, no. 5, pp. 297–303, Jan. 1995, doi: 10.1016/0263-4368(95)92675-A.

[40] X. Wang, Z. Z. Fang, and H. Y. Sohn, “Grain growth during the early stage of sintering of nanosized WC-Co powder,” *Int J Refract Metals Hard Mater*, vol. 26, no. 3, pp. 232–241, 2008, doi: 10.1016/j.ijrmhm.2007.04.006.

[41] Y. Peng, C. Buchegger, W. Lengauer, Y. Du, and P. Zhou, “Solubilities of grain-growth inhibitors in WC-Co-based cemented carbides: Thermodynamic calculations compared to experimental data,” *Int J Refract Metals Hard Mater*, vol. 61, pp. 121–127, Dec. 2016, doi: 10.1016/j.ijrmhm.2016.08.012.

[42] T. W. Penrice, “Alternative Binders for Hard Metals.,” *The Carbide and tool journal*, vol. 20, no. 4, pp. 12–15, 1988.

[43] H. Nie and T. Zhang, “Development of manufacturing technology on WC–Co hardmetals,” *Tungsten*, vol. 1, no. 3, pp. 198–212, Sep. 2019, doi: 10.1007/S42864-019-00025-6.

[44] Y. Li, N. Liu, X. Zhang, and C. Rong, “Effect of Mo addition on the microstructure and mechanical properties of ultra-fine grade TiC–TiN–WC–Mo2C–Co cermets,” *Int J Refract Metals Hard Mater*, vol. 26, no. 3, pp. 190–196, May 2008, doi: 10.1016/J.IJRMHM.2007.05.005.

[45] R. M. Genga, L. A. Cornish, and G. Akdogan, “Effect of Mo2C additions on the properties of SPS manufactured WC-TiC-Ni cemented carbides,” *Int J Refract Metals Hard Mater*, vol. 41, pp. 12–21, Nov. 2013, doi: 10.1016/j.ijrmhm.2013.01.008.

[46] S. Fang *et al.*, “Fabrication of Interference Textures on Cemented Carbides Using Nanosecond and Femtosecond Laser Pulses,” *Procedia CIRP*, vol. 87, pp. 216–221, Jan. 2020, doi: 10.1016/J.PROCIR.2020.02.063.

[47] J. H. Huang, S. G. Huang, P. Zhou, B. Lauwers, J. Qian, and J. Vleugels, “Microstructure and mechanical properties of WC or Mo2C modified NbC-Ni cermets,” *Int J Refract Metals Hard Mater*, vol. 95, p. 105440, Feb. 2021, doi: 10.1016/J.IJRMHM.2020.105440.

[48] S. G. Huang *et al.*, “Microstructure and mechanical properties of (Nb,W,Ti)(C,N)-Ni solid solution cermets with 6 to 20 wt% Ni,” *Int J Refract Metals Hard Mater*, vol. 103, p. 105757, Feb. 2022, doi: 10.1016/J.IJRMHM.2021.105757.

[49] R. M. Raihanuzzaman, Z. Xie, S. J. Hong, and R. Ghomashchi, “Powder refinement, consolidation and mechanical properties of cemented carbides - An overview,” *Powder Technol*, vol. 261, pp. 1–13, 2014, doi: 10.1016/j.powtec.2014.04.024.

[50] Veuphonic, “The Tungsten Carbide Manufacturing Process.” Accessed: May 11, 2021. [Online]. Available: https://www.totalcarbide.com/tungsten-carbide-manufacturing-process.htm

[51] Mikrons, “How Attritor Works.” Accessed: May 13, 2021. [Online]. Available: https://www.attritor.in/attritor_working.html

[52] R. M. German, *Liquid Phase Sintering*. Rensselaer Polytechnic Institute - Troy, New York: Springer Science + Business Media, LLC, 1985.

[53] W. B. James and H. Corporation, "Powder Metallurgy Methods and Applications," vol. 7, 2015.

[54] R. M. German, P. Suri, and S. J. Park, "Review: Liquid phase sintering," *J Mater Sci*, vol. 44, no. 1, pp. 1–39, Jan. 2009, doi: 10.1007/s10853-008-3008-0.

[55] R. M. German, *Sintering: From Emperical Observations To Scientific Principles*, First Edit. Waltham, USA: Butterworth-Heinemann, 2014.

[56] S.-J. L. Kang, *Densification, Grain Growth and Microstructure.*, First Edit. Butterworth-Heinemann, 2005.

[57] R. J. Brook, "Pore-Grain Boundary Interactions and Grain Growth," *Journal of the American Ceramic Society*, vol. 52, no. 1, pp. 56–57, 1969, doi: 10.1111/j.1151-2916.1969.tb12664.x.

[58] R. M. Genga, G. Akdogan, J. E. Westraadt, and L. A. Cornish, "Microstructure and material properties of PECS manufactured WC-NbC-CO and WC-TiC-Ni cemented carbides," *Int J Refract Metals Hard Mater*, vol. 49, no. 1, pp. 240–248, 2015, doi: 10.1016/j.ijrmhm.2014.07.030.

[59] L. De Jonghe and M. Rahaman, "Sintering of Ceramics," in *Handbook of Advanced Ceramics*, Elsevier, 2003, pp. 187–264.

[60] R. K. Bordia, Suk-Joong, L. Kang, and E. A. Olevsky, "Current understanding and future research directions at the onset of the next century of sintering science and technology," 2017, doi: 10.1111/jace.14919.

[61] A. Mortensen, "Kinetics of Densification by Solution-Reprecipitation," vol. 45, no. 2, 1997.

[62] Z. S. Nikolic and F. Wakai, "Three-dimensional computer study of rearrangement during liquid phase sintering," *Math Comput Model*, vol. 55, no. 3–4, pp. 1251–1262, Feb. 2012, doi: 10.1016/j.mcm.2011.10.005.

[63] B. Magee, "Mechanisms of Liquid-Phase Sintering in Fe-Cu Mixtures," The University of British Columbia, 1975.

[64] J. Poetschke, V. Richter, T. Gestrich, and A. Michaelis, “Grain growth during sintering of tungsten carbide ceramics,” in *International Journal of Refractory Metals and Hard Materials*, Elsevier, Mar. 2014, pp. 309–316. doi: 10.1016/j.ijrmhm.2014.01.001.

[65] A. Baldan, “Progress in Ostwald ripening theories and their applications to nickel-base superalloys. Part I: Ostwald ripening theories,” *J Mater Sci*, vol. 37, no. 11, pp. 2171–2202, Jun. 2002, doi: 10.1023/A:1015388912729/METRICS.

[66] M. Eriksson, M. Radwan, and Z. Shen, “Spark plasma sintering of WC, cemented carbide and functional graded materials,” *Int J Refract Metals Hard Mater*, vol. 36, pp. 31–37, Jan. 2013, doi: 10.1016/j.ijrmhm.2012.03.007.

[67] H. Peng, Z. Shen, and M. Nygren, “Formation of in situ reinforced microstructures in α-sialon ceramics: Part III. Static and dynamic ripening,” *J Mater Res*, vol. 19, no. 8, pp. 2402–2409, 2004, doi: 10.1557/JMR.2004.0291.

[68] N. Saheb *et al.*, “Spark plasma sintering of metals and metal matrix nanocomposites: A review,” *Journal of Nanomaterials*, vol. 2012. 2012. doi: 10.1155/2012/983470.

[69] M. Tokita, “Spark Plasma Sintering (SPS) Method, Systems, and Applications,” in *Handbook of Advanced Ceramics: Materials, Applications, Processing, and Properties*, Second Edi., Elsevier Inc., 2013, pp. 1149–1177. doi: 10.1016/B978-0-12-385469-8.00060-5.

[70] P. Cavaliere, B. Sadeghi, and A. Shabani, “Spark Plasma Sintering: Process Fundamentals,” in *Spark Plasma Sintering of Materials*, Springer International Publishing, 2019, pp. 3–20. doi: 10.1007/978-3-030-05327-7_1.

[71] W. D. Schubert, “International conference on tungsten hard metals and refractory alloys,” Annapolis, MD, USA, 2000.

[72] P. Maheshwari, Z. Fang, and H. Y. Sohn, “Early-stage sintering densification and grain growth of nanosized WC–Co powders,” *International Journal of Powder Metallurgy*, vol. 43, no. 2, pp. 41–47, 2007.

[73] E. Brandes and G. Brook, Eds., *Smithells Metals Reference Book*, Seventh. 1992.

[74] Y. Zhou, Y. Yang, G. Yang, D. Yin, Y. Qin, and J. Liu, “Effects of sintering temperature on the densification of WC-6Co cemented carbides sintered by coupled multi-physical-

fields activated technology," *Manuf Rev (Les Ulis)*, vol. 2, 2015, doi: 10.1051/MFREVIEW/2015017.

[75] J. I. A. Lou, B. Gabbitas, D. Zhang, and F. E. I. Yang, "Effects of Initial Powder Compact Thickness, Lubrication, and Particle Morphology on the Cold Compaction Behavior of Ti Powder," *Metallurgical and Materials Transactions A*, no. May, 2015, doi: 10.1007/s11661-015-2925-1.

[76] I. Azcona, A. Ordóñez, J. M. Sánchez, and F. Castro, "Hot isostatic pressing of ultrafine tungsten carbide-cobalt hardmetals," *J Mater Sci*, vol. 37, no. 19, pp. 4189–4195, Oct. 2002, doi: 10.1023/A:1020048105585/METRICS.

[77] G. Y. Akimov, I. V. Andreev, V. I. Sheremet, I. Y. Trosnikova, P. I. Loboda, and T. O. Kosenchuk, "The Structure and Mechanical Properties of WC–8 wt.% Co Hardmetal Produced by Cold and Hot Isostatic Pressing," *Powder Metallurgy and Metal Ceramics*, vol. 61, no. 1–2, pp. 9–17, May 2022, doi: 10.1007/s11106-022-00290-0.

[78] S. Budin, T. R. Jaafar, and M. A. Selamat, "Effect of Sintering Atmosphere on the Mechanical Properties of Sintered Tungsten Carbide," *MATEC Web of Conferences*, vol. 130, Oct. 2017, doi: 10.1051/MATECCONF/201713003006.

[79] M. Kawakami, O. Terada, and K. Hayashi, "Effect of Sintering Cooling Rate on V Segregation Amount at WC/Co Interface in VC-doped WC-Co Fine-Grained Hardmetal," *Journal of The Japan Society of Powder and Powder Metallurgy*, vol. 51, no. 8, pp. 576–585, 2004, doi: 10.2497/JJSPM.51.576.

[80] T. Tomida *et al.*, "Grain Refinement of C–Mn Steel to 1 μm by Rapid Cooling and Short Interval Multi-pass Hot Rolling in Stable Austenite Region," *ISIJ International*, vol. 48, no. 8, pp. 1148–1157, Aug. 2008, doi: 10.2355/ISIJINTERNATIONAL.48.1148.

[81] X. Chen, Y. Liu, J. Ye, L. Wang, and D. Li, "Effect of rapid cooling on microstructure and properties of nanocrystalline WC-9%co-Cr3C2-VC cemented carbide," *Int J Refract Metals Hard Mater*, vol. 109, Dec. 2022, doi: 10.1016/J.IJRMHM.2022.105961.

[82] S. Fang, N. Salán, C. Pauly, L. Llanes, and F. Mücklich, "Critical Assessment of Two-Dimensional Methods for the Microstructural Characterization of Cemented Carbides," *Metals (Basel)*, vol. 12, no. 11, Nov. 2022, doi: 10.3390/met12111882.

[83] H. Engqvist and B. Uhrenius, “Determination of the average grain size of cemented carbides,” *Int J Refract Metals Hard Mater*, vol. 21, no. 1–2, pp. 31–35, Jan. 2003, doi: 10.1016/S0263-4368(03)00005-2.

[84] A. Ali, Y. W. Chiang, and R. M. Santos, “X-ray Diffraction Techniques for Mineral Characterization: A Review for Engineers of the Fundamentals, Applications, and Research Directions,” *Minerals 2022, Vol. 12, Page 205*, vol. 12, no. 2, p. 205, Feb. 2022, doi: 10.3390/MIN12020205.

[85] S. Lay, “Recent progress in the characterisation of cemented carbides at the nanoscale by TEM,” Grenoble, 2019.

[86] C. Wei *et al.*, “Simultaneously high fracture toughness and transverse rupture strength in ultrafine cemented carbide3”, doi: 10.1039/c3ce40211h.

[87] A. Chychko, J. García, V. Collado Ciprés, E. Holmström, and A. Blomqvist, “HV-KIC property charts of cemented carbides: A comprehensive data collection,” *Int J Refract Metals Hard Mater*, vol. 103, p. 105763, Feb. 2022, doi: 10.1016/J.IJRMHM.2021.105763.

[88] H. Engqvist, S. Jacobson, and N. Axén, “A model for the hardness of cemented carbides,” *Wear*, vol. 252, no. 5–6, pp. 384–393, Mar. 2002, doi: 10.1016/S0043-1648(01)00866-3.

[89] Z. H. Xu and J. Ågren, “A modified hardness model for WC–Co cemented carbides,” *Materials Science and Engineering: A*, vol. 386, no. 1–2, pp. 262–268, Nov. 2004, doi: 10.1016/J.MSEA.2004.07.061.

[90] Technical Committee ISO TC 164, “Metallic materials-Vickers hardness test-Part 1: Test method (ISO 6507-1:2018),” 2018.

[91] Technical Committee ISO TC119/SC4, “Hardmetals - Palmqvist toughness test (ISO 28079:2009),” 2009.

[92] S. Palmqvist, “Indentation hardness and fracture toughness in single crystal ,” *JERNKONTORETS ANNALER*, pp. 300–306, 1957.

[93] K. Wang *et al.*, “Interplay of microstructure and mechanical properties of WC-6Co cemented carbides by hot oscillating pressing method,” *Ceram Int*, vol. 47, no. 14, pp. 20731–20735, Jul. 2021, doi: 10.1016/J.CERAMINT.2021.04.063.

[94] H. C. Lee and J. Gurland, “Hardness and deformation of cemented tungsten carbide,” *Materials Science and Engineering*, vol. 33, no. 1, pp. 125–133, Apr. 1978, doi: 10.1016/0025-5416(78)90163-5.

[95] S. Sheikh *et al.*, “Fracture toughness of cemented carbides: Testing method and microstructural effects,” *Int J Refract Metals Hard Mater*, vol. 49, no. 1, pp. 153–160, 2015, doi: 10.1016/j.ijrmhm.2014.08.018.

[96] S. v. Emani, C. Wang, L. L. Shaw, and Z. Chen, “On the hardness of submicrometer-sized WC-Co materials,” *Materials Science and Engineering A*, vol. 628, pp. 98–103, Mar. 2015, doi: 10.1016/J.MSEA.2014.12.106.

[97] S. Yadav *et al.*, “Role of binder phase on the microstructure and mechanical properties of a mechanically alloyed and spark plasma sintered WC-FCC HEA composites,” *J Alloys Compd*, vol. 877, p. 160265, Oct. 2021, doi: 10.1016/J.JALLCOM.2021.160265.

[98] L. Ortiz-Membrado, N. Cuadrado, D. Casellas, J. J. Roa, L. Llanes, and E. Jiménez-Piqué, “Measuring the fracture toughness of single WC grains of cemented carbides by means of microcantilever bending and micropillar splitting,” *Int J Refract Metals Hard Mater*, vol. 98, p. 105529, Aug. 2021, doi: 10.1016/J.IJRMHM.2021.105529.

[99] B. Wang, Z. Wang, J. Yuan, Z. Yin, L. Huang, and K. Zheng, “High temperature fracture mechanism of ultrafine WC-Co cemented carbides containing (Ti,W)C,” *Int J Refract Metals Hard Mater*, vol. 95, p. 105428, Feb. 2021, doi: 10.1016/J.IJRMHM.2020.105428.

[100] M. Lee, “High Temperature Hardness of Tungsten Carbide.”

[101] T. Umemoto, Y. Kuriu, S.-I. Nakayama, and O. Miyano, “The bend deformation of WC-CO cemented carbides at temperatures up to 1273K,” *Tetrahedron Lett*, vol. 23, no. 23, pp. 1471–1474, 1982.

[102] A. V. Shatov, S. S. Ponomarev, and S. A. Firstov, “Modeling the effect of flatter shape of WC crystals on the hardness of WC-Ni cemented carbides,” *Int J Refract Metals Hard Mater*, vol. 27, no. 2, pp. 198–212, Mar. 2009, doi: 10.1016/J.IJRMHM.2008.07.008.

[103] W. Acchar, U. U. Gomes, W. A. Kaysser, and J. Goring, “Strength Degradation of a Tungsten Carbide-Cobalt Composite at Elevated Temperatures,” *Mater Charact*, vol. 43, no. 1, pp. 27–32, Jul. 1999, doi: 10.1016/S1044-5803(98)00056-4.

[104] T. Teppernegg *et al.*, “High temperature mechanical properties of WC–Co hard metals,” *Int J Refract Metals Hard Mater*, vol. 56, pp. 139–144, Apr. 2016, doi: 10.1016/J.IJRMHM.2016.01.002.

[105] Z. Hao, Y. Qiu, Y. Fan, and W. Fu, “Theoretical calculation and analysis of new rare earth cemented carbide based on first-principles,” *Int J Refract Metals Hard Mater*, vol. 101, p. 105688, Dec. 2021, doi: 10.1016/J.IJRMHM.2021.105688.

[106] P. J. Joyce, “Two Experiments to Teach Modulus of Elasticity and Modulus of Rigidity,” in *American Society for Engineering Education Annual Conference & Exposition*, 2004.

[107] J. Krautkrämer and H. Krautkrämer, *Ultrasonic Testing of Materials*. Springer Berlin Heidelberg, 1990. doi: 10.1007/978-3-662-10680-8.

[108] X. mei Liu, H. bin Wang, X. yan Song, and R. Moscatteli, “Elastic modulus of nanocrystalline cemented carbide,” *Transactions of Nonferrous Metals Society of China (English Edition)*, vol. 28, no. 5, pp. 966–973, May 2018, doi: 10.1016/S1003-6326(18)64743-0.

[109] T. (Thomas H. C.) Childs, “Metal machining : theory and applications,” p. 408, 2000.

[110] S. Kalpakjian and S. Schmid, *Manufacturing Engineering and Technology*, Sixth Edit. New Jersey, USA: Pearson Prentice Hall, 2006.

[111] P. Smid, *Programming Handbook Third Edition*. 2007.

[112] I. Korkut and M. A. Donertas, “The influence of feed rate and cutting speed on the cutting forces, surface roughness and tool–chip contact length during face milling,” *Mater Des*, vol. 28, no. 1, pp. 308–312, Jan. 2007, doi: 10.1016/J.MATDES.2005.06.002.

[113] Sandvik Coromant UK, “Milling.” Accessed: Oct. 19, 2021. [Online]. Available: https://www.sandvik.coromant.com/en-us/knowledge/machining-formulas-definitions/pages/milling.aspx

[114] H. B. Hübner and A. J. De Souza, “Evaluation of machining forces in asymmetrical face milling of cast iron DIN GGG50,” *Key Eng Mater*, vol. 656–657, pp. 271–276, 2015, doi: 10.4028/WWW.SCIENTIFIC.NET/KEM.656-657.271.

[115] E. Kuram, “Nose radius and cutting speed effects during milling of AISI 304 material,” *http://dx.doi.org/10.1080/10426914.2016.1198019*, vol. 32, no. 2, pp. 185–192, Jan. 2016, doi: 10.1080/10426914.2016.1198019.

[116] G. Y. Zhao, Z. Y. Liu, Y. He, H. J. Cao, and Y. B. Guo, “Energy consumption in machining: Classification, prediction, and reduction strategy,” *Energy*, vol. 133, pp. 142–157, Aug. 2017, doi: 10.1016/J.ENERGY.2017.05.110.

[117] E. Abele, T. Sielaff, A. Schiffler, and S. Rothenbücher, “Analyzing energy consumption of machine tool spindle units and identification of potential for improvements of efficiency,” *Glocalized Solutions for Sustainability in Manufacturing - Proceedings of the 18th CIRP International Conference on Life Cycle Engineering*, pp. 280–285, 2011, doi: 10.1007/978-3-642-19692-8_49/COVER.

[118] “Maximising manufacturing efficiency to minimise the impact of load shedding.” Accessed: Jun. 23, 2023. [Online]. Available: https://www.engineeringnews.co.za/article/maximising-manufacturing-efficiency-to-minimise-the-impact-of-load-shedding-2023-04-04

[119] “CSIR releases statistics on power generation in South Africa for 2022 | CSIR.” Accessed: Jun. 20, 2023. [Online]. Available: https://www.csir.co.za/csir-releases-statistics-on-power-generation-south-africa-2022

[120] A. Vijayaraghavan and D. Dornfeld, “Automated energy monitoring of machine tools,” *CIRP Annals*, vol. 59, no. 1, pp. 21–24, Jan. 2010, doi: 10.1016/J.CIRP.2010.03.042.

[121] Z. Y. Liu, M. P. Sealy, Y. B. Guo, and Z. Q. Liu, “Energy Consumption Characteristics in Finish Hard Milling of Tool Steels,” *Procedia Manuf*, vol. 1, pp. 477–486, Jan. 2015, doi: 10.1016/J.PROMFG.2015.09.007.

[122] A. Dietmair, A. V.- Energy, and undefined 2009, “Energy consumption forecasting and optimisation for tool machines,” *researchgate.net*, doi: 10.17973/MMSJ.2009_03_20090305.

[123] I. D. Marinescu, W. B. Rowe, B. Dimitrov, and H. Ohmori, “Forces, friction, and energy,” *Tribology of Abrasive Machining Processes*, pp. 95–136, Jan. 2013, doi: 10.1016/B978-1-4377-3467-6.00005-7.

[124] B. Ken, “Milling Inserts Shape Up | Cutting Tool Engineering.” Accessed: Nov. 01, 2021. [Online]. Available: https://www.ctemag.com/news/articles/milling-inserts-shape

[125] M. P. Groover, *Fundamentals of Modern Manufacturing: Materials, Processes, and Systems*, Fourth Edi. John Wiley & Sons, Inc, 2009.

[126] “TTM 2019.1 Face Milling.”

[127] J. Teague, “Dependency of machinability in gray cast iron on nitride-induced age strengthening age,” Missouri University of Science and Technology, 2010. Accessed: Oct. 04, 2021. [Online]. Available: https://scholarsmine.mst.edu/doctoral_dissertations/1949

[128] J. Haider, “Health and Environmental Impacts in Metal Machining Processes,” in *Material Science and materials Engineering*, vol. 8, 2014. doi: 10.1016/B978-0-08-096532-1.00804-9.

[129] “TYPES OF CHIPS - My Engineering.” Accessed: Oct. 04, 2021. [Online]. Available: https://myengineerings.com/types-of-chips/

[130] J. A. G. de Sousa, W. F. Sales, and A. R. Machado, “A review on the machining of cast irons,” *International Journal of Advanced Manufacturing Technology*, vol. 94, no. 9–12, pp. 4073–4092, 2018, doi: 10.1007/s00170-017-1140-1.

[131] S. Upadhyay and K. K. Saxena, “Effect of Cu and Mo addition on mechanical properties and microstructure of grey cast iron: An overview,” *Mater Today Proc*, vol. 26, pp. 2462–2470, Jan. 2020, doi: 10.1016/J.MATPR.2020.02.524.

[132] S. Genculu, “Cast Irons-Properties and Applications.”

[133] R. C. Voigt, R. O. Marwanga, and P. H. Cohen, “Machinability of gray iron—Mechanics of chip formation,” *https://doi.org/10.1080/13640461.1999.11819335*, vol. 11, no. 6, pp. 567–572, 1999, doi: 10.1080/13640461.1999.11819335.

[134] N. Tamil Alagan, P. Zeman, P. Hoier, T. Beno, and U. Klement, “Investigation of micro-textured cutting tools used for face turning of alloy 718 with high-pressure cooling,” *J Manuf Process*, vol. 37, pp. 606–616, Jan. 2019, doi: 10.1016/J.JMAPRO.2018.12.023.

[135] M. Stafe, C. Negutu, N. N. Puscas, and I. M. Popescu, *Pulsed laser ablation of solids*, vol. 62, no. 4. 2010.

[136] S. Fang, V. Pérez, N. Salán, D. Baehre, and L. Llanes, “Surface Patterning of Cemented Carbides by Means of Nanosecond Laser,” *https://doi.org/10.1080/10426914.2019.1628268*, vol. 35, no. 2, pp. 123–129, Jan. 2019, doi: 10.1080/10426914.2019.1628268.

[137] K. Jia, T. E. Fischer, and B. Gallois, “Microstructure, hardness and toughness of nanostructured and conventional WC-Co composites,” *Nanostructured Materials*, vol. 10, no. 5, pp. 875–891, 1998, doi: 10.1016/S0965-9773(98)00123-8.

[138] B. Nagarajan, J. Han, S. Huang, J. Qian, J. Vleugels, and S. Castagne, “Femtosecond laser processing of cemented carbide for selective removal of cobalt,” *Procedia CIRP*, vol. 113, pp. 576–581, 2022, doi: 10.1016/J.PROCIR.2022.09.177.

[139] G. Dumitru *et al.*, “Femtosecond laser ablation of cemented carbides: properties and tribological applications,” *Applied Physics A 2004 79:3*, vol. 79, no. 3, pp. 629–632, Aug. 2004, doi: 10.1007/S00339-004-2675-1.

[140] B. Denkena, A. Krödel, A. Heckemeyer, and M. Murrenhoff, “Pulsed laser micro ablation of polycrystalline cubic boron nitride,” *Procedia CIRP*, vol. 94, pp. 823–828, Jan. 2020, doi: 10.1016/J.PROCIR.2020.09.116.

[141] B. Denkena, A. Krödel, L. Ellersiek, and M. Murrenhoff, “Production of chip breakers on cemented carbide tools using laser ablation,” *Procedia CIRP*, vol. 94, pp. 834–839, Jan. 2020, doi: 10.1016/J.PROCIR.2020.09.114.

[142] J. Yan, Y. Murakami, and J. P. Davim, “Tool Design, Tool Wear and Tool Life,” pp. 117–149, 2009, doi: 10.1007/978-1-84628-368-0_5.

[143] Mitsubishi Materials, “Face milling - Cutting edge damage & solutions.” Accessed: Aug. 21, 2023. [Online]. Available: http://www.mitsubishicarbide.com/permanent/courses/73/cutting-edge-damage.html

[144] C. Allen, M. Sheen, J. Williams, and V. A. Pugsley, “The wear of ultrafine WC–Co hard metals,” *Wear*, vol. 250, no. 1–12, pp. 604–610, Oct. 2001, doi: 10.1016/S0043-1648(01)00667-6.

[145] Hellmut. F. Fischmeister, R. Viswanadham, D. Rowcliffe, and J. Gurland (eds.), *Science of Hard Materials*, vol. 54, no. 11. Springer US, 1983. doi: 10.1016/s0026-0657(00)86290-6.

[146] D. Mari and D. R. Gonseth, “A new look at carbide tool life,” *Wear*, vol. 165, no. 1, pp. 9–17, May 1993, doi: 10.1016/0043-1648(93)90366-T.

[147] D. Zhu, X. Zhang, and H. Ding, “Tool wear characteristics in machining of nickel-based superalloys,” *Int J Mach Tools Manuf*, vol. 64, pp. 60–77, Jan. 2013, doi: 10.1016/J.IJMACHTOOLS.2012.08.001.

[148] B. Bhushan, *Principles and Applications of Tribology*, Second., vol. 10. Wiley, 2013.

[149] E. Rabinowicz, L. A. Dunn, and P. G. Russell, “A study of abrasive wear under three-body conditions,” *Wear*, vol. 4, no. 5, pp. 345–355, Sep. 1961, doi: 10.1016/0043-1648(61)90002-3.

[150] K. H. Z. Gahr, “Wear by hard particles,” *Tribol Int*, vol. 31, no. 10, pp. 587–596, Oct. 1998, doi: 10.1016/S0301-679X(98)00079-6.

[151] B. Basu and M. Kalin, *Tribology of Ceramics and Composites: A Materials Science Perspective*. New Jersey, USA: John Wiley & Sons, Inc, 2011. doi: 10.1038/341191b0.

[152] E. M. Trent, “Wear of Metal-Cutting Tools,” *Wear*, vol. 13, pp. 443–489, 1979, doi: 10.1016/S0161-9160(13)70074-7.

[153] C. Ramirez *et al.*, “Understanding the diffusion wear mechanisms of WC-10%Co carbide tools during dry machining of titanium alloys,” *Wear*, pp. 61–70, 2017, doi: 10.1016/j.wear.2017.07.003ï.

[154] A. Bhattacharyya and A. Ghosh, “Diffusion wear of cutting tools,” *Annals of the C.I.R.P*, vol. 15, pp. 369–375, 1968, doi: 10.1016/0301-679x(72)90148-x.

[155] E. M. Trent and M. Met, “Some Factors Affecting Wear on Cemented Carbide Tools,” in *Proceedings of the Institution of Mechanical Engineers*, 1952, pp. 64–74.

[156] A. V. Antsev, “Cutting tool life prediction in case of rough machining by the fracture model,” *Mater Today Proc*, vol. 19, no. xxxx, pp. 2148–2151, 2019, doi: 10.1016/j.matpr.2019.07.229.

[157] M. C. Shaw, *Metal cutting principles*, Second Edi., no. June. Oxford University Press, 2005.

[158] G. Boothroyd and W. Knight, *Fundamentals of Metal Machining and Machine Tools*, Second. Marcel Dekker, 1989.

[159] I. ISO, “3685: Tool-life testing with single-point turning tools,” 1993.

[160] M. S. H. Bhuiyan and I. A. Choudhury, “Review of Sensor Applications in Tool Condition Monitoring in Machining,” *Comprehensive Materials Processing*, vol. 13, pp. 539–569, Jan. 2014, doi: 10.1016/B978-0-08-096532-1.01330-3.

[161] C. J. Rao, D. Nageswara Rao, and P. Srihari, “ Influence of cutting parameters on cutting force and surface finish in turning operation,” *Procedia Eng*, vol. 64, pp. 1405–1415, 2013, doi: 10.1016/j.proeng.2013.09.222.

[162] Z. Deng, L. Lv, W. Huang, and Y. Shi, “A High Efficiency and Low Carbon Oriented Machining Process Route Optimization Model and Its Application,” *International Journal of Precision Engineering and Manufacturing - Green Technology*, vol. 6, no. 1, pp. 23–41, Jan. 2019, doi: 10.1007/S40684-019-00029-0/FIGURES/10.

[163] W. Sun, Y. Zhang, M. Luo, Z. Zhang, and D. Zhang, “A multi-criteria decision-making system for selecting cutting parameters in milling process,” *J Manuf Syst*, vol. 65, pp. 498–509, Oct. 2022, doi: 10.1016/J.JMSY.2022.10.008.

[164] Š. Andelka and A. Puška, “Integrating Multi-Criteria Decision-Making Methods with Sustainable Engineering: A Comprehensive Review of Current Practices,” *Eng 2023, Vol. 4, Pages 1536-1549*, vol. 4, no. 2, pp. 1536–1549, May 2023, doi: 10.3390/ENG4020088.

[165] M. Stojčić, E. K. Zavadskas, D. Pamučar, Ž. Stević, and A. Mardani, “Application of MCDM methods in sustainability engineering: A literature review 2008-2018,” *Symmetry (Basel)*, vol. 11, no. 3, Mar. 2019, doi: 10.3390/SYM11030350.

[166] S. Qu, J. Zhao, and T. Wang, “Experimental study and machining parameter optimization in milling thin-walled plates based on NSGA-II,” *International Journal of Advanced Manufacturing Technology*, vol. 89, no. 5–8, pp. 2399–2409, Mar. 2017, doi: 10.1007/S00170-016-9265-1/METRICS.

[167] J. Yan and L. Li, “Multi-objective optimization of milling parameters C the tradeCoffs between energy, production rate and cutting quality,” *J Clean Prod*, vol. 52, pp. 462–471, 2013, doi: 10.1016/j.jclepro.2013.02.030.

[168] P. Wu, Y. He, Y. Li, J. He, X. Liu, and Y. Wang, “Multi-objective optimisation of machining process parameters using deep learning-based data-driven genetic algorithm

and TOPSIS," *J Manuf Syst*, vol. 64, pp. 40–52, Jul. 2022, doi: 10.1016/J.JMSY.2022.05.016.

[169] N. Zainal, A. M. Zain, N. H. M. Radzi, and M. R. Othman, "Glowworm swarm optimization (GSO) for optimization of machining parameters," *J Intell Manuf*, vol. 27, no. 4, pp. 797–804, Aug. 2016, doi: 10.1007/S10845-014-0914-7/TABLES/7.

[170] G.-H. Tzeng and J.-J. Huang, *Multiple Attribute Decision Making: Methods and Applications*. CRC press, 2011.

[171] S. Chakraborty, "TOPSIS and Modified TOPSIS: A comparative analysis," *Decision Analytics Journal*, vol. 2, p. 100021, Mar. 2022, doi: 10.1016/J.DAJOUR.2021.100021.

[172] S. Chakraborty, A. M.-2018 18th I. Symposium, and undefined 2018, "A novel TOPSIS based consensus technique for multiattribute group decision making," *ieeexplore.ieee.org*, Accessed: Jun. 27, 2023. [Online]. Available: https://ieeexplore.ieee.org/abstract/document/8587952/

[173] "Importance of honing Mitsubishi." Accessed: Jul. 29, 2022. [Online]. Available: https://carbide.mmc.co.jp/permanent/courses/75/importance-of-honing.html

[174] "Preparation Methods for Metallographic Analysis - QATM." Accessed: Jul. 19, 2022. [Online]. Available: https://www.qatm.com/applications/preparation-methods/

[175] D. K. Shetty, I. G. Wright, P. N. Mincer, and A. H. Clauer, "Indentation fracture of WC-Co cermets," *J Mater Sci*, vol. 20, no. 5, pp. 1873–1882, May 1985, doi: 10.1007/BF00555296.

[176] E. Hu and W. Wang, "The Elastic Constants Measurement of Metal Alloy by Using Ultrasonic Nondestructive Method at Different Temperature," 2016, doi: 10.1155/2016/6762076.

[177] L. N. Ofem, "Improving the machinability of Ti-6Al-4V using innovative laser shock peened cemented carbide inserts," University of Witwatersrand, 2019.

[178] AliExpress, "Multi parameter Digital Portable Surface Roughness Meter Gauge Metric Imperial Tester - AliExpress." Accessed: Mar. 01, 2023. [Online]. Available: https://www.aliexpress.com/item/32556539786.html

[179] Y. Zhang and X. Xu, “Machine learning cutting force, surface roughness, and tool life in high speed turning processes,” *Manuf Lett*, vol. 29, pp. 84–89, Aug. 2021, doi: 10.1016/J.MFGLET.2021.07.005.

[180] K. Xu *et al.*, “Advanced Data Collection and Analysis in Data-Driven Manufacturing Process,” *Chinese Journal of Mechanical Engineering*, vol. 33, no. 1, p. 43, Dec. 2020, doi: 10.1186/s10033-020-00459-x.

[181] L. Sun, T. Yang, C. Jia, and J. Xiong, “VC, Cr3C2 doped ultrafine WC–Co cemented carbides prepared by spark plasma sintering,” *Int J Refract Metals Hard Mater*, vol. 29, no. 2, pp. 147–152, Mar. 2011, doi: 10.1016/J.IJRMHM.2010.09.004.

[182] X. Wang, H. E. Xiaoxiang, and G. Hailiang, “Influence of Mo on the microstructure and mechanical properties of TiC-based cermets,” *Rare Metals*, vol. 29, no. 4, p. 346, 2010, doi: 10.1007/s12598-010-0127-y.

[183] R. M. Genga *et al.*, “Effects of Mo2C, Ni binder and laser surface modification on WC inserts for turning Ti-6Al-4V,” *Int J Refract Metals Hard Mater*, vol. 87, p. 105145, Feb. 2020, doi: 10.1016/j.ijrmhm.2019.105145.

[184] D. Hübler and T. Gradt, “Effect of different binders and secondary carbides on NbC cermets,” *Forschung im Ingenieurwesen/Engineering Research*, vol. 86, no. 2, pp. 197–211, Jun. 2022, doi: 10.1007/S10010-022-00583-1/FIGURES/12.

[185] S. Kim, S. H. Han, J. K. Park, and H. E. Kim, “Variation of WC grain shape with carbon content in the WC–Co alloys during liquid-phase sintering,” *Scr Mater*, vol. 48, no. 5, pp. 635–639, Mar. 2003, doi: 10.1016/S1359-6462(02)00464-5.

[186] M. Labonne *et al.*, “Sintering behavior and microstructural evolution of NbC-Ni cemented carbides with Mo2C additions,” *Int J Refract Metals Hard Mater*, vol. 92, p. 105295, Nov. 2020, doi: 10.1016/J.IJRMHM.2020.105295.

[187] S. G. Huang, J. Vleugels, H. Mohrbacher, and M. Woydt, “Microstructure and mechanical properties of NbC matrix cermets using Ni containing metal binder,” *Metal Powder Report*, vol. 71, no. 5, pp. 349–355, 2016, doi: 10.1016/j.mprp.2016.05.009.

[188] A. Ul-Hamid, *A Beginners’ Guide to Scanning Electron Microscopy*. Switzerland: Springer Nature, 2018.

[189] N. Lin, C. H. Wu, Y. H. He, and D. F. Zhang, “Effect of Mo and Co additions on the microstructure and properties of WC-TiC-Ni cemented carbides,” *Int J Refract Metals Hard Mater*, vol. 30, no. 1, pp. 107–113, Jan. 2012, doi: 10.1016/j.ijrmhm.2011.07.011.

[190] S. G. Huang, J. Vleugels, H. Mohrbacher, and M. Woydt, “NbC grain growth control and mechanical properties of Ni bonded NbC cermets prepared by vacuum liquid phase sintering,” *Int J Refract Metals Hard Mater*, vol. 72, pp. 63–70, Apr. 2018, doi: 10.1016/J.IJRMHM.2017.12.013.

[191] R. Warren, “Microstructural Development During the Liquid-Phase Sintering of Two-Phase Alloys, with Special Reference to the NbC/Co System,” *Journal of Materials Science* , vol. 3, pp. 471–485, 1968.

[192] J. Hegeman, Jt. De Hosson, and G. de With, “Grinding of WC-Co hardmetals,” *Wear*, vol. 248, pp. 187–196, 2001.

[193] R. M. Genga, G. Akdogan, J. E. Westraadt, and L. A. Cornish, “Microstructure and material properties of PECS manufactured WC-NbC-CO and WC-TiC-Ni cemented carbides,” *Int J Refract Metals Hard Mater*, vol. 49, no. 1, pp. 240–248, 2015, doi: 10.1016/j.ijrmhm.2014.07.030.

[194] S. G. Huang, J. Vleugels, H. Mohrbacher, and M. Woydt, “NbC grain growth control and mechanical properties of Ni bonded NbC cermets prepared by vacuum liquid phase sintering,” *Int J Refract Metals Hard Mater*, vol. 72, pp. 63–70, Apr. 2018, doi: 10.1016/J.IJRMHM.2017.12.013.

[195] P. Ettmayer, H. Kolaska, W. Lengauer, and K. Dreyer, “Ti(C,N) cermets — Metallurgy and properties,” *Int J Refract Metals Hard Mater*, vol. 13, no. 6, pp. 343–351, Jan. 1995, doi: 10.1016/0263-4368(95)00027-G.

[196] S. G. Huang *et al.*, “Tailoring Microstructure and Mechanical Properties of NbC-Ni Matrix Cermets for Wear Resistance Applications,” in *20th Plansee Seminar, Reutte*, 2022.

[197] L. Zhang *et al.*, “Fine platelet-like grained WC–Co cemented carbides: Preparation, characterization, properties and application in PVD coating substrates,” *Int J Refract Metals Hard Mater*, vol. 64, pp. 135–142, Apr. 2017, doi: 10.1016/j.ijrmhm.2017.01.015.

[198] C. Qian, K. Li, X. yi Guo, B. Liu, Z. yi Long, and Y. Liu, “Effect of WC grain size on mechanical properties and microstructures of cemented carbide with medium entropy alloy Co-Ni-Fe binder,” *J Cent South Univ*, vol. 27, no. 4, pp. 1146–1157, Apr. 2020, doi: 10.1007/S11771-020-4355-5/METRICS.

[199] J. L. Chermant and F. Osterstock, “Fracture toughness and fracture of WC-Co composites,” 1976.

[200] S. R. Agnew, L. Dong, J. I. Keene, and H. N. G. Wadley, “Mechanical properties of large TiC-Mo-Ni cermet tiles,” *Int J Refract Metals Hard Mater*, vol. 75, pp. 238–247, Sep. 2018, doi: 10.1016/J.IJRMHM.2018.05.005.

[201] G. Ljustina, R. Larsson, and M. Fagerström, “A FE based machining simulation methodology accounting for cast iron microstructure,” *Finite Elements in Analysis and Design*, vol. 80, pp. 1–10, Mar. 2014, doi: 10.1016/J.FINEL.2013.10.006.

[202] L. R. R. Da Silva *et al.*, “Cutting Temperatures in End Milling of Compacted Graphite Irons,” in *46th SME North American Manufacturing Research Conference, NAMRC 46, Texas, USA*, Elsevier B.V., 2018, pp. 474–484. doi: 10.1016/j.promfg.2018.07.056.

[203] A. Senthil Kumar, A. Raja Durai, and T. Sornakumar, “The effect of tool wear on tool life of alumina-based ceramic cutting tools while machining hardened martensitic stainless steel,” *J Mater Process Technol*, vol. 173, no. 2, pp. 151–156, Apr. 2006, doi: 10.1016/J.JMATPROTEC.2005.11.012.

[204] M. B. Da Silva, V. T. G. Naves, J. D. B. De Melo, C. L. F. De Andrade, and W. L. Guesser, “Analysis of wear of cemented carbide cutting tools during milling operation of gray iron and compacted graphite iron,” *Wear*, vol. 271, no. 9–10, pp. 2426–2432, Jul. 2011, doi: 10.1016/J.WEAR.2010.11.030.

[205] F. Klocke, G. Eisenblätter, and T. Krieg, “Machining: Wear of Tools,” *Encyclopedia of Materials: Science and Technology*, pp. 4708–4711, Jan. 2001, doi: 10.1016/B0-08-043152-6/00821-4.

[206] J. Xie, M. J. Luo, K. K. Wu, L. F. Yang, and D. H. Li, “Experimental study on cutting temperature and cutting force in dry turning of titanium alloy using a non-coated micro-grooved tool,” *Int J Mach Tools Manuf*, vol. 73, pp. 25–36, Oct. 2013, doi: 10.1016/J.IJMACHTOOLS.2013.05.006.

[207] Z. Guo, J. Xiong, M. Yang, X. Song, and C. Jiang, “Effect of Mo2C on the microstructure and properties of WC-TiC-Ni cemented carbide,” vol. 26, pp. 601–605, 2008, doi: 10.1016/j.ijrmhm.2008.01.007.

[208] N. T. Alagan, T. Beno, P. Hoier, U. Klement, and A. Wretland, “Influence of surface features for increased heat dissipation on tool wear,” *Materials*, vol. 11, no. 5, Apr. 2018, doi: 10.3390/ma11050664.

[209] N. Kawasegi, H. Sugimori, H. Morimoto, N. Morita, and I. Hori, “Development of cutting tools with microscale and nanoscale textures to improve frictional behavior,” *Precis Eng*, vol. 33, no. 3, pp. 248–254, Jul. 2009, doi: 10.1016/J.PRECISIONENG.2008.07.005.

[210] Z. Fang and T. Obikawa, “Cooling performance of micro-texture at the tool flank face under high pressure jet coolant assistance,” *Precis Eng*, vol. 49, pp. 41–51, Jul. 2017, doi: 10.1016/J.PRECISIONENG.2017.01.008.

[211] R. M. Genga *et al.*, “Laser Shock Peening: A NbC Based Cermet Enhancement Alternative for Improved GCI interrupted face-milling,” in *22nd International Conference on Competitive Manufacturing*, 2023.

[212] J. V. C. Souza, M. C. A. Nono, M. V. Ribeiro, J. P. B. Machado, and O. M. M. Silva, “Cutting forces in turning of gray cast iron using silicon nitride based cutting tool,” *Mater Des*, vol. 30, no. 7, pp. 2715–2720, Aug. 2009, doi: 10.1016/J.MATDES.2008.09.041.

[213] S. N. Grigoriev, S. V. Fedorov, and K. Hamdy, “Materials, properties, manufacturing methods and cutting performance of innovative ceramic cutting tools - A review,” *Manufacturing Review*, vol. 6. EDP Sciences, 2019. doi: 10.1051/mfreview/2019016.

[214] T. Sornakumar, M. V. Gopalakrishnan, R. Krishnamurthy, and C. V. Gokularathnam, “Development of alumina and Ce-TTZ ceramic-ceramic composite (ZTA) cutting tool,” *Int J Refract Metals Hard Mater*, vol. 13, no. 6, pp. 375–378, Jan. 1995, doi: 10.1016/0263-4368(95)00026-F.

A. Appendix:

Research outputs

EFFECT OF FEMTOSECOND LASER SURFACE MODIFIED WC AND NBC BASED INSERTS DURING THE FACE-MILLING OF AUTOMOTIVE GREY CAST IRON (A-GCI)

M. Rabothata[1,2]*, R. Genga[1,2,5], N. Mphasha[1,2], K. Phaka[2], N. Nelwalani[3], S. Ngongo[4], C. Polese[2,5], S. Huang[6], J. Vleugels[6], P. Zeman[7]

[1]Academic Development Unit, Wits University, South Africa
[2]School of Mechanical, Industrial and Aeronautical Engineering, Wits University, South Africa
[3]School of Mining, Metallurgy and Chemical Engineering, University of Johannesburg, South Africa
[4]CHRTEM, Nelson Mandela University, South Africa
[5]DSI-NRF CoE in Strong Materials, South Africa
[6]Department of Materials Engineering, KU Leuven, Belgium
[7] RCMT, Czech Technical University, Czech Republic
* Corresponding author: Mahlatse.Rabothata@wits.ac.za

ABSTRACT

The goal of this study was to design, develop, and produce NbC-Ni based cermet inserts as a potential substitute for conventional WC-Co based inserts for face-milling machining of automotive grey cast iron (a-GCI) which is used for several automotive applications including engine cylinder blocks, fly wheels, clutch plates, and brake discs [1]. As such, the material plays a critical role in the automotive manufacturing industry. Cermets are hardmetals consisting of a predominant hard but relatively brittle carbide phase (WC, TiC) and a metallic reinforcement binder (Co, Ni, Fe) [2]. The WC-Co cutting inserts have been reported to exhibit poor chemical stability during the machining of steels and cast irons due to iron's higher affinity for carbon than tungsten [2], resulting in chemical wear and consequently reduced insert tool life. Furthermore, there has been concerns over WC-Co growing supply risks and unstable market prices [3]. Hence, alternatives such as NbC have been investigated [4]. Niobium carbide has a lower solubility in steels and cast irons than WC [5], slightly lower room temperature hardness than WC, but a significantly higher melting temperature. In addition, NbC has better high-temperature properties to WC and lower density [3, 4]. Nickel can improve hot hardness and resistance to thermal cracking in NbC-based cermets [6]. Molybdenum has been reported to improve the wetting behavior of the binder during sintering. This improved wettability creates a diffusion gradient through the liquid-solid interface enables Mo to diffuse freely into the carbide phase. Consequently, leading to a reduction in interfacial energy during sintering, and improving the bonding between the carbide and binder phases [2]. Furthermore, the addition of Mo has been linked to improved material's hardness properties, and densification [2]. In this study, pulsed electric sintering (PECS), additions of Mo as a partial binder replacement, and TiC and TiCN as secondary hard phases, and femtosecond laser surface modification (LSM) were used in an attempt to improve the machining performance of NbC-Ni cutting inserts during face-milling of a-GCI. For this purpose, cutting inserts with various compositions were produced via liquid phase sintering (LPS) and PECS techniques. The surfaces of the insert cutting edges were modified using femtosecond lasers to create pyramid-LSM (P-LSM) and shark skin-LSM (S-LSM) based micro-patterns.

All the sintered samples, irrespective of the sintering process, had relative densities of above 97%. The LPS WC-10TiC-10[Co/Mo] (wt.%) sample had finest grain sizes compared to all the NbC samples. The fine grains in the WC-based sample were due to TiC addition (which was not fully dissolved during sintering), the partial substitution of Co by Mo, and homogeneously distributed binder pools due to formation of Co-liquid during sintering [2].The PECS produced NbC-Ni based samples had fine grains with higher contiguity and poor binder distribution due to significantly lower sintering temperatures and shorter sintering times than LPS [3, 4]. Additions of Mo, TiC, and TiC_7N_3, to the NbC-12Ni (wt.%) composition reduced the NbC grain size in PECS samples due to grain growth inhibition [2]. Molybdenum fully dissolved during sintering and was detected to be inside the carbide phases of samples by high angular annular dark field (HAADF)-scanning electron transmission microscopy (STEM). Unlike in the LPS samples, TiC and TiC_7N_3, did not fully dissolve

in the NbC grains in NbC-10TiC-12Ni (wt.%), NbC-10TiC-12[Ni/Mo] (wt.%) and NbC-10TiC$_7$N$_3$-12Ni (wt.%) in the PECS samples due to lower sintering temperatures and time [4]. Face-milling tests were conducted at cutting speed (v_c) of 200m/min, depth of cut (a_p) of 1 mm, and feed rate of 0.1 mm/tooth. The main wear mechanisms of cutting inserts during a-GCI machining were characterized by abrasion wear, attrition wear and mechanical fracture. The PECS NbC-10TiC-12[Ni/Mo] (wt.%) S-LSM insert had the lowest flank wear rate (FWR) (1.33 µm/min) among all the inserts with maximum flank wear (VBmax) of 26.67 µm after 20 minutes of machining. This was followed closely by the P-LSM insert of similar composition, and the LPS WC-10TiC-10[Co/Mo] blank (B) insert, with FWRs of 1.44 µm/min and 1.97 µm/min, after 20 minutes of machining respectively. The low FWRs in the PECS samples were attributed to improved surface hardness and cutting edge strengthening due to a formation of a LSM self-carbide coating layer [4], and the good distribution of the nano-sized Ni binder pools (see the HAADF-STEM mapping of PECS NbC-10TiC-12[Ni/Mo] (wt.%) S-LSM insert cutting edge/workpiece interface in Figure 1). The low FWR of the WC-based insert was due to the good combinations of hardness and fracture toughness as well as the presence of undissolved TiC that improved wear resistance [2]. The PECS NbC-12[Ni/Mo] (wt.%) B insert was enhanced by ~ 300% and 900%, respectively, by using the S-LSM and P-LSM micro-patterns. The FWRs were also decreased from 21.04 µm/min after 2 minutes of machining to 5.97 µm/min and 1.94 µm/min after 8 minutes and 20 minutes, respectively. In general, PECS, LSM and additions of Mo, TiC and TiC$_7$N$_3$ improved the wear performance of NbC-Ni based inserts. Thus, increasing insert tool life and reducing the FWRs resulting in better machining performance at semi-finishing conditions of a-GCI.

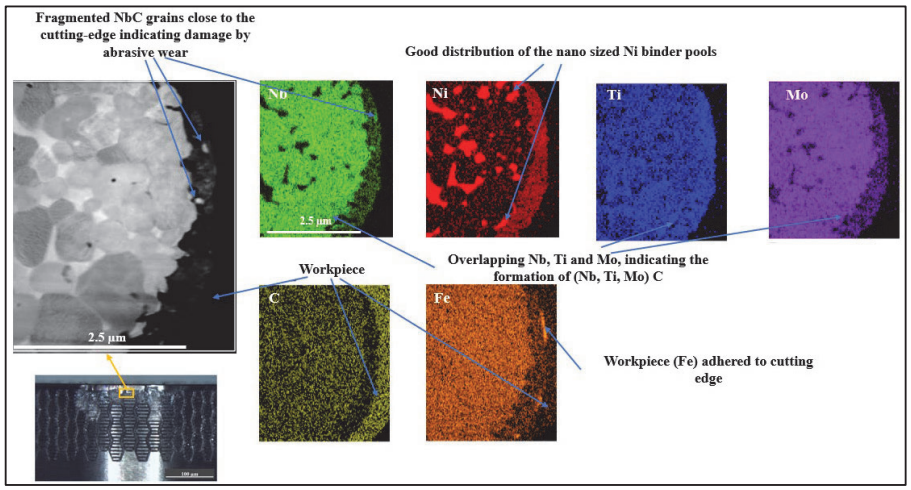


Figure 1. HAADF-STEM map of a cross-section of PECS NbC-10TiC-12[Ni/Mo] (wt.%) S-LSM cutting edge/workpiece interface showing: Nb (green), Ni (red), Ti (blue), Mo (purple), C (yellow), and Fe (orange).

REFERENCES

[1] M. O. Genç and Ç. Imer, "Graphite flake size effects to thermal durability of automobile flywheel under forced slippage," *Proceedings of the World Congress on Mechanical, Chemical, and Material Engineering*, pp. 1–8, 2017.

[2] G. S. Upadhyaya, D. R. Tobergte, and S. Curtis, *Cemented Tungsten Carbides: Production, Properties, and Testing*. Kanpur, India: Indian Institute of Technology, 1998.

[3] A. Rizzo *et al.*, "The critical raw materials in cutting tools for machining applications: A review," *Materials*, vol. 13, no. 6, pp. 1–48, 2020.

[4] R. M. Genga *et al.*, "Roughing, semi-finishing and finishing of laser surface modified nickel bonded NbC and WC inserts for grey cast iron (GCI) face-milling," *Int J Refract Metals Hard Mater*, vol. 86, no. June 2019.

[5] R. M. Genga, L. A. Cornish, M. Woydt, A. Janse van Vuuren, and C. Polese, "Microstructure, mechanical and machining properties of LPS and SPS NbC cemented carbides for face-milling of grey cast iron," *Int J Refract Metals Hard Mater*, vol. 73, pp. 111–120, 2018.

[6] K. Sarin, Vinod, D. Mari, and L. Llanes, *Comprehensive Hard Materials*. Oxford UK: Elsevier, 2014.

TOOL LIFE OF NbC-BASED CERMETS DURING FACE MILLING OF AUTOMOTIVE GCI

M.S. Rabothata[1,2], N.P. Mphasha[1,2], K. Phaka[2], P. Zeman[3], R.M Genga[1,2,4], C. Polese[2,4], S. Huang[5] and J. Vleugels[5]

[1]Academic Development Unit, Wits University, [2]School of Mechanical, Industrial and Aeronautical Engineering, Wits University, [3]Research Centre of Manufacturing Technology, Czech Technical Universiy in Prague, [4]DSI-NRF Centre of Excellence in Strong Materials, Wits University, [5]Department of Materials Engineering, KU Leuven

Cermets, also known as cemented carbides, consist of a predominant hard but relatively brittle carbide phase (WC, TiC) and a metallic reinforcement binder (Co, Ni or Fe)[1]. Albeit the extensive use of WC-Co cemented carbides in tribological applications, niobium carbide (NbC) has been explored as replacement for tungsten carbide (WC). This is mainly due to the growing supply risks and unstable market prices associated with both WC and Co[2]. Furthermore, WC-Co cutting tools exhibit poor chemical stability during machining of steels and cast irons[3].

NbC has better high temperature properties than WC[4]. Nickel can retain its ductile FCC structure at below solidus temperatures[5]. Additionally, Ni has better resistance to corrosion and oxidation compared to Co and can improve hot hardness and resistance to thermal cracking in NbC-based cemented carbides[4]. Despite the promising properties exhibited by both NbC and Ni, NbC-based cutting tools produced by conventional liquid phase sintering (LPS) methods yield low hardness and fracture toughness compared to the WC-Co based cutting tools[6]. Hence, rapid pulsed electric current sintering (PECS) techniques are now used to improve the properties of NbC-based cermets. In this study, the effects of titanium carbide (TiC) and titanium carbonitride (TiC_7N_3) additions as grain growth inhibitors and secondary hardening phases[1,6], and laser surface modification (LSM) on tool life performance during dry face-milling of automotive grey cast iron (GCI) were investigated.

For this purpose, cutting inserts produced by PECS with powder compositions (i) NbC-12Ni (wt%) (N2S), (ii) NbC-10TiC-12Ni (wt%) (R2S), and (iii) NbC-10TiC_7N_3-12Ni (wt%) (TCN1S), were used. A LD50C femtosecond laser was used to create shark skin (S) and pyramid (P) patterns on the cutting edges of the inserts. Machining tests were carried out on a MAHO MH70 milling machine using the milling conditions given in Table 1. The feed (f) of 0.1 mm/tooth and the radial depth of cut (a_r) of 80 mm defined by the diameter of the insert holder (F75SN12080) were kept at constant for all cutting conditions. The machining forces were measured using a Kistler force dynamometer and, the flank wear and crater wear were evaluated using a Nikon optical microscope.

The additions of both TiC and TiC_7N_3 reduced the tool life of the blank (N2S) cutting inserts, from 20 min to 8 min (R2S) and 6 min (TCN1S), respectively. This was attributed to the increased hardness (HV_{30}) and reduced fracture toughness (K_{IC}) in R2S and TCN1S due to those additions[1,6]. The resultant cutting forces in all inserts increased by ≥1% thanks to LSM. Further, LSM improved tool life irrespective of the composition, enabling the inserts to complete the machining duration of 20 min. The flank wear rates (FWR's) of all inserts was < 6.5µm/min and LSM reduced the flank wear rate (FWR) of all the inserts except for N2S (S). The improved tool life and reductions in FWR can be attributed to self-carbide coating layers produced during LSM and resulting in enhanced abrasion and attrition wear resistance in the cutting inserts[6]. Fig. 1 shows the optical microscopic images of the maximum flank wear (VBmax) of (a) N2S, (b) TCN1S (S) and (c) R2S (P) cutting edges, including the respective crater wear (d).

References:
1. Upadhyaya, G.S. (1998) Cemented Tungsten Carbide Production, Properties and Testing. Kanpur, Indian Institute of Technology
2. Rizzo, A. *et al*. (2020) Materials, 13
3. Woydt, M. and Mohrbacher, H. (2015) Int. J. Refract. Met & Hard Mat, 49
4. Sarin, V. *et al*. (2014) Comprehensive Hard Materials. UK, Elsevier
5. Penrice, T.W. (1987) J. Mater. Shaping Technol. 5,35
6. Genga, R.M. *et al*. (2020) Int. J. Refract. Met & Hard Mat, 86 (105128)

Table 1. Face-milling test parameters

Cutting speed (m/min)	Depth of cut, a_p (mm)	Spindle speed (rpm)	Feed rate (mm/min)
200	1	800	80

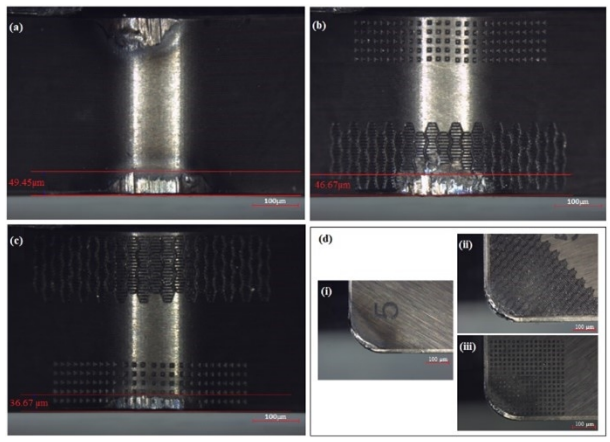


Figure 1. Optical microscopy images showing VBmax of (a) N2S, (b) TCN1S (S) and (c) R2S (P), and (d) the crater wear of the respective cutting edges.

Corresponding author: mahlatse.rabothata@wits.ac.za

EFFECTS OF TiC_7N_3 ADDITIONS AND SINTERING TECHNIQUE ON THE MICROSTRUCTURAL PROPERTIES OF NbC-BASED CERMETS

M.S. Rabothata[1,2], N.P. Mphasha[1,2], R.M. Genga[1,2,3], C. Polese[2,3], P. Zeman[4], S. Huang[5], J. Vleugels[5], A. Janse van Vuuren[6] and N.B. Nelwalani[7]

[1]Academic Development Unit, University of the Witwatersrand, Johannesburg, [2]School of Mechanical, Industrial and Aeronautical Engineering, University of the Witwatersrand, Johannesburg, [3]DSI-NRF Centre of Excellence in Strong Materials, University of the Witwatersrand, Johannesburg, [4]Research Centre of Manufacturing Technology, Czech Technical University in Prague, Czech Republic, [5]Department of Materials Engineering, KU Leuven, Belgium, [6]CHRTEM, Nelson Mandela University, Port Elizabeth, [7]School of Mining, Metallurgy and Chemical Engineering, University of Johannesburg, Johannesburg

Traditionally, cemented carbides consisting of tungsten carbide (WC) bonded with a ductile cobalt (Co) matrix are used in rock drilling, metal machining, and mining[1]. Extensive use of WC-Co parts in engineering applications is due to their superior mechanical properties and excellent wear resistance. However, due to supply constraints and fluctuating market prices for WC and Co, niobium carbide (NbC) and nickel (Ni) have been studied as alternative materials[2,3]. NbC has comparable Vickers (HV_{30}) hardness (~19.6 GPa) to WC (~22.4 GPa) and offers good high-temperature chemical stability[3]. At all temperatures below the solidus (1454.85 °C), nickel retains its ductile face-centered cubic (fcc) structure, providing good high-temperature properties[3]. Spark plasma sintering (SPS) and the inclusion of TiC_7N_3 as a secondary hardening phase can improve the hardness and abrasion resistance of NbC cemented carbides[1].

To study the effect of TiC_7N_3additions on the microstructural and mechanical properties of NbC-based cemented carbides, powders with compositions NbC-12Ni (wt%) (N2-S), NbC-10TiC_7N_3-12Ni (wt%.) (TCN1-S) and NbC-10TiC_7N_3-12Ni (wt%.) (TCN1-L), were investigated. N2-S and TCN1-S were prepared by SPS, while TCN1-L was prepared by liquid phase sintering (LPS). The sintered samples were characterised by optical microscopy, scanning electron microscopy (SEM), and annular dark field (ADF) scanning transmission electron microscopy (STEM).

The backscattered SEM image of N2-S shows smaller carbide grains with poor binder distribution, see Fig. 1. This can be attributed to the lower sintering temperature and shorter dwell time during SPS, which prevented continuous Ostwald ripening. Better densification was achieved for TCN1-L (98.51%) than TCN1-S (97.63%), due to sufficient inter-diffusion between TiC_7N_3, NbC, and Ni during LPS resulting in smaller and more evenly distributed Ni binder pools, see Fig. 2. The addition of TiC_7N_3 resulted in higher Vickers hardness values irrespective of the sintering technique (Table 1). However, TCN1-S had higher hardness than TCN1-L due to restricted inter-diffusion of TiC_7N_3 owing to shorter dwell times during SPS, resulting in undissolved hard phases. The increase in fracture toughness (K_{IC}) during LPS of TCN1-L is ascribed to better binder distribution and the inter-diffusion of NbC and TiC_7N_3 grains into each other. Microstructure evolution revealed that the additions of TiC_7N_3 may be beneficial in improving the material properties of NbC-based cemented carbides, especially in LPS.

References:
1. Upadhyaya, G.S. (1998) Cemented Tungsten Carbide Production, Properties and Testing. USA, Noyes Publications.
2. Penrice, T.W. (1987) J. Mater. Shaping Technol. 5, 35.
3. Genga, R.M. *et al.* (2018) Int. J. Refract. Met. Hard Mater. 73, 111.

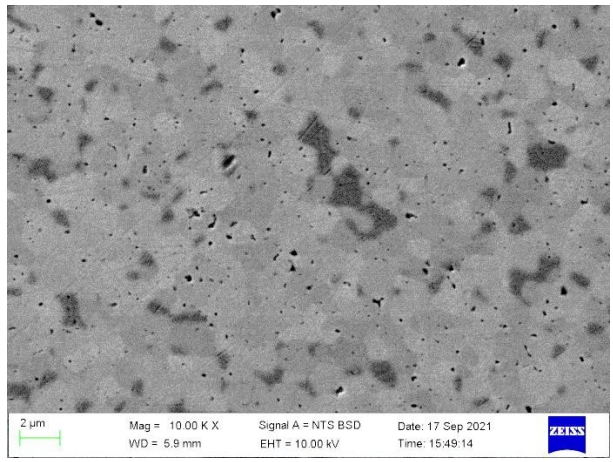


Figure 1. SEM-BSE image of N2-S, showing NbC (light) and Ni (dark) with smaller NbC particles

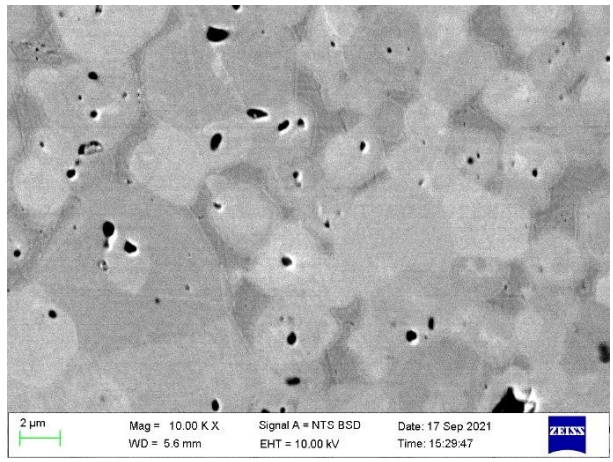


Figure 2. SEM-BSE image of TCN1-L, showing NbC (light) and Ni (dark) with more rounded NbC particles

Table 1. Mechanical properties of NbC-based materials

Grade	HV_{30} (GPa)	K_{IC} (MPa·$m^{0.5}$)
N2-S	11.73±0.33	5.72±0.10
TCN1-S	13.70±0.32	5.50±0.06
TCN1-L	12.77±0.13	9.31±0.53

Corresponding author: 673306@students.wits.ac.za

Physical, Microstructure, and Mechanical Property Effects of Molybdenum Addition to NbC-TiC-Ni and WC-TiC-Co Cermet Binders

M. Rabothata*,**, N. Mphasha***, N. Nelwalani****, A. Janse van Vuuren*****, R.M. Genga*,**,******, C. Polese**,******, S. Huang*******, J. Vleugels*******

*Academic Development Unit (ADU), University of the Witwatersrand, South Africa
**School of Mechanical, Industrial, and Aeronautical Engineering, University of the Witwatersrand, South Africa
***School of Chemical and Metallurgical Engineering, University of the Witwatersrand, South Africa
****School of Mining, Metallurgy and Chemical Engineering, University of Johannesburg, South Africa
*****CHRTEM, Nelson Mandela University, South Africa
******DSI-NRF Centre of Excellence in Strong Materials, University of the Witwatersrand, South Africa
*******Department of Materials Engineering (MTM), KU Leuven

Abstract

The effects of liquid phase sintering (LPS) and pulsed electric current sintering (PECS), the addition of TiC as a secondary hardening phase, and 30 wt% of binder phase substitution by Mo were investigated to improve the physical, microstructure, and mechanical properties of NbC-Ni and WC-Co based cermets. Grain size refinement was achieved through additions of TiC and Mo as well as PECS, with reductions from ~4.6 μm to ~1.3 μm in NbC cermets, giving an HV_{30} hardness >14 GPa and fracture toughness (K_{IC}) > 6 MPa.$m^{0.5}$. Molybdenum addition had contrasting effects on densification in NbC compositions for the PECS technique. The Ni/Mo (70/30) binder phase however improved the K_{IC} in all NbC cermets. Microstructure analyses were conducted by high-resolution scanning electron microscopy (SEM), and Transmission electron microscopy (TEM) to better understand the role and the location of Mo in the binder phase.

Keywords

NbC, PECS, Molybdenum, Hardness, Fracture Toughness, Cermets

ENERGY CONSUMPTION OF NbC BASED INSERTS DURING FACE MILLING OF AUTOMOTIVE GCI

M.S. Rabothata[1,2], R.M. Genga[1,2,3], N.P. Mphasha[4], K. Phaka[2], P. Zeman[5], C. Polese[2,3], S. Huang[6], J. Vleugels[6], S. Ngongo[7]

[1]Academic Development Unit, [2]School of Mechanical, Industrial and Aeronautical Engineering, Wits University, [3]DSI-NRF Centre of Excellence in Strong Materials, [4]School of Chemical and Metallurgical Engineering, Wits University, [5]Materials Research Centre of Manufacturing Technology, Czech Technical University in Prague, Czech Republic, [6]Department of Materials Engineering, KU Leuven, [7]CHRTEM, Nelson Mandela University, South Africa

Over the past decade, South Africa has struggled with significant energy generation and supply challenges, leading the country's power utility to implement various stages of load shedding. In 2023, the situation reached a record low, making it the worst year to date. Like any sector, the automotive manufacturing industry has been severely harmed by the energy crisis. Hence, in this study, the effects of molybdenum (Mo), titanium carbide (TiC) and Mo plus TiC additions as grain growth inhibitors and secondary hardening phases, and femtosecond laser surface modification (f-LSM) on energy consumption and machining performance of niobium carbide (NbC) based cermets during dry face-milling of automotive grey cast iron (a-GCI) were investigated.

A LD50C femtosecond laser was used to create shark skin (S) and pyramid (P) micro textures (patterns) on the cutting edges of inserts produced from pulsed electric current sintering (PECS) NbC-12Ni (N2S), NbC-12[Ni/Mo] (N2MS), NbC-10TiC-12Ni (R2S), and NbC-10TiC-12[Ni/Mo] (R2MS). During the dry face-milling of a-GCI, the feed (f) was 0.1 mm/tooth, the cutting speed (v_c) was 200 /min, depth of cut (a_p) was 1 mm, and the spindle speed was 800 (rpm). The machining forces were measured using a Kistler force dynamometer and, the flank wear and crater wear were evaluated by optical microscopy, scanning electron microscopy (SEM), and high angular annular dark-field (HAADF)-scanning transmission electron microscopy (STEM). Regardless of composition, Mo fully dissolved during sintering and was detected to be inside the carbide phases of samples by HAADF- STEM. In contrast, TiC did not fully dissolve in both R2S and R2MS as shown by the EDS mapping in Figure 1. The undissolved TiC has been reported to enhance hardness and abrasion wear resistance of cutting inserts, improving the performance of inserts during machining[1].

The P-R2MS insert had the lowest energy consumption (U_c) (22.07 J/mm^3) whilst its shark skin counterpart S-R2MS exhibited the highest U_c compared to all the other inserts. In general, the P- micro textured cutting inserts had relatively lower energy consumption than the S- micro textured inserts. This was attributed to the entrapment of relatively higher volumes of chips on the S- textured inserts during machining which increased the cutting forces that are directly proportional to energy consumption. Figure 2 shows optical images of the flank and rake faces of P-R2MS and S-R2MS inserts after 20 minutes of dry face-milling. The main wear mechanisms of cutting inserts during a-GCI machining were characterized by abrasion wear, attrition wear and mechanical fracture. All the cutting inserts apart from S-N2MS achieved the maximum insert tool life of 20 minutes. This exceptional performance was attributed to the S- and P- micro textures by f-LSM technique which improved the hardness, strengthened the cutting edges of the inserts and enhanced abrasion wear resistance[1].

References:

1. Genga et al.,(2019) Int. J. Refract. Met & Hard Mat, 86.

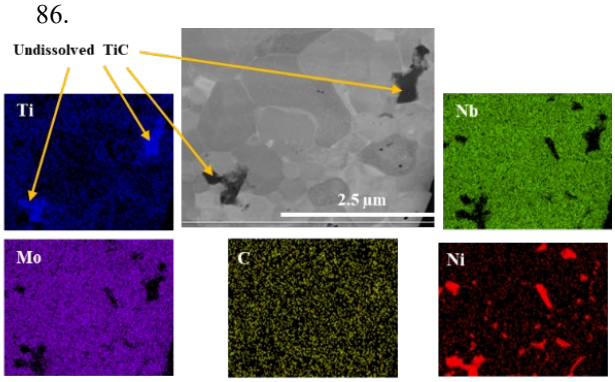


Figure 1. HAADF-STEM image and EDS maps of NbC-10TiC-12[Ni/Mo] (R2MS).sample. showing: Nb (green), Ni (red), Mo (purple), C (yellow), and Ti (blue).

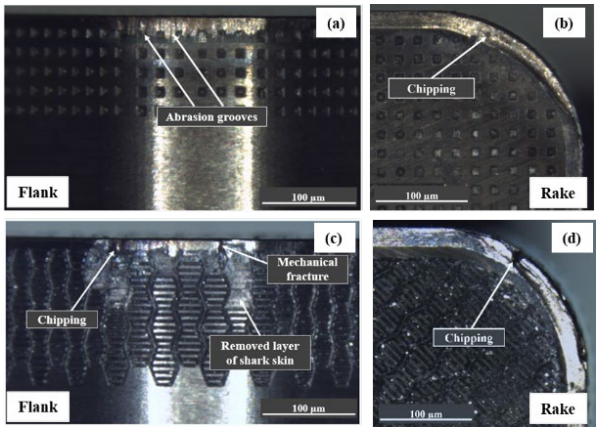


Figure 2. Optical images of (a) flank (b) rake faces of P-R2MS insert, and (c) flank and (d) rake faces of S-R2MS.

Corresponding author: *mahlatse.rabothata@wits.ac.za*